UNIVERSIDAD COMPLUTENSE DE MADRID
FACULTAD DE CIENCIAS FÍSICAS

TESIS DOCTORAL

Análisis de la producción y propagación de la luz de centelleo en el detector de doble-fase WA105

Analysis of the scintillation light production and propagation in the WA105 Dual-Phase demonstrator

MEMORIA PARA OPTAR AL GRADO DE DOCTOR

PRESENTADA POR

Chiara Filomena Lastoria

Directora

Carmen Palomares Espiga

Madrid

UNIVERSIDAD COMPLUTENSE DE MADRID

FACULTAD DE CIENCIAS FÍSICAS

TESIS DOCTORAL

Análisis de la producción y propagación de la luz de centelleo
en el detector de doble-fase WA105

Analysis of the scintillation light production and propagation
in the WA105 Dual-Phase demonstrator

MEMORIA PARA OPTAR AL GRADO DE DOCTOR

PRESENTADA POR

Chiara Filomena Lastoria

DIRECTOR

Dra. Carmen Palomares Espiga

Contents

List of Figures

List of Tables

"Caminante no hay camino,
el camino se hace al andar."

RESUMEN

Los experimentos de oscilaciones de neutrinos de próxima generación, long-baseline, tienen como objetivo responder las mayores preguntas en la física de neutrinos, como la observación de la violación de la fase CP en el sector leptónico y la determinación del orden de la masa de neutrinos. El experimento Deep Underground Neutrino Experiment (DUNE) es uno de estos proyectos, cuyo diseño final está todavía por definir. Su detector lejano (DL), situado a 1300 km de distancia de la producción del haz de neutrinos, en Fermilab, está destinado a tener cuatro cámaras de proyección temporales (TPC) de argón líquido (LAr) de 10 kilotoneladas, que utilizaran tecnologás de una única y de doble fase (DP).

El LAr es un medio convencional para detectores de neutrinos y de materia oscura. En el dise´ no de las LAr-TPC propuesto para el DL de DUNE, la reconstrucción del evento se basa en la señal de carga, producida por la ionización, y en la señal de luz de centelleo, producida por la desexcitación de los excímeros de Ar. Gracias a la fina segmentación del ánodo, la reconstrucción completa del evento permite una excelente resolución espacial a la escala del mm; el tiempo absoluto del evento se proporciona a través de la detección de luz de centelleo. En este tipo de detectores, el sistema de detección de luz (SDL) es esencial para discriminar los eventos que no proceden del haz, y para complementar las medidas calorimetrica del evento.

En las LAr-TPC DP, una región de gas argón (GAr) se mantiene por encima de la masa de LAr, y permite la amplificación de los electrones de ionización en GAr, antes de su recogida al ánodo. Este configuración es particularmente ventajoso en detectores grandes, porqué la amplificación de carga permite cubrir trayectorias de deriva más largas. Sin embargo, ni las tecnologás de fase única, ni la de DP han sido probadas a grande escala; entonces, la operación de pequeños prototipos, que

demuestren su escalabilidad, son cruciales. Para validar el diseño de la tecnologá DP en DUNE, se ha trabajado con dos prototipos con un volumen activo de Ar creciente: WA105, de 3×1×1 m^3 (∼4.2 toneladas), y ProtoDUNE-DP, de 6×6×6 m^3 (∼300 toneladas); ambos han estado expuestos a muones cósmicos.

WA105 comprobó la idoneidad de las LAr-TPC DP en la escala de las toneladas, permitiendo alcanzar importantes hitos tecnológicos, como la extracón y la amplificación de los electrones en una superficie de 3 m^2 . Además, se ha validado el diseño de los dos principales subsistemas para la detección de la señales de carga y de luz.

Esta tesis está dedicada al estudio de la luz de centelleo recogida durante el peródo de toma de datos del prototípo WA105. La primera parte de la disertación se centra en el estudio del funcionamiento del SDL; la segunda sobre la caracterización detallada de las dos señales luminosas producidas en las fases de argon liquido (luz de centelleo primaria, S1) y de argon gaseoso (luz de centelleo electroluminiscente, S2). Los resultados alcanzados han dado pié a conclusiones pioneras que han permitido profundizar la comprensión de la microfísica de LAr.

El SDL utilizado en WA105 estaba compuesto de cinco tubos fotomultiplicadores criogénicos (PMT) con fotocátodos bialcalinos recubiertos con tetrafenilbutadieno, para la conversión de la longitud de onda (wavelength shifter WLS). Las capacidades del SDL se han estudiado comparando las diferentes configuraciones del WLS y de los circuitos divisores de alto voltaje utilizados en las bases de los PMTs. El estudio del rendimiento del SDL ha sido esencial para validar el diseño de este sistema para ProtoDUNE-DP y el módulo de DP del DL de DUNE.

Debido a la amplia aplicación del LAr en los detectores de materia oscura, la mayoría de los estudios sobre la S1 utilizan electrones o retrocesos nucleares como partículas que interactúan con él. Por otro lado, las LAr-TPC dedicadas a experimentos de long-baseline están diseñadas para la detección de partículas cargadas de mayor energía (GeV). Entonces, la exposición a muones cósmicos ha permitido mejorar el conocimiento sobre la producción de la S1 producida por partículas similares a las esperadas en esos experimentos.

El conocimiento exhaustivo de la producción de la S1 es esencial para la mejora de las simulaciones actuales sobre los estudios de sensibilidad física en detectores gigantes de LAr. Entonces, uno de los principales objetivos de esta tesis es la caracterización de los mecanismos de producción de la S1 a partir de la interacción de muones cósmicos con el Ar en el volumen activo. La operación del prototípo en

diferentes condiciones de campo permitió estudiar la reducción del la cantidad de S1 producida por recombinación y observar dos comportamientos inusuales relacionados con el impacto del campo de deriva sobre la probabilidad de desexcitación del argón desde el estado de singlete o triplete y el tiempo de desexcitación desde el nivél de triplete. Estos resultados han proporcionado conclusiones muy innovadoras sobre el estudio de la dinámica de recombinación de LAr.

El segundo objetivo importante de esta tesis es el estudio de la propagación de la S1 en LAr, directamente relacionada con la escalabilidad del SDL a detectores más grandes. La propagación de la luz es particularmente sensible a la longitud de dispersión de Rayleigh, cuya medida sigue siendo contradictoria. En el detector WA105, la evaluación de este parámetro ha sido llevada a cabo mediante la comparación del análisis de datos con simulaciónes Monte Carlo generadas con diferentes longitudes de dispersión de Rayleigh. Debido a las dimensiones del detector, los datos muestran una sensibilidad limitada a este parámetro.

Por último, la disertación está dedicada al análisis de la S2 producida en GAr. El desarrollo de un algoritmo dedicado a su reconstrucción ha permitido su caracterización, así como la medida de la velocidad de deriva de los electrones de ionización bajo campos eléctricos ligeros (≤ 0.5 kV/cm). La amplificación de los electrones en los LEMs representa un mecanismo relativamente innovador, cuyo impacto en la S2 se ha estudiado por primera vez en el detector WA105.

"A journey of a thousand miles begins with a single step."

Lao Tse

ABSTRACT

The next-generation long-baseline neutrino oscillation experiments aim to answer most of the unsolved questions in neutrino physics as the observation of the CP violation in the leptonic sector and the determination of the neutrino mass ordering. The Deep Underground Neutrino Experiment (DUNE) is one of these projects, whose final design is currently to be defined. In particular, the far detector (FD) site is intended to have four 10-kton Liquid Argon (LAr) Time Projection Chambers, using both the single and dual-phase (DP) technologies.

Nowadays, LAr is a conventional medium for neutrino and dark matter detectors. In the LAr-TPC design proposed for the DUNE FD, the event reconstruction is based on the detection of the charge signal, produced by ionization, and the scintillation light provided by the Ar excimers de-excitation. Thanks to the fine anode segmentation, the charge-readout allows an excellent 2-D spatial resolution, reaching the mm scale; whereas, the absolute event time is obtained through the scintillation light detection. In these detectors, the photon detection system (PDS) is essential for triggering non-beam events as well as to complement the calorimetry.

In the DP LAr-TPC, a gas argon (GAr) pocket is kept above the liquid argon bulk, enabling the amplification of the extracted ionization electrons before their collection on the anode plane. This design is particularly advantageous in big detectors for allowing longer drift paths, providing the recovery of the signal deterioration, and reducing the energy threshold. In the case of DUNE, it is expected to be extremely helpful in the detection of low energy events as Supernovae neutrino fluxes and proton decays.

However, neither the single nor the dual-phase technologies have been operated at the kton scale; hence, the operation of smaller prototypes is crucial for demonstrating

their scalability toward larger volumes. To validate the DP technology for the DUNE FD, two prototypes have been worked at CERN with an increasing LAr target mass: the WA105 DP demonstrator of $3\times1\times1$ m^3 fiducial volume ($\sim$ 4.2 tons), and the ProtoDUNE-DP of $6\times6\times6$ m^3 fiducial volume ($\sim$ 300 tons); both of them have been exposed to cosmic muons for long periods.

The WA105 DP demonstrator covered the essential function of proving the suitability of DP LAr-TPCs at the ton scale, leading to important technological milestones. For the first time, the assembling of small LEM units allowed the extraction and the amplification of the electrons in the GAr pocket over a surface of 3 m^2; the innovative design of a non-evacuated cryostat has been validated for its installation in bigger detectors, and the two principal sub-systems for the charge and light detection have been tested. The demonstrator took more than 5×10^6 events in different trigger and electric field conditions.

This thesis is dedicated to the study of the scintillation light collected in the WA105 DP demonstrator during its whole data taking period. The first part of the dissertation is centered on the study of the PDS performance. The second part, on the detailed characterization of the two benchmark light signals produced in LAr (primary scintillation light) and GAr (electroluminescence scintillation light). The achieved outcomes pointed out pioneering results helping to deepen the understanding of the LAr micro-physics.

The PDS consisted of five cryogenic photomultiplier tubes (PMTs) with bialkali photocathodes coated with the Tetra-Phenyl-Butadiene (TPB), as wavelength shifter (WLS) material. The system capabilities are studied comparing the WLS options, differing for the TPB coating configurations, and the high-voltage divider circuits used in the PMT bases. Their performance was essential to validate the PDS baseline design for both ProtoDUNE-DP and the DUNE DP FD module.

Given the wide application of LAr in dark matter detectors, most of the studies describing the scintillation light use electrons or nuclear recoils as interacting particles. On the contrary, LAr TPCs for long-baseline experiments are designed for the detection of higher energy (GeV) charged particles. Hence, the detector exposure to cosmic muons allowed to increase the knowledge about the scintillation light production from particles similar to the ones expected in those experiments.

A deep understanding of the scintillation light production mechanisms is fundamental to improve current simulations for physics sensitivity studies in giant LAr

detectors. Hence, the characterization of the scintillation light production mechanisms from the cosmic muon interaction with the Ar atoms is one of the main goals of this thesis. Due to the simple design of the PDS, the detector represented a good test bench for these kinds of studies. Because of the drift field reduction of the total scintillation light, the demonstrator operation at different drift fields allowed the study of the recombination mechanism. Two unusual behaviors are observed, related to the impact of this field on the probability of populating the singlet or the triplet excited states and the de-excitation time from the triplet energy level, providing innovative results on the LAr recombination dynamics.

The second important goal of this thesis is the study of the VUV photons' propagation in LAr, influencing the PDS scalability to larger detectors. The light propagation is particularly sensitive to the Rayleigh scattering length whose measurement is still contradictory. In the WA105 DP demonstrator, the evaluation of this parameter has been considered comparing the data with Monte Carlo simulations generated with different Rayleigh scattering lengths; however, due to the detector dimensions, a limited sensitivity is found. Nevertheless, the dependence on other factors affecting the light propagation, as the detector components reflectivity for VUV photons, has emerged and suggests the necessity to consider it more carefully in future experiments.

Lastly, the dissertation is dedicated to the analysis of the electroluminescence light signal produced in GAr. The development of an algorithm dedicated to the electroluminescence signal reconstruction allowed its characterization and the measurement of the ionization electrons drift velocity under low electric fields ($\leq$ 0.5 kV/cm). The amplification in the LEMs represents a relatively innovative mechanism, whose impact on the electroluminescence light signal is studied for the first time in the WA105 DP demonstrator.

"You know how it is, exciting and risks come together."

H. Tanaka

CHAPTER 1

NOVEL GIANT LIQUID ARGON TPCS TO STUDY NEUTRINOS

In this chapter, a historical overview of the neutrino physics and liquid argon (LAr) time projection chambers (TPC) evolution are provided in order to describe the experimental context motivating this thesis.

In Sec. 1.1, a brief introduction on the neutrino oscillation mechanism and the current status of its detection in Long Baseline (LBL) accelerator experiments will be given. In Sec. 1.2, the description of the general TPC operation principles up to the novel implementation of the dual-phase configuration for giant neutrino detectors will be provided. Among all the next-generation neutrino experiments, the discussion will be focused on the Deep Underground Neutrino Experiment (DUNE), described in Sec. 1.3. Given the huge dimensions of DUNE, smaller prototypes are necessary to ensure the best detector performance. Two foreseen options are planned in DUNE: the single and the dual-phase (DP) technology; the approach developed for the DP prototypes will be presented in Sec. 1.4.

One of the key features of having LAr-TPCs is the excellent track reconstruction; nevertheless, due to the complexity of the event topology, an alternative and complementary function is covered by the scintillation properties of the LAr; in Sec. 1.5 the role of the light detection in DP LAr-TPC will be discussed.

1.1 Neutrino physics in a nutshell

Neutrinos, like electrons, are leptons; however, in contrast with them, neutrinos are neutral, but both are weakly interacting. Because of their *introverted* nature, neutrinos hypothesis first and their detection later showed to be fascinating and complicated at the same time.

1.1.1 Historical overview on the neutrino physics

Dating back to 1930, after the radioactivity discovery and its puzzling understanding, W. Pauli hypothesized the existence of the neutrino to explain the continuous spectrum observed in nuclear decays, apparently contradicting the principle of energy conservation [1]. Only in 1934, E. Fermi identified in a *massless*, neutral, and weakly interacting fermion the fundamental component for the description of the theory of the beta-decay[2]. He named this particle *neutrino*; the *anti-neutrino* is its anti-particle. The first detection of the (anti)neutrino dates to 1956, by C. Cowan and F. Reines, through the detection of the inverse-beta-decay reaction:

$$p + \bar{\nu}_e \rightarrow n + e^+ \tag{1.1}$$

in a liquid scintillator experiment, using $\bar{\nu}_{\mathrm{e}}$ produced in a nuclear reactor [3]. The evidence of the electron anti-neutrinos was pointed out from the comparison between the counting of events collected with the nuclear reactor on and off. This result led to a cross-section measurement of the order of $1.2^{+0.7}_{-0.4}\times10^{-43}$ cm^2, compatible with the theoretical expectation of $(1.0 \pm 0.17) \times10^{-43}$ cm^2 [4]. In analogy with the lepton families, also neutrinos and anti-neutrinos exist (at least) in three flavors. The muon neutrino, ν_μ, postulated in 1940, was discovered by L. Lederman, M. Schwartz, and J. Steinberger in 1962, from the decay of pions in a spark chamber at the Brookhaven National Laboratory [5]. Finally, the third-flavor neutrino, ν_τ, postulated in 1975 by M. L. Perl [6], was observed only in 2000 by the DONUT experiment [7].

Based on the results of the LEP experiments at CERN, in the '90s, the total number of neutrino families was set at three, through the measurements of the Z^0-boson decay channels [8]. Despite the robustness of the result reported, these observations do not exclude the existence of a massive fourth-neutrino family, the *sterile* neutrino, not observed yet.

The Standard Model of Particles

Neutrinos, as elementary particles, are described by the Standard Model (SM) of the particle physics that is the self-consistent theory able to describe three of the four fundamental interactions describing our Universe: strong, electromagnetic, and weak interactions. The SM is a renormalizable gauge field theory based on the $SU(3)_C \otimes SU(2)_L \otimes U(1)_Y$, corresponding to the strong interaction (described by the quantum chromodynamics, QCD), to the weak isospin and, to the hypercharge group, respectively. Fermions are the basic constituents of matter, they exist in two types, quarks and leptons, interacting mediated by spin-1 bosons ($W^{\pm}$, Z^0, γ, and gluons); the former interacting via the three interactions and the later only via electro-magnetic and/or weak interactions. When fermions are grouped in weak isospin doublets, they can be recognized in terms of their chirality; hence, left-handed neutrinos are in a doublet with the corresponding left-handed charged lepton (ϕ_L) and the right-handed particle are in a weak isospin singlet (ϕ_R). Only left-handed neutrinos have been observed; hence, if a right-handed neutrino would exist, it will interact via none of the mentioned interactions. Neutrino interactions in the SM framework are driven by the exchange of a $W^{\pm}$ boson (charge-current interactions, CC) or via a Z^0 boson (neutral-current interactions, NC). In CC interactions, leptons with the same flavor as neutrinos are involved in the interaction under charge conservation. NC interactions, instead, are flavor-independent; hence, any kind of neutrino interacts with other leptons or quarks. Finally, the particle mass is provided in the SM through the spontaneous breaking of the gauge symmetry through the mediation of the spin-0 Higgs boson. In the SM framework, the right-handed singlets are coupled with the left-handed doublets via the Yukawa coupling; the mass term in the SM Lagrangian is:

$$\mathcal{L}_{\mathrm{Y}} = -M_D(\bar{\psi}_R\psi_L + \bar{\psi}_L\psi_R) \tag{1.2}$$

with M_D, the Dirac mass of fermions and explicitly dependent on both right and left-handed fields; hence, in the SM formalism, the existing neutrinos, observed only as left-handed particles, are expected to be massless.

Although the validity of the SM has been demonstrated by the agreement with the experimental results, it still leaves some physics phenomena unexplained. Neutrinos, for instance, are an example of physics beyond the SM; they are predicted as massless particles, whereas the experimental evidence of neutrino oscillations demonstrates

the opposite.

1.1.2 Neutrino oscillations, what did we learn so far?

Several neutrino sources are present in nature and first studies on neutrinos were based on the ones produced by the Sun. The pioneering Davis experiment in the sixties [9], trying to test the solar model, was the first to measure the neutrino flux from the Sun and to detect a deficit. Initially ascribed to possible limitation affecting the Standard Solar Model (SSM), the so-called *solar-neutrino puzzle* have been confirmed by many experiments, such as GALLEX [10], SAGE [11], and SuperKamiokande [12], suggesting to look for other solutions than limitations in the SSM. Consequently, it was solved only by accepting the hypothesis of the neutrino flavor oscillation mechanism. All the aforementioned experiments, in fact, detected a deficit in the neutrino flux corresponding to $\sim 1/3$ of the prediction. A hint for the neutrino flavor oscillation was observed in the Kamiokande experiment [13] studying atmospheric neutrinos from pion and muon decays. Under the hypothesis of two neutrino flavors, ν_e and ν_μ, the expected flavor ratio should have been at 2:1 for ν_μ:ν_e; nevertheless, the proportionality was not always confirmed, depending on the distance traveled by the neutrinos. As a consequence, the hypothesis of the neutrino oscillation has been proposed and confirmed by Super-Kamiokande in 1998 [12]. Only in 2001, with the sensitivity of the SNO experiment to the three solar neutrino flavors, the anomaly was solved [14]. The SNO experiment was sensitive to both the CC interaction of electronic neutrinos and the three-flavor sensitive elastic scattering channel; the first observation confirmed the solar neutrino deficit observed by other experiments, whereas, the latter was in agreement with the prediction confirming the oscillation of ν_e to another nu flavor. The experimental observation of the appearance of the tauonic neutrino was reported in 2014 by OPERA [15].

Neutrino oscillation formalism

In analogy with the $\mathrm{K}^0 \leftrightarrow \bar{\mathrm{K}}$ oscillation, B. Pontecorvo, in 1957, defined the theoretical formalism describing a neutrino flavor transition, taking place during the neutrino propagation over a distance L, from the production point [16]. After the muonic neutrino observation, the possibility of the neutrino oscillation between the

neutrino families was proposed by Maki, Nakagawa, and Sakata in 1962 [17]. As a consequence of these two contributions, the formalism describing the neutrino oscillation describes the weak interactions by a non-diagonal Hamiltonian in the flavor eigenstates, ν_α through the unitary PMNS matrix, U_{PMNS}[1], and assuming neutrinos as Dirac-particles[2]. The flavor eigenstates are expressed as a linear combination of the neutrino mass eigenstates, ν_k:

$$|\nu_\alpha\rangle = \sum_k U^*_{\alpha k}|\nu_k\rangle, \tag{1.3}$$

the $U^*_{\alpha k}$ matrix is the rotation mixing-matrix. Considering the three flavors eigenstates (e, μ, τ) and the three mass eigenstates (1, 2, 3), the U_{PMNS} matrix is a 3×3 rotation matrix, parametrized by the mixing angles θ_{ij} and a complex phase δ; the total matrix is hence separated in three matrices corresponding to the rotations around each angle as follows:

$$U_{PNMS} = \begin{pmatrix} 1 & 0 & 0 \\ 0 & c_{23} & s_{23} \\ 0 & -s_{23} & c_{23} \end{pmatrix} \begin{pmatrix} c_{13} & 0 & s_{13}e^{-i\delta_{CP}} \\ 0 & 1 & 0 \\ -s_{13}e^{i\delta_{CP}} & 0 & c_{13} \end{pmatrix} \begin{pmatrix} c_{12} & s_{12} & 0 \\ -s_{12} & c_{12} & 0 \\ 0 & 0 & 1 \end{pmatrix} \tag{1.4}$$

in this nomenclature, the c_{ij}=cosθ_{ij} and s_{ij}=sinθ_{ij}. Neutrinos are produced and consequently detected with their flavors, their propagation in vacuum is expressed as a function of the neutrino energy, E_k, of the k-th mass eigenstate, by the Schrodinger Equation:

$$|\nu_\alpha(t)\rangle = \sum_k e^{-iE_k t}U^*_{\alpha k}|\nu_k\rangle; \tag{1.5}$$

it is important to emphasize that, in contrast with the SM description, the detection of a different flavor from the original one is possible only if neutrinos have non-zero mass and different among them. Because of that, the probability of the neutrino flavour to change is expressed as follows:

$$P(\nu_\alpha \to \nu_\beta) = \langle\nu_\beta|\nu_\alpha(t)\rangle = \sum_{i,k} U^*_{\alpha k}U_{\beta k}U_{\alpha i}U^*_{\beta i}e^{-i(E_k - E_i)t} \tag{1.6}$$

$$P(\nu_\alpha \to \nu_\beta) = \langle\nu_\beta|\nu_\alpha(t)\rangle = \sum_{i,k} U^*_{\alpha k}U_{\beta k}U_{\alpha i}U^*_{\beta i}exp\Big(-i\frac{\Delta m^2_{ki}L}{2E}\Big) \tag{1.7}$$

[1]The sub-indexes are referred to Pontecorvo, Maki, Nakagawa, and Sakata, respectively.

[2]If neutrinos would be conceived as Majorana particles, an additional phase would be needed in the U_{PNMS} matrix; however, their contribution would cancel each other in the propagation probability that will be expressed in Eq. (1.7) and Eq. (1.8).

the second equation is obtained from the first assuming the three neutrino mass eigenstates to be relativistic and propagate at the same energies (E $\simeq$p $\gg$m). The aforementioned probability is named *appearance* when $\alpha \neq \beta$; whereas, it is called *survival*-probability when $\alpha = \beta$. In Eq. (1.7), it is important to highlight that the oscillation phase, $\Delta m^2_{ij} L/4E$, depends on the ratio L/E; this dependence is an important factor for determining the design of Long Baseline (LBL) neutrino oscillation experiments. If applied to the anti-neutrinos, previous Eq. (1.7) becomes:

$$P(\bar{\nu}_\alpha \to \bar{\nu}_\beta) = \langle \nu_\beta | \nu_\alpha(t) \rangle = \sum_{i,k} U_{\alpha k} U^*_{\beta k} U^*_{\alpha i} U_{\beta i} exp\Big(- i \frac{\Delta m^2_{ki} L}{2E} \Big) \tag{1.8}$$

Comparing Eq. (1.7) and Eq. (1.8), they differ in the sign of the imaginary phase; hence, applying the Charge-Parity (CP) transformation it is not possible to obtain one equation from the other, meaning that neutrinos and anti-neutrinos violates CP.

One last observation must be given relative to the neutrino propagation in the matter; in this case, the Hamiltonian is modified taking into account the interactions of neutrinos with matter constituents, mostly electrons and protons; because of that, electron neutrinos are more affected than the other flavors.

1.1.3 Overview of the oscillation parameters

As introduced in Sec. 1.1.2, the combination of the results of more experiments was needed to solve the *solar-neutrino puzzle*. The data from solar, atmospheric, reactor, and accelerator experiments can be combined to obtain a global picture of the neutrino oscillation parameters. Besides, depending on the sensitivity of the detector to the neutrino flavors and on the L/E factor, not all the detectors are sensitive in the same way to all the mixing-matrix parameters. Hence, the state-of-the-art of these parameters is obtained combining the results of all the running experiments in order to obtain the most updated version of the U_{PNMS}-matrix. In Tab. 1.1, the values of the mixing angles θ_{ik}, of the Δm^2_{ki}, and of the δ_{CP}-phase are reported, within the framework of three-neutrino oscillations; the values are taken from Ref. [35].

parameter	**best value** $\pm$ **1**$igma$
$\sin^2\theta_{12}$	$0.304\ ^{+0.013}_{-0.012}$
$\sin^2\theta_{23}$	$0.570\ ^{+0.018}_{-0.024}$ $(0.575\ ^{+0.017}_{-0.021})$
$\sin^2\theta_{13}$	$0.02221\ ^{+0.00068}_{-0.00065}$ (0.02240 ± 0.00062)
$\Delta m^2_{21}[10^{-5}eV^2]$	$7.42\ ^{+0.21}_{-0.20}$
$\Delta m^2_{3l}[10^{-3}eV^2]$	$2.514\ ^{+0.028}_{-0.027}$ (-2.497 $\pm$ 0.028)
$\delta_{CP}[^0]$	$195\ ^{+51}_{-25}$ $(286\ ^{+27}_{-32})$

Table 1.1.: Summary of the most updated values of the mixing-matrix parameters obtained from the global fit of the oscillation parameters. The values reported are referred to the ones obtained if neutrino masses follow the *normal-ordering*; in parenthesis, the values expected under the hypothesis of *inverted-ordering* are reported.

1.1.4 Open questions in neutrino physics

Neutrinos produced in the Sun are those that have been studied the longest in the past fifty-five years; thanks to that, the θ_{12}-angle is very well known; however, a discrepancy with Δm^2_{21} is present comparing the measurement of this parameter in reactor experiments or from the solar neutrino flux. The measurement of the θ_{23}-angle and Δm^2_{32} parameters is possible considering the disappearance of ν_μ or $\bar{\nu}_\mu$ in accelerator experiments (as NOνA[18], MINOS [19], and T2K [20]) or from atmospheric neutrino experiments (as Super-Kamiokande and IceCube [21]). However, the data collected so far are still not able to distinguish whether or not θ_{23} is greater or smaller than 45^0; clarifying this information is needed to understand whether the muonic and tauonic neutrinos equally contribute to the mass eigenstates, and corresponding to the maximal mixing between the two flavors. Finally, the θ_{13}-angle has been measured by the disappearance of $\bar{\nu}$ both at reactor (DayaBay [22], DoubleCHOOZ [23], and RENO [24]) and accelerator experiments (T2K).

Despite this well-described picture of the neutrino physics, there are still some open questions waiting to be answered. In the following sections, only the ones that will be investigated in the next-generation of accelerator experiments will be summarized; the remaining ones will be discussed at the end of the section.

Mass ordering

The oscillation probability equations in vacuum furnish only a measurement of the square mass difference between neutrinos; but which one is their ordering?

From the comparison between solar and atmospheric neutrinos, a hierarchy has been pointed out because $\Delta m^2_{21} << |\Delta m^2_{31}| \sim |\Delta m^2_{32}|$. On the other hand, because the sign of Δm^2_{13} is still unknown, two options are possible to solve the so-called mass ordering (or hierarchy) problem: either a *normal-ordering* (NO) such that $m_1 < m_2 < m_3$ or an *inverted-ordering* (IO) which implies $m_3 < m_1 < m_2$ Ref. [25]. A schematic description of the two hierarchies is reported in Fig.1.1; in both cases, the smallest difference remains Δm^2_{21}, but the NO would imply to find $\Delta m^2_{31} > 0$ and IO to find $\Delta m^2_{32} < 0$.

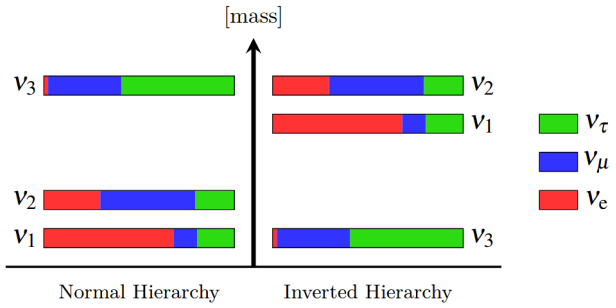

Figure 1.1.: Schematic description of the two neutrino mass hierarchy (or ordering) options: normal hierarchy (**left**) and inverted hierarchy (**right**). The plot is from Ref. [25].

Only next generation neutrino experiments, including the matter effect, would clarify the ordering with a significance $\sim 5\sigma$; in particular, the main contributions are expected by atmospheric (ORCA [26], PINGU [27]), accelerator (HyperKamiokande [28], DUNE[3]) and reactor (JUNO [29]) experiments. Despite HyperKamiokande is a long baseline accelerator neutrino experiment, its baseline is not sufficiently long, such that the measurement that will be performed will be based on the detection of atmospheric neutrinos in the far detector; DUNE, on the contrary, defined its baseline in order to fulfil this as one of its primary goals.

CP violation

The propagation of neutrinos is not the same as anti-neutrinos, do they violate the CP symmetry?

[3] DUNE will be the subject of Sec. 1.3.

The answer of this question would help in clarifying the origin of the baryon asymmetry leading to the matter and anti-matter asymmetry in our Universe [30]. The CP violation has been already observed in kaons and B-mesons; next-generations of accelerator neutrino experiments, such as HyperKamiokande and DUNE, has the discovery of the CP violation in the leptonic sector, by considering the difference between neutrino and anti-neutrino oscillation probabilities, as their primary physics goal[4]. In the SM framework, theoretical models have been proposed describing a violation of the lepton number generation that would explain this asymmetry [31].

Other unanswered questions

In addition to the aforementioned questions, it is important to remind that Eq. (1.4) has been written making the hypothesis of the neutrinos as Dirac particle; hence, only one CP-phase is mentioned that is detectable by oscillation experiments. In contrast, the hypothesis of neutrinos as Majorana particles can be included by adding the Majorana phases[32], and it is tested in 0νdouble-β decay experiments [30]. Moreover, oscillation experiments cannot give direct measurements on the neutrino masses but only of their squared differences; nevertheless, experiments looking at the β-decay energy spectrum of tritium and studying how its endpoint deviates from the hypothesis of a zero-mass neutrino [33] can provide the direct measurement of the electron neutrino mass. Finally, the U_{PNMS}-matrix is based on the three-flavor paradigm; despite the LEP measurements tend to confirm this paradigm, several anomalies contradicting such hypothesis have been pointed out in reactor and accelerator experiments; they can be interpreted assuming the existence of at least one more neutrino flavor (*sterile* neutrino[34]).

1.1.5 Long Baseline Experiments

The long baseline (LBL) experiments represent one of the most controlled scenario where it is possible to study neutrino oscillations; in this kind of experiments the information regarding the neutrino energy (typically at the GeV-scale), and the distance from the production point are decided by the experimental design. The typical geometry of this kind of experiments foreseen a near detector (ND) site,

[4]See Sec. 1.1.5 for more details.

aiming to characterize the neutrino beam, and a far detector (FD) site that will measure the neutrino oscillation probability. In this landscape, Eq. (1.7) can be expressed as a function of L/E in the case of ν_μ disappearance and in the case of ν_e appearance, including the matter effect contribution, as follows:

$$P(\nu_\mu \to \nu_\mu) = 1 - [cos^4\theta_{13} sin^2 2\theta_{23} + sin^2 2\theta_{13} sin^2\theta_{23}] sin^2\left(\frac{\Delta m^2_{31} L}{4E}\right) \tag{1.9a}$$

$$\begin{aligned} P(\nu_\mu \to \nu_e) \approx & sin^2 2\theta_{23} sin^2\theta_{13} \frac{sin^2(\Delta 31 - aL)}{(\Delta 31 - aL)^2} \Delta^2_{31} + \\ & + sin 2\theta_{23} sin 2\theta_{13} sin 2\theta_{12} \frac{sin^2(\Delta 31 - aL)}{(\Delta 31 - aL)} \\ & \Delta_{31} \frac{sin(aL)}{(aL)} \Delta_{21} cos(\Delta_{31} + \delta_{CP}) + \\ & + cos^2\theta_{23} sin^2 2\theta_{12} \frac{sin^2(aL)}{(aL)^2} \Delta^2_{21} \end{aligned} \tag{1.9b}$$

being $\Delta_{ij} = \Delta m^2_{ij} L/4E$, a = $G_F N_e/2$, G_F the Fermi constant, N_e the number density of electrons in the Earth, L the baseline expressed in km and E the neutrino energy expressed in GeV. In vacuum, the maximum oscillation probability is found when

$$\frac{L}{E_n}\left(\frac{km}{GeV}\right) \approx (2n-1)\left(\frac{\pi}{2}\right) \frac{1}{1.267 \times \Delta m^2_{32}(eV^2)} \tag{1.10}$$

being n the n-th oscillation maximum at energy E_n. The corresponding equation for anti-neutrinos is found by substituting a$\to -$a and $\delta_{CP} \to -\delta_{CP}$; the asymmetry term is obtained as follows:

$$\mathcal{A}_{CP} = \left[\frac{P(\nu_\mu \to \nu_e) - P(\bar{\nu_\mu} \to \bar{\nu_e})}{P(\nu_\mu \to \nu_e) - P(\bar{\nu_\mu} \to \bar{\nu_e})}\right] \tag{1.11}$$

that, in the leading order approximation, in the three-flavor paradigm it becomes:

$$\mathcal{A}_{CP} \approx \frac{cos\theta_{23} sin 2\theta_{12} sin\delta_{CP}}{sin\theta_{23} sin\theta 13} \left(\frac{\Delta m^2_{21} L}{4E}\right) + \text{matter effects.} \tag{1.12}$$

From these equations, it arises how LBL experiments can both measure δ_{CP} from the beam data and confirm the CP violation from the measurement of the asymmetry $\mathcal{A}_{CP}$. In the left of Fig. 1.2, Eq. (1.9b) is shown as a function of the baseline; the middle plot shows the effect of CP phase on the oscillation probability and the right plot the effect of matter effects on the same probability for δ_{CP}=0. The colors of the curves are representative of how the probability changes as a function of the baseline L. By considering these plots, it appears how an experiment with energy

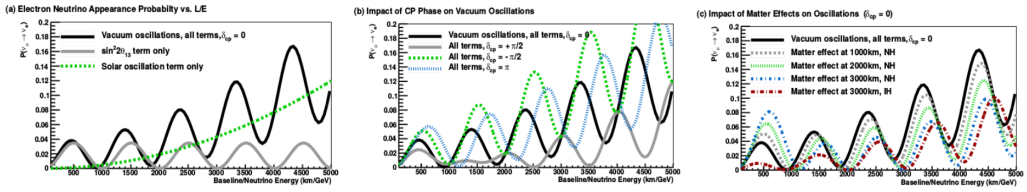

Figure 1.2.: The $\nu_\mu \rightarrow \nu_e$ oscillation probability as a function of baseline/neutrino energy (L/Eν) is given (**left**); the impact of effect of the CP phase in vacuum (**middle**) and in presence of the matter effect (**right**) are reported. The plots are from Ref. [36].

close to the first oscillation maximum and 1300 km far away from the production point would be sensitive to the mass ordering, independently from the δ_{CP}-value.

Current LBL experiments

T2K and NOνA are the two current experiments having as main physics goals the measurement of θ_{23}, Δm^2_{32}, and δ_{CP}. Here, a brief description is given:

- **T2K**: The Tokai-to-Kamioka (T2K) experiment is located in Japan; it has 292 km baseline and the muonic neutrino beam, produced at J-PARC. The far detector is the SuperKamiokande detector, a water-Cherenkov detector, with L/E$\sim$480 km/GeV. Because of the possibility of the off-axis positioning of the near and far detectors, neutrinos arrive within a very narrow energy band centered around 600 MeV.

- **NOνA**: The NuMI Off-axis ν_e Appearance (NOνA) detector is based in the United States, at 810 km away from the Fermilab where a 2 GeV narrow (anti)neutrino beam is produced. The detector is made by segmented liquid scintillators, with L/E$\sim$400 km/GeV, and sensitive to the matter effects.

The T2K experiment provided excellent results, detecting for the first time the ν_e appearance from the ν_μ beam [37] and highlighting the first hint of a non-zero δ_{CP}-phase measurement [38]. Currently, the T2K and NOνAexperiments are carrying out a joint analysis aiming to clarify the slight disagreement found in the preference of the octant for the θ_{23}-mixing angle.

Future LBL experiments

Despite the interesting results that both T2K and NOνA are accomplishing, none of them are expected to give a conclusive measurement of the oscillation parameters. For this reason, a next-generation long-baseline experiments has been planned and it is expected to reach the necessary sensitivity to clarify such precise measurements. Two are the ones currently proposed: Hyper-Kamiokande, at the T2K site, and DUNE, in the USA. The first will have the same baseline as T2K, the second will increase it up to 1300 km.

The Hyper-Kamiokande experiment will still use the same neutrino beam produced at J-PARK after its upgrade for the T2K experiment, but both the near and the far detectors will be improved. Despite the ND will remain the same, its setup will be upgraded in order to enhance the beam characterization and minimize the systemitc uncertainties. The FD, instead, will be a water-Cherenkov detector analogous to Super-Kamiokande, but 10 times larger, reaching $\sim$260 ktons and with a potentiated ultrasensitive light photon-detection system.

On the contrary, DUNE will use time projection chambers based on the liquid argon technology, reaching a fiducial mass of 40 ktons and using the most powerful neutrino beam in the world, whose description will be given in the next section; a wider description of the DUNE experiment in relation with its main physics goal will be given in Sec. 1.3.

1.2 General principles of a LAr-TPC

The Time Projection Chamber detector was conceived by David Nygren in 1974 [42]. His idea was to have a detector able to identify a ionizing crossing particle from its energy deposition and to reconstruct its track three-dimensionally.

The basic idea of a TPC is pictured in Fig. 1.3; it consists of an active volume filled with gas or liquid, where the particles crossing the active volume lose enough energy to ionize the volume atoms. The electrons produced in the ionization process, in the form of swarms, are drifted by a uniform external electric field towards a position-sensitive stage anode that provides a 2-D projection of the particle trajectory in the x-y plane. The segmentation of the anode defines the spatial resolution of the 2-D track reconstruction. The arrival time of the drifted electrons is used to

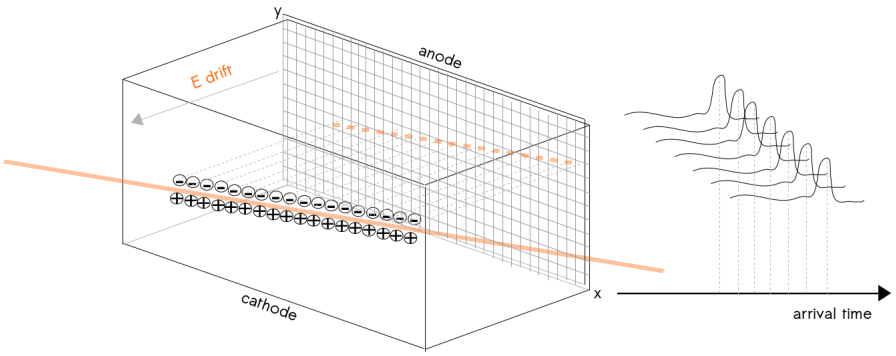

Figure 1.3.: Schematic description of the TPC operation principles. The orange line represents the track of the crossing particles producing ionization electrons and positive ions drifted by the electric field. The 2-D reconstruction of the track projection takes place in the anode plane; the arrival time of the drifted electrons gives the z-coordinate of the track.

reconstruct the z coordinate allowing a 3-D track reconstruction. The identification of the particle is possible measuring the energy loss per unit path (dE/dx) which is proportional to the collected charge per wire and unit time (dQ/dx), making the TPC a good calorimeter. To optimize the TPC performance in terms of the charge signal extraction, the knowledge of all the physics processes related with the transport properties of the electrons is essential. The diffusion of the electrons in the electric field from where they are produced up to the anode plane affects the spatial resolution over long drift distances; in addition, possible attachment of the electrons with the atoms or molecules can degrade the swarm formation [43]. A magnetic field can be applied to provide a measurement of the momentum and the charge of the particle. In order to reduce the electron diffusion, the magnetic field must be parallel to the electric field [44].

First TPCs were filled with noble gases or mixtures, later on, liquids were introduced. The advantage of using liquids comes from their higher density compared with the formers; moreover, ionization charges have greater mobility in liquids and the additional benefit of reduced electron-ion recombination. These features make liquid TPC optimal for the detection of processes with a very small cross-section as neutrino interactions or direct dark matter (DM) interactions, as well as proton decay searches. Being noble gases scintillators, the light produced by the particles crossing the TPC volume can be detected; it can be used in combination or as an

alternative to the information extracted from the drifted charges produced in the ionization. The scintillation light is produced either by excitation of the medium atoms or by the recombination process that can take place after the electron-ion production. From the scintillation light point of view, noble elements are excellent materials since they are transparent to their scintillation light[5].

Various are the liquefied noble gases that can be used in a TPC (He, Ne, Ar, Kr, Xe). The proposal of using pure liquid argon as the TPC active volume was presented by Carlo Rubbia at the end of the 1970s [45]. The choice of having a liquid argon time projection chamber (LAr-TPC) is justified by many reasons, the most important are listed below:

- Ar is dense (1.4 g/cm^3), so the crossing particles deposit significant energy
- Ar is the third most abundant gas in the Earth's atmosphere (1%) so that it can be easily extracted, making it the cheapest noble gas available
- Ar can be easily purified, most of the impurities can be frozen out from its liquid state to very low levels
- Ar has a large dielectric rigidity, that eases the use of high voltage in long drift paths
- Ar scintillation light allows a good pulse shape discrimination
- Ar provides to identifying electromagnetic showers (from the ratio of the secondary over the primary scintillation light signals)

The Ar scintillation light produced from the de-excitation of the Ar dimers is emitted at 127 nm, in the vacuum ultraviolet (VUV) region; this energetic radiation is not able to activate further ionization in such a way the Ar results transparent to its scintillation light. Despite that, to detect the scintillation light with common photomultiplier tubes, a wavelength shifter is required. To build a liquid-argon detector, cryogenic temperatures are needed. Ar in liquid, solid, and gas states coexist in thermal equilibrium (triple point) at T=83.81 K at 0.6889 bar; while the boiling point at which the argon gas liquefies is T=87.30 K. In Fig. 1.4, the phase diagram

[5] A wider description of the role of the scintillation light in liquid argon TPC is available in Chapter 2.

for argon around the triple point is shown. The most significant argon properties and quantities are summarized in Tab. 1.2; all the argon properties can be found in Ref. [47]. It is important to remind that first liquid TPCs were filled with Xe because of its better physical properties in terms of density and electron mobility, but the Ar abundance and cheapness make it the optimal candidate for detectors that must be scaled up to multi-ton scale. To detect very small cross-section interactions big size detectors are needed and LAr density makes it a perfect candidate for the target material. Besides, being the Ar the only element needed in the detector active volume, LAr-TPCs allow having uniform volumes with an excellent reconstruction of all the final particles created. Thanks to the uniformity of the active volume, the three-dimensional topology reconstruction does not suffer from any segmentation. For these reasons, LAr-TPCs have an important role both as neutrino and DM detectors. This dissertation will be focused on the application of LAr-TPCs for neutrino detection, without entering into the details of the LAr-TPC for direct DM searches. Nevertheless, key aspects of LAr-TPCs, used in DM searches, that are worth keeping in mind will be pointed out. In both detectors, the control of the Ar purity is crucial since the presence of electronegative molecules increases the electron attachment probability[6]. Currently, Ar purification systems reached levels where the amount of electronegative impurities is kept at the part-per-trillion (ppt). A big difference between neutrino and dark matter LAr-TPCs concerns the energy range exploited in the two kinds of detectors. At the scale of the neutrino beam interactions, they deposit enough energy to be reconstructed through their tracks. All the neutrino LAr-TPCs operated so far had volumes filled by Ar only in the liquid phase, in the configuration called *Single-*

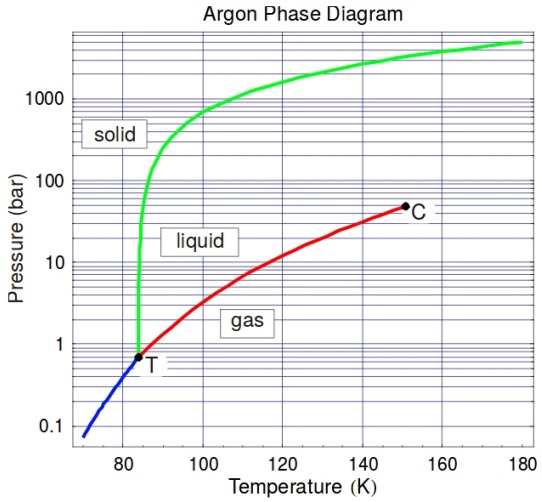

Figure 1.4.: Phase diagram for argon, around the triple point. The plot is taken from Ref. [47].

[6] More details can be found in Sec. 2.3.

Phase (SP). The imaging capability of a such LAr-TPC is determined by the anode segmentation that reached a spatial resolution of mm scale and an angular resolution of the order of one degree. An intrinsic limitation is imposed by the long drift distances that must be covered in bigger detectors by ionization electrons, because of the overlapping of the random diffusion motion with the spatial resolution of the coordinate, the reconstruction in the x-y plane is deteriorated. To minimize such degradation is crucial to have a good knowledge of LAr properties like the electron motion diffusion and the drift velocity of electrons to correct the z coordinate of the reconstructed track. Additionally, the amount of electronegative impurities must be kept at minimum levels. In direct DM searches, the interactions take place at the scale of few keV; on the other hand, the energy scale of the main physics goals exploited the neutrino experiments is of the order of tens of GeV. Due to the energy scale of the detectable processes and to improve the background suppression, the most common LAr configuration used in DM detectors keeps Ar in the gas phase on the top of the Ar liquid phase in the so-called *Dual-Phase* (DP) configuration [52]. As it will be described in Sec. 1.2.2, the DP configuration takes advantage of the amplification of the drifted electrons in the gas volume; such amplification becomes particularly helpful in the detection of low energetic events [192]. Despite that, in this range of energies, one of the main drawbacks given by using LAr is the intrinsic presence of radioactive isotopes present in the natural argon (^{39}Ar, ^{40}Ar and ^{42}Ar) because of their β-decay mode. In particular ^{39}Ar, with its half-life of 269 years, 1.01 Bq/kg and its point spectrum at the order of hundreds of keV, is one of the main intrinsic backgrounds to be distinguished to the searched DM signals (more details can be found in Ref. [46] and [48]). An optimal considered alternative, to minimize also the ^{39}Ar contamination, is the substitution of the natural Ar with Underground Argon (UAr).

As will be described in Sec. 1.3, in the current DUNE plan, both single and dual-phase configurations are foreseen options for the far detector modules. The two configurations will be compared in the next two sections.

For completeness, a brief comparison with water Cherenkov detectors must be mentioned. Already in 1998, the Super-Kamiokande detector[7] demonstrated the robustness at the multi-ton scale of the technology when the neutrino oscillations

[7] The Super-Kamiokande detector was filled by 50 k-ton ultra pure water in a cylinder with 39.3m diameter and 41.4m high.

quantity	value
atomic number (Z)	18
atomic weight	39.948 $g/mole$
mean excitation energy (I)	188 eV
liquid argon energy gap (E_{gap})	14.3 eV
first ionization potential (I_1)	15.7 eV
average energy for ionization in liquid (W_l)	23.6 eV
average energy for ionization in gas (W_g)	26.4 eV
MIP stopping power of liquid	2.105 MeV/cm
nuclear collision length	54.25 cm
nuclear interaction length	85.77 cm
scintillation wavelength (dominant component)	128 nm
Rayleigh scattering length in liquid	90 cm
radiation length in liquid	14 cm
Molière radius in liquid	9 cm
density of the liquid	1.4 g/cm^3
boiling point at 1 atm	87.3 K
triple point	83.81 K, 0.689 bar
heat of evaporation	6.44 kJ/mol
dielectric constant of liquid (ϵ_l)	1.5
critical energy in liquid for electrons	30 MeV
critical energy in liquid for muons	500 GeV
scintillation γ/MeV in absence of drift field	$\approx$ 5x10^3
electron mobility	500 cm^2/Vs

Table 1.2.: Summary of the relevant quantities of the argon, all the values are updated and taken from the PDG [49].

have been observed for the first time. In the initial discussion for choosing the DUNE detector design, both LAr and water Cherenkov detectors have been considered; despite that, LAr showed to have some advantages becoming the final choice (build both detectors was clearly cost-prohibitive). Being its density around 1.4 kg/m^3, LAr is 40% more favorable than water, the interaction length is similar in both media but

the radiation length in LAr is half than in water [79]. Because of these differences, to reach the same sensitivity to measure the CP violation, a fiducial volume of ∼40 kton of LAr is needed instead of ∼200 kton of water [51]. Additionally, being the LAr a scintillator there is no minimum threshold to detect an interaction, while in Cherenkov detector a minimum energy threshold of ∼4 MeV is required. Finally, the excellent imaging capabilities, good energy resolution, high detection efficiency, and good particle identification have been identified as key features to make LAr the final choice for a multi-ton neutrino detector.

1.2.1 Single-Phase technology

In the SP LAr-TPCs, the signal produced by the drifted electrons is collected by wire planes immersed in the LAr: the induction planes face to the drift region and provide a non-destructive signal of the electrons crossing them, while the collection plane is where the electrons are gathered. The drifted charges overpass the induction planes where the signal is bi-polar and needs a deconvolution method to be reconstructed; while, on the collection plane, the signal is unipolar and its reconstruction is easier [54]. As shown in Fig. 1.5, the wires on the three planes cover different, non-orthogonal, angles to give a full 3-D reconstruction.

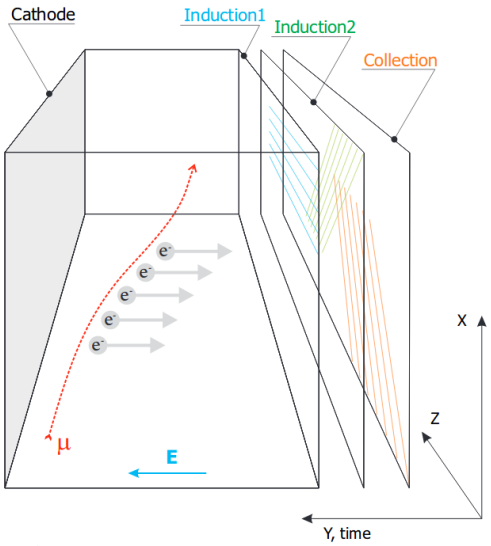

Figure 1.5.: Schematic description of a SP LAr-TPC (picture from Ref. [62]); the active volume corresponds to the whole LAr bulk where the drift field is applied horizontally.

The first SP LAr-TPC ever built at the ton scale was ICARUS-T600 [55]; it represented the final result of a more than a decade of R&D dedicated program made by smaller prototypes needed to fulfil the main technological challenges hidden behind the simplicity of the TPC concept. This conceptual design for a SP LAr-TPC is now the most accredited one, already used in ArgoNeuT [56], LArIAT [57] and the 35-ton prototype [58], and it is the baseline

configuration of all the LAr-TPCs of the Short-Baseline Neutrino (SBN) Program [53] at FermiLab such as SBND [59], MicroBOOνE [60] and the overhauling version of ICARUS-T600 itself. In these detectors, the scintillation light was collected by arrays of Photo-Multipliers Tubes (PMT) positioned behind the wire planes and used to measure the absolute event timing, t_0.

Thanks to the maturity of the SP technology, it will be the first option for two over the four modules of the DUNE far detector. An important step forward in the scaling of the SP technology towards the DUNE far detector modules is the ProtoDUNE-SP [92] detector operating at CERN since 2018. Similarly to the ICARUS design, the ProtoDUNE-SP LAr volume is segmented in two big regions divided by the cathode plane, with a 0.5 kV/cm drift field applied with the maximum drift length of 3.53 m reached so far. Furthermore, in contrast with the antecedent SP LAr-TPC that used PMTs, the photon detection system is made by SiPM directly integrated into the anode plane assembled modules; its design, successfully tested for the first time in the ProtoDUNE-SP detector, consists of two different models of a bar-shaped light guide and the innovative ARAPUCA design to *trap* the photons[8]. More details can be found in Ref. [95], [96], [97]. One of the disadvantages of the SP technology is given by the limitation on the drift path reachable with the minimum degradation of the collected charge. Because of that, big volumes can be reached only paying the price of the fiducial volume segmentation. In addition to that, despite the great S/N[9] ratio achieved in ProtoDUNE-SP, the scaling up to big volumes could limit it and consequently, the accessibility to lower energetic physics studies.

On one hand, the SP technology guarantees the detection of both the overriding DUNE physics at the GeV scale, to study the CP violation, and events at the MeV scale, as solar or supernova neutrinos and nucleon decay searches. On the other, the SP modules will be installed with other LAr configurations to improve the detection of low energetic events, reducing the cost of the detector and have a better handling of systematics. One of those alternative technologies is the *Dual-Phase* option described in the next section.

[8] The term ARAPUCA is the indigenous Guaraní word for "a trap to catch birds".

[9] The definition of S/N used here and in the rest of the thesis is in agreement with Ref. [104] and it corresponds to the ratio of mean waveform amplitude over the average value of the noise RMS.

1.2.2 Dual-Phase technology

The *Dual-Phase* technology is characterized by the coexistence of an argon vapor layer above the liquid argon volume. In this configuration, schematized in Fig. 1.6, the drift of the electrons is vertical. A combination of strong electric fields allows their extraction in the gas argon (GAr) phase and the creation of a Townsend avalanche that multiply the ionization electrons extracted. The collection of the amplified electrons take place in a 2-D anode plane. Two signals characterize the light production in dual-phase LAr-TPCs: a prompt scintillation light signal (S1) immediately generated when a particle crosses the liquid argon, and the secondary scintillation signal generated in the gas argon phase (electro-luminescence light, S2); both processes will be extensively described in Chapter 2. In the DP LAr-TPCs for neutrino detection, these light signals are detected by arrays of PMTs that must be positioned below the cathode of the TPC field cage. The main advantage motivating this TPC design is given by the feasibility to build bigger detectors than the ones allowed by the SP configuration, without any fiducial volume segmentation. Less material inside the LAr volume minimizes possible contaminations, intrinsic sources of background, and decreases the cost of the detector.

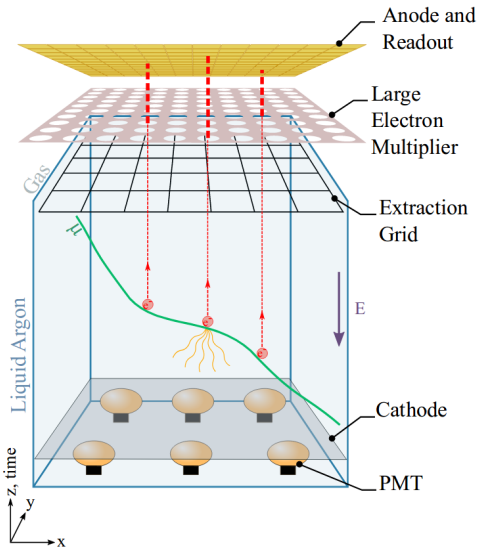

Figure 1.6.: Schematic description of a DP LAr-TPC (picture from L. Zambelli). A pocket of gas argon above the LAr phase allows the extraction and amplification of the ionization electrons; consequently, the drift field is applied vertically.

The idea of amplifying the drifted electrons, activating an avalanche in the gas phase, was proposed for the first time in 1970 by Dolgoshein and its collaborators [65]. The operation of such detectors became quite common in DM experiments since the ratio of secondary light to the primary scintillation light is very useful for background rejection. The application of the DP concept in LAr-TPCs was

successfully tested for the first time in the WArP prototypes where the maximum drift obtained was ∼70 cm [67]. Initially, those detectors avoided the avalanching mode that turned out to be unstable [66] and read only the two light signals through the optical readout of the PMTs. Only with the discovery of the high-gain operation of Gaseous Electron Multiplier (GEM) in noble gases [68], a huge step forward has been made in the application of the avalanche amplification in GAr combined with the charge readout in the anode plane for the detection of rare events. GEMs ensure that the photons produced in the avalanche are confined inside holes; for this reason, they are well suited for operation in pure argon vapor without the use of a quencher gas. Despite the first GEM designs were very delicate devices, since possible electrical discharges have been observed, they were able to provide a large effective amplification factor for the electrons extracted in the gas volume[10].

One solution to develop such DP design coupled with the charge readout has been proposed within the LBNO-DEMO (WA105) Collaboration that was born to study the design of a DP LAr-TPC with a mass that could reach the k-ton [69], [70]. The goal of the proposed DP design is to develop a LAr-TPC where the charge signal amplification recovers the long drift degradation; besides, the detection of both light S1 and S2 signals can be used. In this configuration, the charge signal reconstruction can reach S/N much higher than in a SP LAr-TPC [11]. Significant improvements in the stable operation of these devices have been obtained increasing the thickness of GEM-like detectors in the so-called Thick-GEM (ThGEM) or Large Electron Multiplier (LEM) [72], [73], [74] (an interesting review on cryogenic detectors with electron avalanching can be found here [75]). LEMs are the devices installed in the current DP LAr-TPCs [76]. Their optimization is the result of a long R&D that started over the last decade with the final aim to identify the optimal solution for a scalable device to cover big surfaces; further improvements are still under study in the current prototypes [12].

The anode readout plane is the second key component of the current DP LAr-TPCs. It is made by two perpendicular sets of semi-transparent electrode strips

[10] The gain signal observed in Ar was $\gtrsim 10^4$ [71].

[11] A S/N$\gtrsim$400 for a maximum effective gain∼90 has been measured for minimum ionizing particles in small R&D setups [98]; more details will be given in Sec. 1.4.1.1

[12] The LEMs operation in DP LAr-TPC and their principle of operation will be explained in Sec. 1.4.1 and Sec. 2.4 respectively.

(called *views*) that are separated by a thin insulating layer. The amplification produced inside the LEMs is strong enough to produce an amount of charges that can be split on both views; in this way, it is produced a similar response on both sets of strips that correspond to the x-y coordinate in the 2-D projection. The pitch strip define the anode segmentation which is ∼3mm in current DP LAr-TPCs[13]. Contrary to the signal collected in the induction planes of the SP anode, the 2-D anode collects two mono-polar and symmetric signals that facilitate the event reconstruction [80]. The combination of the LEM's amplification with the collection of the two segmented views is the key feature that guarantees high-performance imaging, constituting a unique property of the dual-phase TPC.

1.3 The Deep Underground Neutrino Experiment

DUNE [61], [62], [63], [41] is an international leading-edge neutrino experiment under construction in the USA. Its main goal is to study the neutrino oscillation parameters, the mass ordering and CP violation in the leptonic sector. It will use the

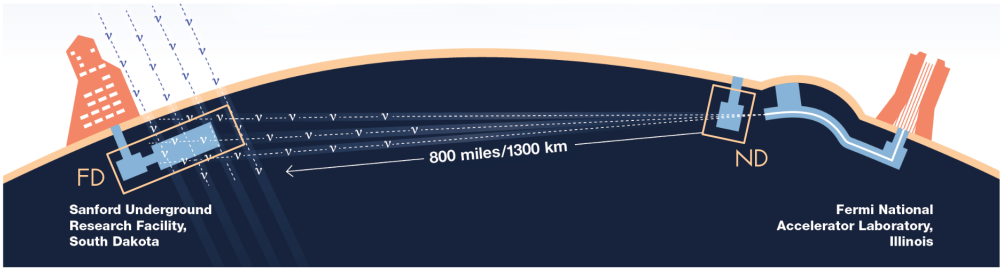

Figure 1.7.: Schematic drawing of the Deep Underground Neutrino Experiment; in the scheme it is possible to recognize the ND, on the right, very close the beam production and the FD, on the left, at 1300 km far away from it.

world's most intense neutrino beam originating at the FermiLab and detected 1300 km away at the Sanford Underground Research Facility (SURF) in South Dakota. The choice of the baseline and, consequently, the far detector site is the result of the optimization studies that ensure a 3σ sensitivity to measure the CP violation at any δ_{CP} value. A schematic description of the DUNE experiment is given in Fig. 1.7. Two are the sites where the DUNE detectors are positioned, the first hosting a near detector (ND) and the second hosting the far detector (FD). The comparison of the

[13] More details on the 2-D segmented anode installed in currently DP TPC will be given in Sec. 3.1.

neutrino energy spectrum between the ND and FD is crucial for discovering new physics in the neutrino oscillations process. The ND target will be built 574 m from the neutrino beam production to characterize the neutrino beam intensity and energy spectrum. The FD will be a giant modular LAr-TPC with a 40 k-ton fiducial mass split in four modules; the cavern that hosts the FD is 1.5 km underground. As described in Sec. 1.2, the combination of the LAr characteristics and the LAr-TPC features is the best option to give a unique neutrino interactions reconstructions with the best imaging precision and resolution.

In the following sub-sections, the DUNE physics goals, the main interactions that are expected to be detected in the DUNE FD detector, the neutrino beam features, and the description of the near and far detectors will be summarized; however, without entering into the details of the physics program nor the details of the DUNE detectors [14] because would not add essential information for the scope of the thesis. On the other hand, more attention will be given to the description of the crucial features of the DUNE experiment, the novelty of the technology employed and the challenging of the experiment to clarify the motivation of building prototypes, like the WA105 DP demonstrator for the dual-phase LAr configuration.

1.3.1 DUNE physics goals

The construction of such a giant detector, as DUNE is, allows exploring a wide physics program. The primary DUNE scientific goals are related to the neutrino oscillation measurements for which ν_μ and $\bar{\nu}_\mu$ wide energy spectrum beam will be used. In the DUNE program, the measurement of the CP phase (δ_{CP}) is the predominant physics purpose, as well as to study the matter-antimatter asymmetry and the neutrino mass ordering (through the measurement of Δm^2_{23} and the θ_{23} mixing angle in the octant where it lies). Answering these questions, DUNE results will be a sensitive test of the three-neutrinos paradigm. Additionally, given the far detector dimensions, non-beam searches are possible. DUNE, in fact, will be sensitive to the detection of the ν_e flux from the core-collapse supernova burst, as well as to study several channels for proton decay searches, and consequently search the baryon number violation that would give a hint for the grand unification theories. Thanks to

[14] The most updated summary, at the time of writing this thesis, on the details on the DUNE experiment can be found in Ref. [61], [62], [63], and [41]

the empowered neutrino beam, the high statistic samples determined by the fiducial mass of the detectors, and very precise particle identification and track reconstruction ensured by the LAr-TPCs, the contribution that the DUNE physics will bring to the present long-baseline neutrino experiments is in the enhanced precision of the measurements that will carry out. Moreover, due to the beam characteristics and the high resolution of the ND, additional physics studies related to the neutrino interactions will be also allowed. In Tab. 1.3, the DUNE scientific program is listed; the detailed description of such a vast and ambitious physics program can be found in Ref. [62].

primary physics goals
mass ordering from Δm^2_{23} and θ_{23} mixing angle *(sensitivity to the three-neutrino paradigm)*
CP violation discovery from the δ_{CP} measurement *(matter-antimatter asymmetry)*
ν_e flux from core-collapse supernova *(information on early stage of core-collapse and possible signature of birth of black-hole)*
proton decay searches *(baryon number violation)*
ancillary physics goals
physics beyond the standard model (BSM) *(Lorentz violation, CPT violation, sterile neutrinos, etc)*
ν_τ appearence
neutrino oscillation from atmospheric neutrinos
neutrino interactions in the ND *(neutrino cross sections and studies of nuclear effects)*
dark matter searches *(searches for light-mass dark matter at the GeV scale in the ND, and searches for boosted dark matter testing different models)*

Table 1.3.: Summary of the DUNE scientific physics program, all the additional details not mentioned in the text are reported in Ref. [62].

1.3.2 LAr as a target for neutrino interactions

Restricting the discussion to the interactions regarding the neutrino oscillation in the FD, the measurement can be done either looking for *disappearance* or *appearance* of a specific neutrino flavor. The former is studied from the survival probability of

the ν_μ or $\bar{\nu}_\mu$ in the beam, while the latter can be found looking for ν_e or $\bar{\nu}_e$ appearance from the ν_μ or $\bar{\nu}_\mu$ oscillation. The tagging of the neutrino flavor is possible only through charge-current (CC) interactions, while neutral-current interactions are considered background signature of the CC interactions. Both in the case of *disappearance* and *appearance* searches, the neutrino interaction with LAr volume is basically with the argon nucleus through four possible CC interactions:

$$\text{disappearance}: \quad \nu_\mu + n \rightarrow p + \mu^-, \qquad \overline{\nu}_\mu + p \rightarrow n + \mu^+ \tag{1.13}$$

$$\text{appearance}: \quad \nu_e + n \rightarrow p + e^-, \qquad \overline{\nu}_e + p \rightarrow n + e^+. \tag{1.14}$$

As shown in Fig. 1.8, depending on the neutrino energy, E_ν, different interactions are possible. For E_ν ~GeV, Ar nuclei remain almost intact in the interaction determin-

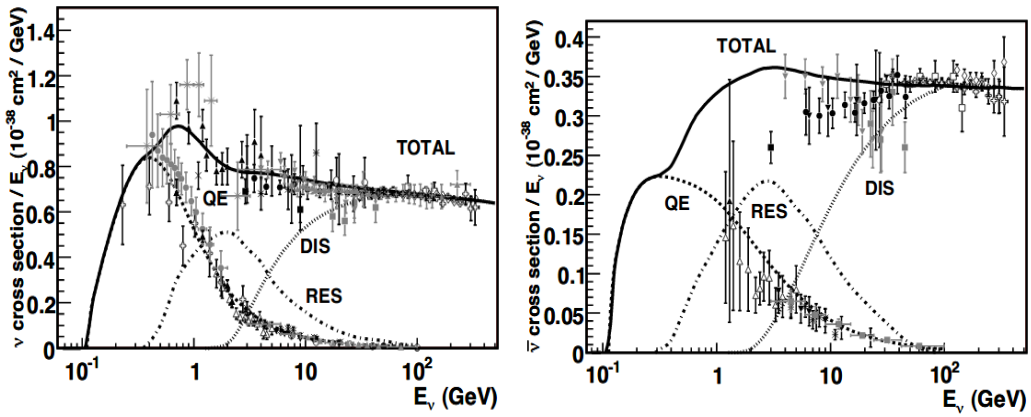

Figure 1.8.: Total muon neutrino **(left)** and anti-neutrino **(right)** CC cross-section as a function of the neutrino (anti-neutrino) energy. The plots are taken from Ref. [81] .

ing a quasi-elastic (QE) scattering. For E_ν between 1 and few hundred GeV, resonances can be produced either with the creation of a Δ or a N* state that decay into a π and another nucleon N'(N can be either referred to a proton or a neutron and π can be π^-, π^+ or π^0) through the following interaction: $\nu_\mu(\overline{\nu}_\mu) + N \rightarrow \Delta + \mu^-(\mu^+)$, where $\Delta \rightarrow \pi + N'$. The case of a π^0 meson in the final state is difficult to be distinguished from the ν_e appearance signature; in both cases an electromagnetic shower is produced and the distinction of the two processes is possible only with the perfect reconstruction of all the products. Finally, for E_ν >10 GeV, the deep-inelastic scattering (DIS) starts to be the dominant process and the ν interacts with the quarks inside the nucleons with the consequent production of hadronic showers. Consid-

ering all these possibilities, the final particle produced by the neutrino interactions with Ar are electrons, muons and hadronic showers.

LAr properties ensure the best track reconstruction for the searched events. However, the detection of low energetic events or the measurements of non-beam events is challenging due to intrinsic presence of ν_e background, Michel electrons, etc... In these searches, an important role is covered by the scintillation nature of the LAr. If most of the DUNE physics searches are guaranteed by the TPC track reconstruction, some non-beam searches, as nucleon decay searches, and new interesting areas of investigations are possible thanks to the detection of the scintillation light. On one side, the light information can give a redundant measurement of that performed by the charge signal to suppress systematic uncertainties and explore new physics; on the other side, the knowledge of the t_0 time of the event is important to correct the charge reconstruction deterioration due to the electron captures or other transport effects, as well as to fiducialize non-beam events and to trigger low energy non-beam processes. The role of the photon detection in the LAr-TPC, alone or in combination with the charge signal to perform complete calorimetric studies, will be described in Sec. 1.5; in the next two sections, the neutrino beam and the near detector features will be presented.

1.3.3 Neutrino beam

The main innovation brought by the DUNE experiment to the current long-baseline neutrino experiments is the powerful proton beam provided by the Proton Improvement Plan-II (PIP-II). In the first phase of the DUNE experiment, the beam power will be 1.2 MW, which corresponds to $1.1\text{x}10^{21}$ protons-on-target (POT) per year [61] in the energy spectrum lying in the (60; 120) GeV range. An important upgrade of the actual accelerator will empower the proton beam up to 2.4 MW, with a consequently important increase in the statistics. The protons are extracted from the Fermilab Main Injector (MI) and transported in the target area where the primary proton beam hits on a cylindrical graphite target (with 16 mm diameter and 2.2 m long) producing hadrons, successively focused on three magnetic horns. From the decay of pions and kaons in a cylindrical decay pipe filled with helium (with a diameter of $\sim$4 m and a length of $\sim$200 m), the neutrino beam is extracted. The neutrino beam is designed to reach the maximum event rate in the energy region

between 0.5 GeV and 8 GeV, at the maximum proton energy of 120 GeV. In Fig. 1.9 a schematic description of the beam production is given; more details can be found in Ref. [62].

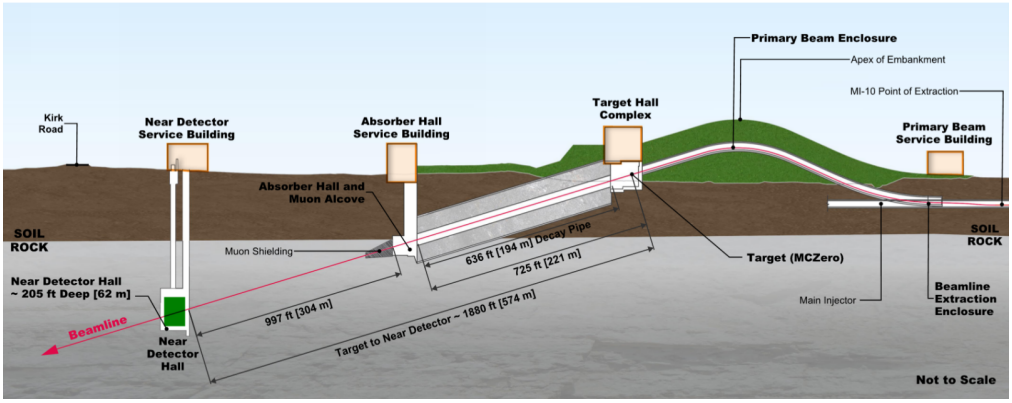

Figure 1.9.: Schematic drawing of the beam production site reaching the near detector. The neutrino beam is produced by the interaction of protons on a graphite target, reaching the near detector 574 m far away from the production point. The picture is taken from Ref. [62].

1.3.4 Near Detector

At the time of writing this thesis, the Near Detector (ND) design is not yet in its final configuration, but the main components and their functionality have been already defined and will be summarized in this section. At the time of writing this thesis, the most updated information on the ND can be found in Ref. [61] and [88], the Conceptual Design Report with additional information is in preparation.

The ND is made by three standalone detectors that give complementary information to reach the best characterization of the neutrino flux and minimize as much as possible systematic uncertainties in the comparison of the neutrino flux measured in the near and far detectors. The main goals of the ND are: provide a high precision measurement of the neutrino flux, the flavor composition and the study of ν-Ar interactions; moreover, from the ND measurements, there will be the possibility to disentangle degenerations biased by the energy resolution in the ND-FD comparison. To achieve the latter goal, the innovative approach, called DUNE-PRISM (DUNE Precision Reaction-Independent Spectrum Measurement) has been developed. This procedure is possible because two of the three detectors can be moved *off-axis* from

the neutrino beam direction to access to many different monochromatic neutrino energies. In Fig. 1.10, the three detectors are visible: the ArgonCube LAr-TPC,

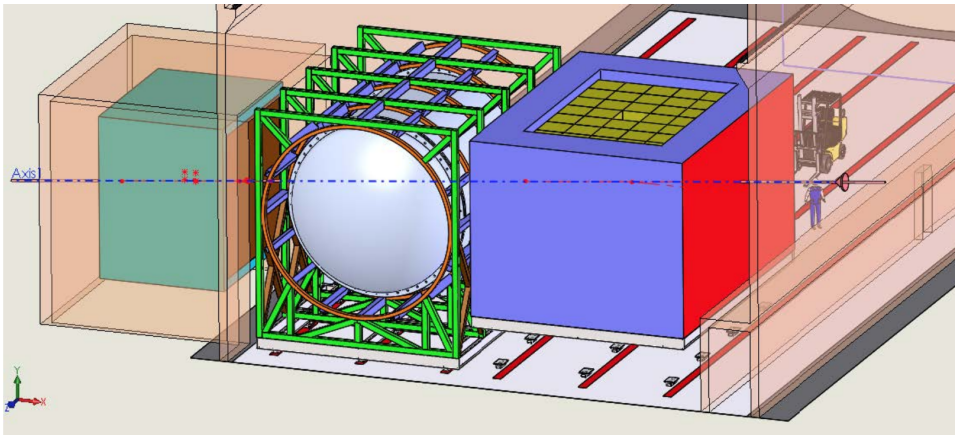

Figure 1.10.: Schematic description of the multi-purpose detector of the DUNE near detector; starting from the **left** it is possible to recognize the 3DST detector and the magnet, the HPgTPC in the **center**, and the LAr-TPC based on the modular design of the ArgonCube detector on the **right**. The picture is taken from Ref. [61].

a high-pressure gas TPC (HPgTPC) surrounded by an electromagnetic calorimeter (ECAL) and a magnet at 0.5 T, together named Multi-Purpose detector (MPD), and a 3-D scintillator Tracker (3DST) surrounded by the KLOE magnet.

The ArgonCube and the MPD are the two components that can be moved. When the three detectors are aligned, the ND configuration is called *on-axis*; while, when the ArgonCube and the MPD detectors are moved, the ND configuration is called *off-axis*. The ArgonCube LAr-TPC, having the same nucleus as the FD, allows having a model-independent extrapolation of the cross-section in the comparison with the FD. The comparison of the neutrino flux between detectors with the same nuclei determines a reduction of the sensitivity to possible nuclear effects and a consequent reduction of detector-based systematic uncertainties. Nevertheless, due to the position of the LAr-TPC so close to the neutrino beam, some differences in the detector structure from the FD LAr-TPC are needed. The ArgonCube detector is big enough to ensure high statistics, expected at $1\times10^8\nu_\mu$ CC events/year, and the complete containment of all the particles produced by the ν-Ar interactions except the muons whose energy is higher than 0.7 GeV/c. Because of the high number of interactions and the necessity to reconstruct also more energetic muons, the Ar-

gonCube detector is downstream by the HPgTPC. The MPD allows the momentum and charge reconstruction of the muons, which is a crucial information to know the E_ν, especially when DUNE will work in the antineutrino mode.

Besides, the lower density of the gas TPC allows having a better reconstruction of the primary interaction vertex in the absence of secondary interactions; this simplified topology allows the improvement of the modelization of the secondary interactions in the denser detector where pile-up is higher. The off-axis movement is a crucial additional degree of freedom for the DUNE experiment since, in this way, a monochromatic ν-beam can be produced. This feature, is very important to minimize the possible bias that can be introduced by the E_ν value, in the ND-FD comparison, due to the convoluted information of the cross-section with the neutrino flux. For this reason, if the comparison includes information obtained from a monochromatic measurement in the ND, the disentangle of this degeneration can be mitigated and, consequently, the systematic uncertainties reduced.

Finally, the 3DST detector is an important monitor of the neutrino flux in both on-axis and off-axis configurations. It is made by plastic scintillator cubes of 1 cm^3 volume that allows very precise tracking of the particles. Moreover, the different target present in the 3DST-S detector will help to test with higher statistics the neutrino models and to compare with the existing measurements from other experiments.

1.3.5 Far Detector

The Far Detector (FD) design is in a more advanced stage. It will consist of four LAr-TPCs with the same fiducial mass of at least 10 k-ton each; two over the four modules will use the SP configuration, while the DP configuration is foreseen for the third module. In the wide DUNE physics program, the sensitivity to the less energetic supernova core-collapse events or the capability to perform searches for physics beyond the standard model, like nucleon decay searches, can be potentiated by implementing the DP LAr-TPCs. This configuration will help in background reduction to distinguish neutral-current interactions from charge-current interactions or to detect low energetic events with a better signal-to-noise ratio compared with the SP option. Moreover, in the SP configuration, the detector size cannot be reached without a modular segmentation of the active volume because of the maxi-

mum drift path that can be covered with minimum degradation; in contrast, the DP configuration will allow longer drift path in a uniform active volume. The fourth module is called a "*module of opportunity*" where other technologies can be implemented if they ensure the same performance to reach the principal DUNE physics goals and allow to explore new physics inside the DUNE project [83].

Each FD module will be hosted in four nearly identical cryostats of 18.9 m×17.8 m×65.8 m, corresponding to 17.5 k-tons of LAr active mass. In each module, the cryostat will be constructed in such a way that it will be aligned with the neutrino beam [85]. Such dimensions have never been reached before and both single and dual-phase technologies have never faced the construction of such a big LAr-TPC before. For this reason, both technologies built and operated prototypes to demonstrate the scaling feasibility; in particular, the DP prototypes' performance is decisive for its installation in the DUNE FD. The DP technology operation at the ton scale was explored for the first time by the WA105 DP demonstrator in 2017 (4.3 tons fiducial mass); the scaling up to ∼300 tons is being demonstrated with the ProtoDUNE-DP detector operation[15]. Being the DP charge readout a less established technology, its doability at the kton scale is more challenging. Due to the final DUNE FD module dimensions, all the TPC components, for both technologies, follow a modular assembling to simplify the detector installation in instrumenting such a big volume. On the left of Fig. 1.11, a schematic picture of the SP module is presented; on the right of the same figure, the drawing of the DP module is shown.

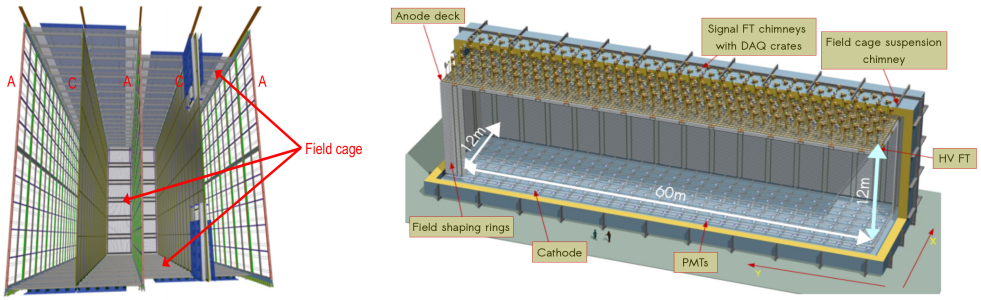

Figure 1.11.: Schematic view of the SP module (**left**) and the DP module (**righ**) that will be installed in the DUNE far detector; the modular assembling of smaller basic components is crucial to simplify the installation. The pictures are taken from Ref. [61].

[15]The description of the WA105 DP demonstrator will be given in Sec. 1.4.1.2; whereas, the ProtoDUNE-DP detector will be described in Sec. 1.4.1.3.

In the SP module, the electric drift field will be applied horizontally and the LAr fiducial mass is segmented in multiple drift regions with a maximum drift length of 3.5 m at the nominal drift field of 0.5 kV/cm. To ensure a good pattern recognition over such drift length, the LAr purity is an essential requirement, the contamination of electronegative molecules (mainly oxygen, water, and nitrogen) must be minimized at the level of the part-per-trillion (ppt) and the electron lifetime must be higher than 3 ms. Moreover, since there is no signal amplification, a very low-noise cryogenic electronics is required to ensure a good S/N (the requirement is to have a S/N $\geq$ 5-10). In the LAr volume, the Anode Plane Assembly (APA) modules and the Cathode Plane Assembly (CPA) ones will be alternated to define the whole fiducial mass, a field cage will surround the drift volume to ensure a uniform drift field. As shown in the figure, each CPA is flanked with two APA on each side. The Photon Detection System (PDS) and its cold electronic will be integrated into the APAs. The PDS baseline module is called X-ARAPUCA [94] and it is the result of the optimization of the innovative photon detection systems implemented in ProtoDUNE-SP.

In the DP configuration the vertical electric drift field, at the nominal value of 0.5 kV/cm, will allow the drift along 12 m thanks to the electron amplification in the GAr phase; the longer is the drift path, the higher is the cathode HV (600 kV will be needed to reach the nominal drift field strength of 0.5 kV/cm). Thanks to the electron amplification in the LEMs devices, the requirements on the noise electronics are less stringent than in the SP case, but a low-noise cold electronic is still needed. Due to the longer drift, the electron lifetime must be higher than 5 ms. The LAr purity can accept a maximum amount of N_2 impurities at the level of the ppt, and a maximum amount of O_2 and H_2O at the ppm level, this requirement can be reached with commercial LAr combined with a non-evacuated vessel recirculation[16]. The charge amplification takes place in 3 m$\times$3 m Charge Readout Plane (CRP)[17] modules (in total, 80 units), where 2880 LEM-anode sandwich units are assembled into an iron-nickel frame that ensures the CRP planarity to face with the possible GAr temperature gradient. The LEM units cover a surface of 0.5 m$\times$0.5 m and the extraction grid, allowing the ionization electron extraction from LAr to GAr, will

[16] The validity of this procedure has been already tested in the ProtoDUNE-SP detector ensuring 7ms electron lifetime.

[17] The description of this innovative structure will be given in Sec. 3.1.3.

be made by 0.1 mm diameter wires defining a surface with a 3.1 mm pitch. With an amplification gain ∼20, in the nominal drift field, a S/N ratio of the order of 95:1[18] can be reached for tracks generated by MIPs crossing the detector 6 m below the anode plane, the S/N ratio would move to 45:1 for tracks crossing the detector 12 m below the cathode. The charge signal is collected in the 2-D anode plane that provides the 2-D track projection from two strips giving the x and y coordinates of the event, with a 3.125 mm pitch used in each strip. The DP photon detection system (PDS) will be made by an array of 720 cryogenic PMTs (R5912-MOD20 model by Hamamatsu [91]), uniformly positioned underneath the TPC cathode, on the floor of the cryostat. A direct coating of a wavelength material on the PMT surface is necessary to allow the VUV light detection after its conversion in visible light; the baseline option for the wavelength material is the tetra-phenyl butadiene (TPB). The HV and the light signal transmission will be possible using a positively biased circuit using a single cable per PMT. Besides, a LED-fiber system will provide visible light to calibrate the system. The definition of such design has been optimized also based on the results that will be presented in this thesis. Additional details on the photon detection system of the DP FD module can be found in Ref. [41], [62]. In next section will be summarized the advantages that would be given by the installation of the DP technology in the DUNE FD and the main challenges this technology must face to be operated at the giant scale.

1.3.5.1 Expected advantages of the DP technology

One of the main advantages brought by the DP technology is the availability of a single and homogeneous LAr volume without any segmentation. This feature is possible thanks to the charge signal amplification in the GAr phase and paves to the possibility to reach longer drift paths facilitating the recovering of the charge signal deterioration. The homogeneous LAr volume reflects an active volume free of materials that can originate intrinsic backgrounds, complicating the event reconstruction. Besides, the same field cage perimeters a higher fiducial mass determining the decreasing of the time needed to reach high statistic; feature particularly precious in long-baseline neutrino oscillation experiments that want to improve their sensitivity to the oscillation parameters and CP violation. The demonstration of the

[18] With this nomenclature the number of multiplied electrons per each electron extracted is given.

DP technology at the giant scale will make wider the energy range of the neutrino interactions that can be explored in DUNE; improvements can be obtained in the detection of the less energetic events as the supernova neutrino flux, the solar and atmospheric neutrino studies. A further very important simplification is given by the 2-D anode structure where the charge signal reconstruction is obtained from the collection of a unipolar signal. Thanks to that, in contrast with the bipolar signals in the SP induction planes, the efficiency reconstruction in DP-TPC increases significantly [84]; the additional advantage in the DP configuration is the readout electronics accessible from outside the cryostat. Finally, the most practical but still important motivation for implementing the DP technology is at the cost level, being lower the number of components to be installed in the TPC, the detector prize also decreases but also the installation logistics is simplified. Nevertheless, the DP configuration, as it has been operated so far, shows still challenges whose overcoming are underway. The inter-space distance between the CRP components and the inter-alignment with the LAr-GAr surface at the mm precision is the very delicate challenge that can limit the charge amplification. Despite the CRP alignment doability has been already demonstrated in laboratory tests, its control over bigger surfaces can be more complicated. A crucial intermediate step will be the ProtoDUNE-DP performance where a $6{\times}6$ m^2 surface is covered by four CRP modules. Additional challenges are related to the light detection as well; as it will be detailed in Sec. 2.2.3, the Rayleigh scattering is the most problematic process that can decrease the light signal. In the DP FD module, assuming the currents values for this parameter, the PDS must be able to collect light produced up to $\sim 12\lambda_{Ray}$ scattering length far away [90]. For this reason, other solutions, as the installation of reflective foils in the top part of the module, are under study in combination with the baseline PDS design. More details can be found in Ref. [41], [62].

1.4 The DUNE FD prototypes at CERN

The preparatory step to the DUNE FD modules consists of a dense program of prototypes built and operating at CERN, intending to demonstrate the potentiality of the single and dual-phase technologies. The main goal of these prototypes is to identify the optimal requirements needed to build the DUNE FD, based on the experience reached with their performance, both in terms of validation of TPC

components and algorithm optimization for the event reconstruction. One of the key points of the two ProtoDUNEs detectors is that they will host the modular elements of the final design of both SP and DP TPCs scaled 1:1 with the ones that will be installed in the DUNE FD. Given the robustness of the SP LAr-TPCs showed during the last decades, the SP technology started testing and optimize the detector design for the DUNE FD based on the performance of the ProtoDUNE-SP detector [92], [63], [93], filled by a total LAr mass of ∼770 tons. ProtoDUNE-SP had the first run of data (phase-I) from the SPS beam during 2018 and is continuing to be exposed to cosmic muons since 2019. Its operation has already shown excellent results [93] and good detector stability; moreover, the charged-particle beam test has allowed calibration measurements improving the reachable physics in the DUNE experiment. Currently, an important technical upgrade of the detector is in preparation to take a second run of beam data (phase-II) in 2022. The DP technology, on the other hand, culminated its dedicated R&D and prototype program started in 2010 with the ProtoDUNE-DP detector, with ∼300 tons LAr fiducial mass and 6 m drift; with the first data taking period ended in Fall 2020 with the exposure of the detector to cosmic muons. The ProtoDUNE-DP construction was possible thanks to the proof of the DP technology at the ton scale in the WA105-DP demonstrator that has been operated in 2017. Important lessons and design improvements have been gained due to the performance and physics results achieved with the previous smaller prototypes, as will be described in Sec. 1.4.1. All the additional details can be found in Ref. [41], [70], [78], [80], [84].

1.4.1 DP prototypes: from R&D setups to ProtoDUNE-DP

In 2010, at CERN, a R&D and prototypes program started to demonstrate the scalability to the giant scale of a DP LAr-TPC where both charge and light signals can be collected. Initially, two small R&D setups have been operated reaching a maximum drift length of 60 cm and 76×40 cm^2 collection surface in the second of the two setups. Then, within the LAGUNA-LBNO European programme [77], the WA105 dual-phase demonstrator [78] has been operated in 2017 exposed to cosmic muons with a collection surface of $3m^2$. The role of the WA105 DP demonstrator detector has been crucial since it demonstrated the possibility to operate standalone charge readout structures feasible to cover large surfaces. Additionally, given the

detector dimension, the study of the scintillation light pioneered the understanding of its propagation in big detectors.

1.4.1.1 Small R&D prototypes

In order to test the main components of the innovative concept of a DP LAr-TPC with both charge and light readouts, two setups were built with increasing size, the "3 liters" (3 L) [98] and the 250 L [101] and they both operated at CERN between 2010-2014, exposed to cosmic muons for relatively short periods. The operation of the 3 L demonstrated for the first time the feasibility of a LAr LEM-TPC. The LEM devices are a more granular and more robust extrapolation of the GEMs devices with millimeter-sized holes and a thickness of about 1 mm. They are produced with the standard Printed Circuit Board (PCB) technique and the holes are practiced in the PCB plate. In this setup, the LEMs demonstrated for the first time stable operation of extraction and amplification of the electrons in the GAr phase. Additionally, the same prototype brought to the definition of the innovative 2-D segmented anode plane, with a 3 mm pitch, where the charge signal was collected. The design is the current baseline for the DP LAr-TPCs. The 3 L setup had a very small volume with a 20 cm drift and 10×10 cm^2 readout surface. The nominal drift field of 0.5 kV/cm was provided by field shapers spaced 5 mm and an electric field of 2 kV/cm was applied to extract the electrons in the gas phase. Below the cathode, only one PMT was used to collect the VUV scintillation light and provide the trigger and the t_0 reconstruction. The 3 L setup was the first proof of the stable operation of a DP LAr-TPC with electron amplification in the LEM units and an adjustable gain. The latter feature is particularly interesting for the LEMs implementation in bigger detectors. The setup operated in stable conditions with an effective gain∼15 that corresponds to a S/N∼60 for MIPs [99].

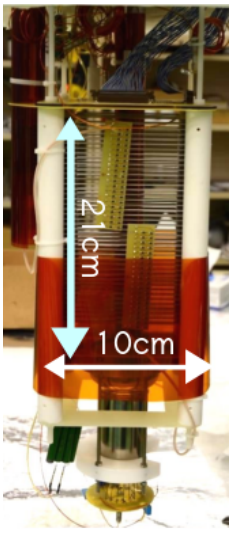

The LEM devices, successfully operated in the 3 L, were then installed in the 250 L setup to cover a more extended surface. In this setup, the charge extraction was demonstrated over a 76×40 cm^2 surface, above 60 cm of maximum drift. Unlike

the LEM modular unit, the detector structure changed a lot compared with the 3 L. In this second setup, the LEMs were coupled with the 2-D anode in a single structure called LEM-anode *sandwich*; two additional extraction grids were added to facilitate the electron extraction in the GAr phase. In the long term operation of this setup the second grid has been found that could limit the transparency of the extracted electrons and this configuration was successively optimized using only one extraction grid. The setup, that operated immersed in the ArDM [103] cryostat, had a field cage structure with field shaper 2 cm equally spaced where the maximum drift field applied was of 0.6 kV/cm. Two PMTs were positioned underneath the cathode, protected by a grounded metallic grid; only one of them was furnished by wavelength shifter. The 250 L setup led to the identification of the optimal configuration of the LEM-anode *sandwich* structure where the LEM and the anode are assembled in a standalone structure that can be used as a basic module to cover large surfaces. The assembling of unitary structures helps in making the device more stable; in this way, possible discharges are confined into the unit module to avoid the propagation of the discharges to one sector to the other [101]. All additional details about the two setups can be find in Ref. [98], [99], [100], [101], [102].

1.4.1.2 WA105-DP demonstrator

The WA105 dual-phase demonstrator [78], also referred in the text as 3×1×1, is the topic of this thesis and it will be widely described in Chapter 3; its design was very similar to the 250 L setup. The main innovative part was the installation of the Charge Readout Plane (CRP) where the charge extraction, amplification and collection in the GAr phase take place. This structure covers a surface of 3×1 m^2 and it is electrically and mechanically independent from the FC structure. Below the transparent cathode, shielded by a metallic ground grid, five 8-inches cryogenic PMTs are positioned to detect the scintillation and electro-luminescence light signals. To detect the VUV light produced in the scintillation, the five PMTs use TPB as a wavelength shifter applied in two different configuration. In view of the definition of the photon detection system design for bigger detectors, two different PMT highvoltage supply configuration have been installed and tested. In Chapter 3 the detailed description of the detector and photon detection system components are available.

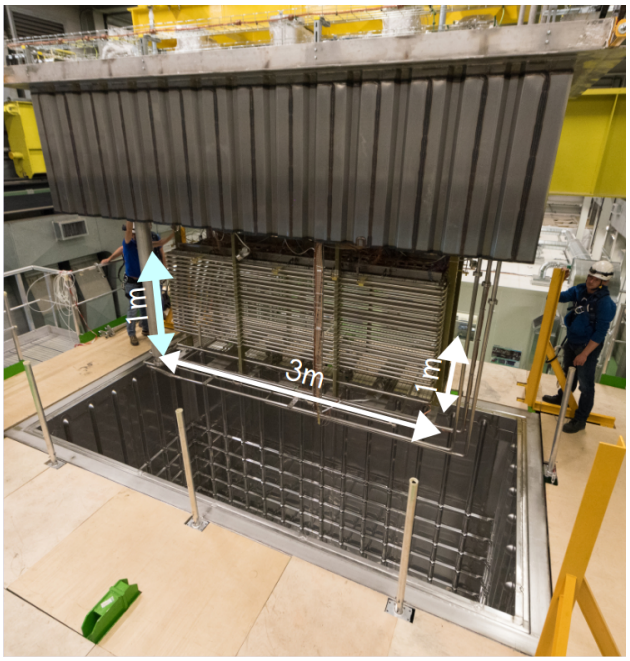

Technological milestones

The role covered by the WA105 DP demonstrator has been very significant since it proved the feasibility of the DP LAr-TPC at the ton scale with a charge track reconstruction over a 3×1 m^2 surface. The most important results regarding the track reconstruction from the charge signal are itemized below (more details can be found in Sec. 3.1.4):

- *Cryogenic system and membrane cryostat*: given the demonstrator dimensions, much bigger than the previous TPCs, the cryostat building itself has

been challenging; this construction has been designed in collaboration with the industry to ensure a thermodynamically stable environment. The cryostat consists of a non-evacuable membrane that endured cryogenic temperatures for the ultra-pure LAr, uniform gas density, and a flat liquid argon surface.

- *Extraction of the ionization charge over an area of 3 m^2*: for the first time, the charge extraction over a surface with such a large area has been obtained.

- *Assembling of multiple LEMs to allow charge extraction over the 3 m^2 surface*: the combined operation of 12 LEM modules was pioneered in the WA105 DP demonstrator. The effective gain$\sim$20, already reached in the operation of the single devices, is expected to be reached in the DUNE FD module. In the WA105 DP demonstrator some limitations in such simultaneous operation have been found affecting the effective gain reached in each LEM module. Despite that, the demonstrator could operate in stable conditions reaching the amplification in the whole surface accepting the compromise to apply a lower electric field in the corner LEMs.

- *Analog front-end electronics and signal readout*: Due to the vertical drift applied in the DP-TPC, the positioning of the front-end electronics close to the anode readout plane was possible. This innovative positioning ensures very useful accessibility during the operation.

As in the previous R&D setups, the light detection system provided a self-trigger for the charge DAQ system. Differently from them, thanks to the detector dimensions, pioneering results have been reached in the study of the scintillation light in LAr and GAr; the deep understanding of the scintillation light production and propagation, in fact, must be improved to scale the LAr-TPCs toward higher dimensions; in particular, determining the requirements for the light detection system to be operated in larger detectors as ProtoDUNE-DP and DUNE far detector. Additionally, the investigation of the electro-luminescence light allowed exploring its correlation with the track topology and the charge reconstruction.

1.4.1.3 ProtoDUNE-DP

The ProtoDUNE-DP detector has 6×6×6 m^3 LAr active volume. In the ProtoDUNE-DP detector, 6 m drift at the nominal value of 0.5 kV/cm is required and four charge readout planes covering a 6×6 m^2 surface; these dimensions allow to test the detector components for the FD module in the 1:1 scale thanks to their modular assembling. In each CRP module 36 LEM-anode units are assembled; compared with the design used in the WA105 DP demonstrator, the LEM's structure has been optimized to ensure a better stability covering the 3×3 m^2 surface and minimizing the possibility of electrical discharges. In the first ProtoDUNE-DP run only half of the surface is fully instrumented. The CRP units have been installed separately from the field cage and, before the installation, the performance of the CRP modules has been examined in a dedicated setup (*cold-box*) to test the planarity, the HV stability, and their operation in the larger LAr-GAr interface. The field cage also has a modular structure made in turn of subunits of 3×2 m^2 sub-units. The photon detection system is made by 36 8-inches PMTs, suitable to tag the t_0 time of the triggered events, whose positioning has been optimized to have the best coverage inside the detector, maximizing the light collection efficiency. The VUV scintillation light is converted using two different wavelength shifters: a direct TPB coating on the PMT photocathode-surface is applied on 6 over the 36 PMTs; on all the other, the innovative Polyethylene naphthalate film is being tested. The performance and the optimization of this photon detection system have been tested in the WA105 DP demonstrator; besides, the complete characterization of the PMT configuration se-

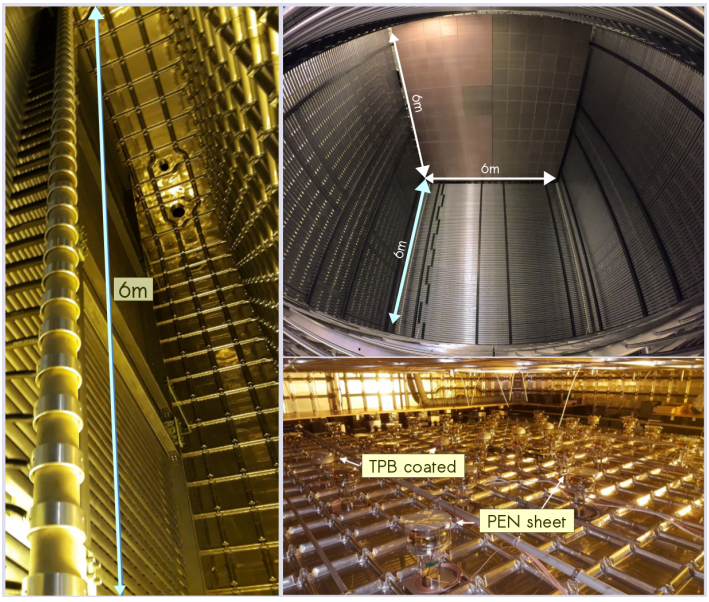

lected for the DUNE FD has been performed in the CIEMAT Laboratory [91]. The photon detection system has shown a very good performance in the ProtoDUNE-DP detector, acquiring millions of data events whose analysis is ongoing.

1.5 The added value of the light detection in a DP LAr-TPC

The scintillation light signal covers an important role in LAr-TPCs giving access to the knowledge of the arrival time of the event, t_0, in the drift direction, allowing the reconstruction of the z-coordinate of the event. Even with very high LAr purity, minimum signal degradation is expected after long drift paths because of the electron diffusion; for this reason, knowing the t_0 time allows the correction of the energy response and the consequent resolution improvement. In the case of the measurement of the neutrino oscillation parameters in DUNE, for instance, this possibility allows decreasing the systematic uncertainties through a cross-check of the charge reconstruction with the light information. Additionally, in the DP LAr-TPC module, where the drift length is much longer than the SP module (12 m instead of 3.5 m drift length), recovering the signal degradation could be more challenging. On one side, the signal amplification in GAr helps in the improvement of the charge signal reconstruction; on the other, being the charge and light systems located at the opposite ends of the detector, only the combination of charge and light signals in a complementary calorimetric approach can enhance the event reconstruction in the whole volume.

One of the advantages of measuring the t_0 is in allowing the fiducializion of the LAr volume around the event to be reconstructed. This characteristic improves the detection of less energetic non-beam events like the detection of supernova burst (SNB) and nucleon decay searches. Although SNB have a typical signature that can be reconstructed from the TPC, the detection of the light produced by these events is extremely useful in the trigger definition for such events. Given the rareness of such events, the availability of independent trigger systems is precious. Besides, the detection of the possible SNB t_0 will allow a good vertex location and a consequent improvement in energy event reconstruction opening access to study cosmological models related to the burst production and neutrino interactions within the core collapsed. In the case of rare events like nucleon decays, background rejection is crucial. The definition of a fiducial volume, given the t_0 arrival time, in the region

where the event has been detected and the requirement of a fully contained event inside the fiducial region, is the only way to distinguish the nucleon decay from events generated outside the detector. For similar reasons, the reconstruction of solar or atmospheric neutrinos interactions is improved through the detection of the light produced in the interaction. These interactions take place in a precise time and a confined volume, so, similarly to the case of the nucleon decays, through the knowledge of the t_0, it is possible to identify such events inside the detector and fiducialize the volume surrounding them.

Especially in the dual-phase DUNE FD module with the 12 m height and the PMT array positioned in the bottom part of the detector, the detection of the light from the upper part of the LAr volume can be complicated due to the Rayleigh scattering that becomes more relevant when the dimensions of the detector increase. Similarly, the detection of the electro-luminescence light signal is not ensured by the actual module configuration. For this reason, improvements in the detector configuration are under study and some of them have been mentioned in Sec. 1.3.5 and can found in [41], like the inclusion of reflective foils in the upper part of the detector and the Xenon doping. Despite that, it is worth reminding important features of the detection of the electro-luminescence light that has been explored in the studies performed in the WA105 DP demonstrator where it gave an alternative measurement of the ionization charge and that is being further investigated in the ProtoDUNE-DP detector. The ratio of the electro-luminescence signal with the prompt scintillation light depends on the particle nature. This feature is already used in DM experiments for background rejection to distinguish electrons from nuclear recoils. Moreover, the S2 signal is strictly dependent on the track topology and it can be used to measure the velocity of the drifted electrons. This knowledge can be used as a cross-check for the correction of the track reconstruction degradation after long paths. The S2 signal intensity as well, is affected by the presence of electronegative impurities and, for this reason, it can be used to have a complementary measurement on the electron lifetime. These and other features of the S2 signal have been deeply investigated in the WA105 DP demonstrator and related results will be presented in Chapter 6.

"Ningún pájaro vuela recién nacido,
pero llega el momento en que el aviso del aire es más fuerte que el miedo de caer."
L. Sepúlveda

CHAPTER 2
WORKING PRINCIPLES OF A DUAL-PHASE LAR-TPC

This chapter summarizes the physics processes taking place in a dual-phase LAr TPC when the LAr bulk is crossed by an interacting particle. The energy lost by a relativistic charged interacting particle with a medium is described in Sec. 2.1. The rest of the chapter is focused on the description of the scintillation light mechanisms in the liquid (Sec. 2.2) and the gas (Sec. 2.4) phases.

In the liquid phase, the propagation of the light and the drift of the electrons toward the GAr phase will be described in Sec. 2.2.3 and Sec. 2.2.4, respectively. The TPC performance critically depends on the concentration of electronegative impurities; in Sec. 2.3, how their presence can deteriorate the light and charge signals will be presented. Finally, the mechanisms governing the electron amplification in the GAr phase and the consequent production of the electro-luminescence light will be described in Sec. 2.4.1 and Sec. 2.4.2.

Controversies about some LAr properties related to the scintillation light production and propagation are present in the literature; their description will be presented in Sec. 2.5, paying particular attention to the ones studied in this thesis.

2.1 Energy deposition in LAr

The interaction of a relativistic charged particle crossing a medium determines the loss of its energy via inelastic scattering with the shell electrons or with the nuclei of the material. The mean rate of the energy loss per unit thickness of material

(typically expressed in $MeVg^{-1}cm^2$) is a function of the particle velocity and it is well described by the Bethe-Bloch equation:

$$-\frac{dE}{dx} = Kz^2\frac{Z}{A}\frac{1}{\beta^2}\left[\log\left(\frac{2m_e c^2\beta^2\gamma^2 W_{max}}{I^2}\right) - 2\beta^2 - z^2 L_2(\beta)\right] \tag{2.1a}$$

$$z^2 L_2(\beta) = \delta(\beta\gamma) + 2\frac{C}{Z}; \tag{2.1b}$$

In the formula, K ($K = 4\pi N_A r_e m_e c^2$) is a constant related to the Avogadro's number, N_A, the classical electron radius, r_e, and the speed of light c; z is the charge of the incident particle, Z is the atomic number and A the atomic mass of the material. β is the velocity of the incident particle normalized to the speed of light c, γ is the Lorentz factor, $W_{max} = \frac{2m_e c^2\beta^2\gamma^2}{1+2\gamma m_e/M+(m_e/M)^2}$ is the maximum energy that can be transferred to an electron in a single collision by the incident particle of mass M, and I is the mean excitation energy of the absorber (I = 188eV for Ar). Independently from the material, instead, the Bethe-Bloch equation shows a minimum (around $\beta\gamma \approx 3$ - 4); a relativistic particle whose mean energy loss rate is at that minimum value is called *minimum-ionizing particle* (MIP). After that, there is the characteristic rise of the equation which is known as the *relativistic rise*. In the Bethe-Bloch equation, the $\delta(\beta\gamma)$ term is the density effect correction needed for energy loss at high energy; at high velocities, the incident particles polarized the atoms of the medium in such a way that the electrons far from the crossing particle will be shielded from the intensity of the full electric field. The density correction determines the lowering of the relativistic rise slope of the Bethe-Bloch equation. At low energies, instead, the stationarity of the electrons compared to the incident particle hypothesis is no longer valid and shell correction, C, must be introduced. A linear correction, $zL_1(\beta)$, introduced by Barkas [112], describes the reduction of the stopping power for a particle with same mass and velocity but a negative charge. More details on the Bethe-Bloch equation and its corrections can be found in Ref. [107] and [108]. The possibility that a large amount of energy is transferred to a single orbital electron is not common, but when it happens this electron can ionize the surrounding atoms. The kinetic energy of this kind of electrons, named δ rays, is in the range $I \ll W \leq W_{max}$. Their production can be described as an elastic scattering at the θ angle between the δ ray electron and the orbital electron at the maximum momentum p_{max}; because of that, the angular distribution can be described by $\cos\theta = (T_e/p_e)(p_{max}/W_{max}))$.

In real detectors with finite thickness, the distribution of the energy loss probability is well described by the Landau distribution, the peak of the distribution represents the most probable value of energy loss and it is described by the following equation:

$$\Delta_p = \xi\left[\log\left(\frac{2m_e c^2\beta^2\gamma^2}{I}\right) + \log\left(\frac{\xi}{I}\right) + j - \beta^2 - \delta(\beta\gamma)\right], \tag{2.2}$$

being $\xi = \frac{K}{2}\frac{Z}{A}\frac{x}{\beta^2}$, x expressed in g/cm^2, and j= 0.2. This expression, including all the corrections, is known as the Landau-Vavilov-Bichsel most probable value of the energy loss. The probability of having δ rays is taken into account in the tails of the Landau distribution expressed in Eq. (2.2); it is important to note that if the dE/dx is independent of the thickness material, the Δ_p/x is not but scales in a logarithmic way with it [108].

In the case of electrons and positrons interacting with matter, their energy loss is caused by ionization and the emission of Bremsstrahlung radiation. The main reason for that is in the identity between the mass of the incident particles and the shell electrons.

Photons and electromagnetic showers

At very high energies, the favored processes of energy loss with the material are radiative. Photon propagation in matter is drastically different from that of charged particles since they are much more penetrating and their energy is not degraded but only attenuated unless they are absorbed. The main phenomena that can take place are determined by the photon energy; starting from the one that needs less energy, they are the photoelectric effect, the incoherent Compton scattering, and the pair production. The critical energy, E_c, is the energy above which radiative processes become dominant; it depends on the particles and the material, E_c ~500 GeV is the critical energy for a muon in LAr. For even higher energies, photonuclear interactions where the target nucleus is broken up can take place [109].

For $e^{\pm}$ energies higher than their E_c, the dominant source for $e^{\pm}$ energy loss in matter is Bremsstrahlung radiation and the photons generated are energetic enough to produce e^+-e^- pairs; the combination of the two processes initiates the so-called *electromagnetic shower*. Its development inside the target material can be defined by two characteristic quantities: the radiation length, X_0, usually measured in g cm^2,

and the Molière radius, R_M. Both quantities are characteristic of each material, in the case of Argon, $X_0 = 14$ cm and $R_M = 9.3$ cm. The electromagnetic shower evolves until the energy of each particle becomes lower than the critical energy, that reaches hundreds of keV in LAr.

2.2 The physics in the liquid phase

When the particle loses its energy, the LAr atoms can be either ionized or excited; both processes, directly or indirectly, generate primary scintillation light in the liquid. Due to the presence of a drift field, the electrons produced by ionization are drifted toward the gas phase.

First comprehensive measurements of the fundamental LAr properties have been concentrated between the end of the 60s and the 90s. Because of the LAr application as a target for DM experiments, the particles used as sources were electrons, α, or fission fragments; only recently, some results obtained from cosmic muons have been provided. In terms of scintillation light, the general expectation is that a cosmic muon traversing LAr at the MIP energy does not behave too differently from an electron at the MIP energy. Nevertheless, additional measurements are needed to improve the understanding of the LAr response to other particles than electrons or neutrons in order to be used as a target in neutrino experiments.

2.2.1 The ionization and recombination process

The energy loss by the incident particle generates three different processes:

- ionization
- excitation
- heat

since the heat contribution must be detected in a different way than in a TPC, it will not be treated in this discussion. Defining E_0 the average energy released to the medium, it is possible to write the following equation:

$$E_0 = N_i \cdot E_i + N_{ex} \cdot E_{ex} + N_i \cdot \epsilon \tag{2.3}$$

being N_i and N_{ex} respectively the number of ion-e^- pairs and excitons[1] produced, E_i and E_{ex} the energy needed respectively to ionize or excite the medium traversed by the particle, and ϵ, average kinetic energy of sub-excitation electrons, that lies in the range (6.3:7.1) eV [117]. Dividing Eq. (2.3) by N_i, it is possible to relate the average energy lost with the W-value, the average energy needed to create a ion-e^- pair:

$$W = E_i + \frac{N_{ex}}{N_i} \cdot E_{ex} + \epsilon \tag{2.4a}$$

$$W = \frac{E_0}{N_i} \tag{2.4b}$$

In the case of argon, the atom ionization energy in liquid is 15.75 eV [118], and 14.2 eV [119], in gas; considering these values, arises that the ion-e^- pair production in gas is facilitated more than in liquid, a W-value = 23.6 eV in liquid and W-value = 26.4 eV in gas have been measured [124].

2.2.1.1 Recombination models

With the creation of ion-electron pairs by the passage of particles in the LAr, a non-negligible probability that charges recombine along the particle path track exists. The recombination process is strictly dependent on the nature of the particle and the density of the medium. For a MIP, the energy loss is expected to be linearly proportional to the number of ion-e^- pair produced (*linear energy transfer* - LET - regime). Due to the ionization process, the interacting particles and possibly δ rays create holes and electrons along their trajectory. The hole is immediately ($\mathcal{O}$ picoseconds) localized by the formation of Ar_2^+ dimers[2]. Depending on the nature of the particle and the particle LET, a different *track structure* is created as a function of the escaping probability of the electrons from the Coulomb cloud structure around the respective ion parents. In Ref. [122], how the *track-structure* changes depending on the mass and LET of the interacting particles is reported. In the LET regime, all the ion-e^- pairs recombine in absence of drift field. Depending on the dynamic of the recombination process, its modelization is still not univocal; the most accredited models will be presented hereafter. In the next section, the influence of the recombination process on the scintillation light production will be described.

[1] The exciton is the way to call the bound-state of an electron and an electron-hole.
[2] A dimer is the excited state of a diatomic molecular.

Accordingly to the Onsager model [126], in the case of light particles, around the hole, it is possible to imagine a sphere with a radius R_C, determined by the Coulomb attraction. Following this description, schematically represented in Fig. 2.1 a cylin-

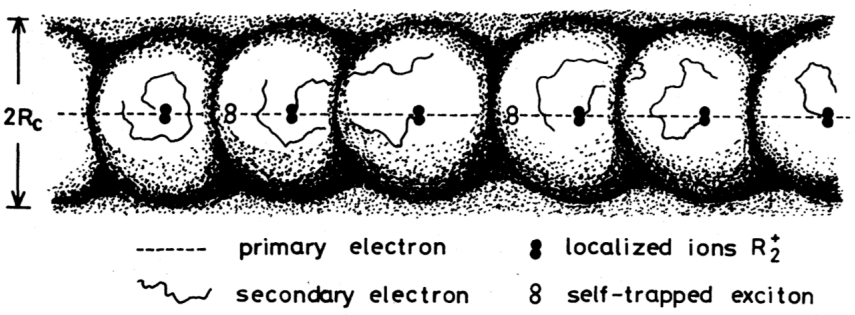

Figure 2.1.: Illustration of the *track structure* and the Coulomb clouds determined by the ionization process of an incident electron; the Coulomb attraction radius R_C is reported. The illustration is taken from Ref. [125].

der tube with radius R_C and length R_0 is formed, here the trapped electrons are distributed in the Coulomb field assumed uniform; the initial density of the ion - e^- pair is $\eta_0 = N_i/\pi R_C^2 R_0$, for 1 MeV e^- in the argon has been measured to be $2{\cdot}10^{-7}\mathrm{nm}^{-3}$ [125]. The electrons produced by the ionization processes just described, can either recombine with the ion parents (*germinate recombination*) or with the localized ions they are attracted to (*columnar or box recombination*); in the scheme reported in Fig. 2.2, all the processes leading either to the ion-e^- recombination or the escaping of the electrons are summarized. The presence of the drift field suppresses the recombination processes. As an alternative to the Onsager's descrip-

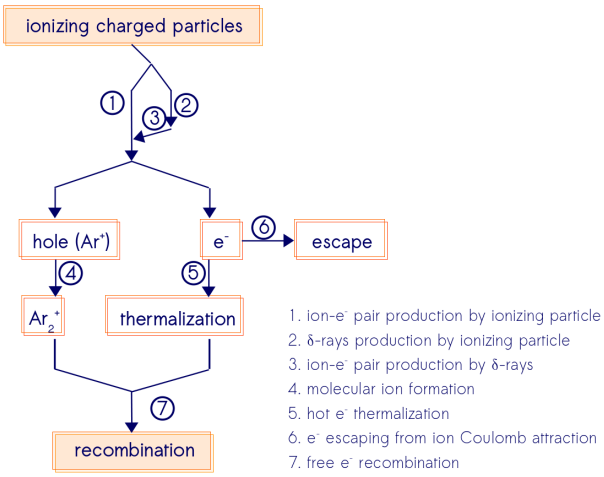

Figure 2.2.: Scheme summarising the general reactions occurring in noble gases excited by ionizing charged particles; re-adapted from Ref. [125].

tion [126], different models have been proposed to describe the recombination factor, $Q(\mathcal{E})/Q_0$, counting for the electrons escaping the recombination at the drift field $\mathcal{E}$ under different energy regimes. Different studies have been reported in literature for low energy electrons [127], [128], [130], muons, and protons [171], [133]. Both the *germinate* and *columnar* recombinations are well described by the Jaffè theory [134] that is valid for relatively strong drift fields ($\mathcal{E} > 0.5$ kV/cm). For less energetic interacting particle the recombination is well described by Thomas-Imel *box* model [130]:

$$\frac{Q(\mathcal{E})}{Q_0} = \frac{1}{\xi} ln(1 + \frac{1}{\xi}) \tag{2.5}$$

where $\xi = \kappa/\mathcal{E}$ is the adjustable parameter, inversely proportional to the electric drift field $\mathcal{E}$ and proportional to the ionization charge density ($\kappa = N_0\alpha/4a^2\mu$ with N_0 the total number of electrons, α is the recombination coefficient, a the size of the arbitrary box, and μ the electron mobility assumed to be independent from the field). As reported in Ref. [130], the model has been demonstrated to be valid up to an electric drift field of 10 kV/cm. If the dependence with the stopping power, $\langle dE/dx \rangle$, is explicitly considered [171], [133], Eq. (2.5) is modifed as follows:

$$\frac{Q(\mathcal{E})}{Q_0} = \frac{A}{1 + k_E/\mathcal{E}\langle dE/dx \rangle}, \tag{2.6}$$

in this expression, A is a normalization constant that, with k, are the two parameters obtained fitting the data. In Ref. [171], the two parameters have been measured from the muon stopping power, in the (0.2, 0.5) kV/cm range: A = (0.800 ± 0.003) and $k = k_E\langle dE/dx \rangle$ = (0.0486 ± 0.0006) kV/cm (g cm^{-2}/MeV).

In Fig. 2.3, the collected charge and the recombination factor as a function of the drift field strength are reported for distinct sets of data and considering the different recombination models; the limitations in the Onsanger's parametrization for drift field strength higher than ∼1 kV/cm are visible in the left-plot.

2.2.2 The primary scintillation light mechanism

The primary scintillation light mechanism is originated by the de-excitation of the argon excimers[3] that emit photons in the Vacuum Ultra Violet (VUV) region. As

[3]The excimer is the strongly bound diatomic molecules in the excited state, it stands as the abbreviation of excited dimer.

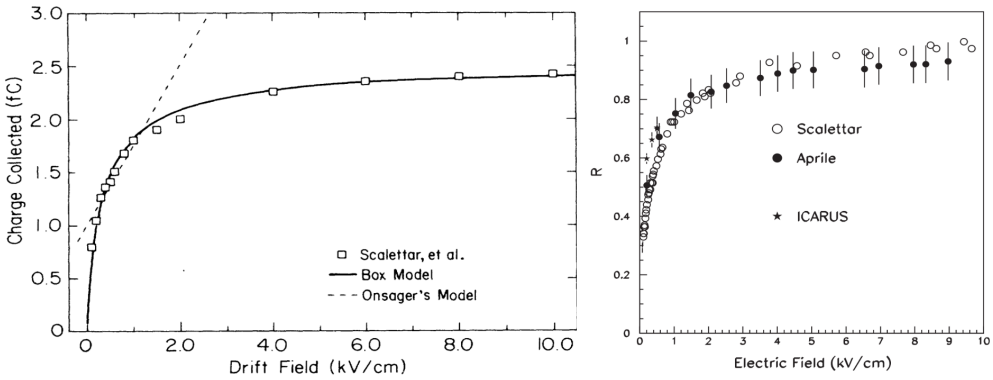

Figure 2.3.: Left: Dependence of the charge obtained from the collection of ionization electron with the drift field. Data points are from ^{113}Sn source [128]. The black line represents a fit obtained from the parametrization given by the *box*-model; for comparison, the dotted line represents the fit obtained using the Onsager's model. The plot is taken from Ref. [130]. **Right:** Dependence of the recombination factor, $R = Q(\mathcal{E})/Q_0$ as a function of the drift field; the full points are the data obtained from MIPs (black stars) [133], and electrons (empty [128] and full [129] circles). The plot is taken from Ref. [133].

reported in Ref. [131], the Ar VUV scintillation light band spectrum is centered at 126.7 nm. The excimer formation can be obtained either directly from the energy loss by the interacting particles or from the ion-e^- pair recombination. In the case of argon, as well as for all the other noble elements, the scintillation processes are similar in the condensed and the gas phases.

The scintillation light mechanism in argon has been studied for different incident particles; for a general particle, x, the reactions leading to the photon emission are the following:

direct excimer formation

$x + Ar \rightarrow Ar^* + x$, particle impact

$Ar^* + Ar \rightarrow Ar_2^{*,v}$, excimer formation

$Ar_2^{*,v} + Ar \rightarrow Ar_2^* + Ar$, relaxation

$Ar_2^* \rightarrow Ar + Ar + h\nu$, VUV light emission

excimer formation from recombination

$x + Ar \rightarrow Ar^+ + e^- + x$, ionization

$Ar^+ + Ar + Ar \rightarrow Ar_2^+ + Ar$

$$
\begin{aligned}
&e^- + Ar_2^+ \rightarrow Ar^{**} + Ar && \text{, recombination} \\
&Ar^{**} + Ar \rightarrow Ar^{*} + Ar + Ar + \text{heat} && \\
&Ar_2^{*} \rightarrow Ar + Ar + h\nu && \text{, VUV light emission}
\end{aligned}
$$

in this nomenclature, the ν index is referred to the vibrational state of the excimer that is null when the excitation is purely electronic; the vibrational relaxations are typically non-radiative and, only occasionally, emit infrared photons. The direct excimer formation is also called *self-trapping* process. From both excimer formation processes, the final state that leads to the VUV photons is the same, consequently the wavelengths photon and their decay de-excitation times are expected to be the same. However, the formation mechanisms leading to the excimer formation by direct excitation or by recombination are not completely understood yet. The excimer formation by direct excitation of the Ar dimer has been estimated to be in the range 1-10 picoseconds [120], [121]. On the contrary, the recombination dynamic in LAr is less known than in other noble gases [122] and few measurements have been reported for the recombination time, T_R, that is found to be longer than *self-trapping* time. In Ref. [123], a T_R <1 ns is reported for 1 MeV electrons; whereas, in [125], in absence of drift field, T_R is found to be (0.8 ± 0.2) ns.

2.2.2.1 Light yield, dependence with the LET and the drift field

In absence of electric drift fields, the number of scintillation light photons is expected to be maximum, $N_{ph} \approx N_i + N_{ex}$, since the recombination contribution to the scintillation light is expected to be maximum as well. Considering the previous expression for N_{ph}, defining the average energy required for the production of a single photon $W_{ph} = E_0/N_{ph}$, and assuming that each formed excimer produces a photon, W_{ph} can be expressed as follows:

$$W_{ph,max} = \frac{W}{1 + \frac{N_{ex}}{N_i}}. \tag{2.7}$$

In contrast with the W-value, the W_{ph} is affected also by the efficiency of the energy transferred to the medium through the direct excimer formation and ionization; this

feature affects, in turn, the detector energy resolution and the linearity of the response. In the case of liquid argon, in absence of electric drift field, the N_{ex} /N_i ratio has been calculated [124] and experimentally measured [135], its value lies in the range (0.19, 0.29) and $W_{ph,max}$ in the range (19.8, 18.4) eV [135]. However, in Ref. [140], N_{ex} /N_i = 0.43 is reported. As a consequence of Eq. (2.7), the scintillation light yield, representing the total scintillation light produced, is a key quantity to have a direct expression of the detector capability. This quantity, originally expected to be independent on the particle LET and maximum in absence of drift field, showed a deviation of about $\sim$ 20% its theoretical estimation; in the case of 1 MeV electron, the scintillation light yield is expected to be 5.03×10^4/MeV, while its experimental measurement is found at 4.1×10^4/MeV [137]. This discrepancy can be explained considering the dependence of the scintillation light production on the particle LET as well as of the role played by the electrons escaping the recombination with the parent ion.

The dependence of the scintillator response as a function of the energy transfer to the medium has been empirically described by Birks [139]; in analogy with Eq. (2.6), the dependence with the particle LET can be included and the dependence of the scintillation light per unit path can be described by the following equation [137]:

$$\frac{dL}{dE} = \frac{A\frac{dE}{dx}}{1 + B\frac{dE}{dx}} + C_0, \tag{2.8}$$

with A, B, and C_0 adjustable parameters that can be obtained fitting the data. In particular, C_0 is the constant term including direct excitation and geminate recombination contributions, while the volume recombination is included in the first term of Eq. (2.8); the two coefficients A and B includes the LET dependence of the volume recombination decreasing the scintillation yield in absence of drift field. Further modifications of the Eq. (2.8) have been introduced to describe very low energetic interacting electrons; more details are available in Ref. [136].

The relative scintillation light yield, measured in liquid argon from a 1 MeV electron [125] and other interacting particles [135], is reported in Fig. 2.4 as a function of the electric drift field for values reaching $\sim$10 kV/cm. To include the dependence on the drift field, the terms in Eq. (2.8) are modified as follows: $dL/dE \rightarrow dL(\mathcal{E})/dE$ and $dE/dx \rightarrow dE(\mathcal{E})/dx$. For a drift field of the order of tens of kV/cm, the scintillation light yield decreases up to $\sim$1/3 of the initial value, meaning that $\sim$(64 - 67)% of the light yield is produced by the recombination processes and the remaining

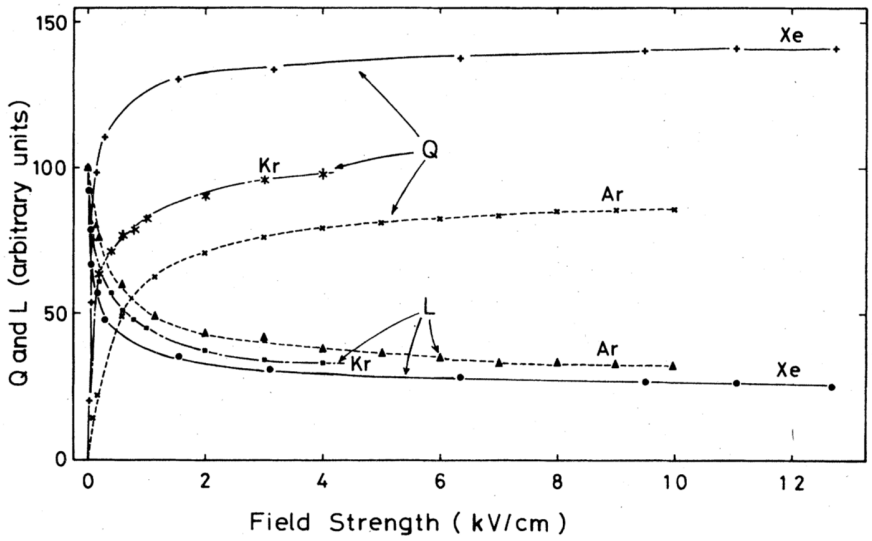

Figure 2.4.: Variation of relative scintillation light, L, and collected ionization charge, Q, as a function of the electric drift field strength produced by electrons with energy in the range (0.976, 1.05) MeV, using various noble gases. Triangle point represent data obtained in LAr in the drift field range reaching up to 10 kV/cm. The plot is taken from Ref. [125].

$\sim$(36 - 33)% is produced by the direct excimer formation [141], [125]. If compared with the behavior of the ionization, it arises that the decrease of the scintillation light corresponds to the increase of the ionization in such a way that the sum of the photon and the collected-electron numbers remain constant, independently from the electric drift field and for almost all particles [123].

2.2.2.2 The scintillation time profile

The VUV scintillation light emission is determined by excimer de-excitation through a transition to the ground energy level from one of the two lowest electronic excited states: the singlet ($^1\Sigma_u^+ \rightarrow {}^1\Sigma_g^+$) or the triplet ($^3\Sigma_u^+ \rightarrow {}^1\Sigma_g^+$). This second transition is strongly suppressed and becomes possible through spin-orbital coupling mixing and, for this reason, it is much slower than from the singlet state. The time dependence of the scintillation light can be expressed by a first-order rate law, characterized by a typical decay time and a normalization constant that expresses the probability amplitude of the de-excitation from each of the two energy

levels. The origin of the de-excitation cannot be distinguished spectroscopically but by the two very different decay times. The equation describing the time dependence of the scintillation light, L(t), is the following:

$$L(t) = \Sigma_{j=f,s} A_j L_j(t) = A_f L_f(t) + A_s L_s(t), \tag{2.9a}$$

$$L_{j=f,s}(t) = \frac{1}{\tau_j} e^{-t/\tau_j}, \tag{2.9b}$$

$$\int_0^\infty L(t)dt = A_f + A_s = 1; \tag{2.9c}$$

the indexes *f* (standing for *fast*) and *s* (standing for *slow*) are respectively referred to the de-excitation from the singlet and the triplet states; τ_j represents the characteristic de-excitation time and A_j the probability that de-excitation comes from one energy level or the other. The nomenclature *fast* and *slow* comes from the duration of the two characteristic decay times. As will be illustrated in the coming description, the modelization of the scintillation time profile is not trivial; several measurements show the limitation of Eq. (2.9) in describing the experimental results. For this reason, some discrepancies have been pointed out for the values of the parameters describing the time profile of the scintillation light. In liquid argon, according to Ref. [145], $\tau_{fast} = (6 \pm 2)$ ns and $\tau_{slow} = (1590 \pm 100)$ ns. However different values are reported in literature for both decay times, τ_{fast} lies in the interval (2-7) ns [141], [125], [142], [143], [144], [146]; if the dependence with the particle energy is considered, τ_{fast} is found to increase in the interval (9-15) ns [147]. On the other hand, τ_{slow} has been measured in the range (1020 - 1634) ns [145], [141], [143], [144], [146]; in Ref. [147], a decreasing of τ_{slow} for more energetic electrons is mentioned. As will be described in Sec. 2.3, a reason justifying such a big range related to the measurement of τ_{slow} to the sensitivity of τ_{slow} to the presence of electronegative impurities. In Tab. 2.1 and Tab. 2.2, all the values of the decay times measured so far are summarized.

2.2.2.3 The intermediate component and proposed hypotheses on its origin

Considering all the mechanisms described so far, only the excimer de-excitation from the singlet or the triplet state are expected to be responsible for the scintillation light formation in argon. Nevertheless, the experimental data show that an

additional *intermediate* component between the fast and the slow ones is needed to reproduce adequately the observed time profile of the scintillation light. Despite the *intermediate* component has been reported by several experiments, a confirmed explanation for its origin has not been identified yet. Two approaches have been adopted during the years to include such contribution, one tends to include it phenomenologically and the other considers different models in order to test explicit hypotheses on its origin.

The first evidence of the *intermediate* component is mentioned in Ref. [125] and its first estimation is reported in Ref. [145]; the *intermediate* component is identified to have a decay time between (20-40) ns and its contribution to the total scintillation light intensity is of about (10-20) %. A similar result is reported in Ref. [143], where a $\tau_{\mathrm{int}} = (34 \pm 3)$ ns, contributing as a 7.4% to the total scintillation light intensity, is observed and measured. Some of the hypotheses proposed to explaining the origin of the *intermediate* component are reported in Ref. [143], [148] and [144] and they can be summarised as follows:

- delayed emission due to the N_2 contaminant traces in LAr; justified by the possible scintillation light emission of N_2^* that are formed by energy transfer between Ar^* atoms, in analogy with what has been observed in gas mixtures [150]
- PMT instrumental effects determining light emission in the last cascade dynode systems that generate after-pulses (expected in the 20-50 ns range after the primary pulse) [151]
- delayed re-emission of the scintillation light from the excitation of the wavelength shifter material (the TPB, as shown in Ref. [148] or different combinations of light guide supports coupled to the photo-sensors and wavelength materials, as shown in Ref. [144])

In the case the *intermediate* component is originated from the re-emission of the wavelength shifter material, the two-exponential model described by Eq. (2.9a) must be modified adding the probability to measure such re-emissions [144]:

$$\mathrm{L(t)} = \Sigma_{\mathrm{j=f,s}}\, \mathrm{A_j}\ \ \Sigma_{\mathrm{l}}^{\mathrm{n_w}}\, \mathrm{f_l} \frac{1}{\tau_{\mathrm{l}} - \tau_{\mathrm{j}}}\, [\tau_{\mathrm{l}} \mathrm{L(t_i, \tau_l, w, t_m)} - \tau_{\mathrm{j}} \mathrm{L(t_i, \tau_j, w, t_m)}]. \tag{2.10}$$

In this expression, the first sum is on the two possible de-excitation states (singlet or triplet) convoluted with the delayed wavelength shifter re-emission modes, $\mathrm{n_w}$,

represented by the second sum; f_l are parameters corresponding to the contributions of WLS visible light re-emission to the scintillation time profile. Hence, two delayed components are expected: the *intermediate* component, measured by most of the experiments, and a fourth additional contribution present at very long times. A direct test of the intermediate component as delayed light re-emission by TPB molecules hypothesis has been discussed in Ref. [148] by measuring the scintillation light produced in LAr with a strong concentration of N_2. As will be explained in Sec. 2.3, in these conditions, the *slow* decay time is strongly suppressed; hence, the measurement of the re-emission spectrum of the TPB is possible. In normal LAr purity conditions, instead, a similar analysis is reported in Ref. [144], using four different combinations of light-guides and wavelength shifter materials. However, only three over the four tested configurations show the *fourth* component, possibly because the *fourth* decay time is longer than the data acquisition window[4]. Both aforementioned studies report the measurement of both the *intermediate* and *fourth* components; but, the corresponding decay times are very different (τ_{int} ∼49 ns, in [148], and τ_{int} ∼132 ns, in [144]; whereas, τ_{4th} ∼309 ns, in [148], and τ_{4th} ∼6658 ns, in [144]). All the values of the *intermediate* and the *fourth* components reported in literature are summarized in Tab. 2.1, Tab. 2.2.

2.2.2.4 Relative contributions of fast and slow components

In contrast with what reported for the decay times, in Ar, a clear dependence of the de-excitation probabilities, A_{fast} and A_{slow}, with the LET has been observed; being the LET a reflection of the nature of the interacting particle, the measurement of the ratio $A_{\text{fast}}/A_{\text{slow}}$ becomes a key feature for particle identification (PID) and is commonly used in DM experiments. According to Ref. [145], the ratio $A_{\text{fast}}/A_{\text{slow}}$ has been measured to be 0.3 for electrons, corresponding to 23% of probability to de-excite from the singlet state and to 77% of probability to de-excite from the triplet state. The same ratio increases up to 1.3 and 3 for α particles and fission fragments, respectively. The increasing of the $A_{\text{fast}}/A_{\text{slow}}$ ratio means that more ionizing particles tend to populate more frequently the $^1\Sigma_u^+$ than the $^3\Sigma_u^+$ electronic energy level; an explanation for that is in the different *track structure* formed by each kind of particle, however, a full description for that has not been found yet.

[4] All the measured values are reported in Tab.3 of Ref. [144]

The measurement of the *intermediate* component leads to the necessity of including its contribution to the total scintillation light when considering the A_{fast} /A_{slow} ratio. An empirical way to do so is given in Ref. [143] where the (A_{fast} + A_{int})/A_{slow} is considered; the value reported for such ratio is 0.35 quite in agreement with the other values present in literature. Besides, as described in Ref. [148] and Ref. [144], the model used to describe the parameters of the scintillation light time profile covers an important role in the relative amplitude probability measurement. In particular, Ref. [144] shows that the absolute contribution of *fast* light to the total scintillation light coming from the de-excitation of the singlet state tends to be underestimated if a *phenomenological* model similar to Eq. (2.9a) is used instead of the model described in Eq. (2.10). On the other hand, until the origin of the *intermediate* and the possible *fourth* components are not clarified, to find the proper modelization remains a delicate aspect. The ratio A_{fast} /A_{slow} has been deeply studied for electrons and high ionizing particles because of the necessity of distinguishing between electrons and nuclear recoils in DM experiments. However, the fraction of singlet over triplet has not been so largely investigated for muons that represent the main signature of ν_μ CC interactions.

An alternative way to provide PID through the scintillation light is the empirical f_{Prompt} factor, defined as follows:

$$F_{Prompt} = \frac{\int_0^{t_F} L(t)dt}{\int_0^{\infty} L(t)dt}, \tag{2.11}$$

t_F is typically chosen to be equal to 90 ns and, in this case, f_{Prompt} is also referred to as f_{90}. Because of its similarities with the A_{fast} /A_{slow} ratio, the higher the particle energy is, the higher the f_{Prompt} factor is. The dependence of the f_{90} factor with the particle energy is reported in [147]; the measurement done in absence of drift field shows that, for electrons, the f_{90} factor decreases for higher energies, while the f_{90} increases at higher energies, when the scintillation light is produced by nuclear recoils or α particless; further investigations can be found in Ref. [149] and [136]. This difference in the behavior between electrons and nuclear recoils is very important for DM detectors; in Tab. 2.1 and Tab. 2.2, all the values measured for the probability amplitudes ratio and the f_{90} factor are reported.

Unlike for the scintillation light yield, no detailed studies are reported in the literature regarding the effect of the drift field on the scintillation time profile; only

in Ref. [141] and [125], few details are reported for a value of the electric drift field that maximizes the recombination process suppression. In these conditions, the ratio A_{fast} /A_{slow} has been measured to be (0.36± 0.06), lower than the central value reported in absence of drift field, A_{fast} /A_{slow} = 0.5. It is important to notice that in this study the *intermediate* component is observed only in absence of drift field but not measured; its effect is included as a systematic error in the A_{fast} /A_{slow} calculation. Due to the lack of knowledge on the effect of the drift field on the scintillation time profile, a pioneering study dedicated to that will be presented in Sec. 4.3 of this dissertation.

2.2.3 Propagation of the scintillation light

Once the scintillation light is produced isotropically, it propagates inside the LAr volume before being detected by the photo-sensors. Two main processes affect the light propagation making finite their attenuation length: the absorption, that causes the loss of the photons; and the Rayleigh scattering, the classical elastic scattering where the photon interacts with the electron on the most external shell of argon atoms, changes its direction, increasing the mean path length. Because of the light absorption, the reflectivity of the detector materials has an important role in determining the efficiency of the light detection. In addition to that, even a small presence of photo-sensitive impurities, such as H_2O, O_2, N_2, can cause strong light absorption. Being the separation of the two contributions very difficult, the total attenuation length, λ_{att}, relates the two mechanism through the following equation:

$$\frac{1}{\lambda_{att}} = \frac{1}{\lambda_{abs}} + \frac{1}{\lambda_{Ray}}; \tag{2.12}$$

here, λ_{abs} and λ_{Ray} take into account the attenuation caused by the light absorption and the Rayleigh scattering, respectively. Based on such definition, in very pure Ar, $1/\lambda_{abs} \to 0$, therefore, the attenuation of the light is determined exclusively by the Rayleigh scattering. In the case of big detectors, under the hypothesis of having a negligible concentration of impurities, the estimation of the Rayleigh scattering length becomes crucial, especially if the scintillation light detection is dedicated to providing the position of the interaction in the active volume.

In LAr, the total attenuation length and the Rayleigh scattering length have been both predicted by theoretical calculations and measured experimentally, either

τ_{fast} [ns]	τ_{slow} [ns]	τ_{int} [ns]	τ_{4th} [ns]	A_{fast} /A_{slow}	f_{Prompt}	A_{int}	drift field [kV/cm]	Ref.
(6.3 ± 0.2)	(1020 ± 60)	observed, not measured	− − −	(0.5 ± 0.2)[a]	− − −	− − −	0.00	[141], [125]
(5.0 ± 0.2)	(860 ± 30)	observed, not measured	− − −	(0.36 ± 0.06)	− − −	− − −	6.00	[141], [125]
4.6	1540	− − −	− − −	0.26	− − −	− − −	0.00	[142]
(6 ± 2)	(1590 ± 100)	(20; 40)	− − −	0.3	− − −	(10; 20)%	0.00	[145]
(9 ± 3)[b]	$(1463 \pm 5_{stat} \pm 50_{syst})$	observed, not measured[c]	− − −	− − −	(0.282 ± 0.009)[d]	− − −	0.00	[147]

Table 2.1.: Summary of the parameters describing the scintillation time profile produced by electrons and/or muons reported in the literature. For each study, the characteristic decay times and de-excitation probabilities from the singlet and triplet states are reported; the main peculiarities are mentioned in the notes.

[a] The big error on the A_{fast} /A_{slow} measurement is because of the treatment of the intermediate component; it has been included either in the *fast* or in the *slow* contribution and the variation introduced in the ratio obtained is included as a systematic error.

[b] The study is done as a function of the particle energy; the value reported here correspond to the lowest electron LET, the dependence with the energy is reported in the reference.

[c] A three-exponential model has been tested to include the intermediate component but it revealed to be not stable as a function of the particle energy; so, the results reported are from a two-exponential model that not include the intermediate component contribution.

[d] For less energetic electrons, the f_{Prompt} increases.

τ_{fast} **[ns]**	τ_{slow} **[ns]**	τ_{int} **[ns]**	τ_{4th} **[ns]**	A_{fast} /A_{slow}	f_{Prompt}	A_{int}	**drift field [kV/cm]**	**Ref.**
(4.9 ± 0.2)	(1260 ± 10)	(34 ± 3)	$- - -$	0.35[a]	$- - -$	7.4%[b]	0.00	[143]
(4.4 ± 2.0)	(1503 ± 41)	(132 ± 11)	(6658 ± 1160)	$- - -$	0.32 ± 0.03	$- - -$[c]	0.00	[144][d]
$(1; 10)$	(3550 ± 500)[e]	(49 ± 1)	309 ± 10	$- - -$	0.27	$- - -$	0.00	[148]
(5.5 ± 0.7)	(1200 ± 200)	$- - -$	$- - -$	$- - -$	$- - -$	$- - -$	0.00	[146]

Table 2.2.: Summary of the parameters describing the scintillation time profile produced by electrons and/or muons reported in the literature. For each study, the characteristic decay times and de-excitation probabilities from the singlet and triplet states are reported; the main peculiarities are mentioned in the notes..

[a] Since the contribution of the intermediate component is measured with a three-exponential model, it is included in the ratio as part of the *fast* component in such a way that the ratio measured here is given by $(A_{\text{fast}} + A_{\text{int}})/A_{\text{slow}}$.

[b] The relative contribution of the *fast* and the *slow* components to the total scintillation light is 18.8% and 73.8%, respectively.

[c] In this study is studied how the modelization affects the calculation of the relative contributions to the total scintillation light intensity; in particular, it is shown how the *"early* light results to be underestimated in comparison with the effective scintillation light produced from the de-excitation from the singlet state. More details are in the text.

[d] The results reported in the table are the ones obtained with the model given in Eq. (2.10); in the reference can be found also the results obtained with an approach that follows a description analogue to Eq. (2.9a) that includes four contributions.

[e] The large *slow* decay time reported in this study is due a high concentration of N_2.

directly or extrapolated by the measurement of other optical parameters as the refractive index [154]. However, from the comparison of the measurements with the calculations, some discrepancies arose. One of the main reasons for that is due to the difficulty of separating the absorption and the Rayleigh scattering length contributions. In addition to that, the lack of understanding in some argon properties, like the dependence of the density with the dielectric constant, or the role covered by the temperature, the argon state, the wavelength, etc., also complicates both the calculation and the measurements of the two parameters.

The first measurement of the total attenuation length is described in Ref. [162] where the relative light yield produced by energetic heavy ions is collected by a PMT positioned at different distances from the source. The experiment reported a value of $\lambda_{\text{att}} = (66 \pm 3)$ cm. A different approach was used in the studies reported in Ref. [164] and [165], where the total attenuation length is measured taking into account the dependence of the light transmittance with the wavelength of the scintillation light. The result obtained for the VUV photons at ∼127 nm corresponds to a low limit for the attenuation length, $\lambda_{\text{att}} > 110$ cm. The fact that this number is higher than the measurement given in [162] is justified by the method used that, in the first case, integrates the scintillation light in a given time range; this approach is considered to be equivalent to integrating over a wavelength range, hence, doing so, the dependence of the attenuation length with the scintillation light wavelength is not properly included and the attenuation length can be underestimated. However, in both studies, it is not excluded a possible quenching of the scintillation light due to the presence of optical active impurities or Xe contaminations. The impact of the optical active electronegative impurities has been reported in a more recent measurement of the total attenuation length, obtained from the scintillation light produced by cosmic muons [163]. In this study, λ_{att} has been measured around ~ 50 cm; from a dedicated Monte Carlo (MC) simulation and from mass spectrometric measurements, such a low value is attributed to the presence of a non-negligible concentration of CH_4.

2.2.3.1 Rayleigh scattering length

The simplest way to define the Rayleigh scattering length was given in 1899 [153] describing the light propagation in gas made by spherical molecules; successively,

corrections were added to treat the case of non-spherical molecules. Because of the thermodynamics fluctuations or due to the anisotropy of the molecules, such a description was not valid for liquids and solids. Following the description given in Ref. [154], [155], and Ref. [156], the Rayleigh scattering length is the mean free path at which such fluctuations appears. The expression of the inverse of the Rayleigh scattering length becomes the following:

$$\lambda_{\mathrm{Ray}}^{-1} = \frac{16\pi^3}{6\lambda^4}\Big[k_B T \rho^2 \kappa_T \Big(\frac{(n^2-1)(n^2+2)}{3}\Big)^2\Big]. \tag{2.13}$$

where λ is the emission wavelength (VUV in the case of Ar), $\mathrm{k_B}$ is the Boltzmann's constant, T is the temperature, ρ the density, κ_{T} is the isothermal compressibility, and n the refractive index. Based on this description, two theoretical calculations are present in the literature to evaluate the Rayleigh scattering length in liquid argon. In Ref. [156], $\lambda_{\mathrm{Ray}} = 90$ cm is obtained following the description given above and making the additional hypothesis of considering LAr as a rare gas. In Ref. [161], instead, the dependence with the temperature is included leading to an estimation of $\lambda_{\mathrm{Ray}} = (55 \pm 5)$ cm. Experimentally, a very recent derived measurement of the Rayleigh scattering length from the measurement of the group velocity of the scintillation light produced by cosmic muons in LAr has been obtained [166]. The Rayleigh scattering length has been found to be $\lambda_{\mathrm{Ray}} = (99.9 \pm 0.8)$ cm; under the hypothesis of treating the LAr as a rare gas, the measurement of λ_{Ray} is found to be (91.7 ± 1.4) cm, close to the calculation given in Ref. [156].

In Tab. 2.3, all the values reported in the literature so far, both for the total attenuation and Rayleigh scattering lengths, are summarized; for all the values, the way how they are obtained is specified. From the comparison of these values, the complexity related to the calculation of this important optical parameters is highlighted; because of that, in Sec. 5.1 and Sec. 5.2.3.1, a contribution to the study of the light propagation in the WA105 DP demonstrator will be presented.

2.2.4 Electron transport properties

In Sec. 2.2.1, the behavior of the ion-e^- pair recombination and its suppression by the strength of the drift field applied have been described. The presence of a homogeneous electric field allows the electrons to drift along the field lines; during the drift, the electron swarm diffuses. In the following sections, the description of

Parameter	Value [cm]	Method and Ref.
λ_{att}	66 ± 3	measured (direct) [162]
	52 ± 7	measured (direct) [163]
	> 110	measured (derived) [165], [164]
λ_{Ray}	90	calculated [156]
	55 ± 5	calculated [161]
	99.9 ± 0.8	measured (derived) [166]

Table 2.3.: Summary of the values reported in the literature of the total attenuation and Rayleigh scattering lengths, either obtained by a theoretical calculation or by direct and extrapolated measurements.

both the drift and diffusion mechanisms will be presented.

2.2.4.1 Drift velocity

In presence of a drift field, the electrons created by ionization form a swarm that moves with a constant drift velocity mostly determined by the drift field strength: $v_{drift} = \mu\ \mathcal{E}$, being μ the electron mobility[5], also dependent on the temperature, T, and $\mathcal{E}$ the drift field. In Ref. [169], the relation describing the drift velocity as a function of both the temperature and the drift field strength is given by the following equation:

$$v_d(T, \mathcal{E}) = (P_1(T - T_0) + 1)\left(P_3\ \mathcal{E}\ \ln\left(1 + \frac{P_4}{\mathcal{E}}\right) + P_5\ \mathcal{E}^{P_6}\right) + P_2(T - T_0); \quad (2.14)$$

here, T_0 is the reference temperature, 90.371 K, and P_i, $i = 1, ..., 6$, are empirical parameters obtained from the fitting of the data[6]. This parametrization, shown in Fig. 2.5 by the light and dark blue lines and tagged as Walkoviak in the legend, has been obtained based on data collected in the presence of an electric field lying in the range (0.5, 12.6) kV/cm and at temperatures in the range (87, 94) K. A linear gradient in the temperature is observed and it corresponds to a variation of (-1.72 $\pm$ 0.08) $\%/K$. Successively, measurements at the temperatures of (87 $\pm$ 1) K [171]

[5] The mobility is the ability of the electrons to move in the LAr bulk in response to an electric field strength pulling them.

[6] Their values can be found in Tab. 1 reported in Ref. [169].

and (89 ± 1) K [170] have been carried out for values of the drift field in the range (0.056, 1.012) kV/cm (corresponding to the points tagged as ICARUS-T600 in the legend of Fig. 2.5). In the common drift field range, a good agreement between Walkoviak's parametrization and ICARUS-T600 measurements is found; however, a disagreement appears for the results obtained at low drift values. In Ref. [170], the proper parametrization of the drift velocity in the whole drift field range has been identified in a P5-polynomial fit directly obtained from the collected data. Although the dependence with the temperature is not explicitly parametrized, the same polynomial fit is able to reproduce also the data collected at other temperatures [171], [172] and the observed gradient with the temperature, for a drift value of 0.5 kV/cm, is consistent with the one predicted by Eq. (2.14). Using an alternative method based on the detection of the UV light produced by a laser, the measurement of the drift velocity in the drift field range (0.2, 1.2) kV/cm, has been studied in Ref. [173] at the temperature of 88.9 K and 89.1 K; the reported results confirm the trend observed in Ref. [170]. In order to explain the discrepancy observed at low field, a different parametrization for the electron mobility has been proposed in Ref. [174], considering the dependence with the temperature proportional to $T^{-3/2}$.

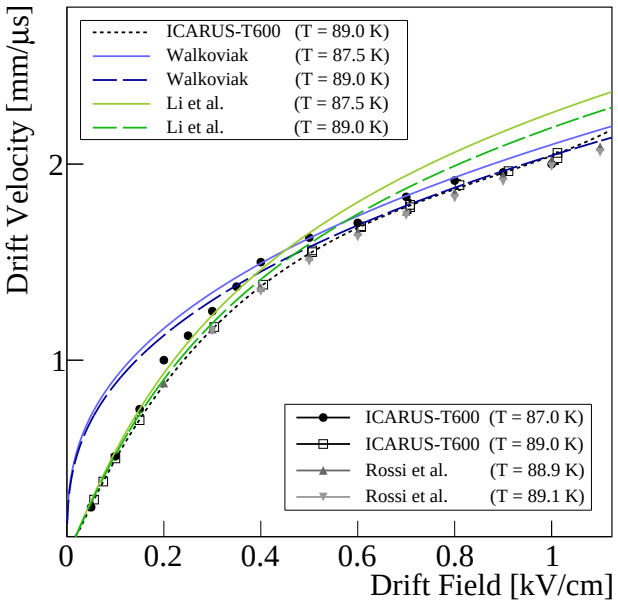

Figure 2.5.: Summary of the studies related to the drift velocity measurement in LAr. Colored lines represent the drift velocity parameterization as a function of the drift field and temperature given in Ref. [169] (Walkoviak) and Ref. [174] (Li). The points correspond to the measurements performed by ICARUS-T600 (Ref. [170] and [171]), and Rossi et al., [173].

Following the description in Ref. [174], using $T_0 = 89$ K as the reference temperature and being a_0 the extrapolated mobility in absence of drift field, the electron mobility is described by the following formula:

$$\mu = \frac{a_0 + a_1\ \mathcal{E} + a_2\ \mathcal{E}^{3/2} + a_3\ \mathcal{E}^{5/2}}{1 + (a_0/a_1)\ \mathcal{E} + a_4\ \mathcal{E}^2 + a_5\ \mathcal{E}^3} \left(\frac{T}{T_0}\right)^{(3/2)}, \tag{2.15}$$

$a_i,\ i = 1, ..., 5$, are empirical parameters obtained from fitting the data[7]. The drift velocity can be obtained from the usual relation $v_{drift} = \mu\ \mathcal{E}$. The study reports values in the drift field range $(10^{-2},\ 4)$ kV/cm; at very low fields, the mobility is constant while it linearly increases with the drift field up to ∼0.1 kV/cm. In this drift field range, the parametrization (tagged as Li in the legend of Fig. 2.5) improves a lot the measurements reported Ref. [170], [171], [172], [173]; however, a discrepancy with the measurement of the drift velocity under stronger drift field is pointed out.

The comparison of all the results reported in the literature on the measurement of the drift velocity in LAr is summarised in Fig. 2.5; the discrepancies among them confirms the difficulty in describing the electron transport properties especially at low fields. In the analyses performed in the WA105 DP demonstrator, a dedicated study of the drift velocity around 0.5 kV/cm will be presented in Sec. 6.2.

Without entering into the details, it is necessary to mention that, besides the strength of the drift field applied and the temperature, the transport of the electrons in the liquid argon is also very sensitive to the presence of impurities; more details can be found in Ref. [167].

2.2.4.2 Electron diffusion

The diffusion causes a spread of the electron swarm over long drift paths. At zero field, with the electrons in equilibrium with the liquid, the diffusion is isotropic. In this condition, the diffusion coefficient, D, can be evaluated from the Einstein equation: $eD/\mu = kT$. When the drift field is applied, an asymmetry in the transversal, D_T, and in the longitudinal, D_L, components of the diffusion coefficient appears. The knowledge of the diffusion coefficient is very important to evaluate the deterioration of the accuracy in the time and position measurements of the charge signal. In LAr, only a few measurements are available, showing that D_L is much lower than

[7] In Ref. [174], the values of the parameters are reported in the Appendix.

D_T [171], [168], [175]. The best results in terms of good control of systematic uncertainties is reported in Ref. [174], for a 0.5 kV/cm drift field, $D_L = 7.2$ cm ^{2}/s and $D_T = 12.0$ cm ^{2}/s. The longitudinal diffusion is derived from the measurement of the drift velocity: $D_{L,M} = v^3_{drift}\ \sigma^2_L/2d$; being σ_L the longitudinal diffusion width in time, and d the distance covered by the electrons. Similarly to the measurement of the drift velocity, a disagreement with other results in the drift field range (0.1, 0.35) kV/cm is observed.

2.2.4.3 Space Charge Effect and drift field lines distortion

At the same time that an electron is produced by the ionization process and drifted with a velocity of the order of the mm/μs for a drift field of 0.5 kV/cm, an ion is produced with much lower mobility. The ion drift velocity is $\sim$5 orders of magnitude slower than the electron drift velocity, for the same drift field [176], [177]. Such a difference in the mobility makes that when the latter are collected in the anode, the former remain in the LAr bulk for a longer time. The main effect expected for having the Ar positive ions moving slowly in the LAr bulk is the field line distortion attributed to the space-charge effect (SCE). At least two outcomes are expected as a consequence of the SCE: the bending of the track trajectory [177], [179], [181], induced by the field lines distortion itself, and the increasing of light at the level of the single photo-electron (SPE) uncorrelated with the position of the track that initially crossed the detector [178], [182].

Based on the study of the ion impact proposed in Ref. [178], a very recent study developed a modelization, the *Ion Transport Model*, able to describe the transport of the positive ions in LAr and their interaction with possible electronegative impurities [183]; the model provides a description of the drift field line distortion and of the increasing the SPE rate consistent with the data on which the model has been tested. As a consequence of the SCE, the electron drift velocity is modified; in contrast with the linear relation with the electron mobility through the drift field, the drift velocity formula is adjusted in order to take into account the effect of the drift field distortion as follows:

$$v_e(x) = \mu_e(\mathcal{E}_0) \cdot (\mathcal{E}_0 \mathcal{E}(x))^{1/2} \tag{2.16a}$$

$$v_+(x) = v_-(x) = \mu_\pm \cdot \mathcal{E}(x) \tag{2.16b}$$

being $\mathcal{E}_0$ the electric field in absence of SCE, $v_{e(\pm)}$ the drift velocity of the electrons (positive ions and electronegative impurities, respectively), and $\mu_{e(\pm)}$ the corresponding mobilities. The goodness of this modelization has been preliminarily demonstrated on the experimental data collected in ProtoDUNE-SP showing a good agreement with them; despite that, a tuning of the model parameters is still ongoing.

2.3 Effect of the electronegative impurities

In the commercial LAr, the presence of electronegative impurities (mostly O_2, N_2, and H_2O) is not excluded. The interaction between impurity molecules and Ar excimers can be described by a two-body collision that not only deteriorates the charge signal collection but also affects the scintillation light signal. The two processes can be described by the following reactions:

$$\begin{aligned} e^- + X &\rightarrow X^- && \text{electron attachment} \\ Ar^* + X &\rightarrow 2Ar + X && \text{light quenching} \end{aligned}$$

here X stands for a general impurity atom. When free electrons are attached by electronegative molecules, their life time becomes shorter; whereas, when the presence of impurities is seen from the light point of view, the light yield is quenched and the decay times decrease, being especially noticeable for the slow component. Independently from the excimer state the light is emitted, an additional effect is reported affecting the scintillation VUV light absoption length. The measurement both of the electron lifetime and of the τ_{slow} are alternative ways to evaluate the LAr purity and they have been used in dedicated studies to the measurements of the LAr purity in the WA105 DP demonstrator, the description of the second method will given in Sec. 4.2.1.

2.3.1 Ionization electrons attachment

Under the hypothesis of having low initial electron concentration, $[e^-]$, the attachment process decreases the electron concentration following an exponential behaviour proportional to the impurity concentration [X] through a rate constant k_e

and inversely proportional to the electron life time, τ_e, [143]:

$$\frac{d[e^-]}{dt} = -k_e[X][e^-] \Rightarrow [e^-](t) = [e^-](t=0)\ e^{t/\tau_e} \tag{2.17a}$$

$$\frac{1}{\tau_e} = k_e[X]. \tag{2.17b}$$

As described in Ref. [184], the constant rate k_e depends on the drift field applied, being function of the capture cross-section and the velocity distribution of the electrons. In particular, under strong drift fields, the electrons are no longer in thermal equilibrium with the atoms of the liquid argon but gain energy from the electric field; at the same time, the energy distribution becomes asymmetric and the electron mobility decreases.

Despite that, not all the impurities have the same effect on the drift velocity; as reported in Ref. [167], even small traces of N_2 ($\sim$ppm) increases the drift velocity of the electrons. In this case, the electrons cannot lose their energy through inelastic scattering but they can lose energy exciting impurity molecules to the vibrational states. The drift velocity is inversely proportional to square root of the cross-section of the electron attachment [168], hence the drift of the electrons is facilitated.

2.3.2 Scintillation light quenching

Strong quenching on the excimer formation dynamic and of the τ_{slow} decay time is caused by the presence of electronegative impurities in the LAr. The light quenching comes from the non-radiative response in the two-body collision Ar_2^*-X, that competes with the de-excitation process leading to the VUV scintillation light. In this case, Eq. (2.9) is no longer constrained to the unit but is smaller than one; defining Q_F, in the range $0 \leq Q_F \leq 1$, as an overall quenching factor representing the ratio between the total intensity of the emission light when there are impurities compared to the case of pure Ar, the following equation is valid:

$$Q_F = \int_0^\infty L'(t)dt = A'_{fast} + A'_{slow} \leq 1. \tag{2.18}$$

Consequently, both singlet and triplet lifetime decrease as a function of the impurities concentration in such a way that it is possible to write:

$$\frac{1}{\tau'_j}([X]) = \frac{1}{\tau_j} + k[X], \tag{2.19a}$$

$$A'_j(|X|) = \frac{A_j}{1 + \tau_j k|X|}; \tag{2.19b}$$

here $\tau_j^{'}$ and $A_j^{'}$ are the effective lifetime and amplitude quenched by the presence of the impurities.

Dedicated studies have been performed to evaluate the effect of the most common kind of contaminants that can be found in commercial Ar such as O_2 [152] and N_2 [143]. The main results are reported in Fig. 2.6; the τ_{slow} decrease becomes visible for $[O_2]$ >10 ppb and $[N_2]$ >300 ppb. It is important to notice that in both cases a saturation on the decreasing of the τ_{slow} is reached for concentrations higher than ∼10 ppm and ∼400 ppm for O_2 and N_2, respectively. According to Eq. (2.19b), also the relative probability amplitudes are affected by the presence of impurities that, in the case of N_2 [143], is reported on the top-right of the same figure. Other impurities that can be found in commercial Ar are moistures of H_2O molecules, whose effect on the scintillation light has been studied only in GAr [185] and it is not expected to be significant for concentrations lower than 10 ppb.

2.3.3 Enhancement of the scintillation light absorption

If contaminants are photo-sensitive molecules, independently from the type of precursor originated the scintillation light (singlet or triplet), the VUV photons can be absorbed in their propagation in the medium, affecting the photon mean free path length. In this case, the probability per unit path length of the photon absorption can be expressed as a function of the impurities concentration and the following equations are valid:

$$k_A(\lambda) = \sigma_A(\lambda) n(X) \tag{2.20a}$$

$$\frac{1}{\lambda_{abs}} = k_A(\lambda)[X]; \tag{2.20b}$$

in Eq. (2.20a), $k_A(\lambda)$ is the absorption coefficient (function of the wavelength, λ, expressed in units of ppm^{-1} cm^{-1}), $\sigma_A(\lambda)$ and $n(X)$ are the cross-section and the concentration of the contaminants, respectively. In Eq. (2.20b), the photon mean free path length, λ_{abs}, is shown as a function of the absorption coefficient. In the bottom-right of Fig. 2.6, the relation of the transmittance at the distance x ($T_A(x, \lambda, [X]) = e^{-x k_A[X]}$, Beer's law) as a function of O_2 impurity concentration is shown [152].

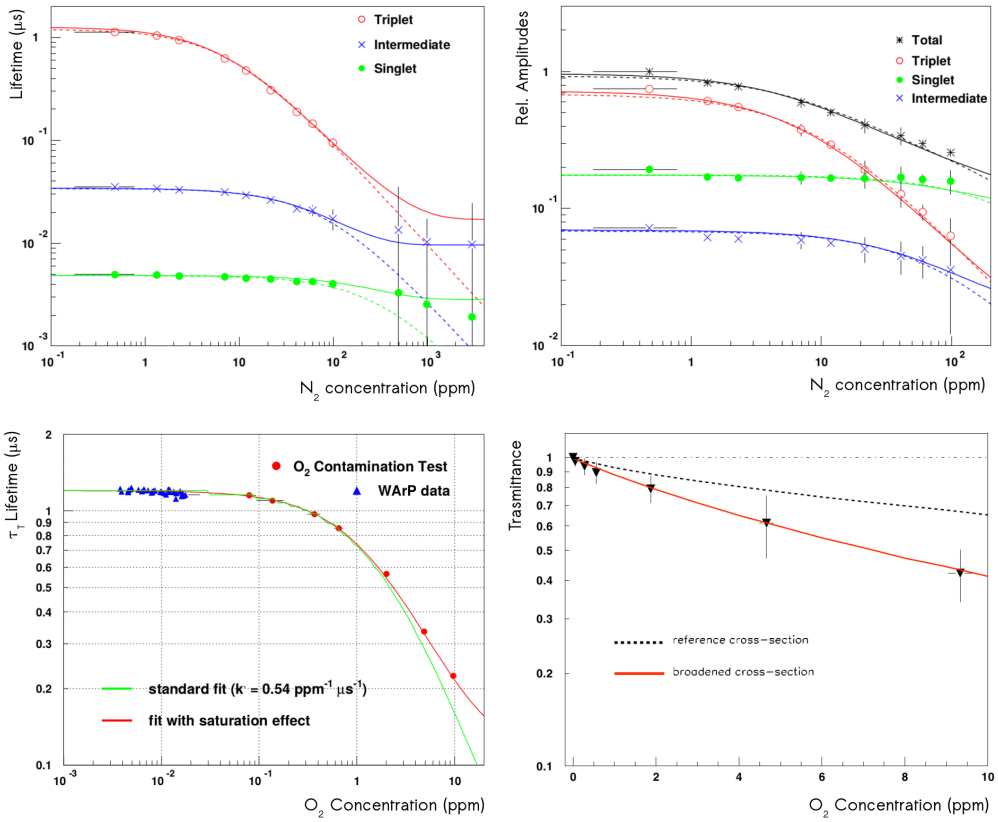

Figure 2.6.: Values of the τ_i decay times in presence of N_2 **(top-left)** and O_2 **(bottom left)** impurities studied at different concentrations. According to Eq. (2.19b), also the relative probability amplitudes are affected by the presence of impurities; the effect of N_2 is reported in the **(top-right)**. In the **(bottom-right)**, the effect of increasing O_2 concentrarions on the VUV photon transmittance is reported. The plots are taken from Ref. [152] and [143].

2.4 The physics in the vapour phase

The characteristic feature of the DP TPC is the amplification of the ionization electrons extracted in the gas-phase, that allows recovering the signal degradation caused either by the long paths or the presence of impurities. The DP concept and the advantages it can bring have been already introduced in Sec. 1.2.2; in the next sections the description of the physics that determines the electron extraction and amplification, as well as the electro-luminescence light, will be provided.

2.4.1 Electrons extraction, amplification, and collection

As soon as free electrons reach the liquid-vapor interface, they can be extracted in the gas phase. Their behavior can be described by one-dimensional potential energy distribution with height V_0, the conduction band in liquid. Given an electric field orthogonal to the liquid-gas interface, $\mathcal{E}_{l(g)}$, of the order of few kV/cm, the potentials in liquid, V_l, and in gas, V_g, as a function of the distance to the interface in the two phases are the following [187]:

$$V_l = V_0 - q_e\, \mathcal{E}_l\, x + A_l \qquad x < 0 \quad \text{(liquid)} \tag{2.21a}$$

$$V_g = -q_e\, \mathcal{E}_g\, x + A_g \qquad x > 0 \quad \text{(gas)} \tag{2.21b}$$

$$A_{l,g} = \frac{-q_e^2}{4(x + \beta x/|x|)} \; \frac{(\epsilon_l - \epsilon_g)}{\epsilon_{l,g}\; (\epsilon_l + \epsilon_g)} \; ; \tag{2.21c}$$

$A_{l,g}$ is a coefficient dependent on the dielectric constants in liquid, ϵ_l, and in gas, ϵ_g, and β is a cutting parameter depending on the distance from the interface; $V_0 = (-0.20 \pm 0.03)$ eV for Ar. Depending on the way the extraction of the electrons takes place, their extraction belongs to two different typical times scales. The electrons extracted in a very short time are the so-called "*hot*" electrons that are sufficiently energetic to be able to overcome immediately the barrier potential ("*fast*"-time $\sim 0.1\ \mu$s). On the other hand, the so-called "*thermal*" electrons are the ones that do not pass into the gas phase at the first attempt but they are back-reflected in the liquid bulk; after multiple-scattering, they are thermalized and evaporate in the gas with a "*slow*"-time of the order of 0.1 ms. It is important to not confuse the meaning of "*fast*" and "*slow*" nomenclature used in this contest that is different from the one used in Sec. 2.2.2. Both times are affected by the strength of the drift field applied; as reported in Fig. 2.7, the

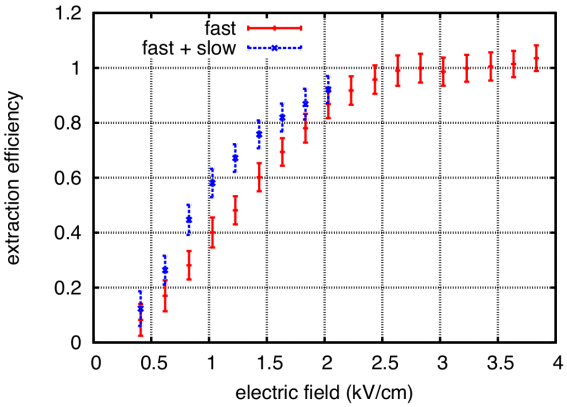

Figure 2.7.: Extraction efficiency of electrons as function of the applied electric field at T = 90 K. The plot is taken from Ref. [188].

higher the strength, the higher the emission efficiency is [188]. Finally, the *extraction electric field*, $\mathcal{E}_{\text{extr}}$, is determined by the voltages applied between the grid and the bottom LEM electrode, positioned at the distance D, and it is inversely proportional to extraction grid-liquid interface distance, d_l. Its definition is the following:

$$\mathcal{E}_{extr} = \frac{\Delta V_{grid-LEM_{bot}}}{d_l(1-\frac{\epsilon_l}{\epsilon_g}) + D\frac{\epsilon_l}{\epsilon_g}}; \tag{2.22}$$

ϵ_l and ϵ_g are the dielectric constants of the liquid and the gas phases, respectively.

When extracted in GAr, the electrons can be easily accelerated under an electric field stronger than the one used for the extraction that gives them enough energy either to excite or to ionize gas argon atoms. The de-excitation of GAr atoms produces a secondary scintillation light, named *electro-luminescence* light, whose description will be given in Sec. 2.4.2, while the ionization process initiates a Townsend avalanche through the formation of the secondary electrons cascade [107]. The operating principle of the amplification in the LEM's layers guarantees the confinement of the Townsend avalanche in the LEMs where the multiplication takes place. The characteristic factor describing the avalanche creation is the gain represented by the exponential law $G = e^{\alpha d}$; in the relation, α is the first Townsend coefficient and d, the gap thickness between the LEMs layers. The Townsend coefficient is itself a function of the field applied, $\alpha(E) = A\rho e^{-B\rho/E}$, being ρ the gas density, A and B parameters depending on the gas as well. Because of that, the gain becomes a tunable parameter dependent on the electric field strength applied at the LEM's layers. Following the description given in Ref. [99], the amplification obtained crossing the LEMs is better described by the *effective gain*, given by:

$$G_{\text{eff}} = T\ \exp(A\rho\ \text{x}\ e^{-B\rho/(\kappa E_0)}). \tag{2.23}$$

Such relation combines the Townsend avalanche formation with the LEMs and grid transparency, T, as well as with effective mitigation of the nominal electric field due to the effective path, x, covered by the electrons within the LEMs gap; κ=0.95, is evaluated experimentally [100].

When amplified in the LEMs, the electrons are successively drifted through the anode plane following the lines of the induction field. The charge signal is given by the induction current on the anode and it can be described by the Shockley-Ramo theorem [189], [190]. The charge moving in the induction field generates a current

$i = -\Sigma_k q_k \ v_k \cdot \mathcal{E}_w$; q_k is the charge with velocity v_k, while $\mathcal{E}_w$ is the weighted field that depends on the geometry of the electrodes and it does not take into account the contribution of the free charges. If the TPC is approximated by infinite parallel chamber with a uniform electric field, the induction current depends on the induction charge position, d, such that $i = qv/d$ and $Q = qz/d$ is the total charge collected in the anode wires. As described in Sec. 1.4.1, the typical design of the segmented anode is made by two views where are collected the charge Q_0 and Q_1; the effective gain for MIP can be expressed in terms of the collected charge on the two views as described by the following formula:

$$G_{eff} = \frac{\langle \Delta Q_0/\Delta s_0 \rangle + \langle \Delta Q_1/\Delta s_1 \rangle}{\langle \Delta Q/\Delta s \rangle_{MIP}} \tag{2.24}$$

being the $\Delta Q/\Delta s$ terms introduced to take into account the Bethe-Block behaviour and the charge amplification furnished by the LEMs. The effective gain needs a relaxation time, about 1.5 days, before becoming stable; in this time the initial G_{eff} decreases up to $G_{eff} \approx G^0_{eff}/3$, due to the charging up of the dielectric material inside the LEMs. The maximum effective gain for MIP has been reached in the R&D prototypes settings reported in Sec. 1.4.1, corresponding to an amplification field $\mathcal{E}_{ampl}$= 33 kV/cm, an induction field $\mathcal{E}_{ind}$= 5 kV/cm, and the extraction field at $\mathcal{E}_{extr}$= 2 kV/cm (ensuring 90% extraction efficiency [105]), in addition to the typical values of the drift field set at $\mathcal{E}_{drift}$= 0.5 kV/cm (ensuring ∼70% of recombination suppression [133]). This setting allowed to reach the effective gain $G_{eff} \sim 20$ [98].

2.4.2 The secondary scintillation light production

Similarly to what happens in the liquid phase, when the electrons reach the gas-phase they are energetic enough to promote Ar atoms to their excited states. The mechanism of the secondary scintillation light is determined by the transition from the 4p → 4s states of the excited Ar molecules. In addition to that, the electro-luminescence process is particularly energy-efficient because any excited state is expected to be a precursor to the VUV-scintillation. The de-excitation mechanism of the rare gas is well understood [191] and it showed to provide stable operation in several DP LAr-TPC based on the electro-luminescence signal for DM searches, as reported in Ref. [192], [193], [194].

For every electron reaching the gas phase, the number of photons produced is

proportional to the drift path of these electrons and the electric field strength. The relation between the electro-luminescence light yield and the electric field is described by a linear relation [197]:

$$\frac{Y}{N} = \frac{1}{N}\frac{dN_{ph}}{dx} = a\frac{\mathcal{E}}{N} - b, \tag{2.25}$$

being Y/N the electro-luminescence light yield per unit path (also referred as *electro-luminescence gain* and expressed in the number of photons·cm^2/e), $\mathcal{E}$/N the reduced field, normalized to the number of atoms per cm^2, and N = $\mathcal{N}_A\rho$/A (with the usual meaning of the symbols); a and b are empirical coefficients depending on the rare gas. In LAr, the correlation, experimentally measured [197], [199] and simulated [200], is reported in Fig. 2.8. As shown, the secondary scintillation light production is a threshold mechanism, found at $\mathcal{E}/N \approx (4 \pm 1) \cdot 10^{-17}$ Vcm^2/atom [118], [198]. From the figure, two features arise: a clear inconsistency up to a factor 2 in the electro-luminescence yield measured by the two experiments in Ref. [197] and [199], and an over-exponential behavior observed in the electro-luminescence yield Y/N for higher reduced field. In Ref. [199], the electroluminescence light yield is obtained from the S2 signal detected by the PMTs after the ionization electron extraction in GAr; on the other hand, the setup used in Ref. [197] is very small compared to DP LAr-TPC in Ref. [199]. In the same figure, also a MC simulation, optimized to describe the apparatus setup in Ref. [197], is reported; from the data-MC comparison, at E/N>10.0·10^{-17}V cm^{2}atom^{-1} a discrepancy arose suggesting that some phenomenon affecting the *electroluminescence gain* could not be

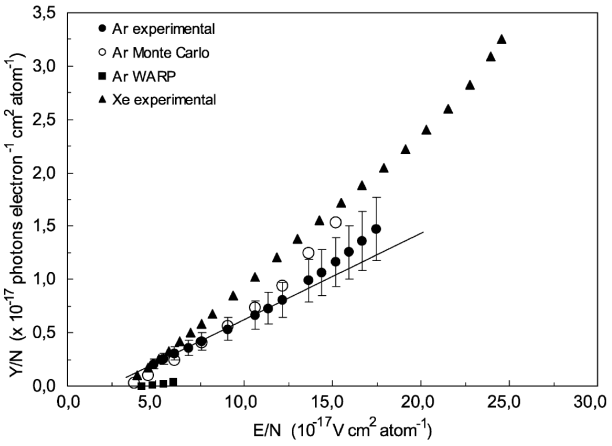

Figure 2.8.: Electroluminescence yield as a function of reduced electric field produced in Argon from measurements (full dots from Ref. [197] and Ref. [199]) and simulations (empty dots from Ref. [200]). The plot is taken from Ref. [197].

properly taken into account in the simulation. In addition to that, the photon production in the simulation of the photons in the GAr is supposed to be isotropic. On the contrary, a very recent study, Ref. [201], shows that the LEM design tends to boost the photons produced in a very narrow cone. If this is the case, more photons are expected to be emitted downwards to the liquid phase.

In the case of a DP LAr-TPC with the additional amplification of the electrons in the GAr phase, the effects of the amplification on the electroluminescence signal are almost unknowns due to the novelty of this DP configuration. In Chapter 6, innovative results will be presented as outcomes of the characterization of the electro-luminescence light in the WA105 DP demonstrator.

2.4.3 Secondary effects

As reported for the physics mechanisms taking place in the LAr phase, also in the GAr phase physics secondary effects complicate the proper description of the charge and light production. An example is given by the disagreement between the electro-luminescence light yield measured by two experiments reported in Sec. 2.4.2. Some of these effects will be briefly described in this section; more details can be found in Ref. [202], [203], and [182].

Photon and ion back flow

A collateral effect regarding the Townsend avalanche creation is caused by the photons produced in the GAr phase. Such photons are energetic enough to produce electrons from the LEMs layer's material via the photoelectric effect [202], [203]. As a consequence, secondary avalanches can be initiated by the electrons and the proportionality expected between the amplified charge and the electro-luminescence light can be altered. Analogously, as the electrons are extracted in the GAr phase, the ions can flow back to the LAr phase [182]. This effect can alter the homogeneity of the drift field in the LAr phase and worsening the SCE, strained by additional ions slowly drifting in the LAr bulk. Despite that, in other amplification devices has been demonstrated that this effect can be mitigated by the geometry of holes [205].

As initially described in Ref. [204] for other noble gases (e.g. Xe), the operational condition of the LEMs (or equivalent amplification devices) affects the avalanche

formation and consequent secondary effects. As investigated for Ar and reported in Ref. [201], the voltage applied to the LEMs changes the position where both the photon feedbacks and secondary avalanches take place; as a consequence, it can be tuned to diminish discharge probability. Besides, both the photon feedback contribution and the ion backflow in LAr are considered as a possible explanation of the higher electro-luminescence gain measurement at certain values of E/N.

2.5 Discussion on the LAr properties

Although the main features of the Ar are known, there are several properties whose knowledge or description demonstrated to be controversial and needs a deeper investigation to be completely understood.

The processes producing the primary scintillation light have been identified in the de-excitation of the Ar excimers from either the singlet or the triplet energetic levels (Sec. 2.2.2). Under this hypothesis, the scintillation time profile, which can be described in terms of an exponential law, would need only two characteristic times corresponding to *fast* and *slow* components. Nevertheless, in order to reproduce the experimental shape, an *intermediate* component, lying between the few ns time scale of the singlet de-excitation and the μs time scale of the triplet de-excitation, is observed and it can be described by a third decay time (Sec. 2.2.2.3). Despite its empirical evidence, a univocal explanation for its origin has not been found yet. The most accredited hypothesis that has been proposed so far interprets the *intermediate* time as a delayed re-emission of the scintillation light by the wavelength shifter molecules. For this interpretation to be valid, a second delayed re-emission is expected to be observed; some experiments reported such measurement reinforcing such description. However, several discrepancies still persist in the measurements reported so far. In the WA105 DP demonstrator, a detailed description of the scintillation time profile produced by crossing muons will be presented in Chapter 4 confirming the presence of the *intermediate* component, providing its measurement, but not a conclusive observation on the *fourth* delayed contribution to the total scintillation time profile.

The excimer formation takes place either due to the direct formation as a consequence of the energy loss by the interacting particles or via the ion-e^- recombination. The latter process is directly suppressed by the presence of an electric field helping

the electrons drifting toward the TPC anode. If the effect of the drift field on the scintillation light yield is quite well understood (Sec. 2.2.1), that is not the case of its impact on the scintillation time profile, in terms of the probability amplitudes and the characteristic times.

There is a strong consensus on the particle energy loss and the track structure; hence, the probability of de-excitation from the singlet or triplet state represents a key observable for particle identification (Sec. 2.2.2.4). Despite that, it is not trivial to understand how and why the de-excitation probabilities and the characteristics decay times are influenced also by the intensity of the drift field. Some hints have been reported indicating that there is a preference for one excitation level over the other when the scintillation light is produced via the direct formation of the excimers or via a recombination process, which is suppressed in the presence of an electric field. The plausibility of this possibility in LAr has been only vaguely reported in a quite old study (Sec. 2.2.2.4); on the contrary, in LXe, whose dynamic is much faster than in LAr, the effect of the drift field on the recombination dynamic, manifested as a modification of the scintillation time profile, has been observed and explained as a suppression of the de-excitation from vibrational states typical of the excimer formation through the recombination process (Ref. [214]). Because of the incertitude of such understanding, pioneering studies related to this topic will be presented in this dissertation (see Chapter 4).

As introduced in Sec. 1.5 and explained in Sec. 2.2.3, the knowledge of the Rayleigh scattering length represents a critical aspect related to the operation of big LAr-TPCs since it can strongly limit the scintillation light detection. A recent study reports a derived experimental measurement of the Rayleigh scattering length (λ_{Ray} $\sim$100 cm Ref. [166]); however, the discrepancies arising from the comparison with other studies, where the light propagation is attenuated by the photon absorption either with the setup or the impurities, reinforces the difficult in the determination of this important optical parameter. In this dissertation (see Chapter 4 and Chapter 5), dedicated studies both from data analysis and MC simulation will be presented; due to the setup and dimensions, the impact of the light absorption in the TPC elements will be described.

Similarly, the description, in different drift field strength ranges, of the drift of the electrons in the LAr phase, as well as how their motion can be impacted by the presence of the slower ions, do not have a univocal interpretation (Sec. 2.2.4). In

particular, the description of the drift velocity as a function of the drift field strength and LAr temperature, empirically obtained from data collected up to ∼10 kV/cm, shows an evident discrepancy in low fields regime ($\mathcal{E}$ <0.5 kV/cm) where lies the typical operation of the LAr-TPC. In this dissertation, an additional measurement of the drift velocity of the electrons is reported aiming to bring more experimental data in order to improve the understanding of the electron mobility in LAr (see Chapter 6).

If on one side an overview of the mechanisms producing the primary scintillation light taking place in liquid Ar is available; the whole picture of the phenomena contributing to the electro-luminescence light, in the gas state, when the amplification of the electrons happens in the LEMs layer has not depicted yet. Few studies are available describing the electro-luminescence light produced only by the extraction of the electrons in the GAr pocket; despite that, some inconsistencies have been pointed out in the comparison of the results, mostly due to the differences in their operating conditions or geometries (Sec. 2.4.2). On the contrary, the contribution of the electron amplification in the LEMs (or similar devices) to the S2 signal has been only poorly explored. Given the lack of information present so far, the results obtained from the analysis of the electro-luminescence light produced in the WA105 DP demonstrator (see Chapter 6) represent an important starting point for advancements in this description.

"Il diavolo si nasconde nei dettagli."

Proverbio

CHAPTER 3

THE WA105 DEMONSTRATOR FOR A LARGE SCALE DUAL-PHASE LAR-TPC

In this chapter, the description of the WA105 DP detector components, and the technological milestones reached in the first operation at the ton scale of this kind of a DP LAr-TPC, will be given in Sec. 3.1. In particular, a detailed description of the photon detection system installed in the demonstrator will be presented in Sec. 3.2. In order to trigger on crossing muons, two alternative systems were installed: an external Cosmic Ray Taggers (CRT) system (Sec. 3.3) and a PMT self-trigger (Sec. 3.4), allowing the collection of more than 5×10^6 events (Sec. 3.5) in different detector conditions. The role of the CRT trigger demonstrated to be crucial to have always access to the cosmic muon track topology (Sec. 3.3), independently from the track reconstruction in the CRP.

The analysis framework developed to access the data and define the main variables to reconstruct the events and the light signal (Sec. 3.6); the characterization of the photon detection system response (Sec. 3.7), and the description of the main features of the scintillation light produced by the cosmic muons (Sec. 3.8) will be discussed. Finally, the basic performance of the photon detection system will be presented in Sec. 3.9.

3.1 Detector description

The experimental setup of the WA105 DP demonstrator is based on the DP LAr-TPC concept described in Sec. 1.2.2. The demonstrator TPC covers a 3×1×1 m^3 fiducial volume corresponding to ∼4.2 LAr tons. In order to be operated, it is immersed in a passively insulated cryostat with 23 m^3 internal volume, which guarantees the operation of LAr in thermodynamically stable conditions, a uniform gas density, and a flat liquid argon surface. As shown in Fig. 3.1, the WA105-DP detector consist of four main components:

- cryostat
- charge readout plane
- field cage
- photon detection system

The more external element is the cryostat made by an insulation layer and a corrugated membrane in the region in contact with the LAr, which must be kept at the uniform temperature of 87 K (LAr boiling point).

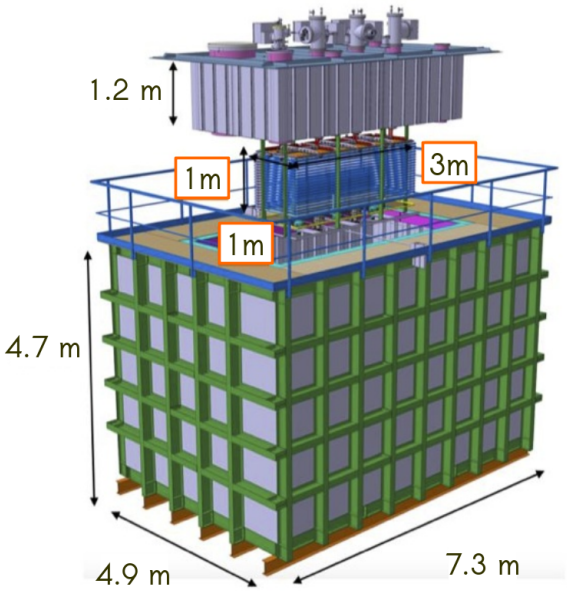

Figure 3.1.: Main components of the WA105 DP demonstrator and corresponding dimensions. Starting from the top, the *top-cap*, the field cage and the outer cryostat are visible.

The main vessel of the cryostat membrane structure is hermetically closed by a 1.2 m thick insulating roof, named *top-cap*; coupled to it, the TPC field cage (FC) is suspended from eight G10 pillars. The FC is made by nineteen field shaping rings and the cathode connected by resistors to propagate the HV to its whole volume. The first field shaper (FFS) at the top of the FC is 20 mm distant from the extraction grid. The extraction, the amplification, and the collection of the drifted electrons

produced in the ionization process take place in an independent structure named charge readout plane (CRP). The CRP includes the extraction grid, the LEMs, and the anode; the maximum distance between the extraction grid and the anode plane covers only 13 mm. The CRP alignment with the GAr-LAr interface and the field cage positioning under the liquid level are delicate requirements; the first to avoid the damage of the LEMs and the second because it affects the distance between the extraction grid and the LAr level. For this reason, the CRP is electrically and mechanically autonomous from the field cage structure and its adjustment over the LAr-GAr interface is done remotely. The photon detection system units, five photomultiplier tubes, are suspended at the bottom of the TPC, hung in a support frame positioned at the bottom-most part of the pillars. Between the PMTs and the cathode, the ground grid protection is positioned to shield the PMTs from the cathode HV.

In Fig. 3.2, pictures of the main components and their positioning inside the detector are shown; whereas, in Tab. 3.1, the dimensions of the main elements are specified.

In addition to the main detector components, several ancillary elements are needed to guarantee its correct operation. Auxiliary level meters, reaching a 1 mm precision, are installed close to the CRP support structure and in the FC pillars. Additionally, the LAr temperature is controlled by several temperature probes (platinum resistor thermometers) placed inside the cryostat main volume to control that is kept stable at 87 K. The thermometers, either fixed to the TPC or glued on the membrane surface, cover a temperature range from (50, 350) K, with a precision better than 0.5 K. The cryostat operating pressure of the LAr volume is set a 1000 mbar (slightly higher than the atmospheric pressure at CERN), while the insulation space is kept at 600 mbar; the monitoring of such pressures, as well as the atmospheric pressure, are constantly controlled by a set of 9 transducers to ensure that the detector is safely operated. Finally, four identical digital video cameras capable of operating in cryogenic conditions are placed inside the cryostat; five LED strips, provide the illumination needed to be operated. Three of the cameras are positioned 30 cm above the CRP frame, in the GAs phase, to monitor the LAr-GAr interface stability; the fourth one is situated under the ground grid protection facing the CRP frame. Because of their orientations, they can detect potential electric discharges. The cameras and the LED lights generate noise that can deteriorate the charge readout

component	value	unit
cryostat outer dimensions (l×w×h)	7.34×4.76×4.88	m^3
cryostat inner dimensions (l×w×h)	4.76×2.03×2.38	m^3
top-cap (l×w×h)	5.30×2.08×1.20	m^3
LAr volume	18.01	m^3
GAr volume	4.08	m^3
LAr height	1590	mm
GAr height	440	mm
TPC structure (l×w×h)	3×1×1	m^3
charge readout surface	3×1	m^2
LEM-anode surface units (×12)	0.5×0.5	m^2
extraction grid surface	3×1	m^2
LAr mass in the TPC	4.2	tons
field cage (l×w×h)	3155×1155.75×950	mm^3
field shaper diameter	34	mm
cathode-anode distance[1]	1000	mm
1^{th}field shaper-anode distance[2]	16	mm
field cage height[3]	984	mm
PMT cathode-surface distance[4]	206	mm
number of charge readout channels	1280	—
number of light readout channels	5	—

Table 3.1.: Dimensions of the main elements installed in the WA105 DP demonstrator.

[1, 2, 4] The distance is calculated from the border of the cathode.

[3] The distance is calculated from border-to-border of the field shapers.

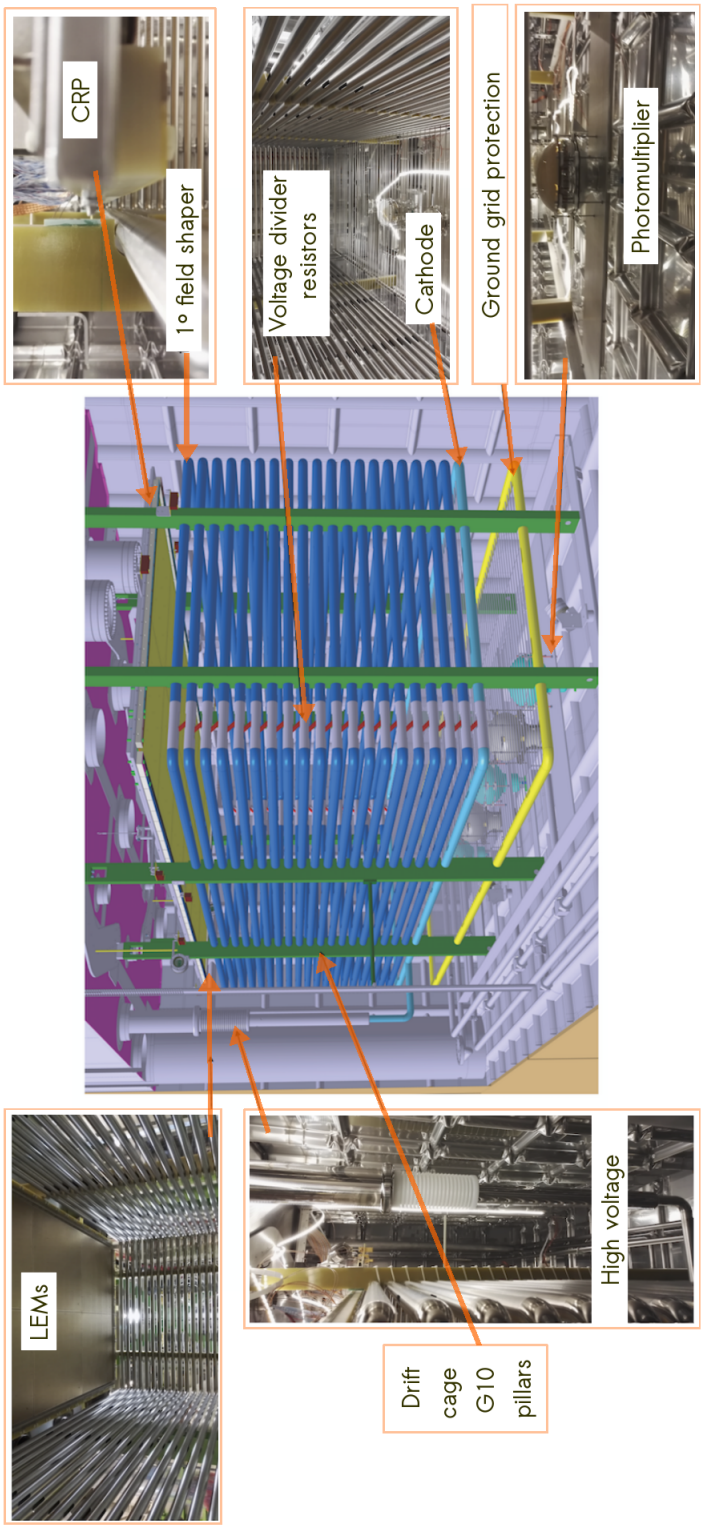

Figure 3.2.: Central scheme: Schematic drawing of field cage rings, the cathode, and the PMTs. **Pictures:** View of the demonstrator's elements from the inside. The images are taken from [78].

electronic performance as well as the PMT operation; for this reason, they are switched off during the data taking.

In this section, the main features of such elements will be describe; all the additional information that may be missing can be found in Ref. [78].

3.1.1 Cryostat, cryogenic and LAr purification systems

The cryostat is the result of strong synergy studies between the WA105 DP demonstrator requirements and industry[1]. Due to the relatively small dimensions of the whole volume, it is split into two separate parts: the main vessel, and the *top-cap*. Both components includes by passive insulation and a corrugated *membrane*. The thermal insulation is made by a sandwich of glass-reinforced polyurethane foam (GRPF) between two layers of plywood; three layers of such sandwiches are superimposed providing uniform insulation of about 1 m thick. The innovative design of the *membrane* is intended to match the cryostat geometry; the shrinkage is calculated to absorb the thermal stress during the cool-down phase. Twenty *chymneys* with different diameters cross the *top-cap* to allow the hosting of the feedthroughs that interface with the cryogenic system. A carbon-steel exoskeleton covered by 6 mm stainless steel plates is installed out of the cryostat to provide mechanical support and to sustain the over-pressure forces from the inner vessel.

A cryogenic and LAr purification systems are installed in the cryostat with the main goals of throwing out the air during the LAr filling phase, ensuring a level of electronegative impurities at the ppt level during detector operation, and guaranteeing the best operation environment inside the cryostat in terms of stable pressure and temperature. After the detector closure and prior to the LAr filling, the gas argon is injected to eject the air from the cryostat and cool it down. This operation is done by the so-called "piston purge" method that, through several loops, it additionally ensures the purification of the argon environment. As shown in Fig. 3.3, in the WA105 DP demonstrator, an *open* and a *closed* loops preceded the *cooling-down* phase; the amount of oxygen, nitrogen, and moisture impurities present in the gas sample are measured by three residual gas tracer analyzers (RGTA); the pink bands correspond to the injection of pure gas argon in order to decrease the nitrogen con-

[1] The design used in the WA105 DP demonstrator has been licensed by the French GTT engineering company

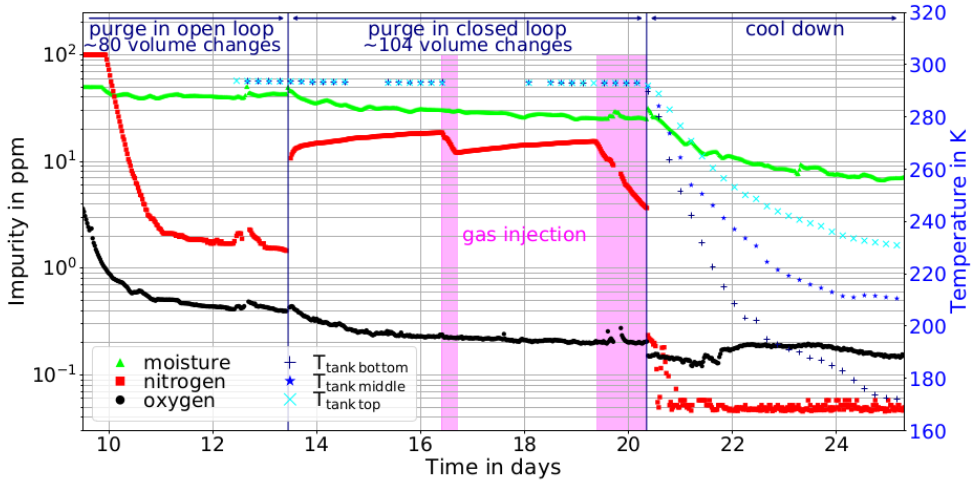

Figure 3.3.: Evolution of the impurities measured in the WA105-DP demonstrator in the different purge and cooling down phases. The temperature measured in the main cryostat volume is reported in blue on the right vertical axis. The plot is taken from [78].

centration below 10 ppm level. The concentrations of the impurities measured at the end of the *open* and *closed* loops are reported in Tab. 3.2.

Element	end of the open loop	end of the closed loop	precision
Oxygen	0.4 ppm	0.2 ppm	± 100 ppb
Nitrogen	1.7 ppm	3.5 ppm	± 20 ppb
Moisture	43 ppm	25 ppm	± 20 ppb

Table 3.2.: Measurement of the impurities' concentration obtained from the RGTA in WA105-DP demonstrator at the end of the open and closed loops [78].

Finally, in the *cooling down* phase, the argon gas at room temperature and liquid argon at 87 K are injected from the corners of the detector through gas atomizing nuzzles. After the cooling down, the detector is filled with LAr from the bottom until the whole FC is immersed completely.

The Ar purity is a key requirement for the TPC operation; although there was no external monitoring of the LAr purity during the detector running, the LAr was continuously recirculated and purified in a dedicated *pump tower* that communicates with the liquid and gas argon volumes. The cryogenic system and nitrogen cooling down allowed to keep flat the liquid surface, to mantain uniform the liquid

and gas temperatures at $T_{liquid} = 87$ K and $T_{gas} = 101$ K, and to monitor the pressure stable at $P_{cryostat} = (999.5 \pm 1.4)$ mbar. Two alternative analyses studied *a-posteriori* the LAr purity and its stability in time; both of them demonstrated the good performance of the cryogenic and purification systems, representing one of the achievements in the WA105 DP demonstrator operation and fulfilling the minimum requirements of a dual-phase TPC operation at the ton scale.

3.1.2 Field Cage

The field cage is constituted by twenty field shaping rings equally spaced on the vertical axis with a 50 mm pitch. Each ring is made by 2 mm thick stainless steel tube with 34 mm external diameter and 2 cm oval-shape openings that ensure the gas flow during the purge process. The bottom-most field-shaping serves as the cathode of the field cage; its shape is slightly different from the other rings with 4 mm stainless steel diameter that surrounds a grid with a 20 mm pitch. The cathode is electrically connected to the high voltage feedthrough and the top-most field-shaping ring (named also first field shaper - FFS) is grounded outside the cryostat via a resistor. All the field shaper rings are interconnected via HV resistors with a resistance that forms a voltage divider chain ensuring a uniform electric field inside the whole TPC volume and allowing the drift of the electrons toward the extraction grid. The field uniformity is a critical requirement for the TPC operation, the fulfillment of this requirement is completed by the oval-shape of the ring design. The HV set at the cathode is generated by a commercial power supply, it is delivered by the custom-made feedthrough and it is distributed at each field shaper ring through the resistors. The nominal drift field required is 0.5 kV/cm (corresponding to -56.5 kV applied at the cathode).

3.1.3 Charge Readout Planes

The innovative concept of a charge readout plane independent from the rest of the detector structure has been introduced and tested for the first time in the WA105-DP demonstrator. The CRP decoupling from the detector allows a pre-assembling of all the components in a clean room and previous tests of its performance in a dedicated setup before the installation in the TPC. In Fig. 3.4 (a), a schematic

description of all the CRP elements is given. The CRP is made of modular units grouped to cover the 3 m^2 surface. In Fig. 3.4 (b) and (c), pictures of the elements seen from the bottom are shown; in particular, in (c) a closer view of the LEM-anode sandwich is visible. The bottom-most element is the extraction grid, a single

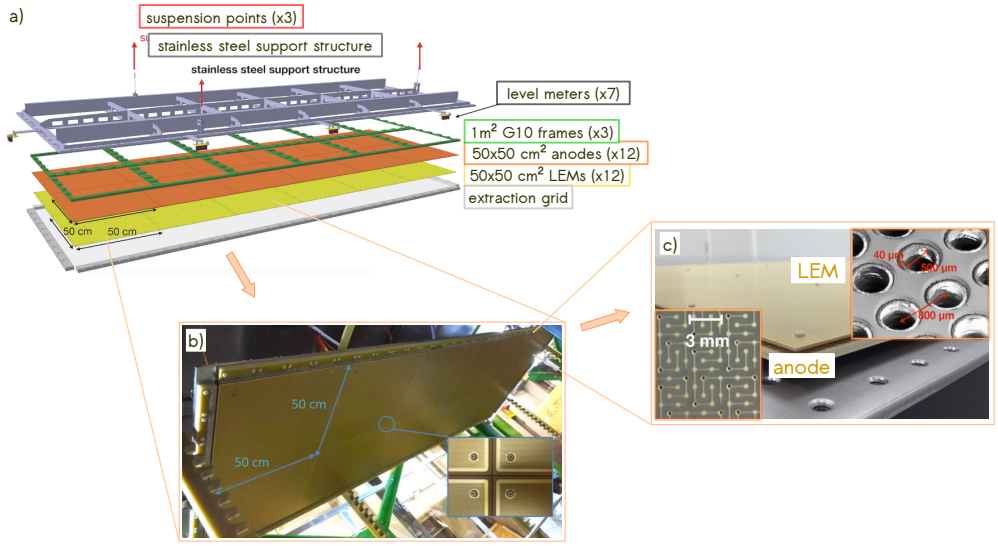

Figure 3.4.: Schematic view of CRP and main constituent components **(a)**, bottom view of the twelve 50×50 cm^2 LEM units **(b)**, and zoom of the anode and LEM structures **(c)**. The images are taken from [78].

3×1 m^2 element with a 3.125 mm pitch made by 100 μm diameter wires in stainless steel; the precision of the pitch is required to be 50 μm and it is verified with microscopical measurements after the soldering of each wire. Twelve 50×50 cm^2 LEM-anode units are placed above the extraction grid. They are almost in contact and surrounded by 2 mm inactive border. The three layers are suspended from twelve G10 stainless steel frames that ensure the mechanical guide and rigidity both in warm and cold temperatures. Both LEM and anode units are fabricated by the industry[2] in large quantities and accessible costs. Before the installation, both components are controlled with quality tests. While the anode is quite simple to be produced, the LEMs are more complicated and their uniformity is a delicate and crucial requirement, so that they need to be examined also with time-consuming procedures.

[2]The WA105 DP demonstrator LEM and anode units have been manufactured by ELTOS in Italy.

The LEMs are obtained from 1 mm thick cladded epoxy plates covering 50×50 cm^2 area. The holes are drilled in a honeycomb pattern with 800 μm pitch, each hole has 500 μm diameter, corresponding to about 180 holes per cm^2. The inside of each hole is made by 40 μm dielectric rim, while the LEM electrode is made in copper and has a thickness of 60 μm. Finally, each LEM unit has a 2 mm border protection to avoid high voltage discharge that is surrounded in turn by a 2 mm copper guard ring. To ensure the optimal CRP performance, the LEMs thickness and uniformity are required to be of the order of 30 μm.

The anode unit is made of four PCB layers having orthogonal strips with the 3.125 mm pitch, the two strips correspond to the x-y coordinates (respectively called *view 0* and *view 1*). The pitch defines the spatial resolution of the track reconstruction; the strip pattern, visible in the bottom-left corner of Fig. 3.4, is printed on the bottom-most layer and it has been optimized to equally split the charge between the two views into two unipolar signals, facilitating the track projection reconstruction. The *view 0* is made of 320 strips with 3 m length, while the *view 1* of 960 strips with 1 m long. The readout strips are read in groups of 32 for a total of 1280 channels. The anode pitch and the extraction grid pitch have the same size in such a way to ensure the uniform extraction field and avoid charge shadowing caused by the grid wires.

The CRP assembling is done on an optical table in a clean room that allows verifying the inter-distance between each component and their endurance in cryogenic conditions. Finally, the CRP is hung from the *top-cap* by three cables connected with dedicated feedthroughs for the high voltage applying and the remote control of the panel for positioning and adjustment. The CRP alignment with the LAr-GAr interface, the positioning in the detector, as well as the μm precision of the CRP component planarity are summarised in Tab. 3.3; these are the critical parameters affecting the high voltage setting to reach the nominal gain of the electron multiplication in gas.

3.1.4 Demonstrator operation

The WA105 DP demonstrator covered a key role in the scaling of the DP technology at the ton scale because, for the first time, the drifted electrons have been extracted, amplified and collected over a 3 m^2 surface through the multiple assem-

component	distance [mm]
3 m anode strip to ground	—
1 m anode strip to ground	—
50×50 cm^2 LEM-top to anode plane	2
50×50 cm^2 LEM-top to LEM-bottom	1
50×50 cm^2 LEM-top to neighbour LEM-top	4.5
50×50 cm^2 LEM-top to extraction grid	10
3×1 m^2 cathode to ground	200

Table 3.3.: Dimensions and distances of the CRP components and its positioning inside the demonstrator; the inter-stage distances and CRP alignment with LAr surface are reported.

bling of smaller units.

As explained in Sec. 2.4, one of the characteristic parameters for a DP TPC is the effective gain, G_{eff}, that describes the electron multiplication in the LEMs after their extraction in the GAr phase. The G_{eff} is affected by the amplification in the LEM and by the overall transparency of the extraction grid, LEM, and anode to the drifted electrons. In addition to that, the adjustment of the CRP over the liquid surface plays a key role, because is strictly related to the extraction field that can be applied through the distance, d_l, between the LAr-GAr interface and the grid, as given by Eq. (2.22). In the operation of the previous prototypes, a G_{eff} ≈20 has been attained; in order to reach this value, for a nominal drift field of 0.5 kV/cm, a combination of $\mathcal{E}_{extr}$= 2 kV/cm, $\mathcal{E}_{ampl}$= 33 kV/cm and $\mathcal{E}_{ind}$= 5 kV/cm is required; the corresponding high voltage values applied to the extraction grid and the LEMs (ordered from bottom to top on the left of Fig. 3.5) must be -6.8 kV, -4.3 kV and -1 kV, respectively. In Fig. 3.5, the nominal values of the extraction, amplification, and collection fields expected to be applied in the WA105 DP demonstrator, with the corresponding voltages applied, are given on the left; moreover, the typical distance between the CRP constituents as well as their pictures are shown on the right. However, technical issues related to the extraction grid performance limited the demonstrator operation. Three main reasons have been identified from further investigations and visual inspections after the dismantling phase: a short circuit in a defective high voltage contact on the extraction grid or due to weak soldering of

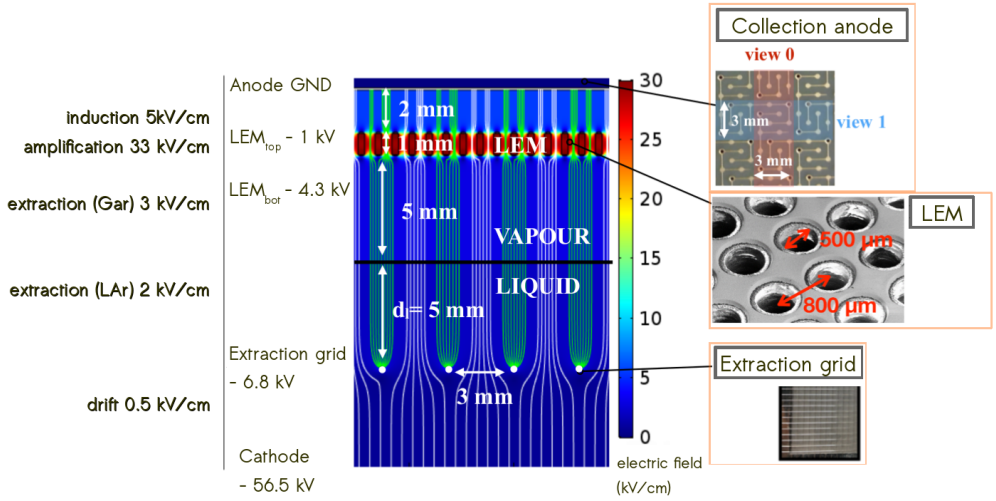

Figure 3.5.: Schematic drawing of the charge extraction and amplification in the GAr phase. The nominal values expected to be reached in the WA105 DP demonstrator for each field applied are reported on the left of the figure. On the right, pictures of the charge readout components are shown. The figure has been readapted from Ref. [78].

a group of wires, a small curvature in the CRP, and isolated discharges have been detected dropping the performance of the corner LEMs[3]. Because of the first issue, the lowest voltage that could be applied to the extraction grid, without generating any electrical discharge, was -5 kV; nevertheless, the demonstrator performance has been maximized with the complete immersion of the extraction grid in the liquid, $d_l = (9.460 \pm 0.004)$ mm, re-adjusting all the other field settings, and introducing a non-uniformity of the gain applied to the LEM units over the whole CRP area.

Despite the technical limitations to which the detector has been subjected, the operation of the demonstrator allowed to collect cosmic data with a good S/N ratio for the charge reconstruction in the anode plane and reaching the maximum $G_{eff} \sim 3.5$. In Ref. [78], a detailed description of the WA105 DP demonstrator operation and performance is given. In the table 3.4, a comparison between the nominal and the working settings are shown; the value given on the amplification field refers to the typical LEM setting with the corner LEMs operated at a lower electric field than the others. In the top of Fig. 3.6, an example of the charge imaging reconstruction of a cosmic muon event collected in the conditions just described is shown. The

[3]It is important to notice that, thanks to the LEM's unit design, none of these discharges have been propagated to the nearby LEMs.

electric field	applied voltage [kV/cm]	nominal value [kV/cm]	scanned range [kV]
Induction	GND	5	1 - 5
Amplification	-1	33	23 - 31
Extraction (in gas)	-4.3	3	0.6 - 2.5
Extraction (in liquid)	-6.8	2	.....
Drift	-56.5	0.5	0.18 - 0.7

Table 3.4.: Nominal and scanned values corresponding to the field applied the TPC components; starting from the top, the values are referred to the cathode, extraction grid, LEM_{bot}, LEM_{top} and anode [78].

event contains two tracks, in the dotted rectangular the "through-going" muon can be recognized; the reconstruction of the event on the *view 0* and the *view 1* are respectively given on the left and the right of the figure. In this reconstruction no noise filtering is used; despite that, comparing the waveforms collected by each channel in both views, Fig. 3.6-bottom, two important features arise: the amplitude of each waveform is clearly above the noise baseline, and the amplitude of the channels in both views are comparable confirming the 50:50 sharing of the signal on both views. The integral of the waveform corresponds to the energy locally deposited by the ionising particle, ΔQ_0 and ΔQ_1 respectively on *view 0* and *view 1*. The z coordinate of the event is retrieved matching the endpoint of the track on both views [106]; the 3-D track reconstruction is necessary to know the track length, Δs_0 and Δs_1 respectively on *view 0* and *view 1*. From the total collected charge and the track length, it is possible to measure the energy deposited per unit path.

In the demonstrator, the events have been triggered by two alternative systems: a set of Cosmic Ray Tagger panels (the so-called *CRT trigger*), and a self-PMT trigger (referred to as *PMT trigger*) based on the detection of the prompt scintillation light signal. Both systems will be widely described in Sec. 3.3 and Sec. 3.4; before, the description of the photon detections system is reported in the next section.

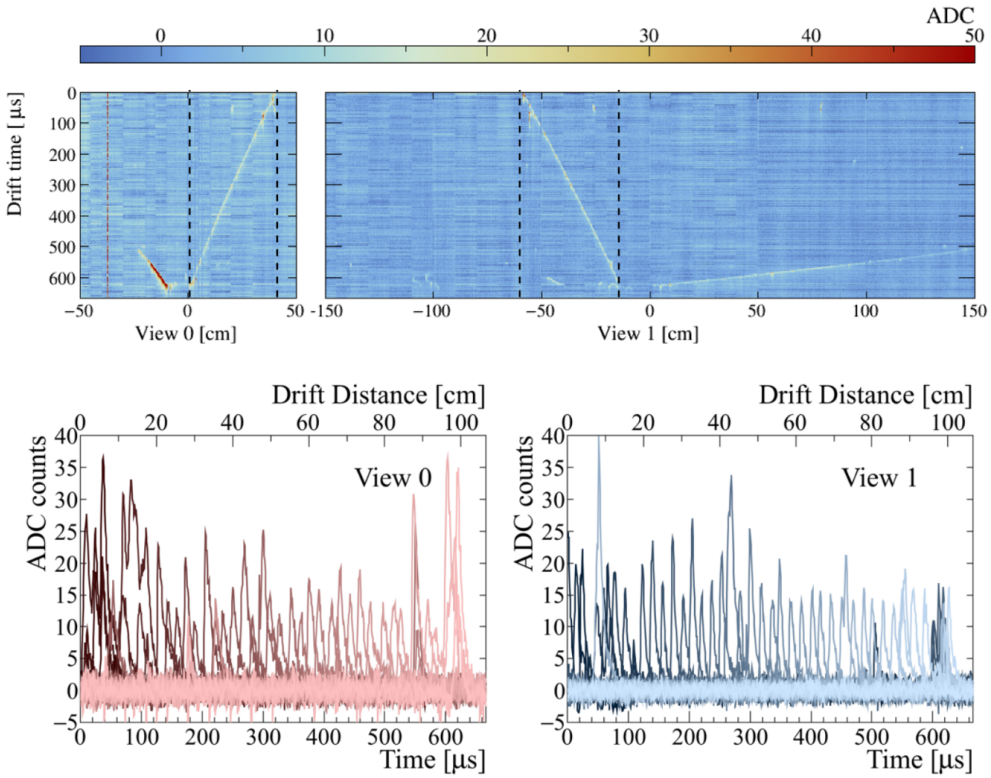

Figure 3.6.: **Top:** Reconstructed cosmic muon crossing the entire drift volume of the WA105 DP demonstrator; the corresponding drift distance is computed assuming 1.60 mm/μs as the electron drift velocity. An off-time track crossing close to the anode is also visible. **Bottom:** Waveforms of the reconstructed cosmic muon recorded by each channel; the waveforms correspond to the region defined by the dashed lines in the top-plot. The plots are taken from Ref. [78].

3.2 Photon detection system

The photon detection system installed in the WA105 DP demonstrator includes an array of five cryogenic R5912-02Mod Hamamatsu photomultiplier tubes, positioned underneath the cathode and the ground-grid protecting them from possible discharges in the FC. Each PMT unit has an 8-inch diameter borosilicate window and a 14-dynode chain to compensate for the gain-loss expected at cryogenic temperature (CT); at room temperature (RT), the gain can reach 10^9. Since the scintillation light is produced in the VUV region and because the borosilicate window absorbs the VUV photons, a wavelength shifter (WLS) material is needed to detect such

light. Based on the information provided by the manufacturer, the photo-cathode quantum efficiency (QE)[4], function of the photon wavelength, is maximum around 400 nm. For this reason, in the WA105 DP demonstrator a thin layer of 1,1,4,4-Tetraphenyl-1,3-butadiene (TPB) is used to convert the VUV photon wavelength into 420 nm.

One of the goals of the photon detection system is to test different PMT configurations in order to identify the optimum design to be installed in future detectors (e.g. ProtoDUNE-DP and the DUNE FD module); for this reason, two different PMT-base polarity configurations (respectively named positive and negative bases) and WLS coatings have been installed. In particular, the TPB has been applied using two different methods: a direct coating over the PMT photo-cathode, in three PMTs, or coated a poly-methyl methacrylate (PMMA) plate installed above the PMT surface, in the other two PMTs. The description of both the base and WLS designs will be presented in the following sections; in Tab. 3.5, a summary of the configurations is reported.

PMT n.	base-polarity	WLS
1	negative (NB)	TPB direct
2	negative (NB)	TPB on PMMA plate
3	positive (PB)	TPB direct
4	positive (PB)	TPB on PMMA plate
5	negative (NB)	TPB direct

Table 3.5.: Summary of the PMT-base polarity and WLS configurations installed in each PMT.

3.2.1 Wavelength shifter options

In both coating methods, a thin layer with $\sim$0.2 mg/cm^2 density is homogeneously evaporated either on the PMT photo-cathode surface or on the PMMA plate. The TPB deposition is performed under vacuum in the CERN thin film laboratory, following the same procedure used for the installation of similar PMTs in previous experiments [206]. In the top of Fig. 3.7, the two TPB options are visible.

[4]The quantum efficiency is defined as the percentage of incident photons converted into photo-electrons on the PMT photo-cathode surface via the photo-electric process.

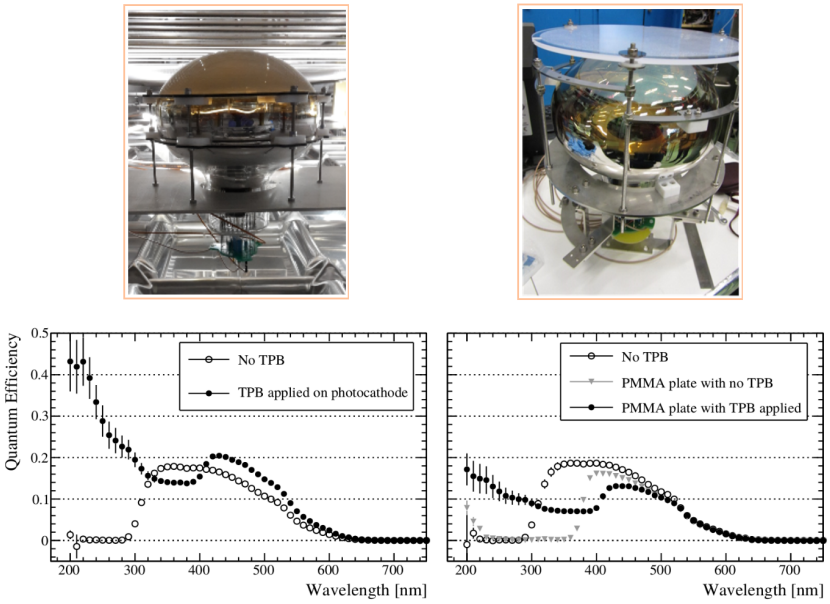

Figure 3.7.: Top: Pictures of the two WLS options: the direct TPB coating on the PMT photocathode surface is reported on the **left**, and the TPB coating on the PMMA plate is shown on the **right**. **Bottom:** Corresponding measurements of the relative quantum efficiency performed at room temperature, for the two WLS configurations, as a function of the incident wavelength light.

Before the installation, a comparison between the PMT quantum efficiency (QE) in the two WLS configurations has been performed at RT. A relative measurement of the QE has been performed using a dedicated setup at CERN before and after the TPB coating; in the case of the TPB coating on the PMMA-plate, also the intermediate measurement of the QE through the uncoated plate is reported. Using a light source of wavelengths between 200 and 800 nm, a photo-diode and each PMT were illuminated simultaneously. The QE is extrapolated as a relative measurement to the absolute value reported by the photo-diode previously calibrated. In the bottom-plots in Fig. 3.7, the relative QE measurements for the two WLS configurations are reported. The QE measured without TPB, at 420 nm, is in agreement with the manufacturer specifications (∼20%). When the TPB is applied, the enhancement of the QE at low wavelengths is visible in both configurations; becoming the curve almost flat for wavelength below 250 nm, the value at 128 nm is expected to be the same observed at 200 nm. Comparing the two plots, however, the QE is higher

when the TPB is directly coated on the PMT surface. The main factors that have been identified to explain this observation are related to the light absorption by the acrylic plate of UV photons and possible reflections in the TPB-PMMA interface. Additionally, a geometrical acceptance reduction is expected due to the coverage ensured in the two configurations, which is wider in the direct TPB deposition. Despite that, the handling of the PMMA plate during the coating operation, the storage, and the installation is much easier.

3.2.2 PMT High Voltage divider circuits

The main difference in the PMT base configurations is in the polarity of the supplied bias voltage of the divider circuit. In Fig. 3.8, a summary of the two configurations is given, the negative base (NB) is presented in the top of the figure and the positive-base (PB) in the bottom; in both figures, the scheme of the bias

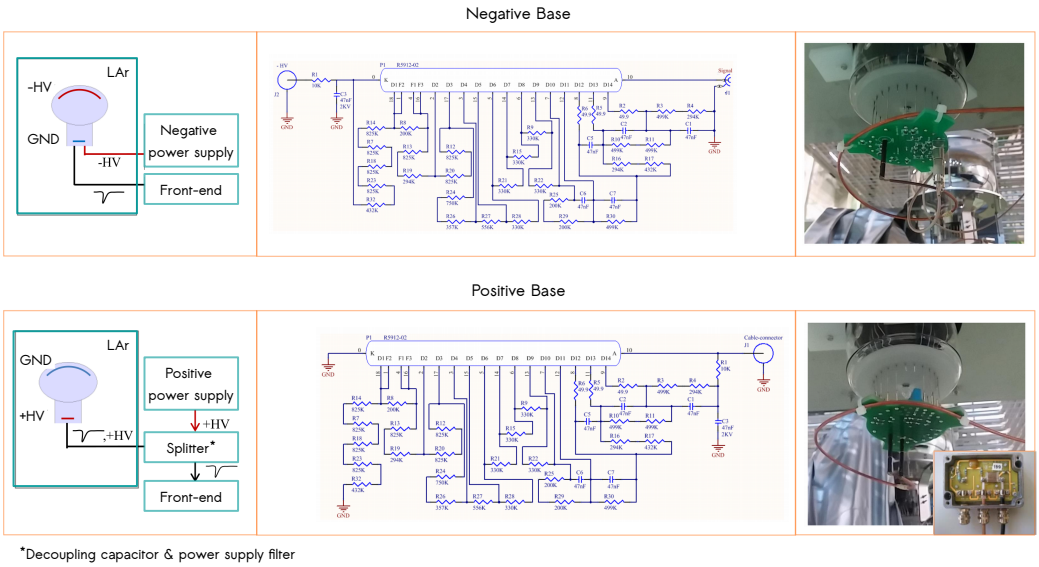

Figure 3.8.: Schematic description **(left)**, dynodes diagram **(middle)**, and two pictures **(right)** of the negative base (NB) **(top)** and the positive-base (PB) **(bottom)** configurations installed in the WA105 DP demonstrator.

voltage configuration and connection with the PMT are shown on the left, the voltage divider resistors diagram in the middle, and two real pictures on the right.

In the NB, the negative bias voltage is carried by a cable to the photo-cathode

while the PMT-anode is grounded; an additional cable is needed for the readout of the PMT signal. On the contrary, in the PB, the photo-cathode is grounded, whereas the positive biasing is applied at the anode. In this configuration, only one coaxial cable is needed having the double function to supply the HV and readout the signal. The two signals are split through a decoupling circuit (DC), also referred to as splitter in the text, that is installed outside the cryostat. The PB splitter design is made of a capacitor with the function of decoupling the PMT signal from the DC power supply through an RC low-pass filter to remove noise from it. Before the photon detection system has been operated in the WA105 DP demonstrator, the two base designs have been studied in a dedicated setup in the CIEMAT laboratory to characterize their response. The description of the main findings of this study is reported in Ref. [91]. Some advantages are expected in the PB design: the splitter installation outside the cryostat that facilitates its replacing or modification, the noise removal by the RC filter, minimization of the number of feedthroughs and cables, and the photo-cathode grounding to reduce the dark current induced by spurious pulses from current leakage. However, the choices of the capacitor and the cable connection with the feedthrough are delicate aspects to be evaluated in order to avoid the signal distortion. As will be described in Sec. 3.9.3, the splitter design used in the WA105 DP demonstrator introduces two deformations in the waveform that limits their application in most of the physics studies that will be presented in this thesis.

3.2.3 Light Data Acquisition

Independently from the base design, the light analog signal detected by the PMTs is acquired by commercial electronics and digitized by the CAEN v1720 analog-to-digital converter (ADC) board, with the maximum dynamic range of 2 V. The waveform digitization is done in 12 bit sampled at 250 MHz frequency, such that each waveform is collected with 4 ns sampling. Two digitization lengths were used: a short one reaching the maximum time window length of 4 μs and a longer one reaching 1 ms length; the first one was mostly used to characterize the primary scintillation light, whereas the length of second is motivated by the necessity of detecting the whole S2 signal given the electron drift velocity expected at the nominal drift field. In the 4 μs time window, 0.5 μs are set for the pre-trigger and 22.85 μs are set for

the pre-trigger in the 1 ms window. Finally, the CAEN board is read out via an optical link to a PC equipped with a CAEN A2818 PCI CARD.

3.2.4 PMT calibration

Different campaigns have been performed to measure the PMT gain at the LAr temperature, using a random trigger from a pulse generator operated with 100 Hz frequency. Different runs are collected applying an increasing voltage; for each voltage, the charge spectrum is obtained integrating every fluctuation from the baseline that is found in the waveform. Due to the trigger used, the expected signal is dark current at the level of the single photo-electron (SPE). An example of the charge spectrum is reported on the left of Fig. 3.9. It consists of two Gaussian distributions

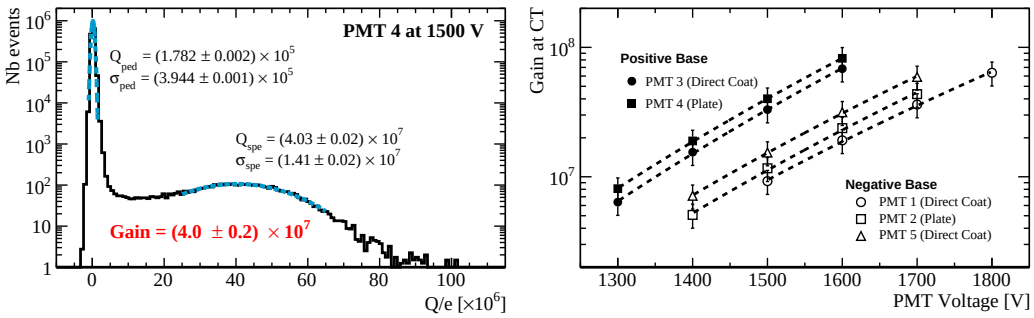

Figure 3.9.: Left: Example of the integrated charge spectrum analyzed for one PMT and corresponding gain computation. **Right:** PMT gain measured for different operating voltages for NB PMTs (empty dots) and the PB ones (full dots); the fitted power law is superimposed in each set of data for every PMT.

centered at zero and at the SPE; hence, the PMT gain is obtained from the distance between the two peaks. Finally, the gain calibration curve is obtained considering the dependence of the PMT gain with the voltage applied. The relation is described by the power-law: $G = A\ V^B$, being A and B the fit parameters related to the PMT design (number, material, and structure of the dynodes). On the right of Fig. 3.9, the five calibration curves corresponding to the five PMTs are reported; in Tab. 3.6, the gain and the voltages applied to the PMTs during the WA105 DP demonstrator operation are listed. Initially, the PMTs were operated at the gain of 10^7 and, successively, decreased to the 10^6 to avoid the ADC saturation. Equalizing as much as

PMT n.	gain	voltage [V]	gain	voltage [V]
1	0.93×10^6	1200	1.06×10^7	1500
2	1.28×10^6	1200	1.35×10^7	1500
3	$2.06(1.26)\times10^6$	1150 (1100)	0.93×10^7	1320
4	$2.68(1.64)\times10^6$	1150 (1100)	1.03×10^7	1300
5	1.55×10^6	1200	1.70×10^7	1400

Table 3.6.: PMT gain measurement corresponding to the photon detection operation in the WA105 DP demonstrator.

possible the PMT response is useful to uniform the light detection system response; for this reason, during the demonstrator operation, the PMT voltage of the two PB PMTs was lowered slightly more to improve the response uniformity.

3.3 Cosmic Ray Taggers as an external trigger system

Four plastic scintillator movable panels of Cosmic Ray Taggers (CRT) are positioned outside the cryostat external walls, along the 3 m side, as an external trigger system. This kind of trigger, which has already employed in other experiments [208], provides the time and the 3-D reconstruction of the cosmic muons crossing the detector. In the WA105 DP demonstrator, each CRT panel covers a 1.8×1.9 m^2 surface, corresponding to a 1.8×1.8 m^2 active area. Each panel is composed of 16 strips; two panels per side allow to have a matrix with 112.5 mm^2 hit accuracy, providing the 3-D coordinates of the triggered track. In the top of Fig. 3.10, a picture of one of the two CRT panels installed in the WA105 DP demonstrator is shown; in the bottom of the same figure, a picture of the strips in a CRT module is displayed. The charge deposited in each strip is read through an optical wavelength shifter fiber by two Silicon Photomultipliers (SiPMs); a dedicated Front-End Board, connected to the CRT-DAQ computer via Ethernet connection, is used to amplify, process and digitize the SiPM signal. The trigger signal sent both to the light and charge data acquisition systems is defined over at least four-fold coincidence among the CRT panels, above 500 ADC counts minimum threshold per strip.

The CRT trigger system covered a fundamental role in the analysis of the scintillation light in the WA105 DP demonstrator. Thanks to it, the cosmic muon track

coordinates are always available, independently from its reconstruction in the anode plane. Consequently, the initial characterization of the scintillation light features allowed identifying the main observables to define the logic of the PMT self-trigger that will be presented in Sec. 3.4. Prior to that, in this section, the topological variables that can be extracted from the CRT coordinates of the track reconstruction will be described.

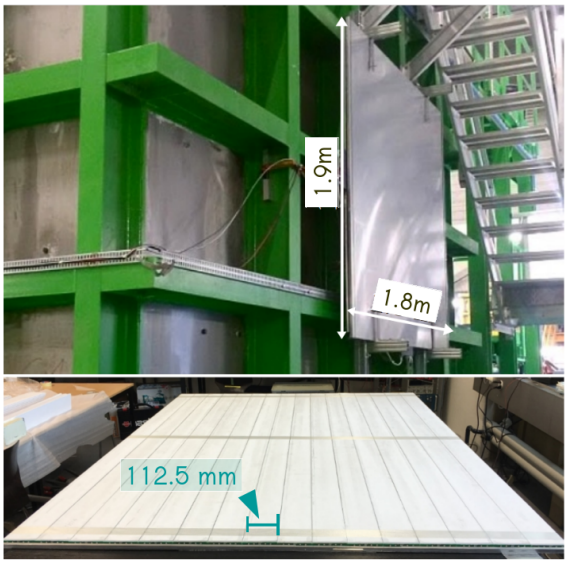

Figure 3.10.: **Top:** CRT panels positioned on the WA105-DP cryostat walls. **Bottom:** picture of the CRT strips installed in each panel (taken from Ref. [208]).

In order to reproduce the track topology expected in the DUNE-FD module, the two CRT panels have been initially installed in alignment with the FC center (referred to as *CRT-parallel* geometry). However, this geometry was particularly sensitive to the triggering of *muon-bundles* [5]. For this reason, in a second step, the CRT panels were shifted in the asymmetric *CRT-shifted* geometry. Unfortunately, in both cases, the CRT trigger rate is very low (∼0.3 Hz) because the cosmic muon flux following a $\sin 2\theta$ law. A descriptive sketch of both CRT geometries is reported in Fig. 3.11; in the sketch, the detector is shown from the *front*-view. A specific nomenclature, that will be used in all the analyses, has been assigned to CRT elements and variables in the two geometries. As pictured in the drawing, the position of the PMTs inside the detector follows the ascending order such that the CRT panel closest PMT-1 is called *wall*-side and the other is named *door*-side. In the *CRT-shifted* geometry, the *wall-side* panel was raised by 15 cm and the *door-side* panel was lowered by 90 cm.

[5] With the nomenclature *muon-bundles* it is referred to as a shower of cosmic-muons tracks reaching the Earth's surface generating a multiple-strip coincidence in the CRT panels.

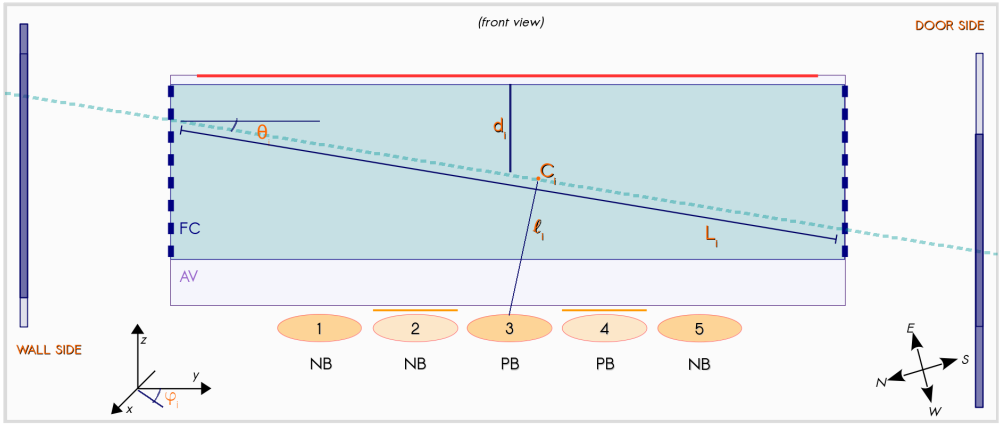

Figure 3.11.: Descriptive sketch (not scaled) of the track reconstruction given by the CRT external system trigger; the two CRT geometries are reported.

3.3.1 CRT reconstruction of the muon tracks

A cosmic muon crossing the LAr volume at the MIP's energy is expected to produce a long, well-defined track. For this reason, a CRT muon-track is defined when the triggered event fired only one hit per panel; all other events, in most of the cases recognized as *muon-bundles*, as well as electrons and showers, are considered as background events and rejected. The reconstruction of the track trajectory is obtained from the position of the fired strips. A left-handed system of coordinates, centered in the FC volume, is defined as in the sketch of Fig. 3.11: the 3 m long side corresponds to the y-axis and the two panels lay in the x-z planes. The PMTs are in x=0 and z=-698 mm of the x-y plane and their y-coordinates are the following: (-1000, -500, 0, 500, 1000) mm.

In this section, all the CRT variables that can be retrieved from the CRT coordinates defining the track topology will be presented. In order to study the CRT track reconstruction performance, two very long runs (30 days of data for CRT-parallel geometry and 61 days for the CRT-shifted one) are analyzed. The CRT variable definition has been implemented in a dedicated library that is included in the raw data processing in such a way to be available for any kind of analysis.

ToF

With the position of the hits, the hit time is recorded as well. The time of flight is defined as the time difference between the values reported in the two sides. In Fig. 3.12, the ToF distributions observed in the two geometries are reported. Two Gaussian distributions, centered around ±22 ns and a σ of ∼6 ns are obtained for both geometries. In order to include the delays introduced by the cable length and

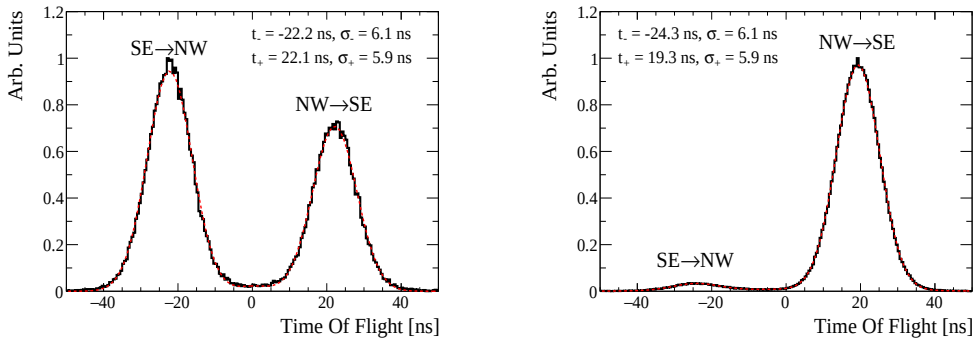

Figure 3.12.: Typical time of flight distribution of *muon-like* events triggered by the CRT system in the two CRT geometries (*CRT-parallel* on the **left** and *CRT-shifted* on the **right**).

the electronics, an offline correction is applied. An asymmetry in the population of the two peaks is observed in the *CRT-parallel* geometry due to the geography of the surroundings of the detector; the presence of the Jura mountains determines a natural shielding to the cosmic muon flux. As expected, the population of one of the two peaks is drastically suppressed in the *CRT-shifted* geometry.

Angular distributions

In Fig. 3.13, the (θ-ϕ) phase space of the *muon-like* events is reported; the θ and the ϕ angles are defined in the y-z and y-x planes, respectively, as shown in Fig. 3.11, their distributions are reported for both CRT geometries. The *CRT-shifted* geometry introduces the asymmetry in the y-z plane; additionally, in both cases the negative θ-angle is shadowed by the presence of the Jura mountains that attenuate the muon flux. The angular distribution in the y-x plane, instead, remains unchanged. In Tab. 3.7, the CRT acceptance in the two geometries is reported; it is maximum in the *CRT-shifted* geometry reaching $\theta_{max} \sim$ - 22^o.

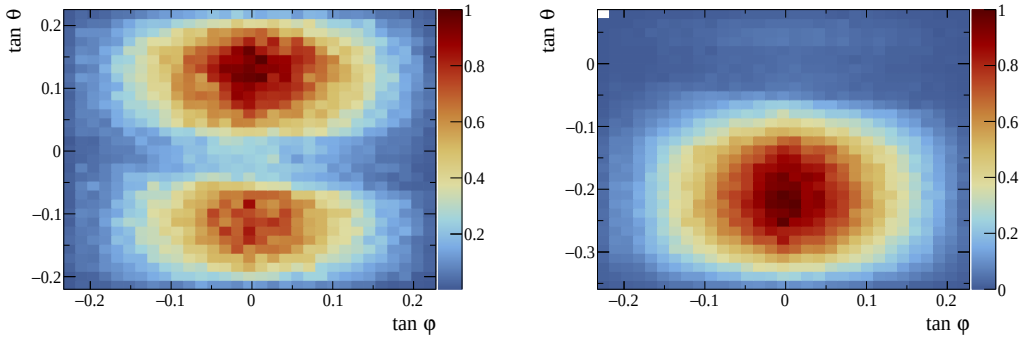

Figure 3.13.: Typical angular distributions observed with the CRT trigger system in the *parallel* geometry, on the **left**, and in the *shifted* ones, on the **right**.

geometry	**acceptance (θ-angle)**	**acceptance (ϕ-angle)**
CRT-parallel	[-11; 11]^o	[-11; 11]^o
CRT-shifted	[-22; 6]^o	[-11; 11]^o

Table 3.7.: Geometrical acceptance of the CRT system allowed by the two panel positions in the y-z (*theta*-angle) and x-y (*phi*-angle) planes; the typical ($\theta - \phi$) space in the *CRT-parallel* geometry is shown on the **left**, and in *CRT-shifted* geometry, on the **right**.

Track-PMT distance, closest point coordinates and electron drift distance

Besides the two angles, additional variables that relate the track to the PMT position are defined: the minimum approach distance between the track and the center of the PMT-surface, the coordinates of the closest point, and track length. The closest point coordinates are used to select geometrical regions confining the track position inside the detector. Connected to the closest point coordinates, the drift length of the electrons is defined in turn. This distance is defined as the shortest distance covered by the ionization electrons to reach the anode-plane.

Fiducial volume definitions and track length

The total LAr mass in the WA105 DP demonstrator corresponds to a volume of 18.01 m^3; however, depending on the analyses performed, different fractions of this volume are considered. The definitions that will be given here are assigned from the

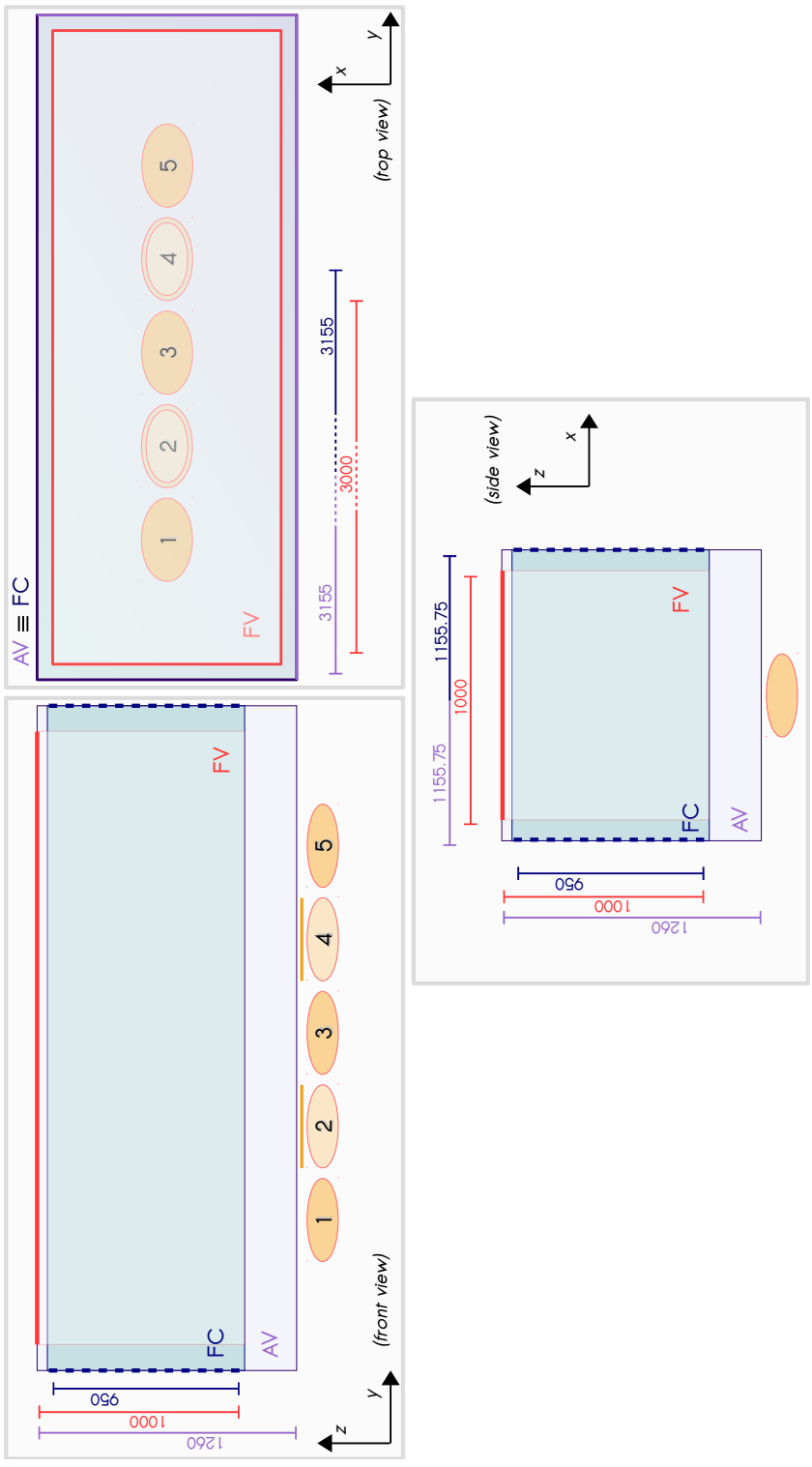

Figure 3.14.: Schematic description of the fiducial volumes defined to describe different regions of the detector; the active volume (AV), the field cage (FC) volume, and the fiducial volume (FV) are reported in the following colors: AV in violet, FC in light cyan, and FV in red, respectively. The detector is seen from the front (in **top-left**), from the top (in **top-right**), and from the side (in **bottom**). As a reference, the PMT numbering is reported following the description that will be given in Sec. 3.2).

scintillation light production point of view, so a volume different to the enclosed one by the field cage can be used. In particular, the following definitions are given:

- LAr active volume (AV): LAr volume where the scintillation light detectable by the PMTs can be produced (including the volume within the FC plus the volume between the cathode and the PMTs),
- Field cage (FC) volume: LAr volume filling the field cage,
- LAr fiducial volume: LAr volume within the field cage, underneath the CRP surface.

A schematic representation of the three volumes is given in Fig. 3.14 and their dimensions are summarized in Tab. 3.8. From the technical implementation point of

nomenclature	**dimensions**	**unit**
LAr active volume (l×w×h)	3155×1155.75×1206	mm^3
field cage volume (l×w×h)	3155×1155.75×950	mm^3
fiducial volume (l×w×h)	3000×1000×1000	mm^3

Table 3.8.: Dimensions corresponding to the sub-volumes dividing the LAr bulk in order to study the scintillation light: LAr active volume, field cage volume, and fiducial volume.

view, the volume definition is based on the *Ray-Box Intersection Algorithm* [209] that is implemented in the track-parameter library as a class of ROOT. The algorithm ensures the proper intersection of the track in the volume defined as a box in the reference system. When the track is partially contained in the volume, only the part of the track inside the volume is considered for the reconstruction. Additionally, the proper coordinates in the sides of the box are assigned to define the corresponding track-length and a flag is assigned to each volume. All this information is stored in the processed files and it can be used to simplify the track selection. The scintillation light that can be detected by the PMTs is the one produced in the LAr AV. However, since the cathode and the grid are the main elements absorbing the light, only the events produced above the them are considered in order to keep the same proportionality between produced and detected light. Analogously, when the electroluminescence light signal is studied, only the light produced in the FV has a direct correlation with the amplified charge signal produced by the drifted electrons

and reconstructed in the anode plane; for this reason, only the light produced in the FV is considered.

3.3.2 CRT-PMT DAQ communication

The CRT trigger and the photon detection event builder are two independent systems that assign a unique time-tag with ns precision to the triggered event; thanks to that, an offline matching of the events based on the time information available in both systems was possible. A schematic description of the CRT-PMT DAQ match logic is described in Fig. 3.15. When the CRT panels verify the trigger condition, the trigger signal is sent to the PMT-DAQ system, that being continuously recording events information, opens the pre-trigger window, collects the waveform, and stores the time information of the event. Simultaneously, the event information is published in the CRT-DAQ; however, the CRT and the PMT DAQ systems are connected through a common ethernet connection (Socket connection), slower than the trigger speed. Hence, the off-line matching associates only events collected at the same time with ms precision based on the recorded event trigger time, independently from the CRT time published in the CRT-DAQ server. On the contrary, if more than one event are published corresponding to the same trigger time, the matching is not found. Because of the different time scales between the trigger time ($\mathcal{O}ms$) and the event publishing time ($\mathcal{O}s$), the pulling of the server is systematically done with 1 s frequency and the possibility to find a CRT event in correspondence with more than one event is not negligible. Consequently, due to the communication logic between the CRT trigger

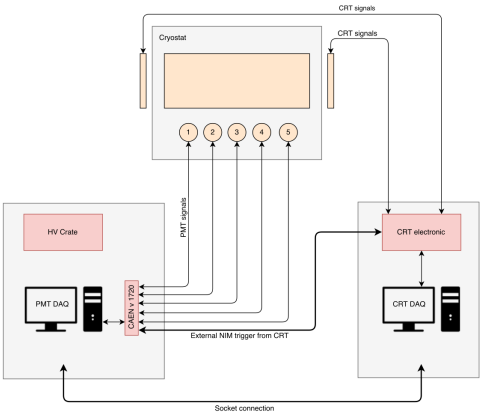

Figure 3.15.: Schematic description of the CRT and PMT-DAQ communication.

and the light systems (CRT-PMT match), a not negligible inefficiency is observed in the number of unmatched events corresponding to ∼56.4% of the initial number of the events[6].

3.4 The PMT self-trigger as internal trigger system

The alternative trigger system implemented in the WA105 DP demonstrator is a self-trigger based on the primary scintillation light signal detected by the five PMTs. The PMT self-trigger logic, described on the left of Fig. 3.16, is based on the simple requirement of having a five-fold coincidence within 80 ns[7] among the five S1 PMT signals if exceed a fixed threshold. In order to be compatible with the network limitations of the experimental hall, the PMT trigger threshold has been defined to be lower than 3 Hz at the nominal drift field; as shown in the threshold scan reported on the right of Fig. 3.16, the corresponding trigger threshold is at 3750 ADC counts, that has been kept fixed during the trigger operation. By comparing

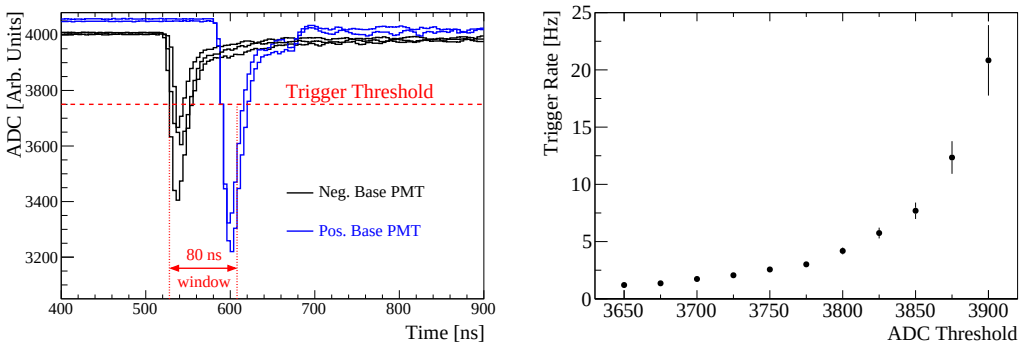

Figure 3.16.: Left: PMT self-trigger configuration illustrated considering the waveforms detected in one raw event.
Right: Trigger rate shown as a function of the ADC threshold set to the five PMTs.

with the typical trigger rate of the CRT system, one of the advantages of this trigger configuration is given by the higher trigger rate. However, given its intrinsic logic, the PMT self-trigger facilitates the inclusion of showers and *muon-bundles* in the initial sample of triggered events. Since the CRT and the PMT triggers are used

[6] This number is obtained by analyzing all the runs collected with the CRT system in the *shifted*-geometry; in total, 14 runs, with 44374 events out of 101818 triggered events.

[7] The delay present in the t_0-time is due to the different length of the cables used for the negative and positive PMTs.

alternatively, only if the track reconstruction in the anode plane is available, then *muon-like* events can be selected among all the PMT triggered events. With a view of having a good track reconstruction, stable runs collected with a sufficient amplified charge signal are needed; however, as described in Sec. 3.1.4, very few runs satisfy these conditions. For this reason, in the analyses of the light that will be presented in the rest of the thesis, two quality cuts have been defined, independently from the availability of the charge-track reconstruction, in order to clean as much as possible the *muon-like* event sample. Their definition will be given in Sec. 3.7 and it is motivated by the characteristic response of the PMTs in both trigger conditions that will be presented hereafter.

3.5 Total events collected for the light analyses

The WA105 DP demonstrator performance has been studied exposing the detector to cosmic muons; its operation took place in two phases: the commissioning phase, when the basic response of the detector systems have been optimized, and the second phase, when the demonstrator worked in more stable conditions. The detector commissioning started in March 2017, while more stable conditions have been reached around June 2017. With the lowering of the PMT gain and the shifting of the CRT panel (around July, 23^{th}), an improvement in the stability of the detector operation has been reached. The detector has been operated until November 2017, when the cryostat emptying started. In Fig. 3.17, the total number of events, $\sim 5 \times 10^6$, collected with both trigger systems are reported; the strength of the drift field applied is represented by the color scale and the red line represents the cumulative number of events acquired. For the basic features related to the characterization of the scintillation light given at the end of this chapter, all the runs triggered by the CRT external trigger and collected in absence of the drift field have been used; thanks to the CRT reconstruction of the muon tracks, relevant analyses can be retrieved from them. Moreover, the same sample of events allowed the study of light propagation, which will be presented in Chapter 5. Additionally, by including also the data acquired without the reconstruction of the track from the charge system and triggered by the photon detection system, a detailed study on the light production has been performed and explained in Chapter 4. Finally, the characterization of the electroluminescence light signal that will be detailed in Chapter 6, is based on all

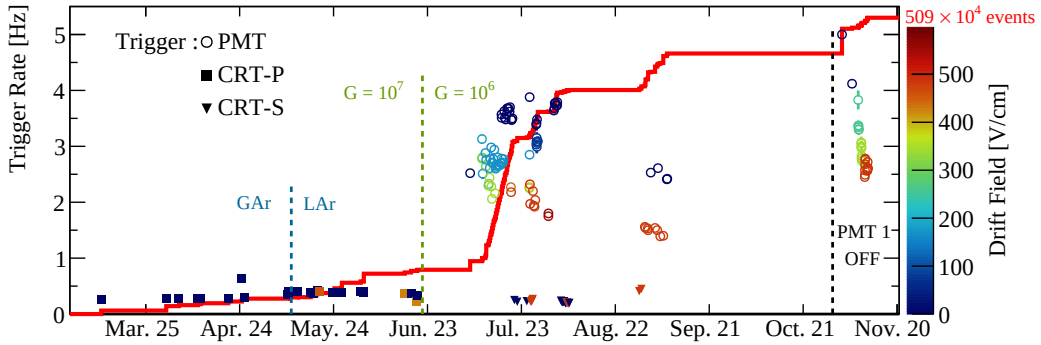

Figure 3.17.: Summary of all the scintillation light data collected. Each point corresponds to a single run given HV and trigger conditions of the detector. The colored scale reported on the right corresponds the drift field strength applied in each run. The red line represents the cumulative number of collected events.

the data collected at the nominal drift field value of 0.5 kV/cm and with different amplification field settings, in both trigger configurations.

3.6 Analysis framework

In the same PC where the PMT raw-data are stored, a first processing of the raw data collected is done using the DAQ MIDAS framework [207], converting the raw information in more manageable ROOT files, where the basic information related to the PMT waveform digitization and the CRT panels are stored into two ROOT trees. In particular, for each event triggered by the CRT system, the following information is stored: the header of the event in the CRT DAQ system, the trigger identification number and the number of events present in the CRT buffer system, the timestamp of the trigger and the event time when published in the server, the signal in each strip of each plane, the total charge of the event, the time of flight, the total number of hits, and the CRT coordinates in each CRT side. Regarding the information on the photon detection system stored for each event, they are: the header number, the timestamp of the trigger and the publishing times in the CRT server, the number of channels connected to the ADC, the digitization sampling, the waveform and the corresponding length for each PMT. At this level, the offline matching has already been done based on the timestamps recorded by the CRT and the photon detection

systems, and this information is stored in the ROOT files through a flag.

Accessing to the processed ROOT files, a specific analysis framework is conceived to directly access raw information stored in the processed ROOT files to give a deep characterization of the event. Dedicated libraries have been developed to:

- distinguish between multiple-hit events and the candidates for the reconstructed muons, by looking at the number of strips fired in each event
- define the CRT reconstruction variables and the fiducial volumes defined in Sec. 3.3.1 of the event
- analyze the PMT waveforms, reconstructing the observables associated with the S1 and the S2 signals[8]

As a second step, an improved offline processing allowed combining the light and the CRT information with the charge reconstruction of the event. This analysis tool has been named Derived Physics Data (DPD). In contrast with the conception of the analysis framework libraries, the DPD philosophy is to furnish a simplified analysis tool that overcomes the raw reconstruction of the event and only the most relevant observables are stored and being accessible to the analyzer. Concerning the light and CRT information, most of the observables that have been stored in the DPDs have been obtained from the algorithms developed for the libraries to reconstruct the events in the analysis framework.

3.6.1 PMT waveforms

In this section, the description of the algorithm developed to identify the S1 is given. From them, the following quantities can be retrieved:

- the waveform pedestal (mean value and noise RMS)
- the S1 peak (time, amplitude, and integrated charge)

In Fig. 3.18, the typical waveform generated by a crossing muon and detected by the PMTs is shown on the left. On the right of the figure, the zoom around the S1 peak is given. In this section, only the definitions related to the S1 signal will be

[8] The description of the algorithms for the S1 reconstruction will be presented in the rest of the text, whereas the ones developed for the S2-signal will be given in Sec. 6.1.1.

described; the description of the algorithm dedicated to identifying the S2-signal, instead, will be presented in Sec. 6.1.1 where its correlation with the track topology will be discussed.

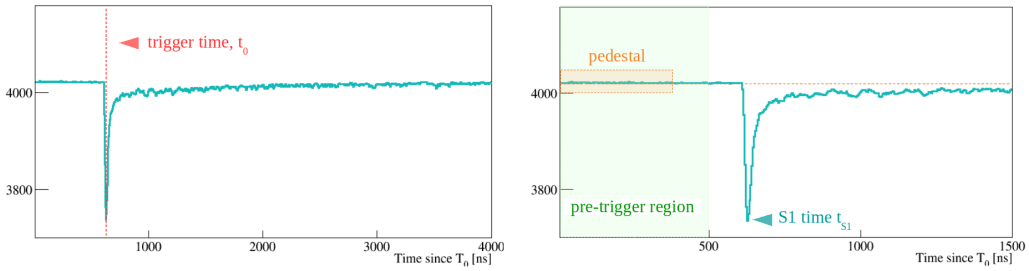

Figure 3.18.: Left: Typical raw PMT waveform generated by a crossing muon and detected by a single PMT (NB PMT shown in the plot). **Right:** Zoom of the same event around the S1-peak, showing the main observables characterizing the S1 signal.

Independently from the origin of the trigger signal, a pre-trigger interval is included in the waveform by the ADC, allowing to determine the baseline or pedestal. The pre-trigger length changes depending on the time acquisition window length (500 ns in the 4 μs window and 228500 ns in the 1 ms window). The S1 peak is expected to arrive just after the pre-trigger interval. In order to have a unique definition that does not depend on the time acquisition window and neither on the pre-trigger length, the pedestal is calculated event-by-event considering the waveform fluctuations in 400 ns range before the expected S1-peak, as shown by the following equation:

$$\text{Ped}_{\text{mean}} = \frac{1}{\text{base}_{\text{Ped}}} \sum_{t_0}^{t_1} \text{Light(t)}\ \text{dt}, \tag{3.1}$$

the integration range, base_{Ped}, changes depending on the time window acquisition length and it is set as (0; 400) ns, in the 4 μs time acquisition window, and (228000; 228400) ns in the 1 ms one. In correspondence with the Pedestal mean, also the RMS is obtained from the usual relation, $\text{Ped}_{\text{RMS}} = \sqrt{\Sigma_{\text{base}_{\text{Ped}}}(x_i - x_{\text{mean}})^2/(n-1)}$, being x_i the waveform content at the bin-i and x_{mean} the mean of the pedestal obtained from Eq. (3.1). Similarly, knowing the pre-trigger length, the S1 peak is the minimum of the waveform found within 500 ns range starting 100 ns before the expected time of the S1 signal. When the S1-minimum is identified, the S1-amplitude is defined as the difference between the S1 minimum and the pedestal

mean. The integrated charge is considered for the total recorded waveform, in runs collected in the 4 μs time window, including the 500 ns pre-trigger, and in three different shorter ranges as defined by the following equations:

$$S1_{Charge} = \frac{\Delta T \cdot \text{ADC conv.}}{\text{Resistence}} \frac{q_{e^-}}{\text{Gain}} \Big[\text{Tot. Charge} - \text{Ped}_{mean} \times R\Big], \tag{3.2a}$$

$$\text{Tot. Charge} = \sum_{T_{S1}-40\ ns}^{T_{S1}+T_{max}} \text{Light(t) dt} \tag{3.2b}$$

being T_{S1} the time corresponding to the maximum amplitude and T_{max} = 40 ns, 90 ns and 1 μs if a different integration range from the maximum one is considered. The meaning of all the other factors are the following:

- ΔT = 4 ns sampling
- ADC conversion = 2/4096, being 1 ADC count = 2 V/4096 digits
- R = 50 Ω, the impedance resistance
- q_{e^-} = - 1.602·10^{-19} Coulomb, the electron charge with its sign
- Gain, the PMT gain assigned considering the values given in Tab. 3.6
- R the total integration range, either [-500; 3500] ns or [-40; T_{max}] ns

3.7 Characterization of the PMT response

The PMT response has been studied considering two main features:

- the probability of saturating the ADC dynamic range
- the conservation of the linear PMT behavior as a function of the detected signal intensity

The ADC dynamic range saturation can be mitigated by adjusting the PMT gain. However, independently from it, the PMT base design slightly changes the shape of the waveform; hence, if the PMT gain is equalized to have a homogeneous PMT response, the probability of ADC saturation depends on the base design. In addition to that, as observed in the studies performed in the CIEMAT laboratory [91], the PMT anode shows a saturation when a big number of photons, detected in a short

time, are amplified by the dynode chain. The amplification in the last dynode is affected differently in the NB and PB PMTs and the linearity is lost sooner in the NB design. As will be presented hereafter, a similar effect is observed also in the WA105 DP demonstrator for events crossing the detector very close to the PMT surface. The goal of the two following analyses is the performance comparison of the two base configurations.

3.7.1 ADC dynamic range saturation

For signals larger than 2V, ADC dynamic range saturation is observed. Independently from the PMT gain, the PMT base design makes that the waveform tends to be narrower and higher in the PB PMTs, instead it is slightly broader and shorter in NB PMTs. Because of that, the probability of saturating the ADC dynamic range in the case of PB PMTs is higher than in the NB PMTs. An example of these events is reported on the right of Fig. 3.19. In order to reduce the ADC dynamic range saturation probability, the PMTs that were initially operated at a gain of 10^7, have been lowered at $\sim 10^6$ during the stable operation of the demonstrator.

3.7.2 PMT linearity

Although the response of the PMT should be linear in a wide dynamic range, a deviation of the linear response is expected for high-intensity pulses due to the PMT anode saturation. In order to characterize this phenomenon and identifying a common cut that discards events saturating the PMT response, the correlation of the S1-amplitude with the integrated S1-charge[9] is considered. As shown in Fig. 3.19, a saturation of the S1-amplitude appears for signals with the S1-amplitude higher than $\sim$300 ($\sim$75) PE at a gain of $10^6(10^7)$. The saturation is stronger at the higher gain and more evident in NB than PB PMTs. In particular, as pointed out in a more evident way in the bottom-right plot corresponding to a gain of 10^6, the loss of PMT linearity in PB PMTs is not observed since in most of the cases it is hidden by the saturation of the ADC dynamic range. The different behavior between the two base configurations is similar to what investigated in the measurements performed

[9] Only for this analysis, since it has been performed during the detector commissioning-phase, the charge integration range is of 80 ns instead of 90 ns as given in the previous definitions; despite that, the conclusions do not depend on this kind of difference.

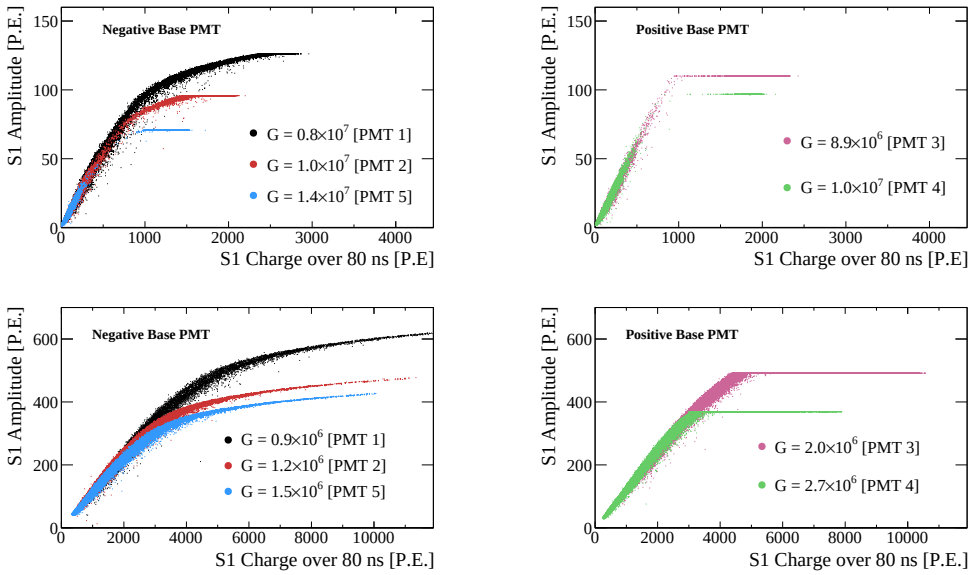

Figure 3.19.: Dependence of the S1-amplitude with the integrated S1 charge over 80 ns, expressed in P.E., for the NB, on the **left**, and PB, on the **right**, in the two gain regimes: at 10^7, in the **top**-plots and at 10^6, in the **bottom** ones.

at the CIEMAT laboratory and reported in Ref. [91], both at room and cryogenic temperature, considering the same PMT model with an analogous electronic base design. In these studies, a laser head, with a pulse width of less than 500 ps FWHM at 405 nm wavelength, is used. The observation in the laboratory points out that the linearity between the number of photons expected and measured is lost at 200 PE for gain of 10^7 in CT; furthermore, the linearity is lost sooner in NB PMTs than in PB PMTs. Moreover, from the comparison of the results obtained with a 40 ns pulse LED, the shorter the pulse, the earlier the linearity is lost. The PMT response observed in the WA105 DP demonstrator data is in agreement with these measurements; hence, the definition of a common cut rejecting the events in the non-linear region has been defined.

The cut definition needs to include the differences in the waveforms introduced by the two distinct gain-regimes in which the PMTs have been operated, and the dependence of the scintillation light with the drift field[10].

[10]The effect of the drift field on the scintillation light signal will be widely described in Sec. 4.3.

In order to define the cut rejecting events beyond the linear behavior of the PMTs as general as possible (e.g. independently from their specific gain in the two regimes and all the drift field strengths), a conservative approach has been considered, based on the correlation of the S1-amplitude with the S1-charge profile, shown in the x-axis in Fig. 3.19. A linear fit is performed in an increasing S1-amplitude range, starting from 0 and adding a 50 ADC counts step each time. For each of these fits, the χ^2/ndf is plotted as a function of the maximum of the S1-amplitude range used in the corresponding fit. An example is given for the NB PMTs in Fig. 3.20. The PMT response is considered linear up to values of S1-amplitude for which χ^2 <2, as a consequence, all the events with the S1-amplitude larger than 1400 ADC counts are rejected. The values applied in the two gain regimes for the two base configurations are listed in Tab. 3.9 and the average percentage of events found in the PMT response saturation regime is reported in Tab. 3.10, separately for all the PMTs.

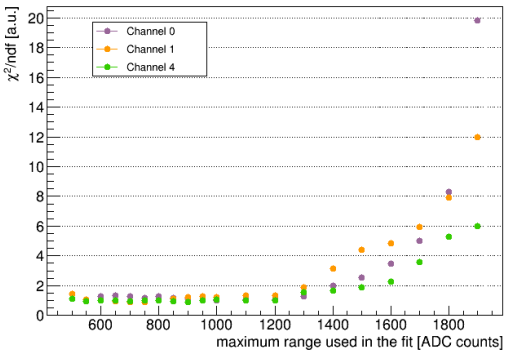

Figure 3.20.: χ^2 minimization developed to identify a common cut rejecting all the events saturating the PMT response. For this specific purpose, the S1-amplitude is expressed in ADC counts.

PMT base	gain	cut [ADC counts]	gain	cut [ADC counts]
NB	10^6	1400	10^7	3000
PB	10^6	3500(3000)	10^7	4000

Table 3.9.: S1-amplitude cut values applied to reject events saturating the PMT response, differentiating for the two base configurations and the two gain operation regimes; the cut is expressed in ADC counts and it is valid for all the PMTs with the same base design. The value given in parenthesis for the PB PMTs at 10^6 corresponds to the value applied when the gain has been lowered (see Tab. 3.6).

Even though the PMT response saturation is consistent with the PMT linearity saturation observed in the laboratory measurements, attributed to the anode

PMT n.	**1 (NB)**	**2 (NB)**	**3 (PB)**	**4 (PB)**	**5 (NB)**
CRT tr. [%]	1.4	0.9	0.9	0.6	17
PMT tr. [%]	15	15	12	2	1

Table 3.10.: Typical rejection percentage, reported per PMT, corresponding to the number of events saturating the PMT response in the two trigger configurations. Events triggered by the CRT system are collected in the *CRT-shifted* geometry.

saturation, it is not possible to exclude that the PMT *fatigue*-effect observed for high-frequency pulses [91] is also competing in saturating the PMT response. As shown in Fig. 3.21, considering the same sample of triggered events, average waveforms are built including events laying in different ranges with increasing amplitudes. For most of them, the shape is the same; however, for the higher amplitudes, the shape starts to be distorted. This effect has been explained as an additional saturation of the PMT response for very energetic events. The reason for that is justified by the behavior of the correlation between the fast and the slow components of the scintillation light signal, expressed in terms of the integrated S1-charge in 80 ns after the S1 peak and the integration of the S1-charge between 1 and 4 μs, respectively. The correlation is shown in Fig. 3.22; for both base configurations, after a linear relation between the fast and the slow integrations, while the fast component still increases, the slow part decreases up to a factor 2.5. Given the shape of the correlation, the phenomenon has been named *comet*-effect. An interpretation for that is given by considering the slow component as a train of large signals over a relatively long period. The pulses forming the slow component, in fact, produce a high average output current that limits the recovery of the discharging on the last dynode of the capacitors after the first pulses, until the end of the pulse train, and determines the loss of the PMT collected charge.

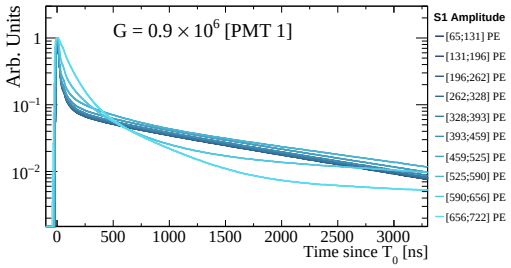

Figure 3.21.: Averaged normalized waveforms for one PMT in slices of S1 maximum amplitude; each waveform is obtained in ranges of 250 ADC.

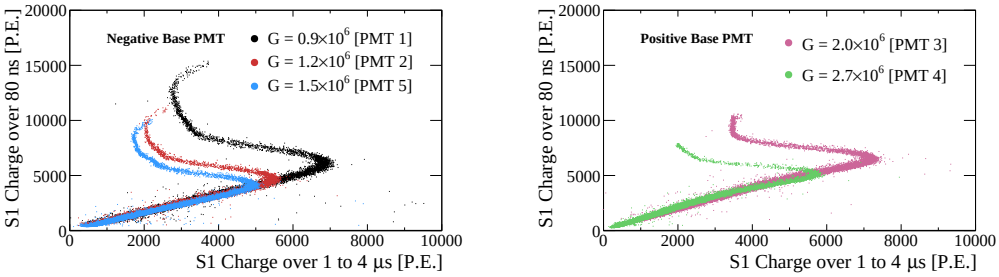

Figure 3.22.: Typical correlation of the integrated S1-charge over 80 ns (y-axis) and in the [1; 4] μs range (x-axis), both expressed in P.E.; given the shape of the correlation the effect has been named *comet-effect*. The effect is visible in both base configurations, NB on the **left** and PB on the **right**; the result is related to the PMTs operation with gain of $\sim 10^6$.

In order to avoid the misinterpretation of the physical meaning of the results obtained from the S1 signal, the rejection of the events laying in the *comet*-region, having a distorted waveform, is critical. Due to the conservative definition found for discarding events saturating the linear PMT response, the events in the *comet*-region are always indirectly rejected by the cut applied on the rejection of the PMT response saturation. For simplicity and because it is not possible to disentangle the two phenomena, the nomenclature "*comet-effect*" is used to describe all the events saturating the PMT response either due the anode saturation or the *fatigue*-effect.

Comments on quality cut selection in the PMT self-trigger

In order to study the LAr response to the cosmic muons crossing the demonstrator, the development of an event selection aiming to include only *muon-like* events is crucial. As will be described in Sec. 3.8, this is guaranteed by the CRT selection; however, the proper *muon-like* event selection of the data sample triggered by the PMT-self trigger is possible only by considering the event reconstruction in the anode-plane. Consequently, in order to allow the analysis of the data collected with the PMT-self trigger in absence of drift field, two quality cuts are applied to exclude the aforementioned saturations (ADC dynamic range and PMT response). In particular, the rejection of events in the *comet*-regime strongly suppresses the possibility of including more energetic events other than muons (like *muon-bundles* which is the topology expected to be facilitated by the PMT trigger if none track-

selection is applied). On the other hand, the requirement in the PMT self-trigger logic of accepting only events generating enough light to be detected by the five PMTs is very helpful to exclude random coincidences or very local low energetic events. The combination of these two requirements ensures to have events crossing the detector diagonally enough to be considered as *muon-like* events but not too much energetic as the case of the muon-bundles.

3.7.3 PMT Pedestal and RMS stability

The performance of the light detection system has been studied considering the PMT response in all the runs collected and their stability in time during the detector operation. In Sec. 3.7.1 and Sec. 3.7.2, the basic characterization of the differences induced by the base configuration in the PMT response has been already presented. In this section, the PMT stability is presented in terms of the pedestal mean and PMT noise; as shown in Fig. 3.23. At the top of the figure, the pedestal variation

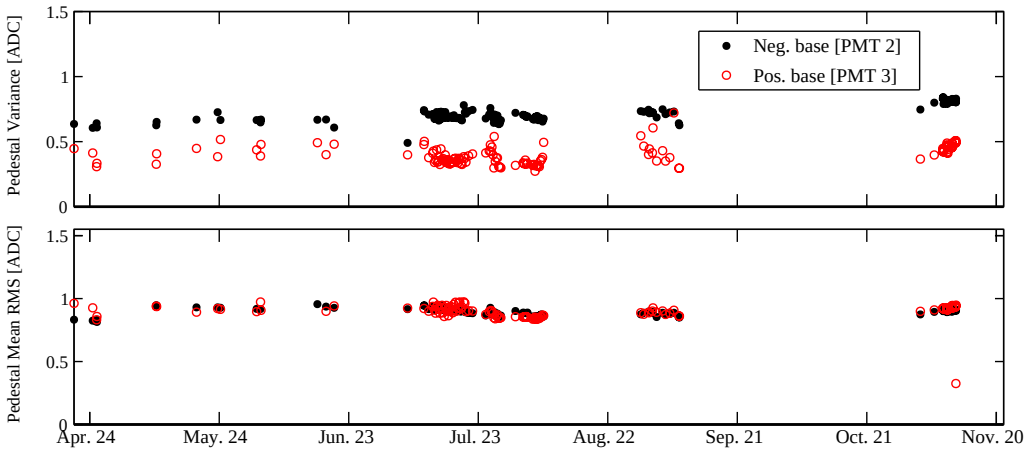

Figure 3.23.: Monitoring of the PMT performance during the whole demonstrator operation period reported for a PB PMT (empty dots in red) and a NB one (full dots in black).
Top: Pedestal variation measured in each run.
Bottom: Pedestal Mean RMS corresponding to each collected run.

is reported considering all the data collected during five months; the comparison between one NB and one PB PMTs is obtained by comparing the black and red points. In the bottom-plot, the pedestal RMS is shown for the same period and the same PMTs. The results are consistent in the five PMTs; moreover, the data

included have been triggered by both trigger systems but no differences are observed nor expected. In both base configurations, the pedestal noise is always around 1 ADC count; whereas, the pedestal stability is slightly better in PB than NB PMTs.

3.8 Muon-like event selection from the CRT external trigger

In order to study the scintillation light produced by the cosmic muons triggered by the CRT system and the photon detection system performance, a subsample of events must be extracted from the initial number of events triggered by the CRT external system. As a first step, only events with matched PMT and CRT information are included. Successively, a set of quality cuts fulfilling specific features selecting *muon-like* events is presented. The list of cuts is based on the CRT reconstruction of the track and on the PMT signal response.

First, among all of the events that fired the CRT strips only the ones that created exclusively one hit per panel are considered as muons reconstructed by the CRTs. Although a dedicated study has not been performed, due to the multiplicity of the hits fired by these events, they have been interpreted mostly as bundles of muon-tracks creating a coincidence in the two sides of the detector; an example comparing the two topologies of events are reported in Fig. 3.24. Among all the matched events, the percentage of events recognized as muons reconstructed by the CRT is found to be only 20.3%; the remaining 79.7% of events are *muon-bundles* or showers that fired more than one hit per panel. Successively, only the events crossing the LAr AV are accepted. Besides, a combination of cuts is applied to exclude CRT trigger inefficiencies corresponding to events triggered by the panels that not created scintillation light detected by the PMTs or events whose time-of-flight (ToF) is far away from the center of the distributions (ToF$\in$[-40, 40]ns, as reported in Fig. 3.12); all the other events are considered as random coincidences to be rejected. Finally, all the events whose waveform is not reconstructed univocally are rejected, which means the rejection of events that either saturated the ADC dynamic range or the PMT response. In addition to them, also less energetic events, possibly corresponding to PMT noise, are removed by requiring a minimum of the S1-amplitude. In particular, the condition is $S1_{\mathrm{Ampl.}} > 10$ P.E.; it is obtained requiring that at least one PMT collects light and considering the correlation of the minimum and the maximum S1-amplitudes of the PMTs detecting light in each event.

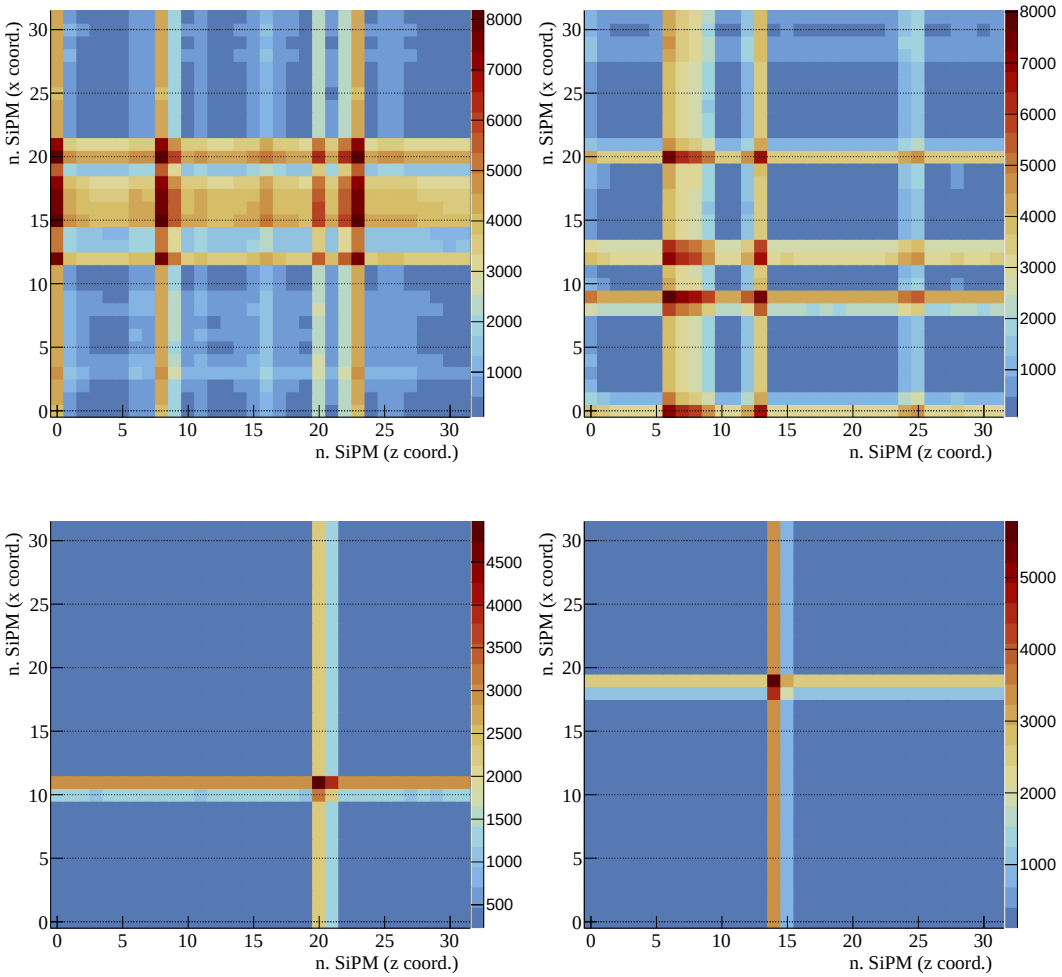

Figure 3.24.: Top: *Muon-bundles* event creating more hits per panel and rejected from the analysis.
Bottom: *Muon-like* event selected by requiring the presence of only one hit per CRT pair, in the two detector sides.

The complete list of cuts ensuring the optimized *muon-like* event selection is the following:

1. CRT reconstruction (only one fired hit per panel)

2. rejection of events saturating the ADC dynamic range

3. tracks inside the Active Volume (AV)

4. rejection of random or fake CRT coincidences (events triggered by the CRT panel without generating visible light detected by the PMTs)
5. ToF∈[-40, 40]ns
6. S1-amplitude > 10 P.E.
7. non linear PMT response (*comet*-cut)
8. additional requirements on the track position inside the demonstrator as FC volume or FV (facultative and dependent on the analyses specifications)

A way to evaluate the goodness of the track selection is to consider the f_{90} distribution, because of the sensitivity of this observable to the nature of the particle producing the scintillation light, as explained in Sec. 2.2.2.4. The f_{90} factor is calculated using the following definition:

$$f_{90} = \frac{\sum_{t_0}^{t_*} Light(t)}{\sum_{t_0}^{t_F} Light(t)}; \tag{3.3}$$

being t_0 = (T_{S1} - 40) ns, t_* = (T_{S1} + 90) ns, t_F = (T_{S1} + 3500) ns and T_{S1} is the time of the S1-peak. Given the low CRT trigger rate, with the goal to maximize the statistics, all the data triggered by the CRT external trigger in the *shifted* geometry, in absence of the fields, are included; in total, 14 runs are used, corresponding to 13875 selected events, out of 44374 matched events. The correlation between the f_{90} factor with the measured ToF is considered. As reported in Sec. 3.3.1, the ToF distribution is expected to be symmetric and centered around |ToF|= 22 ns, although for most of the events a positive ToF is observed because of the CRT geometry. Following the order of the CRT selection cuts presented above, the evolution of 2-D f_{90} -vs-ToF distribution at each additional cut applied is shown in Fig. 3.25; the cut reported in the legend is the latest cut applied at each step. In the first plot on the top-left, only the events matched in the two systems are included. In this case, the f_{90} factor has a peak around 0.27 ± 0.17, with long tails ending with two peaks at 0 and ∼0.5; in the ToF distribution, instead, is not possible to distinguish the two peaks because of the high number of events with a null ToF, corresponding to random coincidences generated by showers or *muon-bundles*. The requirement of rejecting all the events that fired more than one hit per CRT panel drastically suppresses the excess around ToF = 0 ns; however, the f_{90} distribution still shows the

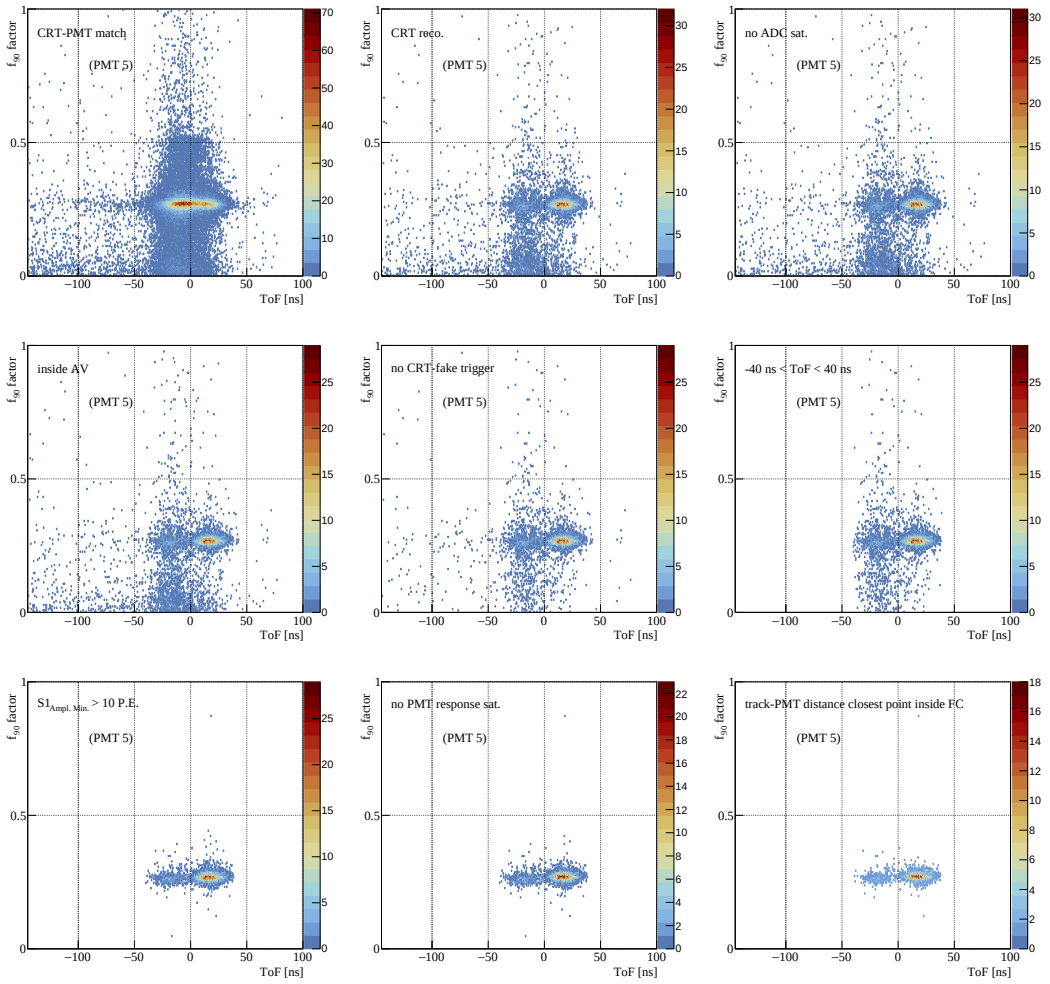

Figure 3.25.: Correlation of the f_{90} distribution with the ToF observed at each additional cut applied in the CRT selection. Starting from the **top-left** plot, the distribution obtained by including all the events with matched information between CRT and PMT system is reported; only one cut per plot is added moving toward the **bottom-right** plot, where the distribution for the final *muon-like* selection is reported. In the legend, only the last cut applied at each step is advised.

peak around 0. As shown in the bottom-left plots, only the requirement of rejecting events with the S1-amplitude lower than 10 P.E. is crucial to clean efficiently the f_{90} distribution; the percentage of the events constituting the low-energetic background events is of about ∼4.% of the events in the expected ToF window [-40; 40] ns. Finally, it is interesting to point out that, among all the events crossing the LAr AV, ∼5.7% of the events are still fake CRT trigger or random coincidence.

A better explanation of the most effective cuts for the f_{90} distribution is given in Fig. 3.26; as before, the cut reported in the legend correspond to the last cut ap-

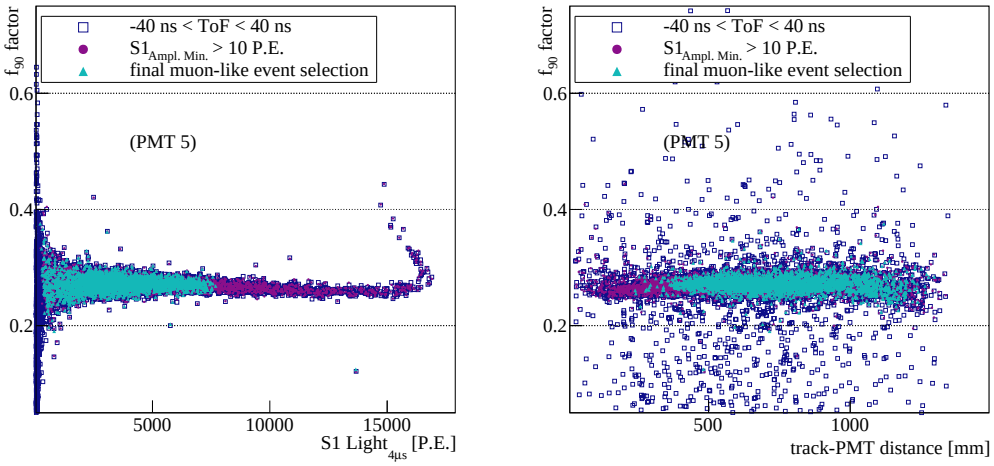

Figure 3.26.: Correlation of the f_{90} distribution with the total integrated S1 light (**left**) and with the minimum approach distance (**right**) at different levels of the *muon-like* event selection, obtained with the CRT system, by considering: all the *muon-like* event inside the LAr AV (**dark blue**), removing very low energetic events (**magenta**), and selecting *muon-like* events inside the FC (final CRTselection, **cyan**).

plied in the selection. The f_{90} factor is shown as a function of the total integrated light, on the right, and the minimum approach distance between the track and the PMT surface, on the left. Two essential features are pointed out: the presence of an intrinsic background constituted by very low-energetic events (dark blue points), and muons saturating the PMT response (magenta points); both kinds of events are rejected from the final selection. The identification of low-energetic events as an intrinsic background is motivated by their uncorrelation with the f_{90} factor - plot on the left - and their reconstructed position inside the detector - plot on the right. The evidence supporting the hypothesis that the events saturating the PMT response are muons crossing the detector too close the PMTs is shown in the plots in Fig. 3.27. In such plots, the detected light (S1 signal integrated into 1 μs) is shown as a function of the minimum approach distance; in magenta, the events saturating the PMT response are included, whereas, in cyan, only the *muon-like* events inside the FC volume are shown. As pointed out from the comparison of the two distributions, the events crossing the LAr AV less than 300 mm far away from the PMT

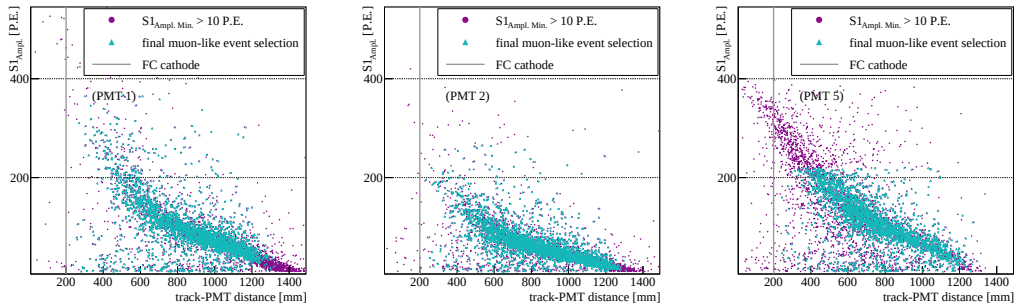

Figure 3.27.: Distribution of the S1-amplitude as a function of the minimum approach distance shown at different levels of the *muon-like* event selection, obtained with the CRT system, by considering: all the *muon-like* event with a minimum S1-amplitude>10 P.E. (**magenta**) but including events saturating the PMT response, and rejecting the seconds (**cyan**). Events saturating the PMT response are *muon-like* tracks crossing close to the PMT surface.

surface (as a comparison, the cathode-PMT surface distance is 200 mm; whereas, the maximum distance of events inside the FC is around ∼1300 mm) are those lying in the *comet*-regime. This characteristic is more evident in PMT-5 because of the CRT shifted track topology and because the gain is slightly higher than in the other PMTs. The feature confirms the hardware origin of the *comet*-effect distorting the PMT waveforms because of the PMT linearity loss.

3.8.1 Topology of muon-like selected events

When the *muon-like* event selection is applied, the topology of the CRT tracks is represented by the distributions of all the geometrical variables defined from the CRT coordinates.

Due to the width of the CRT strips (∼112.5 mm), the uncertainties affecting the CRT reconstruction are evaluated *a-posteriori* and added at analysis level when needed by each study. The definitions showed in Sec. 3.3.1 are based on the CRT coordinates evaluated in the center of each strip ($\overline{x}_{\text{wall/door}}$); in order to quantify the impact of the strip precision, the definition of each variable is obtained considering the CRT coordinates evaluated in the two extreme edges ($\overline{x}_{\text{up/down}} = \overline{x} \pm 112.5$ mm); the typical impact implies a shift quantified as a 6.5% systematic uncertainty.

In Fig. 3.28, the angular distributions (in terms of the tanθ and tanϕ), the typical

track length in the three defined volumes (L_{AV} in the AV, L_{FC} in the FC volume, and L_{FV} in the FV), and the minimum approach track-to-PMT distance for the five PMTs, d_i are shown. The tanθ distribution reflects the typical *shifted*-selection of

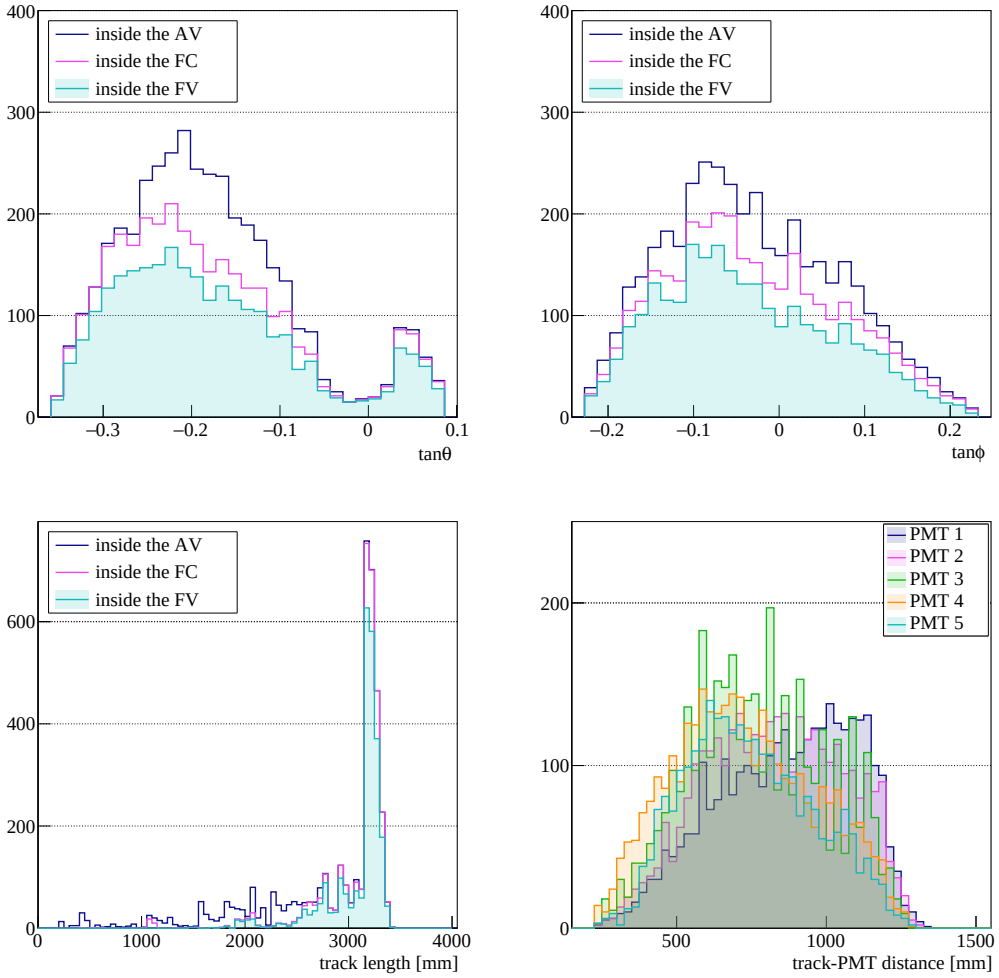

Figure 3.28.: Distributions showing the track topology identified as a consequence of the CRT selection, corresponding to *muon-like* events crossing the FC volume. **Top:** Angular distributions in terms of the θ (**left**) and ϕ (**right**) angles. **Bottom-left:** Distribution of the track length in the three fiducial volumes defined in Sec. 3.3.1. **Bottom-right:** Distribution of the minimum approach distance between the *muon-like* event's track and the photo-cathode surface, for each PMT.

the CRT panels with most of the tracks with a negative tan$\theta \sim$ -0.2, corresponding to a typical track inclination of $\sim$ -11^o; the tanϕ distribution points out the expected

asymmetry induced by the Jura's mountains mentioned in Sec. 3.3.1 that makes the distribution not flat. From the comparison of the track length distributions arises that the minimum length of the track to be completely inside the FC volume is 3150 mm. Finally, in Tab. 3.11, the mean minimum approach distances of the tracks to each PMT are reported; given the geometry of the CRT panels, the distance increases from PMT-1 to PMT-3, the shorter distance measured in PMT-5 than in PMT-4 is caused by the rejection of events saturating the PMT response passing too close to PMT-5.

	(PMT-1)	**(PMT-2)**	**(PMT-3)**	**(PMT-4)**	**(PMT-5)**
$\mathbf{d}_{i,comet}$ **[mm]**	924 ± 61	840 ± 55	779 ± 51	707 ± 46	651 ± 42
$\mathbf{d}_{i,AV}$ **[mm]**	930 ± 61	843 ± 55	782 ± 51	710 ± 46	712 ± 46
$\mathbf{d}_{i,FC}$ **[mm]**	865 ± 56	823 ± 54	772 ± 50	726 ± 47	744 ± 48

Table 3.11.: Mean of the minimum approach distance measured from every PMT including or rejecting the events saturating the PMT response, in the active volume.

3.9 Performance of the photon detection system

Based on the *muon-like* event selection described in Sec. 3.8, the characterization of the basic features of the primary scintillation light produced by the muons crossing the demonstrator, in order to define basic guidelines for the MC simulation, is presented. The main outcomes allowed identifying specific features regarding the impact of the WLS and HV base designs; moreover, the comparison between the configurations helped in identifying the preferred PMT unit design for bigger detectors (e.g. ProtoDUNE-DP and DUNE FD module).

3.9.1 Basic features of the prompt scintillation light signal

As a first step, the correlation of the primary scintillation light detected by pairs of PMTs is considered in order to evaluate the overall photon detection performance and have an indirect cross-check of the matching between CRT and PMT DAQ systems. The study is obtained from the analysis of a single long run (∼64 hours) collected during the commissioning phase, at null drift field triggered by the CRT

system. For this specific analysis, in addition to the complete CRT selection, only long tracks completely crossing the AV ($L_{AV} > 3150$ mm) are included in order to minimize effects induced by short localized tracks. The integrated S1 charge,

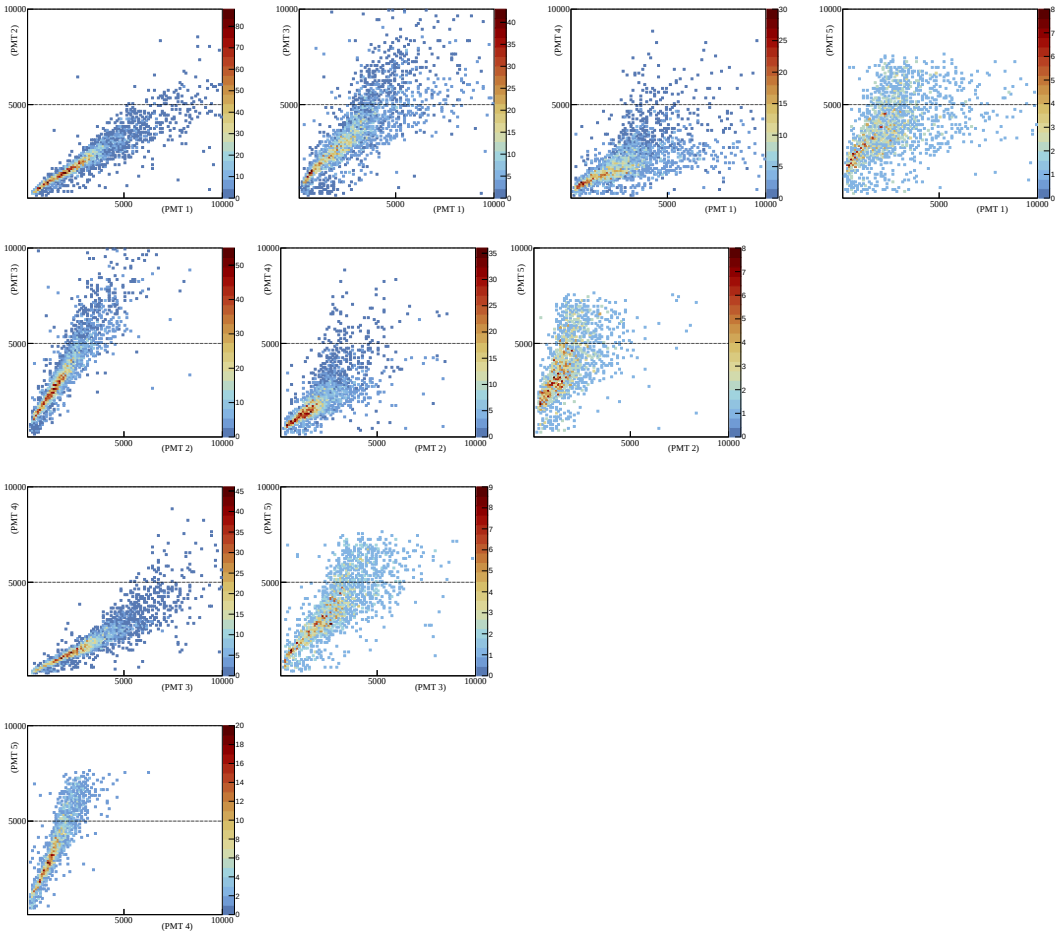

Figure 3.29.: Correlation of the integrated S1 charge over 4 μs collected by each PMT with respect to each of the others PMTs, after applying the complete CRT cut sequence.

over 4 μs, collected by a single PMT is reported in correlation with the integrated S1 charge detected in each of the other PMTs for the same event; in Fig. 3.29, all the combinations of pairs are shown. Every PMT pair distribution shows a strong correlation between the integrated S1 charge in the two PMTs, confirming the goodness of the event selection and of the matching between the CRT trigger and light detection system. The slope of the distributions changes depending on the considered pair due to the detection efficiency reduction induced by the WLS

configuration that will be commented in the next section.

Secondly, the detector response to the total scintillation light produced by the muons crossing the demonstrator AV (independently from the individual direction and length of the track) is studied in terms of the scintillation light spectrum. Several factors affect the mean of the detected scintillation light by each PMT, and they can be synthesized as follows:

- the total geometrical acceptance influenced by the position of the PMTs inside the detector (the PMTs closer to the FC walls can be more sensitive to the light absorption or reflection in the demonstrator components)
- the direction of the tracks due to the position of the CRT panels
- the presence of the PMMA plate that limits the individual geometrical acceptance of the corresponding PMTs
- secondary effects due to the pulse shape induced by the base configuration designs

Because of that, the goal of the analyses that are going to be discussed in this section intends to disentangling and evaluating the impact of the aforementioned factors; for both of them, all the 14 runs collected in absence of drift field and triggered by the CRT external system are used. First of all, the impact of the PMMA plate will be studied; hence, the influence of the base design on the collected charge will be discussed. The outcome of the first analysis has been validated by comparing the behavior observed in the data with the one simulated in the Monte Carlo; the discussion is presented in Chapter 5.

3.9.2 Reduction in the geometrical acceptance due to the PMMA plate

In order to minimize the impact of the base configuration in the PMT waveform, the evaluation of the geometrical acceptance reduction caused by the WLS design is estimated considering the S1 amplitude distribution for each PMT. The mean value of the S1-amplitude is obtained fitting the distribution by a Landau function and considering the most probable value (MPV); as shown in the plots reported on the

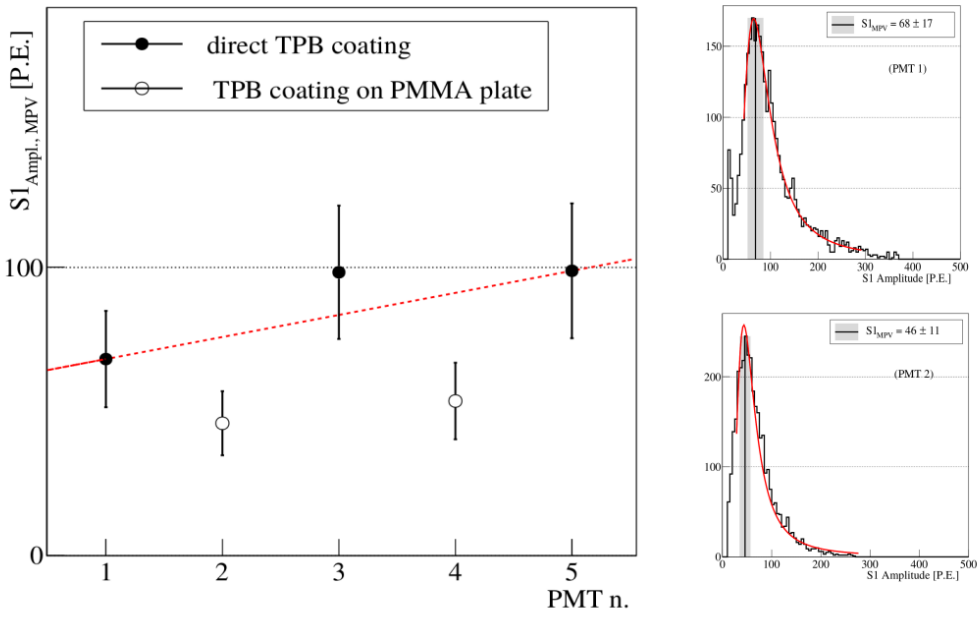

Figure 3.30.: Left: MPV of the S1-amplitude distribution produced by muon-like events crossing the demonstrator FC and triggered by the CRT system, expressed as a function of the PMT numbering; the error reported in the y-axis for each PMT is given by the σ of the Landau-distribution.
Right: Example of S1-amplitude distribution of one PMT with direct TPB coating (**top**) and TPB coated on the PMMA plate (**bottom**).

right of Fig. 3.30, for PMT-1 and PMT-2. Consequently, the MPV is shown for each PMT on the left of Fig. 3.30; the error assigned to each point corresponds to the σ of the Landau-distribution. The characteristic dependence of the S1-amplitude MPV with the PMT is determined by the track geometry selected by the CRT panel position and the PMT distance from the FC walls. The PMT-3 has the highest value of the S1 amplitude because of its central position inside the detector. The S1-amplitude measured in PMT-5 is higher than in PMT-1 because of the typical CRT track diagonality. Finally, a clear decrease is observed in the MPV of the S1-amplitude in PMT-2 and PMT-4, due to the reduced geometrical acceptance induced by the TPB coating on the PMMA plates. The red line in the left-plot gives an estimation of the expected S1-amplitude that the PMTs under the plate would have detected if they had the same WLS configuration as the others, considering their position inside the detector. A lower limit of the detection efficiency reduction

induced by the PMMA plate is evaluated by quantifying the variation of the measured S1-amplitude MPV in PMT-2 and PMT-4 from the expected one given by the red line. In Tab. 3.12, the MPV of the S1 amplitude distribution and the spread

PMT n. **WLS config.**	**1 (NB)** **direct**	**2 (NB)** **plate**	**3 (PB)** **direct**	**4 (PB)** **plate**	**5 (NB)** **direct**
S1$_{\text{Ampl.}}$ **[P. E.]**	68±17	46±11	98±23	53±13	99±23
variation [%]	—	-40	+18	-40	—

Table 3.12.: Most probable value of the measured for the S1-amplitude distribution and corresponding variation induced by the presence of the PMMA plate.

of each distribution are reported for the five PMTs; moreover, the variation with respect to the expected S1-amplitude, in both NB and PB PMTs with the TPB coating on the PMMA plate is given. Independently from the base configuration, a reduction of at least ∼40% is observed. It is important to remind that, as explained in Sec. 3.2.1, the reduction induced by the PMMA plate can be enhanced due to the light absorption and reflection inside the PMMA plate material itself; however, the disentangling of the two contributions is not possible from this study.

3.9.3 Impact of the HV divider configuration on the collected charge

An analogous behavior as the one described in the previous analysis is expected by considering the integrated S1 charge. If the effect of the base configurations on the waveform is negligible, the results should be independent of the integration range considered for the S1-charge. However, as arises from the comparison between the NB and PB waveforms shown in Fig. 3.31, two distortions (referred to as reflections, in the rest of the text) are visible in the PB PMTs. The first reflection is caused by the capacitance used in the divider circuit and the second is due to an impedance mismatch in the cryostat feed-through; in particular, the capacitance in the two PB is not the same (200 nF in PMT-3 and 300 nF in PMT-4) such that the shape of the second reflection is different in the two PMTs.

The impact of the reflections in the integrated S1-charge is then evaluated by

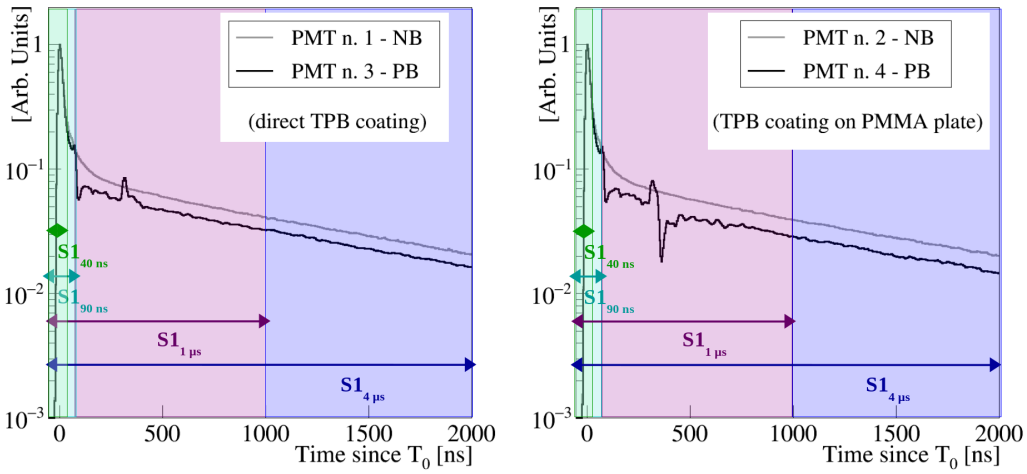

Figure 3.31.: Average waveforms of the NB (in grey) and PB (in black) PMTs, in the two WLS configurations. In both cases, the colored rectangles correspond to the integration ranges: 40 ns (**green**), 90 ns (**cyan**), 1 μs (**magenta**), and 4 μs (**dark blue**). **Left:** PMTs with TPB direct coating. **Right:** PMTs with the TPB coating on the PMMA plate.

considering the variation of the MPV of the S1-charge distribution as a function of the PMT numbering when different integration ranges are examined. In particular, the distribution of the scintillation light is analyzed by integrating event-by-event the PMT waveform in four different ranges corresponding to the colored rectangles shown in Fig. 3.31. To normalize for the gain of each PMT, the integrated S1 charge is expressed in number of photon-electrons (P.E.), using Eq. (3.2a). Following the same approach described in the previous section, the mean value of the scintillation light and the corresponding error in each PMT is obtained fitting the distribution by a Landau function and considering the MPV and the σ of the distribution, as reported on the right of Fig. 3.32, integrating the S1-charge over 4 μs, for PMT-1 and PMT-2. The correlation with the PMT position inside the detector is considered for the four integration ranges; on the left of Fig. 3.32, an example is reported by integrating the S1-charge over 4 μs; the full dots represent the MPV measured by the PMTs with the TPB coating directly applied on the PMT surface, whereas the S1-charge detected by the PMTs with the TPB coated on the PMMA plate are represented by the empty dots. Finally, the variation of the MPV of the S1-charge from the estimated value is evaluated, in PMT-2, PMT-3, and PMT-4, by

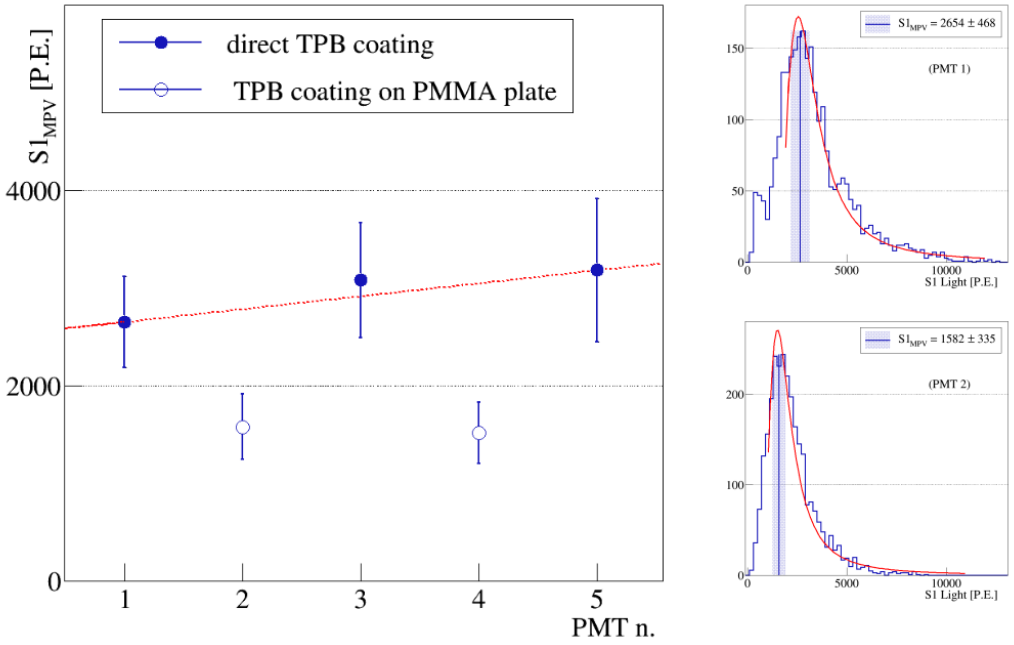

Figure 3.32.: **Left:** MPV of the integrated S1 charge distribution produced by muon-like events crossing the demonstrator FC triggered by the CRT system as a function of the PMT numbering; the error reported in the y-axis for each PMT is given by the σ of the Landau-distribution.
Right: Example of S1-charge distribution, integrating over the whole 4 μs time window, of one PMT with direct TPB coating (**top**) and TPB coated on the PMMA plate (**bottom**).

the red line reported in the same plot. The same study is done for all the considered integration ranges; the results are summarised in Tab. 3.13. Independently from the WLS configuration, both PB PMTs show a dependence on the variation of the integrated S1-charge from the expected light with the integration range; however, the dependence with the integration range is slightly different in the two PB PMTs due to the difference in the shape of the second reflection. The impact of the base configuration in the PB PMTs introduces a bias in the charge calculation that is important to keep in mind, especially in the comparison of the data with the simulations, as will be discussed in Chapter 5.

PMT n. **WLS config.**	**1 (NB)** **direct**	**2 (NB)** **plate**	**3 (PB)** **direct**	**4 (PB)** **plate**	**5 (NB)** **direct**
S1$_{4\mu s}$ [P. E.]	2654±468	1582±335	3085±557	1509±334	3183±735
variation [%]	—	-43	6	-51	—
S1$_{1\mu s}$ [P. E.]	1584±342	941±248	1893±405	1036±205	1894±351
variation [%]	—	-43	10	-43	—
S1$_{90ns}$ [P. E.]	614±150	377±106	809±191	485±102	756±175
variation [%]	—	-42	18	-33	—
S1$_{40ns}$ [P. E.]	478±113	294±81	738±143	375±85	639±112
variation [%]	—	-43	32	-37	—

Table 3.13.: Most probable value of the S1 integrated charge distribution obtained from a Landau fit; the error reported in each PMT is given by the σ of the Landau-distribution. For the two PMTs with the TPB coating on the PMMA plate, the variation from the expected value is reported; as a comparison, to take into account the difference introduced by the base design in the PB PMTs, the variation observed in PMT-3 is also reported.

3.9.4 t_0 time

Finally, the distribution of the t_0 time (the time position of the S1 signal) measured by the five PMTs is considered; the spread of this distribution gives information on

PMT n.	**1 (NB)**	**2 (NB)**	**3 (PB)**	**4 (PB)**	**5 (NB)**
t_0 time [ns]	(633 ± 9)	(633 ± 9)	(697 ± 9)	(697 ± 8)	(642 ± 8)

Table 3.14.: Mean and RMS of the t_0 time distributions observed for the five PMTs; the typical RMS is of the order of 8 ns.

the *jitter* time[11] of the PMT and on possible delays due to the propagation inside the demonstrator. In Fig. 3.9.4, the distributions of the five PMTs are shown, the shift in the mean of the NB and PB distributions are due to the delay introduced by the different cable length installed. Each distribution can be fitted by a gaussian function to evaluate their mean and the RMS; the values obtained for

[11]From the measurement reported by the manufacturer, the typical jitter time is of about ∼3 ns.

the five PMTs are reported in Tab. 3.14. In the distribution of the five PMTs, the RMS of the distribution is of ∼8 ns; this value takes into account both the PMT jitter time, possible delay induced by the light reflection on the FC walls and the digitization sampling of the acquisition system.

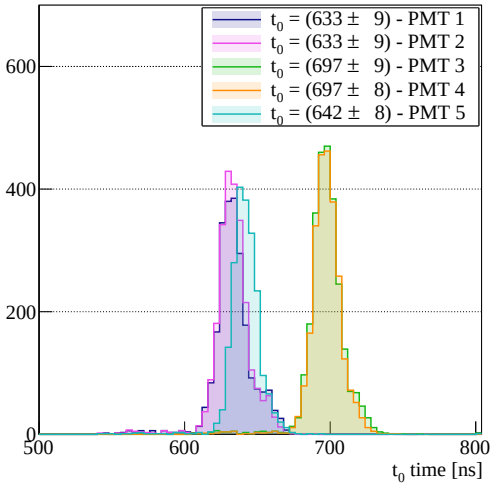

Figure 3.33.: Distributions of the t_0 time at which the *muon-like* events produce the scintillation light signal detected by the PMTs.

3.9.5 Validation of the photon detection system design for future detectors

The comparison of the light detection system performance based on the different options tested in the WA105 DP demonstrator leads reaching two important conclusions in terms of the impact of the WLS and base configurations.

The first result is related to the WLS design. The presence of the PMMA plate used as a support for the TPB coating facilitates the TPB deposition and its installation inside the detector. Despite that, a strong reduction in the geometrical acceptance is observed and it determines ∼40% suppression of the detected light in comparison with the alternative WLS design. The main reason for that are the geometrical acceptance of the PMMA plate and the light absorption or reflection in the plate itself. On the contrary, in the case of the direct TPB coating, all the top part of the PMT glass is covered by the TPB. This allows even the more diagonal VUV photons to be converted into visible light, that are not detected otherwise. The direct evaporation of the TPB is the preferred option for the ProtoDUNE-DP light detection system design.

On the other hand, important inputs are obtained about the impact of the PMT base design; although, several factors must be balanced to choose the best design. Three features have been considered:

- the pedestal stability
- the linearity of the PMT response
- the costs of the base design and cabling

Both base configurations demonstrated to be very stable in terms of the baseline noise for all the typologies of events detected; however, the PB PMTs demonstrated to have better linearity than the NB PMTs. Even if the NB PMTs have a very definite signal, the origin of the two reflections present in the PB PMTs has been identified to be hardware in such a way that a good choice of of the decoupling splitter design and feedthrough connectors can avoid the alterations of the signal shape. Moreover, the number of cables would be halved in the case of the PB PMTs, decreasing drastically the costs of the light detection system, especially in big detectors. For all these reasons, the positive base configuration is favored in the design of the ProtoDUNE-DP light detection system[12]. Despite that, the presence of two reflections in the PB signal limits their utilization in most of the physics studies carried out in the WA105 DP demonstrator as will be discussed in the following chapters.

[12] Additional studies have been performed in order to provide a complete characterization of the photon detection system for ProtoDUNE-DP and they are summarised in Ref. [91].

"Ti insegneranno a non splendere,
e tu splendi invece."
P. P. Pasolini

CHAPTER 4

THE SCINTILLATION LIGHT PRODUCTION IN THE LIQUID PHASE

In this chapter, the complete characterization of the primary scintillation light (S1) produced in the liquid phase of the WA105 DP demonstrator will be presented. Preliminary results have been reported in Ref. [210] and Ref. [211]; however, in this chapter, a consistent improvement in the analysis's strategy and better interpretation of the main findings are achieved.

In Sec. 4.1, the modelization of the primary scintillation time profile to retrieve the specific decay times and the relative probability amplitudes will be described. Dedicated studies to optimize the fit procedure (Sec. 4.1.1) and to assign the proper systematic uncertainties (Sec. 4.1.2) will be discussed.

The characteristic scintillation light emission in LAr has been initially studied in absence of drift field (Sec. 4.2). In these conditions, the monitoring of the τ_{slow} decay time allowed to investigate the purification system performance in the demonstrator (Sec. 4.2.1). Thanks to the good and stable LAr purity conditions, all the data taken in the same drift field conditions can be analyzed together. The effect of the drift field on the total scintillation light and on the scintillation time profile will be explained in Sec. 4.3. From these analyses, pioneering results have been found related to LAr micro-physics and their analysis will be addressed in the last section Sec. 4.4; preliminary conclusions, possible interpretations, and the interest for future measurements in the next DP LAr-TPC will be discussed.

4.1 Study of the scintillation time profile

As explained in Sec. 2.2.2, the primary scintillation light is produced by the Ar_2^* de-excitation from the singlet or the triplet states to the ground energy state. The relative fraction of light produced by these two mechanisms as well as the characteristic de-excitation decay times can be extracted by the study of the scintillation time profile through the measurement of the parameters that define its shape. The goal of the study presented in this section is dedicated to identifying a common approach to provide the scintillation time profile parameters for all the runs collected during the data taking in the same drift field conditions, for both trigger and data acquisition configurations. Among all the runs collected, only runs with more than 100 events are included; in addition to them, also few runs, with at least 10 events, have been include after the individual check of the results. In total, more than 100 runs have been analyzed, ∼45% of them have been collected in absence of the drift field. Depending on the trigger conditions, the corresponding selections have been applied. In runs triggered by the CRTs, only muon-like events are included; in the case of the data triggered by the PMT self-trigger, only events saturating either the ADC dynamic range or the PMT response are rejected. Based on the explanation given in Sec. 3.7.2, the rejection of events that saturated the PMT response (in the *comet*-regime) is crucial to avoid including events with a scintillation time profile artificially distorted. For each run, an average waveform is defined after subtracting the pedestal noise and normalizing the waveform to the S1-amplitude event-by-event. Due to the time spread of the S1 peak shown in Fig. 3.9.4, each waveform is centered in 0. In Fig. 4.1, an example of all the waveforms generated by *muon-like* events collected in the same run ($\mathcal{E}_{\text{drift}}$= 0 kV/cm - CRT trigger) by an NB PMT are shown.

Averaging the waveform every 4 ns, the scintillation time profile is obtained; the error assigned in each bin is the standard deviation from the mean value. Examples of the time profiles obtained for both the PB and the NB PMTs are shown in the top of Fig. 4.2. In order to reproduce the average time profile collected by each PMT and to retrieve the parameters characterizing the scintillation time profile, a fit is performed based on the phenomenological modelization reported in Eq. (2.9a). However, a third exponential is needed to accurately represent the data. The two-exponential function is represented for comparison in the top-left plot of Fig. 4.2. In

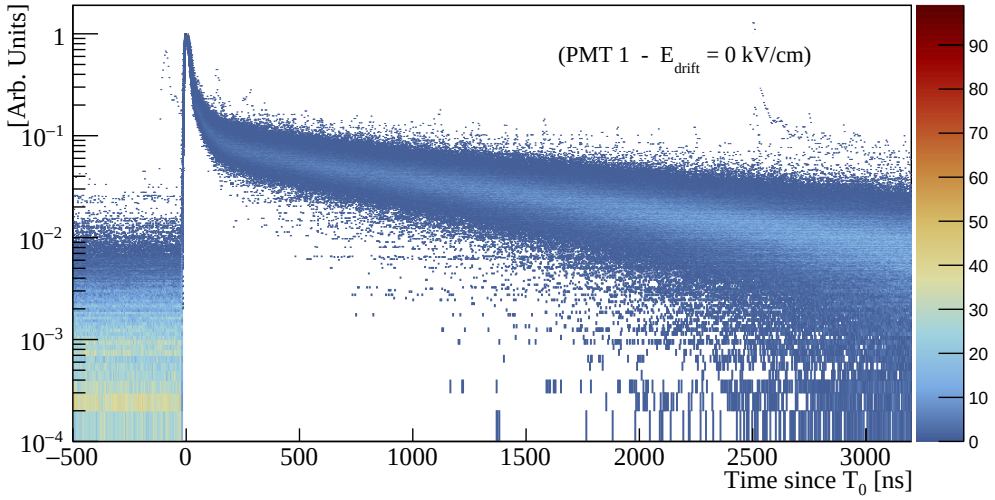

Figure 4.1.: Example of all the waveforms collected by an NB PMT, in a single run with $\mathcal{E}_{\text{drift}}$= 0 kV/cm and triggered by the external CRT system.

the same figure, the bottom-plot shows the improvement in the agreement of the fit function with the data when the *intermediate* component is included. Furthermore, the detector response needs to be modelled as well; hence, the fit function is the convolution of a Gaussian function with three exponential functions as described by the following equations:

$$F(t) = P + G(t - t_0, \sigma) \otimes \sum_{j=f,i,s} (A_j/\tau_j) \times \exp(-(t - t_0)/\tau_j) \tag{4.1a}$$

$$F(t) = P + \sum_{j=f,i,s} \frac{A_j}{2\tau_j} \times \exp\Big(\frac{\sigma^2}{2\tau_j^2} - \frac{t - t_0}{\tau_j}\Big) \times \Big[1 - \text{Erf}\Big(\frac{\sigma^2 - \tau_j(t - t_0)}{\sqrt{2}\sigma\tau_j}\Big)\Big] \tag{4.1b}$$

The j-index is referred to the *fast*, the *intermediate*, and the *slow* components respectively; t_0 and σ are the Gaussian mean and width, corresponding to the PMT transit time and the PMT transit time spread respectively. From the convolution performed analytically given in Eq. (4.1b), the normalization constants, A_j, can be found; they correspond to the contribution of each one of the three component to the total scintillation light; finally, P is the pedestal noise. Each of all the runs available is adjusted with Eq. (4.1b) by performing a likelihood fit; only when this fit fails, a χ^2-fit is done and a systematic error[1] is added in quadrature with the error provided

[1] See Sec. 4.1.2 for the description of this systematic uncertainty.

by the fit. Both fit procedures are based on the TMinuit package implemented in ROOT [212]. In both cases, the pedestal is kept fixed at 0 in the fit procedure. Because of having data collected in both time acquisition windows (4 μs and 1 ms), the fit is always performed up to 3.5 μs after the T_0 time; this fit range corresponds to considering ∼95% of the scintillation time profile. In the case of runs collected

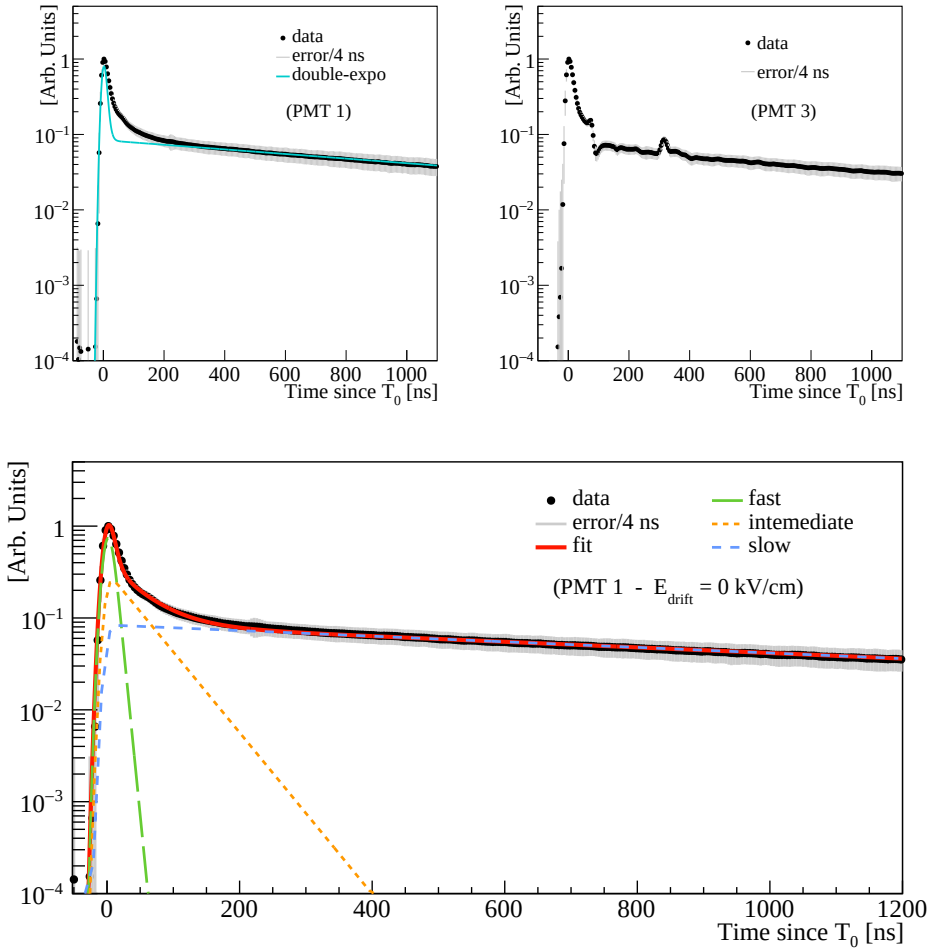

Figure 4.2.: Top-left: Example of the average waveform for an NB PMT; in cyan, a two-exponential function is shown as a comparison demonstrating the necessity of adding a third component to reproduce the data. - **Top-right:** Example of the average waveform for an PB PMT; the two reflections induced by the splitter capacitor are visible around 100 ns and 350 ns.

Bottom: NB average waveform (**black points**) and corresponding fit function described by Eq. (4.1b) drawn in red; the *fast*, the *intermediate*, and the *slow* contributions are shown in **green**, **orange**, and **azure**, respectively.

with the amplification field, the S2 contamination in the S1 profile is excluded by rejecting all the events whose S2-starting time is found before 10 μs; in the case the S2 reconstruction is not available and the amplification field is lower than 20 kV/cm, the scintillation time profile is fitted up to 2.5 μs and a systematic error[2] due to shorter fit range is added in quadrature with the fit error. Finally, since the 4 ns digitization sampling limits the fit sensitivity to the τ_{fast} and the σ measurements, the τ_{fast} parameter is kept fixed at 6 ns in accordance with the value measured in Ref. [145]. Both the validation of the fit procedure and the assignment of systematic uncertainties will be motivated and described in Sec. 4.1.1 and Sec. 4.1.2, respectively. In the bottom-plot of Fig. 4.2, an example of the fit function and the *fast*, the *intermediate*, and the *slow* contributions are reported. As arises comparing the two average waveforms in the top-right and the bottom of Fig. 4.2, the reflections present in the PB PMTs do not allow to obtain a fit with reliable results for all the parameters. The first reflection with the same shape in both PB PMTs tends to bias the *intermediate* decay time measurement and the A_i normalization constants being they related to the integral underneath the corresponding regions. Whereas, the value obtained for the τ_{slow} can be biased by the second reflection, although in a different way, as the reflections have a different shape in the two PB PMTs. For all of these reasons, the PB PMTs will not be included in the studies related to the time profile; however, the trend of the τ_{slow} can still be considered for the monitoring of the LAr purity, as will be presented in Sec. 4.2.1.

The robustness of the fit procedure, the impact of the 4 ns digitization sampling, and the effect of fixing τ_{fast} have been evaluated through the development of a toy-MC. The results obtained are presented in the next section.

4.1.1 Test of the fit procedure through a toy MC

The analyses presented in this section are motivated by the necessity of verifying the ability of the fit to retrieve an unbiased measurement of the waveform parameters and to provide a correct estimation of their uncertainties, given the digitization sampling of the PMT waveform and the correlation between the parameters. The accomplishment of all these requirements have been verified through the development of a toy-MC that reproduces the scintillation light profile observed in the data

[2] See Sec. 4.1.2 for the description of this systematic uncertainty.

for given sets of the inputs of the parameters.

The fit function, given in Eq. (4.1b), needs nine strongly correlated parameters to properly describe the scintillation time profile. The correlation matrix of the parameters, given in Fig. 4.1.1, is obtained from the data (long CRT run, ∼50000 triggered events, collected in absence of drift field and in the *CRT-shifted* geometry) by performing a likelihood fit; for this specific case, τ_{fast} is left free to be fitted. The color scale represents the intensity of the correlation. Because of the average waveform construction, the pedestal parameter is kept fixed at zero and it is not included in the matrix. As shown in the figure, most of the parameters are very correlated such that a biased measurement of one of them can effect the measurement of the others. As a consequence, the fit procedure becomes very delicate and difficult to be controlled when automatized over a big number of runs. The necessity of performing such a big number of fits, one per run and per PMT, requires a stable procedure that must not need individual preliminary tuning of the parameters. The 4 ns digitization sampling can be a limitation in the fit sensitivity to some parameters as the very narrow PMT transit time spread (∼3 ns, as defined by the manufacturer) and the very short *fast* decay time. Furthermore, the bin error assigned to the average waveform is dependent on the run statistics (that goes from few hundreds to several tens of thousands of events) because the lower it is, the lower the weight of the RMS in each bin is.

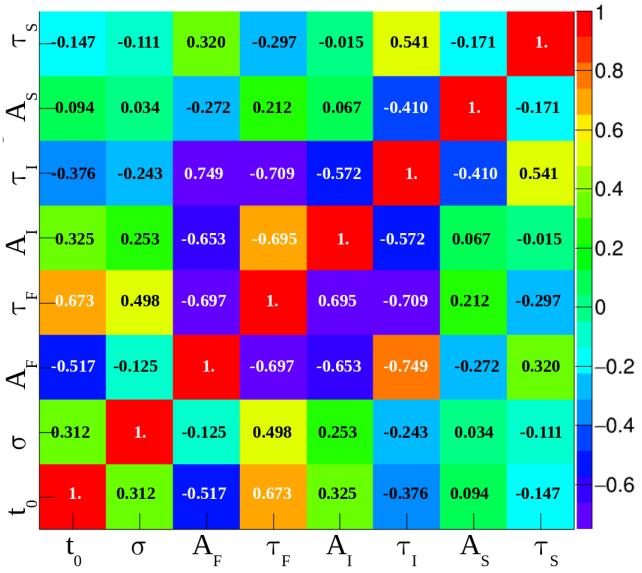

Figure 4.3.: Correlation matrix of the parameters needed in Eq. (4.1b) to reproduce the scintillation time profile. The color scale represents the intensity of the correlation.

For this purpose, a toy-MC has been developed in order to test the fit procedure

described in the previous section, using waveforms simulated with a known set of parameters. Hence, each waveform is a PDF generated from Eq. (4.1b) with a seed used as an input for each parameter, determining the waveform's shape. Consequently, it is fitted using the same function that wants to be generalized for the data analysis. Both a likelihood and a χ^2-fit have been performed; in Sec. 4.1.1.1 will be shown how only the likelihood fit ensures the retrieving of unbiased values. In order to assign a reasonable value for the seeds, a preliminary evaluation of the fit parameters has been obtained by a data-driven estimation. Two average waveforms obtained in two very long runs, in the two trigger configurations, have been fitted using Eq. (4.1b); independently from the trigger, the obtained parameters agree and they are chosen as inputs for the toy-MC seeds. In Tab. 4.1, the input parameters are listed. The error assigned to each bin is the statistical error ($1/\sqrt{N}$, being N

parameter	**input**
Pedestal	0 arb. units [fixed]
t_0	randomly generated in (0, 4) ns
σ	5 ns
A_{fast}	3.3 arb. units
τ_{fast}	6 ns [fixed]
A_{int}	3.3 arb. units
τ_{int}	50 ns
A_{slow}	24 arb. units
τ_{slow}	1400 ns

Table 4.1.: Seeds for the inputs of the scintillation time profile parameters used in the toy-MC waveform generation.

the number of entries per bin) that varies depending on the number of generated events in each waveform. As a first step, the τ_{fast} parameter is kept fixed; in the next section, the effect of fixing this parameter will be described. Because of the 4 ns digitization sampling, the t_0 time is randomly assigned with a value thrown in the (0, 4) ns range. The statistics of each waveform (number of generation) is chosen to be high enough to simulate events with a well defined S1 scintillation time profile; to be as general as possible, each waveform is generated in a time range that

includes the ending of the S1 signal, roughly 10 μs. However, for comparison with runs collected with low statistics, also less populated waveforms are simulated; the result will be commented in Sec. 4.1.1.1. To be consistent with the fitting of the data, the range fit is chosen to be up to 3.5 μs; the effect of varying this interval will be commented in Sec. 4.1.2. In Fig. 4.4, an example of the waveform generated by the toy-MC, using the inputs given in Tab. 4.1, is shown; in red, the fit function is reported and, in the legend, the measurement of each parameter retrieved by the likelihood-fit are given.

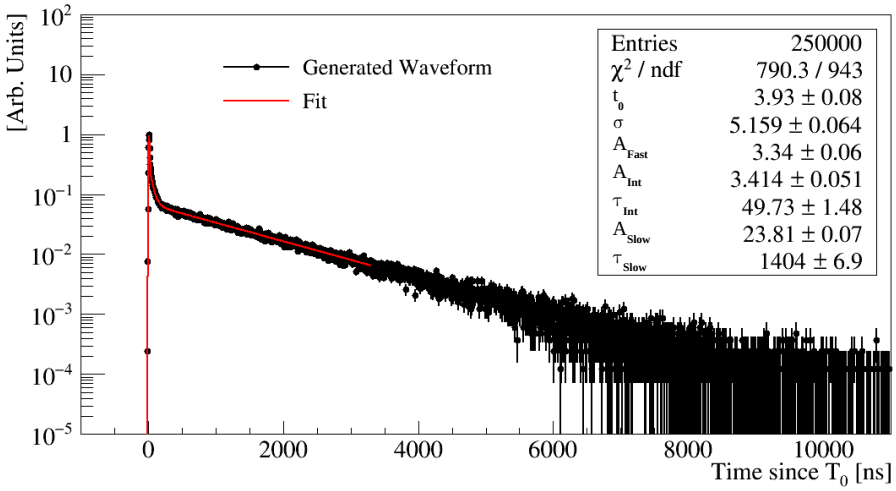

Figure 4.4.: Example of the toy-MC waveform generated from parameters' seeds reported in Tab. 4.1 and fitted through Eq. (4.1b) function - red line. The parameters retrieved by the fit function are shown in the legend.

Two important features can be studied through the toy-MC after fitting the generated waveforms:

- the presence of possible bias introduced in the measurement of the parameters obtained from the fit
- the goodness of the error assigned to each parameter given the initial error assigned in each bin due to the statistics of the waveforms

To do so, the fit is done over a big number of waveforms (number of iterations), so that, at each iteration, the fit results are stored. Calling μ_{exp} the input used for the

parameters, μ_{meas} the parameters retrieved by the fit, and $\sigma\mu_{meas}$ the error assigned to each parameter by the fit, a *pull-distribution* for each parameter is defined as follows:

$$\text{pull distribution} := \frac{\mu_{\text{meas}} - \mu_{\text{exp}}}{\sigma\mu_{\text{meas}}} \tag{4.2}$$

Given its tautological definition, the *pull-distribution* is expected to be a Gaussian function centered in zero and with a $\sigma = 1$. Any kind of shift from zero in the Gaussian mean is a hint of bias introduced by the fit procedure; whereas, $\sigma > 1$ ($\sigma < 1$) corresponds to an underestimation (overestimation) of the assigned error in the fit procedure. Furthermore, the statistics on which is built each *pull-distribution* must be high enough to reach realistic conclusions of the fit procedure. In this study, the pull distribution, obtained from the analysis of waveforms as the one reported in Fig. 4.4, with the seeds and conditions given in Tab. 4.1, and by performing 5000 iterations are shown in Fig. 4.5. Comparing all these distributions, some common features are observed:

- the mean of most of the distributions is centered around zero within less than 2σ; however, a clear bias is reported in the σ-parameter
- the σ of the *pull-distribution* is always slightly smaller than 1, corresponding to a conservative assignment of the error; this feature is more evident in the *pull-distribution* of the A_{slow} parameters.

The precision in the centering of the *pull-distribution* around zero is mostly determined by the number of iteration performed[3]. The absence of bias in the mean of the pull distribution validates the choice of the inputs used in the toy-MC driven by the data and proves the capability of the fit of retrieving them. The positive shift observed in the mean of the σ parameter corresponds to an overestimated measurement of the parameter in comparison with its input. This effect is induced by the 4 ns digitization sampling; as will be explained in the next section. The tendency to a conservative assignment of the error is characteristic of the likelihood-fit and not of the χ^2-fit. As will be explained in Sec. 4.1.1.1, both procedures have been tested; however, a bias is observed when the statistics is not high enough. Despite in the

[3] Preliminary studies have been performed varying the number of iterations, from 2000 up to 10000; however, in order to perform the complete analysis, 5000 iterations has been accepted as a good compromise between CPU consuming and reliability of the results.

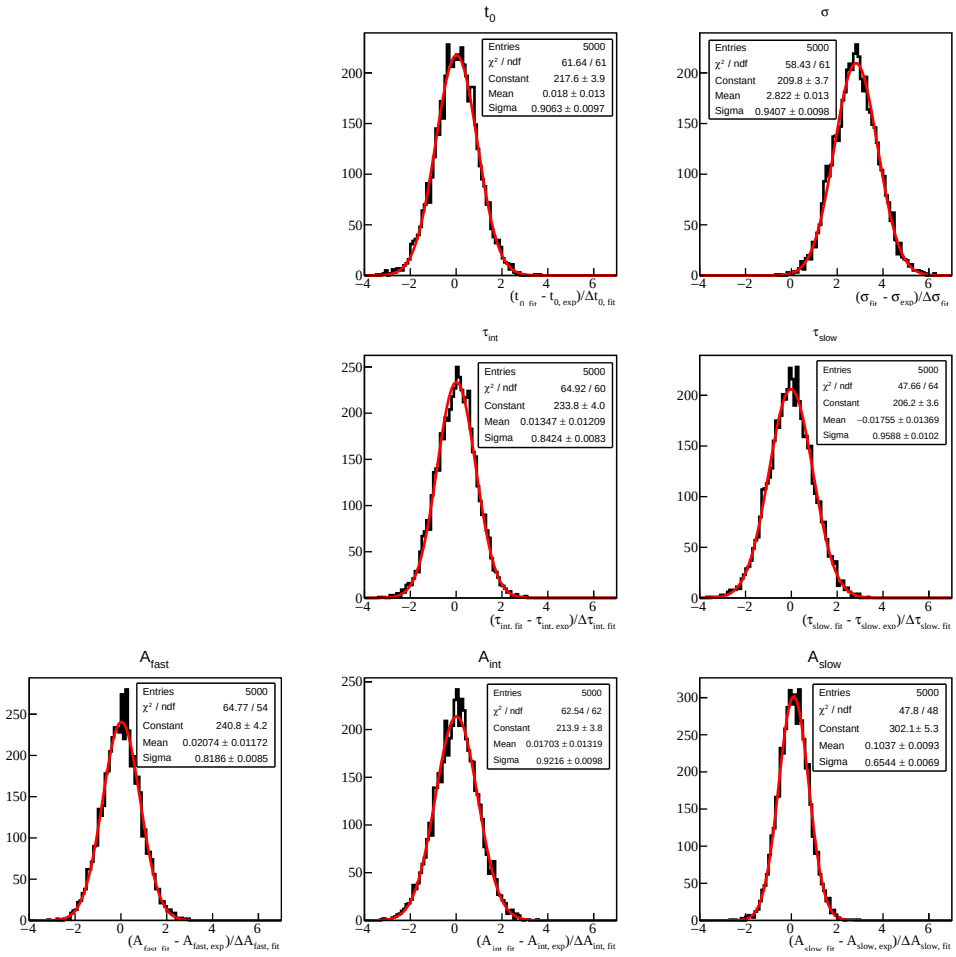

Figure 4.5.: Pull distributions of all the parameters extracted from the fit of the scintillation time profile, using Eq. (4.1b). Each *pull-distribution* is filled with the results obtained from 5000 iterations (number of fitted waveforms).

case of the χ^2-fit the error doesn't seem to be overestimated, the likelihood method is preferred because of the goodness ensured in retrieving results.

4.1.1.1 Optimization of the fit procedure

The different statistics present in each run analyzed in the data is simulated in the toy-MC by generating a different number of entries in the waveform histogram. Each waveform is generated using the seed inputs reported in Tab. 4.1, except τ_{slow} input

that, only for this analysis, is 1500 ns[4]. Each waveform is fitted using Eq. (4.1b), with τ_{fast} fixed at 6 ns; in one case, by minimizing the χ^2 and, in the other, by maximizing the likelihood function. Depending on the histogram statistics, the fit results obtained with both methods are compared. The parameters retrieved by the two fit approaches are reported in a 2-D plot, having on the x(y)-axis the parameter recovered by the χ^2(likelihood)-fit. Three different numbers of entries are generated: 5×10^3, 250×10^3, and 300×10^4 (roughly corresponding to few tens, few hundreds, thousands of events respectively). The results are shown in Fig. 4.6; for simplicity, only those related to τ_{slow}, τ_{int}, and A_{slow} are reported, being negligible the variation observed in the other parameters. In the top-plots, the comparison for the waveforms generated with the lowest statistic is reported; the statistic increases going from the top to the bottom plots. The two decay times and the *slow* normalization constant manifest a bias when the χ^2-fit is performed that disappears only at high statistics (bottom-plots). The likelihood fit results, instead, are unbiased even for very low statistics. Because of that, the likelihood-fit is the baseline method chosen to get the time profile parameters; however, the χ^2 fit is performed when the likelihood fit fails and the bias that can be introduced is taken into account with a systematic uncertainty, as will be described in Sec. 4.1.2.

4.1.1.2 Impact of the 4 ns digitization sampling

As shown in Fig. 4.5, the mean of the *pull-distribution* of the σ-parameter displays an evident bias, being it centered around 2.82.

As described in Eq. (4.1b), the σ-parameter is referred to PMT transit time spread whose estimation given by the manufacturer is around 3 ns, lower than the 4 ns sensitivity determined by the digitization sampling. Because of that, the shift in the mean of the *pull-distribution* is suspected to be introduced by the sampling itself. To verify this hypothesis two analyses have been performed through the toy-MC: the first one studies the dependence of the bias with the sigma input value and the second one tries to verify the effect of the sampling by decreasing its simulated value.

Being the σ-parameter very correlated with the *fast* decay time, the first analysis studies the variation of the *pull-distribution* mean and RMS as a function of the input used for these two parameters. Different from the inputs given in Tab. 4.1,

[4]This different choice does not affect the analysis results.

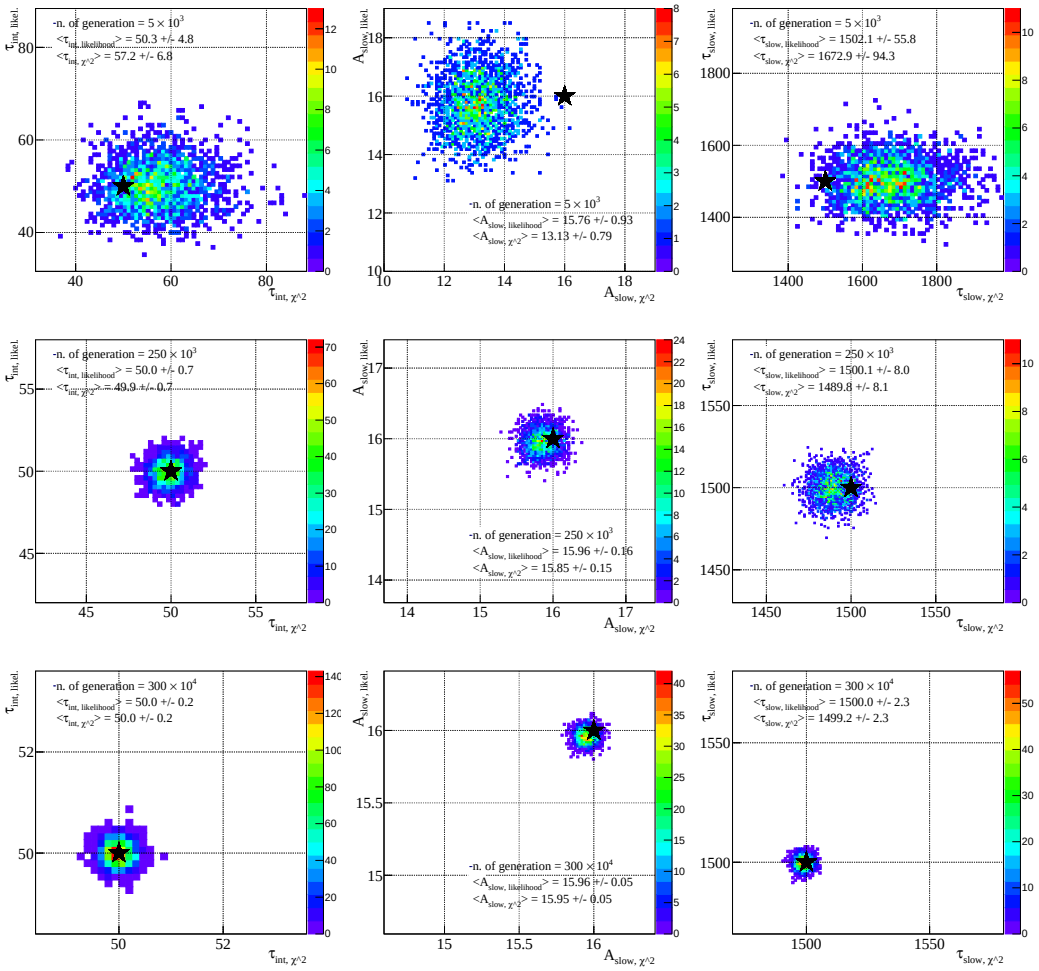

Figure 4.6.: Comparison between the measurement of τ_{int} (**left**), A_{slow} (**middle**), and τ_{slow} (**right**) retrieved from the fit performed by maximizing the likelihood function (on the y-axis of each plot) or minimizing the χ^2 (on the x-axis of each plot), simulating different statistics conditions: $5{\times}10^3$ (**top**), $250{\times}10^3$ (**middle**), and $300{\times}10^4$ (**bottom**) number of generated waveforms. The black star indicates the true value for the corresponding parameter.

the input values used for the σ and the τ_{fast} are the following:

- σ = 3, 4, 5, 6, 7, 8 ns
- τ_{fast} = 5, 6, 7, 8, 9, 10 ns

For each combination of them, the *pull-distribution* of the σ-parameter is determined; the mean and the σ of the distribution are drawn in 2-D plots having on

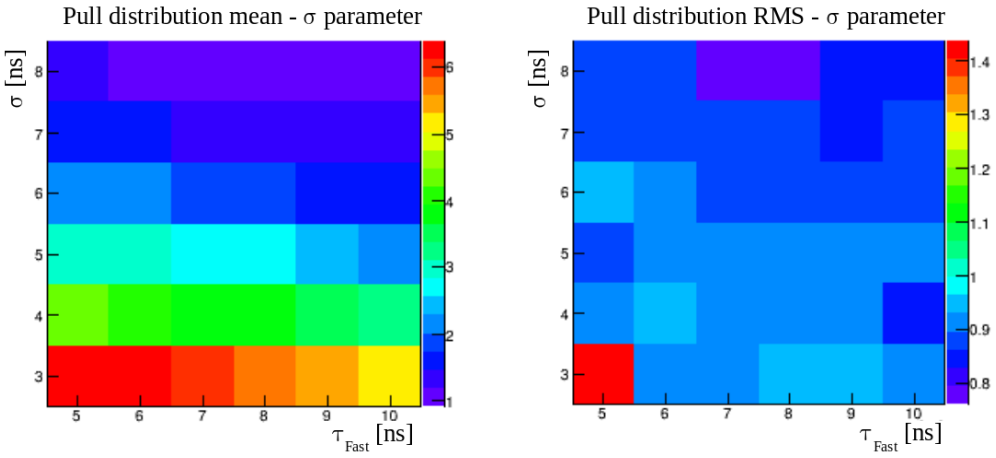

Figure 4.7.: *Optimization-grids* of the σ-parameter obtained using the values given in the x and y axes as seeds for the corresponding parameters. The color-scale in both plots is determined by the mean (**left**) and the RMS (**right**) of the *pull-distribution* of the σ-parameter.

the x and y axes the values given as inputs for τ_{fast} and σ respectively. A grid is created with the input values on the axis and the color scale of the plots determined by the value of the mean or the σ of the *pull-distribution*; the way to refer to this plot will be *optimization-grids*. The ones regarding the σ-parameter are shown in Fig. 4.7. The bias in the mean decreases when σ inputs are larger than 6 ns; however, correspondingly, the error becomes underestimated. On the contrary, there is not a strong dependence on τ_{fast} input values. This finding is important since it is suggesting that the fit can retrieve an unbia-

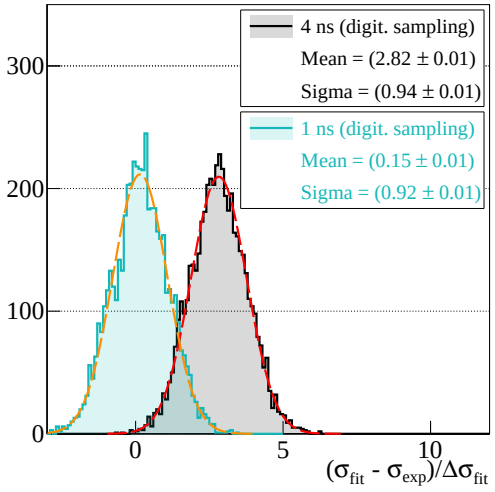

Figure 4.8.: *Pull distribution* of the σ-parameter obtained simulating a waveform with 1 ns (light blue) and 4 ns (in black) digitization sampling.

sed value for the two parameters only if it is not limited by the sensitivity imposed by the digitization sampling. In order to verify this hypothesis, the *pull-distribution* of the σ-parameter obtained by generating a toy-MC waveform with 1 ns sampling is considered. In Fig 4.12, the two *pull-distributions* are compared; in light blue, the one obtained with 1 ns sampling and, in black, the one obtained with 4 ns sampling are shown. Only the mean of the former is centered around 0, confirming the hardware origin of the bias.

In summary

The 4 ns sampling introduces an evident limitation on the calculation of the PMT transit time spread that is expected to be around 3 ns from the measurement of the Hamamatsu manufacturer. The mean of the corresponding *pull-distribution* distribution shows a bias that disappears if the waveform digitization sampling is lowered down to 1 ns.

4.1.1.3 Impact of keeping τ_{fast} fixed

In the analysis presented in this section, the effect of keeping τ_{fast} fixed at 6 ns in the fit procedure is evaluated. As shown by the correlation matrix, in addition to the correlation with σ, τ_{fast} is correlated with τ_{int}. For this reason, the *optimization-grid* is built considering the inputs for τ_{int} and the values at which τ_{fast} is fixed using a univocal input for it, as follows:

- $\tau_{\text{fast,seed}} = 6$ ns
- τ_{fast} is fixed at: 5, 6, 7, 8, 9, 10 ns
- $\tau_{\text{int,seed}} = 45, ..., 85$ ns, with 5 ns step

The idea is then to evaluate the impact on τ_{int} of fixing τ_{fast} at distinct values than the generated one during the fitting procedure. The results are shown through the *optimization-grids* reported in the top of Fig. 4.9; on the left, the color scale is determined by the mean *pull-distribution* for τ_{int} and, on the right, by the σ of the same *pull-distribution*. For all the combinations, independently of the τ_{int} seed, the *pull-distribution* mean suffers a bias depending on the value chosen for fixing τ_{fast}; only when it is fixed at the input value, the mean of the *pull-distribution* is centered

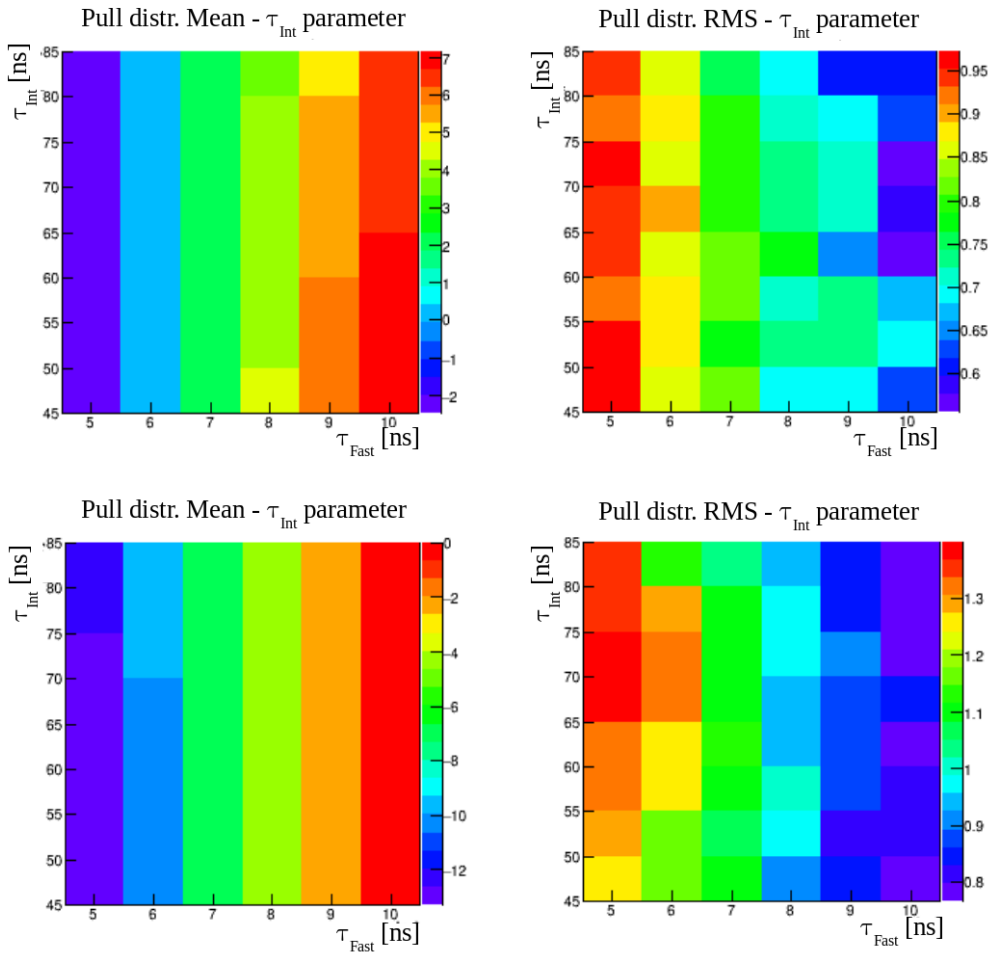

Figure 4.9.: *Optimization-grids* of the $\tau_{\rm int}$ -parameter obtained using as $\tau_{\rm int}$ seeds the values given in the y-axis; whereas, $\tau_{\rm fast}$ is fixed at the values given on the x-axis. The true value of $\tau_{\rm fast}$ used in the waveform generation is 6 ns (**top**) and 10 ns (**bottom**). The color-scale in all the plots is determined by the mean (**left**) and the RMS (**right**) of the *pull-distribution* of the $\tau_{\rm int}$ -parameter.

at 0. Nevertheless, the σ of the *pull-distribution* decreases proportionally to the biasing induced by fixing $\tau_{\rm fast}$ at the wrong value. These behaviors, in particular, the decrease of the σ of the *pull-distribution*, show how the $\tau_{\rm int}$ and the error assigned by the fit procedure compensate for the wrong assignment to the $\tau_{\rm fast}$ parameter. By comparing with the typical relative error attributed to $\tau_{\rm int}$ (Tab. 4.5) in the data analysis, a typical 12% uncertainty is assigned by the fit procedure, able to take into account the possibility that the true value of $\tau_{\rm fast}$ can be different than the

chosen one. In the data, the attempt of keeping τ_{fast} free in the fit has been done; in this case, the measurement of τ_{fast} is moved around 11 ns and τ_{int} around 75 ns. Considering these results, a new toy-MC is generated with 10 ns seed for τ_{fast}; the *optimization-grids* using this second configuration are shown in the bottom plots of Fig. 4.9. The results obtained are analogous to previous results with 6 ns seed. Given the measurements of τ_{fast} reported in the literature and the impact of the digitization sampling on the parameters pointed out in the previous section, the decision of fixing τ_{fast} has been preferred.

In summary

Given the correlation between τ_{fast} and τ_{int}, the impact on the latter of fixing τ_{fast} is considered. Two different inputs have been used for τ_{fast} (6 ns and 10 ns) and, in both cases, it is assigned to a set of values different from the true one. Unless τ_{fast} is fixed to the input value, τ_{int} tends to compensate for the wrong assignment of the fixed τ_{fast}. However, the error assigned to τ_{int} in fit procedure always takes into account for possible biases. Due to the impact of the 4 ns digitization sampling on the σ parameter showed in the previous section and due to the measurements reported in the literature for τ_{fast}, a conservative approach has been preferred; in order to avoid misinterpretations of the result, in the fit procedure, τ_{fast} is fixed at 6 ns based on the measurement reported in Ref. [145].

4.1.2 Study of the systematics

In this section, the systematic uncertainties that are induced by the fit procedure and how they are evaluated to be included in the error assignment will be explained.

The main sources of systematic uncertainties are two:

- the possible bias introduced by the χ^2-fit performed when the likelihood-fit fails
- the range over the fit is performed

Their impact is evaluated from the data and it is cross-checked through the results obtained from the toy-MC simulations.

Fit procedure

As explained in the fit procedure described in Sec. 4.1.1.1, the bias induced by performing a χ^2-fit becomes stronger for runs with low statistics. Knowing that the best parameter measurement is obtained through a likelihood-fit, the systematic uncertainties assigned due to the discrepancy of the parameter estimated through a χ^2-fit when the other approach failed is estimated directly from the data. Considering all the runs collected in absence of drift field, for each parameter, the values obtained by performing a likelihood or a χ^2-fit are compared; the evaluation of the systematic uncertainty comes from the following formula:

$$\Delta\mu[\%] \;=\; \frac{\mu_{\text{meas},\chi^2} - \mu_{\text{meas,likel.}}}{\mu_{\text{meas,likel.}}} \tag{4.3}$$

when μ is the general way to refer to each parameter measurement given by the fit. In Tab. 4.2, the discrepancies calculated using Eq. (4.3), differentiating the results for the five PMTs, are reported. For comparison, the results obtained for the PB PMTs are shown but considering only the parameters that are not affected by the reflections are reported. In the last column, the systematic uncertainty to be assigned is given; among all the variations observe per PMT, the choice of a conservative value is preferred. In the last row of the table, among all the runs analyzed, the percentage of runs fitted through the χ^2 procedure is provided. In contrast with what is predicted by the toy-MC, a discrepancy between the two approaches is observed in all the parameters. For this reason, each time a χ^2-fit is performed instead of the likelihood procedure, in each parameter, the conservative systematic uncertainty that is reported in the last column of Tab. 4.2 is summed in quadrature to the error assigned by the fit.

Fit range

As described in the previous section, the fit procedure aims to be as generic as possible to fit all the runs available despite the differences in their data-taking conditions or individual statistics. In particular, in the presence of the amplification field, both the primary and the secondary scintillation light signals are detected, and, depending on the track-topology they can be very close in time. For this reason, it is essential to prevent S2 contamination in the S1 time profile to avoid the

	PMT-1	**PMT-2**	**PMT-3**	**PMT-4**	**PMT-5**	**syst. unc.**
Δt_0 [%]	-17.84	-11.37	-15.88	-5.58	-10.74	18
$\Delta\sigma$ [%]	+9.35	+6.71	+6.95	+3.79	+4.44	9
ΔA_{fast} [%]	+6.34	+3.37	—	—	+3.63	6
ΔA_{int} [%]	-6.74	-6.62	—	—	-7.98	8
$\Delta\tau_{int}$ [%]	+12.12	+10.16	—	—	+7.80	12
ΔA_{slow} [%]	-3.62	-0.68	—	—	-3.26	3
$\Delta\tau_{slow}$ [%]	-0.66	-0.03	+0.54	-0.51	-1.09	1
affected runs [%]	35	53	75	33	30	

Table 4.2.: Discrepancies observed in the parameter calculation induced by performing a χ^2 fit when the likelihood fit fails. In the last column, the conservative systematic uncertainty assigned to each parameter is given.

misinterpretation of the results. As will be detailed in Chapter 6, the S2 reconstruction algorithm allows me to identify the starting time of the S2 signal. Thanks to that, in runs acquired in the 1 ms time window, the requirement of accepting only events with the S2 starting time after 10 μs is added. Despite that, in the 4 μs time window runs, the S2 signal is not available; for this reason, the S2 contamination is excluded performing the fit in a shorter range, up to 2.5 μs only for runs with the amplification field lower than 20 kV/cm[5].

Ideally, as will be demonstrated through the toy-MC, decreasing the fit range should not affect the parameter measurement. Using the same seed given in Tab. 4.1, the likelihood-fit is performed considering three different ranges: up to 9.5 μs, up to 3.5 μs, and up to 2.5 μs. The results are shown in Tab. 4.3, comparing any possible variation registered in the *pull-distribution* mean and σ. As expected, no variations are observed, meaning that the fit range does not affect the parameter measurements.

However, if the same study is performed in the data, a relevant discrepancy is

[5]All the runs collected with higher amplification field than 20 kV/cm are excluded from the analyses because the decreasing of the range is not sufficient in avoiding the S2 contamination in the S1 signal.

	fit range 9.5 μs	**fit range 3.5 μs**	**fit range 2.5 μs**
Δt_0	Mean = 0.02, σ = 0.92	Mean = 0.01, σ = 0.92	Mean = 0.02, σ = 0.91
$\Delta\sigma$	Mean = 2.80, σ = 0.92	Mean = 2.82, σ = 0.92	Mean = 2.79, σ = 0.91
ΔA_{fast}	Mean = 0.03, σ = 0.82	Mean = 0.03, σ = 0.84	Mean = 0.03, σ = 0.83
ΔA_{int}	Mean = 0.03, σ = 0.93	Mean = 0.02, σ = 0.95	Mean = 0.02, σ = 0.93
$\Delta\tau_{int}$	Mean = 0.02, σ = 0.87	Mean = 0.01, σ = 0.89	Mean = 0.01, σ = 0.86
ΔA_{slow}	Mean = 0.11, σ = 0.58	Mean = 0.11, σ = 0.68	Mean = 0.10, σ = 0.77
$\Delta\tau_{slow}$	Mean = 0.02, σ = 0.98	Mean = -0.01, σ = 1.04	Mean = 0.01, σ = 0.97

Table 4.3.: Mean and sigma of the *pull-distribution* obtained performing a likelihood-fit, considering three fit ranges: 9.5 μs, 3.5 μs, and 2.5 μs.

observed in the two extracted decay times. Using the runs collected in the 1 ms time window and in the absence of all the electric fields, the same sample of runs is fitted up to 3.5 μs or 2.5 μs. The discrepancy observed in the results obtained fitting in the shortest range compared to the fit done up to 3.5 μs are evaluated by the following formula:

$$\Delta\mu_{range}[\%] = \frac{\mu_{meas,2.5\mu s} - \mu_{meas,3.5\mu s}}{\mu_{meas,3.5\mu s}} \tag{4.4}$$

The comparison between the two results, in the NB PMTs and differentiating between the runs fitted by the two minimization procedures (likelihood and the χ^2), is reported in Tab. 4.4. In the last row of the same table, the percentage of runs that have been fitted in the shorter range is quantified. For each of them, a systematic uncertainty is added in quadrature with the error attributed by the fit procedure to the two decay times. In the last column of the table, the conservative value assigned is reported.

	PMT-1		**PMT-2**		**PMT-5**		
	χ^2	$\mathcal{L}$	χ^2	$\mathcal{L}$	χ^2	$\mathcal{L}$	**syst. unc.**
$\Delta\tau_{\text{int}}$ [%]	0	-4.48	0	-3.96	-4.06	-4.38	5
$\Delta\tau_{\text{slow}}$ [%]	-2.41	-3.61	-3.68	-2.91	-2.87	-3.50	4
affected runs [%]	24		23		23		

Table 4.4.: Discrepancies observed in the parameter calculation induced by performing the fit up to 2.5 μs instead of up to 3.5 μs; only the reported parameters are affected. In the last column, the conservative systematic uncertainty assigned to each parameter is given.

Hints of a fourth component in the NB PMTs

The unexpected observation of the parameter measurement dependence with the fit range in the NB PMTs finds an explanation if the whole S1 time profile shape, up to 25 μs, is considered. An example, studying a CRT-trigger run collected in absence of drift field, is reported on the left of Fig. 4.10 (in the figure, the result from PMT-2 is shown but the behavior is the same in the other three NB PMTs). In grey, the fit function obtained using the three-exponential model given by Eq. (4.1b) is reported; after $\sim$5 μs, the function deviates from the data, showing that it is no longer suitable for reproducing them. On the other hand, in red, a four-exponential function is used in the fit; this alternative modelization adds a fourth exponential in Eq. (4.1b) to model the data after $\sim$5 μs. Only in this way, they are correctly reproduced in the whole range. In the legend of the same figure, the parameters extracted by using a four-exponential model are reported; if compared with the results, given in Tab. 4.7, that will be explained in next section, all the parameters in common to the two models agree within the errors. Although with a big error, the fourth decay time is found to be around 6340 ns. The result found in this run is in agreement with the value reported in Ref. [144], $\tau_{4\text{th}} = (6658 \pm 1160)$, that attributes the *fourth* decay time to the delayed re-emission of the scintillation light by the TPB molecules. Nevertheless, different from the NB PMTs, in the PB PMTs both the three and four-exponential models reproduce adequately the data; an example is shown on the right of Fig. 4.10 for PMT-3, but the same result is

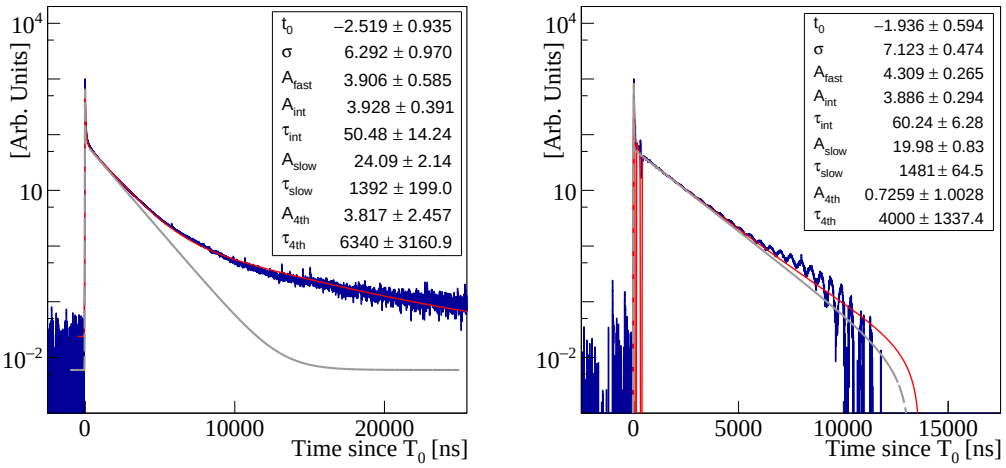

Figure 4.10.: Scintillation time profile showed up to 25 μs for an NB PMT (**left**) and up to 12 μs for an PB PMT (**right**). For the NB PMT a *fourth* exponential is needed to reproduce correctly the data in the whole range; the three-exponential function after $\sim$5 μs is no longer able to reproduce the data. Otherwise, in the PB PMT the three-exponential function is still valide to reproduce the time profile.

found in PMT-4. However, the waveform shape reports a train of peaks, possibly corresponding to the discharges induced by the splitter decoupling; hence, even if not observed, it is not possible to exclude the presence of the fourth component in these PMTs. Due to the difference between the two configurations and the lack of runs with sufficient statistics to carry out a robust analysis, it is not possible to study the nature of the fourth component in the WA105 DP demonstrator.

In summary

Two main sources of systematic uncertainties have been identified and taken into account in the generalization of the fit procedure. The first corresponds to the bias introduced by performing a χ^2-fit minimization when the likelihood fit fails; whereas, the second is induced by the decreasing of the fit range to avoid the S2 contamination in runs collected with the short acquisition window. In addition to the error attributed to each parameter by the fit procedure (a likelihood-fit up to 3.5 μs), the relative systematic uncertainty is added in quadrature when one of the previous options is verified. For comparison with the systematic uncertainties

evaluation, the typical relative error assigned to each parameter, by the standard-fit procedure, is reported in Tab. 4.5.

	PMT-1	**PMT-2**	**PMT-3**	**PMT-4**	**PMT-5**
$\Delta t_0/t_0$ [%]	31	29	24	37	36
$\Delta\sigma/\sigma$ [%]	13	10	10	15	14
ΔA_{fast} $/A_{fast}$ [%]	13	11	—	—	16
ΔA_{int} $/A_{int}$ [%]	10	9	—	—	11
$\Delta\tau_{int}$ $/\tau_{int}$ [%]	15	13	—	—	17
ΔA_{slow} $/A_{slow}$ [%]	1	1	—	—	2
$\Delta\tau_{slow}$ $/\tau_{slow}$ [%]	3	2	2	4	4

Table 4.5.: Relative error assigned by the fit procedure to each parameter; the evaluation is based on the likelihood-fit performed in the data, collected in absence of the drift field.

The studies performed through the toy-MC demonstrated the robustness of the fit procedure if the waveform is generated as a sum of three exponential contributions convoluted with a Gaussian function; in this case, the decreasing of the fit range does not introduce any miscalculation in the parameter retrieved by the fit. Nevertheless, in the data, this operation exhibits a discrepancy in the extracted value of the *intermediate* and the *slow* decay times. This effect is present only in the NB-PMTs whose waveforms need a fourth component to be adequately reproduced in a longer range than 3.5 μs. To deeper investigate this effect, very long runs would be needed to exclude any statistical fluctuations and be sure that the origin of the fourth component observed has a physical meaning, such as the delayed TPB re-emission mentioned in Ref. [148] and [144]. Unfortunately, only very few runs taken with no S2 signal and with a long acquisition window are available; hence, in the WA105 DP demonstrator, it is not possible to develop a dedicated analysis for that.

4.2 Characterization of the scintillation time profile in absence of drift field

In this section, the characterization of the scintillation time profile obtained analyzing all the runs collected in the absence of the drift field, spanning over the

whole period of data taking, following the fit procedure, and the error assignment described in the previous section, is presented. Runs collected in both trigger configurations are included and the usual *muon-like* event selection to data triggered by the CRT system is applied; events saturating either the ADC dynamic range or PMT response are always removed.

4.2.1 Monitoring of the LAr purity through the τ_{slow} decay time

As explained in Sec. 2.3.2, the presence of O_2, N_2, and moisture even at the ppm level, is one of the main cause of the scintillation light quenching and the slow decay time is the most sensitive parameter to the impurity concentration. In the WA105 DP demonstrator, as reported in Fig. 3.3, at the end of the cooling down phase, the quantity of O_2, N_2, and moistures were measured to be at 0.1 ppm, 50 ppb, and 7 ppm respectively. Nevertheless, when the detector has been operated in stable conditions, information from the RGTA was no longer available but a continued LAr recirculation and purification was expected to ensure an improved and maintained LAr purity at the best levels. For this reason, a way to control the LAr purity is through the monitoring of the τ_{slow}, which is the main goal of the analysis described in this section. In Fig. 4.11, the results obtained along the data taking from two over five PMTs are presented; as an example, the result form an NB (in the top) and PB (in the bottom) PMTs are compared. Both positive and negative base PMTs confirm the stability of the τ_{slow} during the whole data taking, without any evident variation in the LAr purity for more than four months. For each PMT, the average value of the *slow* decay time is obtained performing a linear fit of all the points reported in their corresponding plot; the results are summarised in Tab. 4.6. The error assigned to each PMT measurement takes into account both the error assigned by the fit procedure in each point and the dispersion among all the runs that are added in quadrature. For the NB PMTs, the measurement of the τ_{slow} has been cross-checked by performing a global simultaneous fit of all the runs collected in absence of the drift field. Around 50 runs are fitted per PMT; for this reason, the statistics is expected to be very high and the fit is done by performing the χ^2 minimization, based on the MINUIT package [213]. The modelization function is the same as the one used in the single fit, given by Eq. (4.1b); in particular, the Gaussian

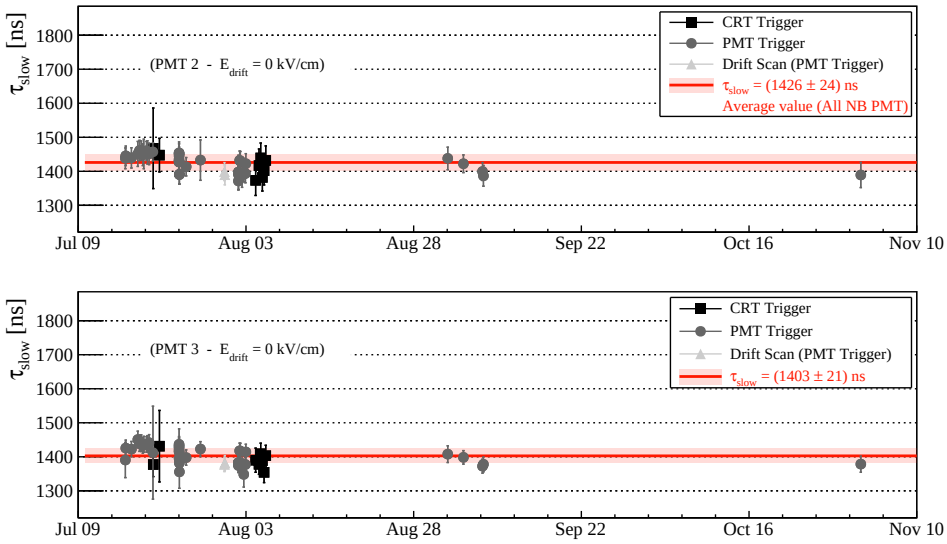

Figure 4.11.: Monitoring of the LAr purity through the τ_{slow} decay time measurement. Results obtained by an NB PMT (**top**) and an PB PMT (**bottom**) are shown as examples; all the other PMTs report a consistent behavior. The monitoring of τ_{slow} showed good stability for the whole period of the demonstrator operation. In the NB PMT plot, the red line is the combination of the results obtained from the three NB PMTs, corresponding to the average measurement of the τ_{slow}.

σ and the three decay times are considered as common parameters; whereas, all the others are considered as local parameters that may vary run by run. To be consistent with the single fit procedure, both the pedestal and τ_{fast} are kept fixed at 0 ns and 6 ns, respectively. The results are in good agreement with the previous method and they are reported in the last row of Tab. 4.6. Moreover, in the plot related to the

PMT n.	**1 (NB)**	**2 (NB)**	**3 (PB)**	**4 (PB)**	**5 (NB)**
τ_{slow} [ns]	1415±11	1421±17	1403±21	1445±14	1442±13
$\tau_{slow,global}$ [ns]	1421±5	1422±4	—	—	1440±5

Table 4.6.: Measurement of the τ_{slow} obtained performing a linear fit of the single τ_{slow} measurements of all the runs collected during the detector operation in absence of drift field or performing, per each PMT, a simultaneous fit of all the runs.

NB PMTs in Fig. 4.11, the displayed red line is the combination of the results of the three NB PMTs, corresponding to the average measurement of the τ_{slow} that will

be commented in the next section. For comparison, also the monitoring obtained using the PB PMTs is reported. The good operation of the recirculation system has been confirmed by the stable measurement of τ_{slow} monitored from the moment the detector filling was completed until the starting of the detector emptying.

Highlights

The control of the concentration of impurities in LAr is a crucial requirement for the optimization of the TPC operation; the *slow* decay time is the most sensitive scintillation time profile parameter to that and its decreasing would be the signal of the quenching processes induced by the impurities. The monitoring of τ_{slow} showed good stability of the LAr purity for the whole period of the demonstrator operation. Thanks to that, it is possible to study the scintillation light production mechanisms by a robust analysis of the scintillation time profile features, based on all the data collected in the same field conditions, excluding any kind of effect induced by the impurity instabilities.

4.2.2 Measurement of the slow and the intermediate decay times

Once the stability of the LAr purity is demonstrated, the characterization of the scintillation time profile parameters is possible; the results are based on the data collected in absence of the drift field. In Tab. 4.7, the calculation of the parameters found for the NB PMTs are reported. The values given in the table are the weighted average from all the runs included and fitted separately using the procedure described in Sec. 4.1. The error assigned to each parameter includes statistics and systematics uncertainties propagated to the weighted average and the dispersion among all runs. The measurements of the parameters obtained in each run do not show any correlation with the trigger conditions nor with the different WLS coating; for this reason, the values reported in the table do not take into account such separations. The three NB PMTs give a consistent measurement of all the parameters. In this section, the discussion is focused on the measurement of τ_{int} and τ_{slow}. As already mentioned in section Sec. 2.2.2.3, τ_{int} is a very controversial parameter and a new measurement can provide additional information about its origin. Since the

fit parameter	PMT1	PMT2	PMT5	average ± error
t_0 [ns]	-2.51±0.15	-2.34±0.14	-2.65±0.14	-2.49±0.25
σ [ns]	6.51±0.26	6.61±0.27	6.66±0.28	6.59±0.47
τ_{fast} [ns]	6 [fixed]	6 [fixed]	6 [fixed]	—
τ_{int} [ns]	49±2	51±1	49±2	49.7±3.0
τ_{slow} [ns]	1415±11	1421±17	1442±13	1426±24
A_{fast} [a.u.]	3.92±0.13	3.97±0.13	3.90±0.08	3.93±0.20
A_{int} [a.u.]	4.01±0.25	3.75±0.18	4.16±0.12	3.97±0.33
A_{slow} [a.u.]	27.78±1.00	26.52±0.92	28.34±0.07	27.56±1.36

Table 4.7.: Summary of all the fit parameters obtained by analyzing all the data collected in absence of drift field.

goal of this study is to get a value comparable to other experiments, the PB PMTs are not considered. Combining the individual results obtained from the NB PMTs, the *intermediate* decay time is found to be $\tau_{\text{int}} = (49.7 \pm 3.0)$ ns; the result is in agreement with the value reported in Ref. [148] that observed a $\tau_{\text{int}} = (49 \pm 1)$ ns.

The *slow* decay time is found to be $\tau_{\text{slow}} = (1426 \pm 24)$ ns; in agreement with the value reported in Ref. [147] - $\tau_{\text{slow}} = (1463 \pm 5_{\text{stat}} \pm 50_{\text{syst}})$ ns - but it is slightly lower than other values reported in the literature, in particular in Ref. [145] - $\tau_{\text{slow}} = (1590 \pm 100)$ ns - and [144] - $\tau_{\text{slow}} = (1503 \pm 41)$ ns. The measurement of the τ_{slow} is consistent with the impurity concentrations registered by the RGTA at the end of the filling phase (O_2 ∼0.1 ppm, N_2 ∼50 ppb, and H_2O ∼7 ppm.) and the electron lifetime measurement performed in alternative charge analyses (τ_e∼4 *ms* [78]). Under the hypothesis that the *slow* decay time is of the order on 1590 ns, as reported in Ref. [145] and considering the dependence of the *slow* decay time with the electronegative impurities concentration reported in Ref. [152] and Ref. [143], the impurity concentrations measured in the WA105 DP demonstrator are of the same order of the ones needed to obtain the observed reduction.

Highlights

The main findings of the analysis described in this section allowed me to characterize the decay times of the scintillation time profile measured in the absence of

the drift field. The measurement of the *intermediate* decay time has been achieved finding $\tau_{\text{int}} = (49.7 \pm 3.0)$ ns. Additionally, the *slow* decay time has been measured at (1426 ± 24) ns.

4.2.3 Relative probability amplitudes and the f_{90} factor

In Sec. 2.2.2.4, it is explained how the probability of de-excitation from the singlet or triplet state is related to the nature of the interacting particle. This feature is particularly interesting in scintillation light detectors for particle identification. However, most of the results reported in the literature are based on the interaction of electrons or more massive particles and the few results are obtained from the scintillation light produced by cosmic muons.

In this section, the measurement of the relative amplitudes and the f_{90} factor for cosmic muons, based on the data triggered by the CRT system is presented; a comparison with the data collected with the PMT self-trigger will be discussed. The relative contribution of each of the three components to the total scintillation light can be measured in terms of the relative amplitudes defined as follows:

$$\frac{A_j}{\sum_{j=f,i,s} A_j}, \tag{4.5}$$

being A_j the j-th normalization constant found with Eq. (4.1b). In absence of drift field, considering the values reported in Tab. 4.7, Eq. (4.5) gives their relative contributions to the total scintillation light that is found to be 11%, 11%, and 78% for the *fast*, the *intermediate*, and the *slow* components, respectively. The *slow* component represents the largest contribution to the total scintillation light. For the purpose of studying the scintillation light production, the ratio $(A_{\text{fast}} + A_{\text{int}})/A_{\text{slow}}$ is considered; this definition allows to include also the relative contribution of the *intermediate* component. Under the hypothesis of being the intermediate component independent from the Ar_2^* de-excitation, its contribution could be included either in the numerator or in the denominator. Two additional motivations are identified in supporting the choice of the ratio defined above:

- the necessity of having a comparison with the results reported in the literature
- the possibility of a comparison with a complementary method

In most of the references ([141], [145], [142]), it is not well documented how the *intermediate* contribution is treated when mentioned and not always the A_{fast} /A_{slow} ratio is given with errors. Since in Ref. [143] the ratio (A_{fast} + A_{int})/A_{slow} is considered, the same definition proposed in there is used to compare with the same observable. As will be detailed hereafter, this definition can be cross-checked with the f_{90} factor, which is independent of the fit procedure and its modelization. Including the results from all the data collected in the absence of the electric drift field, reported in Tab. 4.7, the $(A_{fast} + A_{int})/A_{slow}$ ratio measured by the NB PMTs is found; the results for the NB PMTs is given in Tab. 4.8. From the comparison of the results obtained in the two trigger conditions emerges

$(A_{fast}+A_{int})/A_{slow}$	**PMT 1**	**PMT 2**	**PMT 5**
CRT trigger	0.269±0.011	0.275±0.010	0.285±0.007
PMT trigger	0.287±0.004	0.292±0.004	0.283±0.005
average ± std	0.286±0.010	0.290±0.017	0.284±0.004

Table 4.8.: Measurement of the $(A_{fast} + A_{int})/A_{slow}$ reported for each of the three NB PMTs, in absence of drift field, separating the results depending on the trigger configurations.

that, in the PMT trigger, all the PMTs give consistent results within the errors; whereas, in the CRT trigger, a correlation with the PMT position inside the detector seems to arise. Although the reason for that is not straightforward, a correlation with the track topology has been pointed out (see also Sec. 4.2.3), possibly due to the small concentration of impurities present in the detector. Averaging the results from the three PMTs and in the two trigger conditions, the ratio $(A_{fast} + A_{int})/A_{slow}$ has been measured to be 0.287 ± 0.020, in agreement with the A_{fast} /A_{slow} measurement reported for the electrons in Ref. [141] (A_{fast} /A_{slow} = 0.5 ± 0.2) and [145] (A_{fast} /A_{slow} = 0.3). However, even if no errors are reported in the $(A_{fast} + A_{int})/A_{slow}$ ratio measurement for cosmic muons in Ref. [143], the mean value obtained in the WA105 DP demonstrator is lower than the one reported in the other study ($(A_{fast} + A_{int})/A_{slow}$ = 0.35). An explanation for that could be in the method used to obtain the average waveform which is different from the approach considered in this thesis. In Ref. [143], the low value measured for τ_{slow}, despite the high purity of the experiment, is explained by the deconvolution of the

PMT response before performing the fit. A similar effect can affect the slow relative amplitude, which is found to be 74% of the total [143], and, consequently, it could increase the measurement of the ratio reported.

As a cross-check, the f_{90} factor has been measured event-by-event in the two trigger conditions for all the data collected without the drift field. The f_{90} factor is obtained from Eq. (3.3). On the left-side of Fig. 4.12, the f_{90} factor is shown in a 2-D plot, as a function of the total scintillation light[6]; data collected with the CRT trigger are always shown on the top-left plots and the data collected with the PMT self-trigger are shown on the bottom-left plots. The f_{90} projection, in the two trigger configurations, is given in the plot on the right of the same figure. The results obtained with each NB PMT are summarized in Tab. 4.9; combining all of them, the f_{90} factor measured in absence of the drift field is found to be 0.277 ± 0.016, compatible with the value of the $(A_{fast} + A_{int})/A_{slow}$ ratio.

f_{90}	**PMT 1**	**PMT 2**	**PMT 5**
CRT trigger	0.266±0.013	0.269±0.014	0.272±0.011
PMT trigger	0.276±0.013	0.277±0.012	0.271±0.011
average ± std	0.274±0.007	0.280±0.012	0.273±0.007

Table 4.9.: Measurement of the f_{90} factor for each of the three NB PMTs, in absence of drift field, separating the results depending on the trigger configurations.

The f_{90} distributions taken in the two trigger configurations are both very clean. The CRT trigger is the only system between the two able to guarantee the selection of the muons based on the track reconstruction in absence of the drift field. In PMT trigger data, the muon selection cannot be applied in this drift field condition because of the absence of the event reconstruction in the anode-plane; consequently, the presence of electrons and/or electro-magnetic showers cannot be excluded *a-priori*. Nevertheless, by looking at the f_{90} comparison, the same behavior as in the $(A_{fast} + A_{int})/A_{slow}$ ratio arises; in particular, the f_{90} distribution for PMT-5 agrees with that of the *muon-like* candidates selected for the CRT triggered data for the same PMT. The sharpness of the f_{90} distribution and the agreement observed in PMT-5 is particularly important in the case of the PMT trigger, being the rejection

[6] In these plots, the total scintillation light is integrated in the whole 4 μs range.

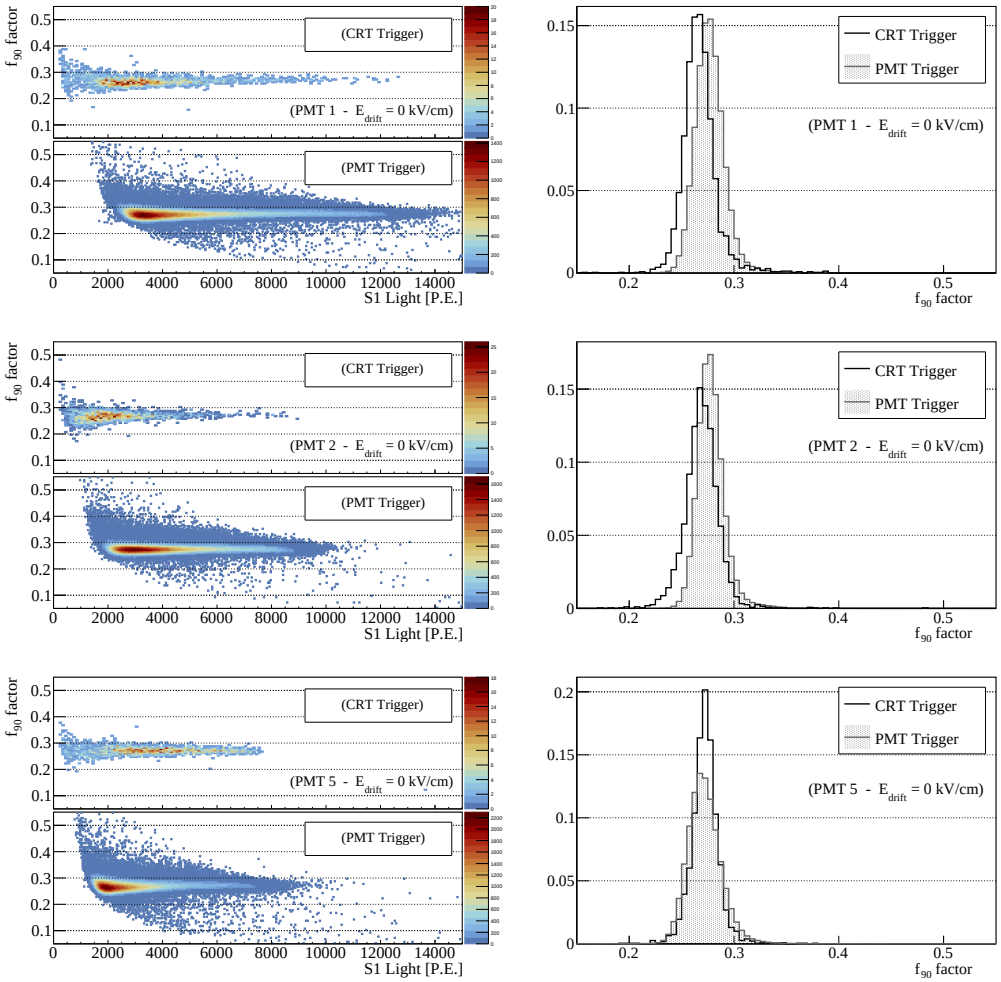

Figure 4.12.: Left: Correlation of the f_{90} factor with total scintillation light measured in the three NB PMTs. In the **top**-part of each plot, the *muon-like* events are triggered by the external CRT system, in the bottom-part plot by the PMT-trigger. For the latter, only events saturated the PMT response or the ADC dynamic range are rejected. **Right:** Projection of the f_{90} factor distribution in the two trigger configurations; no evident differences arise from their comparison.

of the more energetic events (mostly *muon-bundles*, electromagnetic and/or hadronic showers) the only requirement.

Furthermore, the f_{90} average value found in the WA105 DP demonstrator is in agreement with the values reported in the literature: 0.3 for the muons Ref. [144], and (0.282, 0.391) for the electrons Ref. [147]. This outcome confirms how challenging the discrimination between muons and electron recoils is when only based on

the scintillation light profile.

Highlights

The relative probability of de-excitation from the singlet or triplet state has been measured for muons at the MIP. Two complementary observables have been considered for this purpose: the $(A_{fast} + A_{int})/A_{slow}$ ratio, 0.287 ± 0.020, measured through the normalization constants of the scintillation time profile fit, and the f_{90} factor, 0.277 ± 0.016, that can be computed event-by-event. The measurement of both methods at the null drift field gives consistent results. An overall agreement is observed between the two trigger configurations if the average among the three NB PMTs is considered. This last finding leads to a general property of the scintillation light and a specific conclusion on the event selection applied in the PMT self-trigger mode. Firstly, the scintillation light produced by $\mathcal{O}$(MeV) electrons, and/or electromagnetic showers, and cosmic muons at MIP have common features that cannot be distinguished by considering the profile shape; and the event selection used in the data triggered by the PMT self trigger is good enough to exclude any contamination of more energetic events, avoiding the bias of the scintillation light profile.

Dependence of the f_{90} factor on the distance from the detection point

As demonstrated in the previous section, both the $(A_{fast} + A_{int})/A_{slow}$ ratio and the f_{90} factor distributions showed a dependence on the PMT position inside the detector for the data triggered by the CRT external system in the *CRT-shifted* geometry. In particular, both observables decrease when measured in PMT-1 that detects the light produced by the farthest muons crossing the detector. *A priori*, a different impact of the propagation on the fast and slow components of the scintillation light signals is not expected. Consequently, a possible interpretation for this behavior can be related to the effect induced by the attachment of the small concentration of electronegative impurities in the demonstrator.

A simple test of this hypothesis is reported in Fig. 4.13. For the *muon-like* events, the f_{90} factor is shown as a function of the ToF (top-plots) and the $\tan\theta$ (bottom-plots); the comparison is reported for the outermost PMTs, PMT-1 on the left and PMT-5 on the right. For instance, in the case of PMT-1, the closest tracks must have

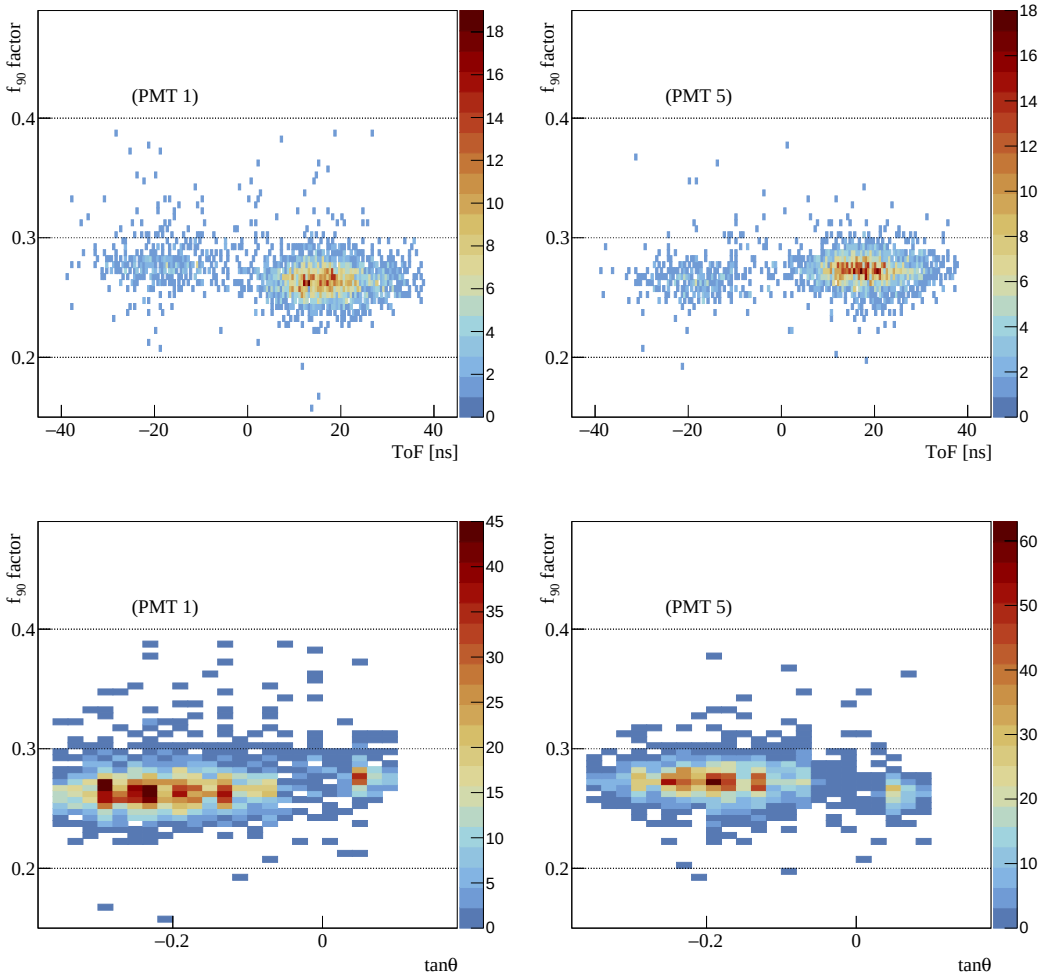

Figure 4.13.: Correlation of the f_{90} distribution obtained for the *muon-like* selected events with the ToF (**top**) and with the *tanθ* (**bottom**); the results are shown for PMT-1 (**left**) and PMT-5 (**right**).

a negative ToF and a positive tanθ; these events are the ones with a higher f_{90} factor than the others that cross the detector farther. In PMT-5, the behavior of the f_{90} is the opposite, reinforcing this hypothesis for the dependence of the f_{90} factor, and $(A_{fast} + A_{int})/A_{slow}$ ratio, with the distance from the PMT.

4.3 Effect of the drift field on the scintillation light

The presence of the drift field suppresses the recombination between ion-e^- pairs with the main consequence of lowering the amount of primary scintillation light produced through the recombination processes, as it is explained in Sec. 2.2.2. However, it is not well understood whether the contribution from singlet and triplet decay is the same for direct excitation and recombination processes. In addition, since the recombination depends on the particle type and the track structure, the effect of the drift field on scintillation light produced by cosmic muons at MIP could be different to the electrons used in most of the studies reported in the literature. In this section, the results on the suppression of the light yield at the nominal drift field strength, 0.5 kV/cm are reported. In the second part of the section, a new analysis dedicated to the effect of the drift field on the scintillation time profile is presented.

4.3.1 The light recombination factor

The description of the scintillation light yield decreasing as a function of the drift field strength and the complementary increase of the collected charge at the anode is well described by the empirical Birks' law (Sec. 2.2.1.1 and Sec. 2.2.2.1). The goal of the analysis presented in this section is to validate such a description also in the case of the scintillation light produced by the cosmic muons. All the data triggered by the CRT external trigger in shifted geometry, at null and the nominal drift field are used; the reason why the PMT self-trigger data, collected during a dedicated drift-field scan, cannot be included will be motivated at the end of this section. Since the goal is to study the effect of the drift field, in addition to the typical CRT muon selection listed in Sec. 3.8, a further cut is needed to ensure the selection only of muons crossing the LAr AV where the drift field is uniform. The CRT reconstruction gives the 3-D coordinate of the closest point of the muon track to the PMT; among all the muons crossing the LAr AV, only the ones with the closest point inside the FC volume are accepted. In this way, any possible contamination of the light produced by the tracks crossing the LAr AV outside the FC, where the drift field is not uniform, is excluded. Moreover, since in the runs collected at the nominal drift field strength the extraction and the amplification field were switched on, only events where the S2 starts 4 μs after the S1-peak have been considered

to exclude S2 contaminations in the S1 integration. Only the data collected at the nominal and null drift field strengths will be considered in this study.

The observable that needs to be considered is the $S_{1,drift}/S_{1,0}$ ratio to evaluate the fraction of scintillation light lost due to the recombination process; $S_{1,drift(0)}$ is the S1 light produced at the nominal (null) drift field, integrated in 4 μs. On the left of Fig. 4.14, the distributions of the scintillation light in the two drift field conditions are compared; a shift to lower values of the mean of the scintillation light distribution caused by the presence of the drift field is clearly seen. However,

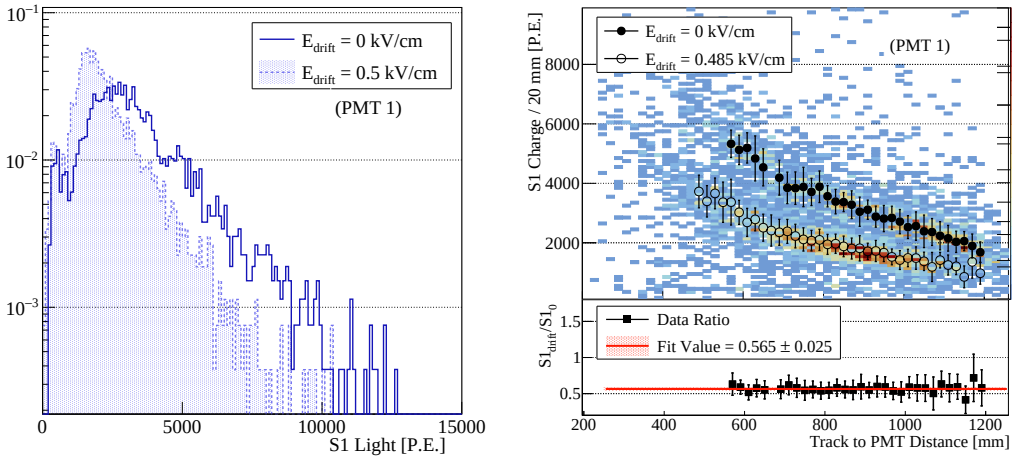

Figure 4.14.: Left: S1 charge spectrum of muon-like tracks obtained integrating the PMT waveform in 4 μs in absence and at the nominal drift field strength.
Right-top: S1 charge integrated in 4 μs as a function of the minimum approach distance, in absence (empty dots) and at the nominal (full dots) drift field strength.
Right-bottom: Ratio of the $S_{1,drift}/S_{1,0}$ measured in 20 mm bins.

to disentangle the effect of the drift field from the light attenuation, the amount of light collected by each PMT must be considered as a function of the minimum approach distance. The correlation of the S1 light, integrated over 4 μs time window, with the minimum approach distance is shown in the top-right plot of Fig. 4.14 at the nominal drift field value, by the empty dots, and in the absence of drift field, by the full dots. Every 20 mm, the $S_{1,drift}/S_{1,0}$ ratio is computed and its correlation with the minimum approach distance is displayed in the bottom-right plot of the same figure. As expected, the ratio is constant and does not depend on the track-PMT distance; the five PMTs give consistent results. Performing a linear fit of the

values obtained by the five PMTs, the $S_{1,drift}/S_{1,0}$ ratio at the nominal drift field strength of 0.5 kV/cm[7] is 0.577 ± 0.022; as reported in Fig. 4.15.

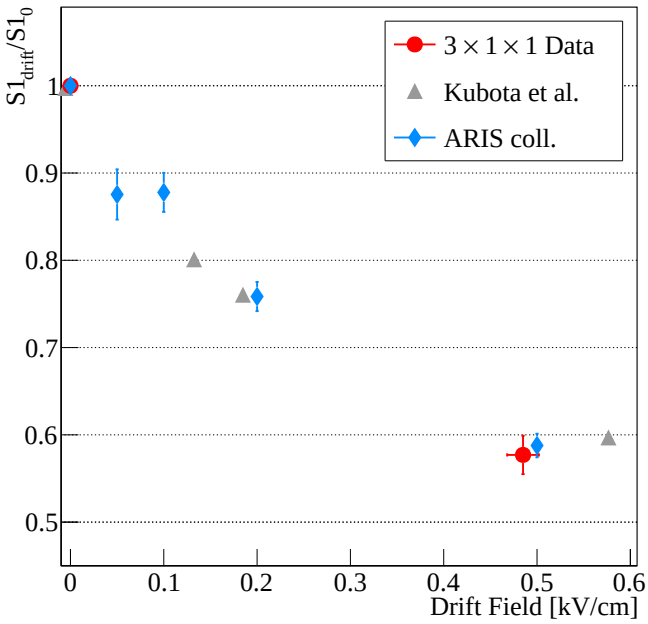

Figure 4.15.: Measurement of the $S_{1,drift}/S_{1,0}$ ratio, at 0.5 kV/cm, produced by the cosmic muons traversing the WA105 DP demonstrator LAr volume (red point) in comparison with the $S_{1,drift}/S_{1,0}$ ratio produced by $\mathcal{O}$(MeV) electrons reported as a function of the drift field strength in Ref. [125] (grey points) and in Ref. [136] (light blue points).

In the same figure, the $S_{1,drift}/S_{1,0}$ ratio at the nominal drift field of 0.5 kV/cm is compared with previous results reported in the literature (Ref. [125], [136]) showing a good agreement with them. In particular, it is possible to confirm that almost 40% of the total scintillation light detected without the drift field comes from the recombination process. It is worth noticing that both mentioned studies used electrons; in particular, for the comparison with Ref. [136], where the $S_{1,drift}/S_{1,0}$ ratio has been studied as a function of the particle energy, the points reported in the

[7]The drift field is computed as the differential potential between the cathode and the first field shaper (FFS). In all the data collected during the stable operation of the detector, the cathode voltage fluctuations are of the order of per mille level; however, in this and the following analyses, a 3.5% uncertainty is considered in order to include variations induced by the FFS-cathode distance due to the field cage ring diameter.

plot are the ones measured at the maximum energy (corresponding to electrons at 300 keVee). In the WA105 DP demonstrator, instead, the result reported is obtained from the scintillation light produced by crossing muons. The agreement between studies on the scintillation light produced by $\mathcal{O}$(MeV) electrons and muons at MIP is confirming that the two particles behave similarly in the excitation of the LAr excimers.

Ideally, the whole scintillation light should be considered and the waveform integration should be performed up to the end of the S1 signal. However, the runs included in the analysis are collected in both 4 μs and 1 ms time windows; for this reason, to avoid any artificial bias introduced by considering different integration ranges, the S1 light is always obtained integrating the waveform in the same range; the result shown in Fig. 4.14 comes from considering 4 μs time integration range. If the excimer formation does not affect the scintillation time profile, the $S_{1,drift}/S_{1,0}$ ratio should not depend on the integration range. In order to verify such interpretation, the role covered by the integration range has been studied; in addition to the 4 μs window, two other ranges are considered: 90 ns and 1 μs. The results for the three integration ranges are shown in Fig. 4.16 and summarized in Tab. 4.10. The results obtained for the $S_{1,drift}/S_{1,0}$ ratio are not the same. The highest ratio is measured integrating S1 light up to 90 ns, corresponding to considering mostly the fast S1 light. Consequently, the smallest decrease of light yield is obtained in an integrating window of 90 ns, corresponding to consider mostly the *fast* component, meaning that the slow component looks to be more affected by the suppression of the excimers formed in the recombination process.

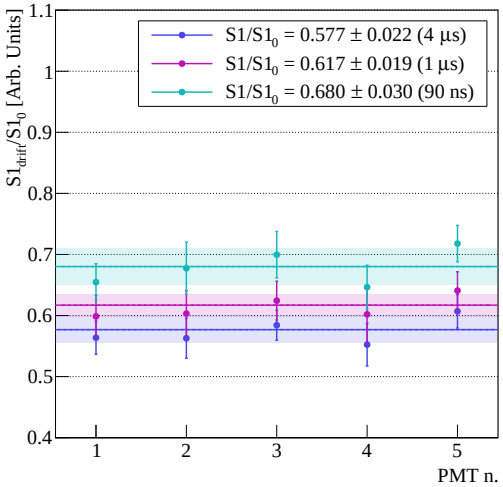

Figure 4.16.: Measurement of the $S_{1,drift}/S_{1,0}$ ratio PMT-by-PMT obtained integrating the S1-charge in 90 ns (cyan), 1 μs (magenta), and in 4 μs (blue).

average value (all PMTs)	$\mathbf{S_{1,90\ ns}}$	$\mathbf{S_{1,1\ \mu s}}$	$\mathbf{S_{1,4\ \mu s}}$
$S_{1,drift}/S_{1,0}$	0.680±0.030	0.617±0.019	0.577±0.022
% of suppressed light	32	38	42

Table 4.10.: Measurement of the $S_{1,drift}/S_{1,0}$ ratio measured integrating the S1 light in 90 ns, 1 μs, and in 4 μs; the suppression of the scintillation light produced through the recombination process at 0.5 kV/cm is reported.

Highlights

The suppression of the recombination process contributing to the total scintillation light, produced by crossing muons, due to the presence of the drift field has been studied. The $S_{1,drift}/S_{1,0}$ ratio measured at the nominal drift field value, averaging the results obtained by the five PMTs, is found at 0.577 ± 0.022, corresponding to almost 40% less light than the one produced by the muons in absence of the drift field. In addition to this finding, a dependence of the $S_{1,drift}/S_{1,0}$ with the S1-light integration range is observed, suggesting that the drift field affects differently the fast and the slow contribution to the scintillation time profile.

Limitations introduced by the PMT self-trigger logic in the study of the light recombination factor

During the detector commissioning, a dedicated drift field scan has been performed to explore the effect of the drift field in the range (0.00; 0.56) kV/cm. The events have been collected using the PMT self-trigger in the 4 μs acquisition window, without the event reconstruction through the charge information. Although they would have been a precious set of data to study the LAr recombination, the trigger logic does not select the same sample of events in all the runs of the drift scan affecting the final interpretation of the result. Because of the short time acquisition window, hence of the absence of the reconstruction of the S2 signal, it is not possible to consider the correlation of the scintillation light with the distance of the track from the PMT. Despite that, as a first approximation, the PMT quality cut selection is applied and the $S_{1,drift}/S_{1,0}$ ratio is obtained from fitting the S1 distribution with a Landau-function and by considering the MPV value. The five PMTs always

give a consistent calculation of the $S_{1,drift}/S_{1,0}$ ratio among them. The comparison of the $S_{1,drift}/S_{1,0}$ obtained from this set of data with the ones from the CRT trigger analysis is shown by the empty red dots in the top-plot in Fig. 4.17, and the discrepancy between the two analyses is evident. The main reason for that is the fixed threshold applied in the PMT self-trigger logic. As shown in the bottom-plot of Fig. 4.17, this feature is visible also in the PMT trigger event rate that is not constant when reported as a function of the drift field strength, for the same set of data. As known, the stronger the drift field, the lower is the scintillation light. If the threshold remains fixed, the same event (in terms of topology and energy) that may be triggered at the null field would not be accepted at a higher field, as its amplitude is lowered by the drift field, and this track would not overcome the acquisition threshold. With similar reasoning, an event that would saturate the PMT response at no field, as it falls in the comet-regime, could be included in the event sample selected at a higher field since less amount of light is produced. This interpretation is reinforced by the trend dependence with the drift field of both the trigger rate and of the $S_{1,drift}/S_{1,0}$ that changes their slope at around 0.1 kV/cm.

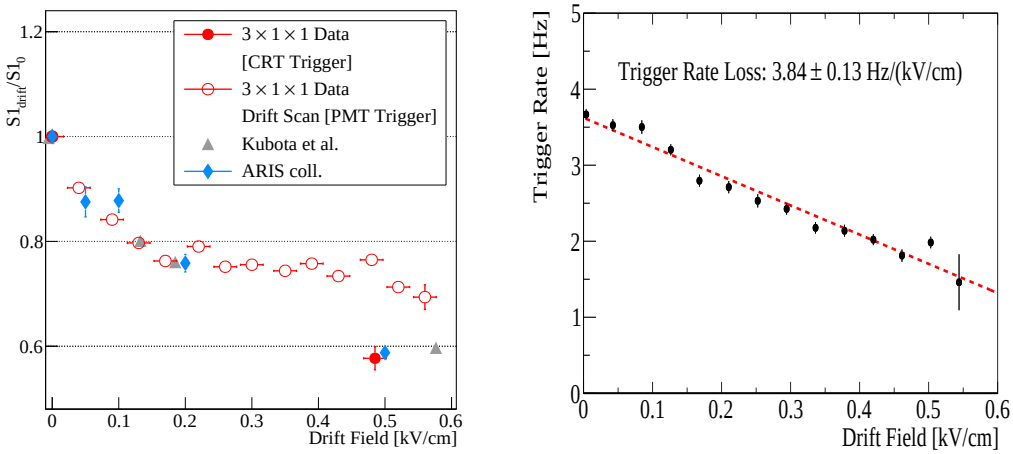

Figure 4.17.: Top: Measurement of the $S_{1,drift}/S_{1,0}$ ratio in the data of the drift field scan using the PMT self-trigger. **Bottom:** Measurement of the PMT self-trigger rate as a function of the drift field strength for the same set of data.

4.3.2 The impact of the drift field on the scintillation time profile

In contrast with what was reported on the effect of the drift field on the total scintillation light in LAr, few searches are describing its effect on the scintillation time profile parameters; only a comprehensive study related to that is reported in Ref. [125]. The scintillation light produced by a source of $\mathcal{O}$(MeV) electrons under the application of a drift field whose strength reaches ∼6 kV/cm is considered; for this value of the drift field, the recombination is expected to be completely suppressed by the drift field, hence the scintillation light observed is due to the direct de-excitation of the excimer formed by *sellf-trapping*. Two interesting hints of the behavior on the A_{fast} /A_{slow} and the τ_{slow} [8] are reported. In particular, the comparison with the results obtained at the maximum drift field applied, allowed to measure the relative population of the singlet and triplet states, and the τ_{slow} only produced by the direct dimer excitation:

$$\frac{A_{fast}}{A_{slow}}[\text{Rec}] = 0.5 \pm 0.2 \qquad \frac{A_{fast}}{A_{slow}}[\text{Exc}] = 0.36 \pm 0.06$$

$$\tau_{slow}[\text{Rec}] = 940 \qquad \tau_{slow}[\text{Exc}] = 860 \pm 30$$

Based on these findings, a decrease of both the A_{fast} /A_{slow} and the τ_{slow} is expected when the scintillation light is produced only by the direct excitation of the Ar-excimers. Since the study has never been confirmed, the analysis presented in this section is dedicated to investigating these results in more detail.

In Fig. 4.18, the scintillation time profile obtained at intermediate values of the drift field (0 kV/cm, 0.04 kV/cm, 0.17 kV/cm, 0.52 kV/cm) are shown; an example of an NB and PB profiles are compared on the left and on the right of the figure, respectively. In both cases, it is clear that the drift field changes the time profile shape. In the next sections, the effect of the drift field in the range (0, 0.56) kV/cm on the time profile is quantified. Spanning in the whole data taking period, data with the two trigger configurations are analyzed separately. The results from runs taken in the same drift field conditions are represented in the following plots as a single point corresponding to the weighted average of the data in the same drift field

[8] Despite it is not clearly mentioned in the text, the values reported for the τ_{slow}, ∼1 μs, suggests a low control of the impurities.

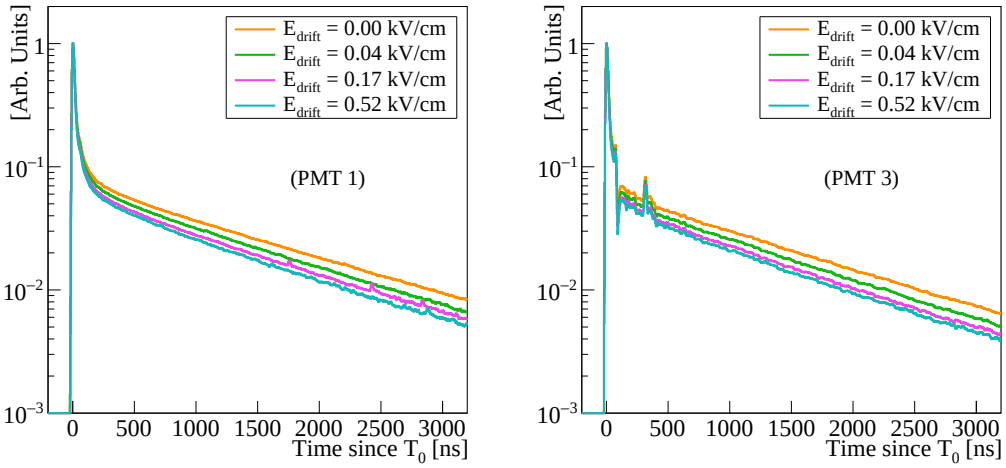

Figure 4.18.: Scintillation time profile observed in an NB (**right**) and an PB (**left**) PMTs measured for the increasing strength of the drift field.

conditions. This approach is justified by the necessity of assigning the proper weight to the short runs with low statistics; the usual CRT and PMT selection are applied. Besides, data collected in the dedicated drift field scan, with a total duration of two hours, are used as a reference.

4.3.3 Variation of the relative amplitudes and enhancement of the $(A_{fast} + A_{int})/A_{slow}$ ratio

As a first step of the analysis, the behavior of the $(A_{fast} + A_{int})/A_{slow}$ ratio under the increasing drift field strength is considered. The results for the three NB PMTs are reported in the left-side plots in Fig. 4.19. The three NB PMTs observe an opposite trend from what reported in Ref. [125]; the result is robust with all the data analyzed and it does not show any evident connection with the trigger conditions. The interpretation of the result is helped by the right-side plots shown in the same figure. Here the dependence with the drift field of the *fast*, *intermediate*, and *slow* relative amplitudes is presented. It is important to emphasize the stability of the *intermediate* relative amplitude in contrast with the variation observed in the *fast* and *slow* amplitudes.

At the nominal drift field value of 0.5 kV/cm and averaging on the three NB PMTs, the $(A_{fast} + A_{int})/A_{slow}$ ratio is found to be 0.383 $\pm$ 0.019. The ratio is

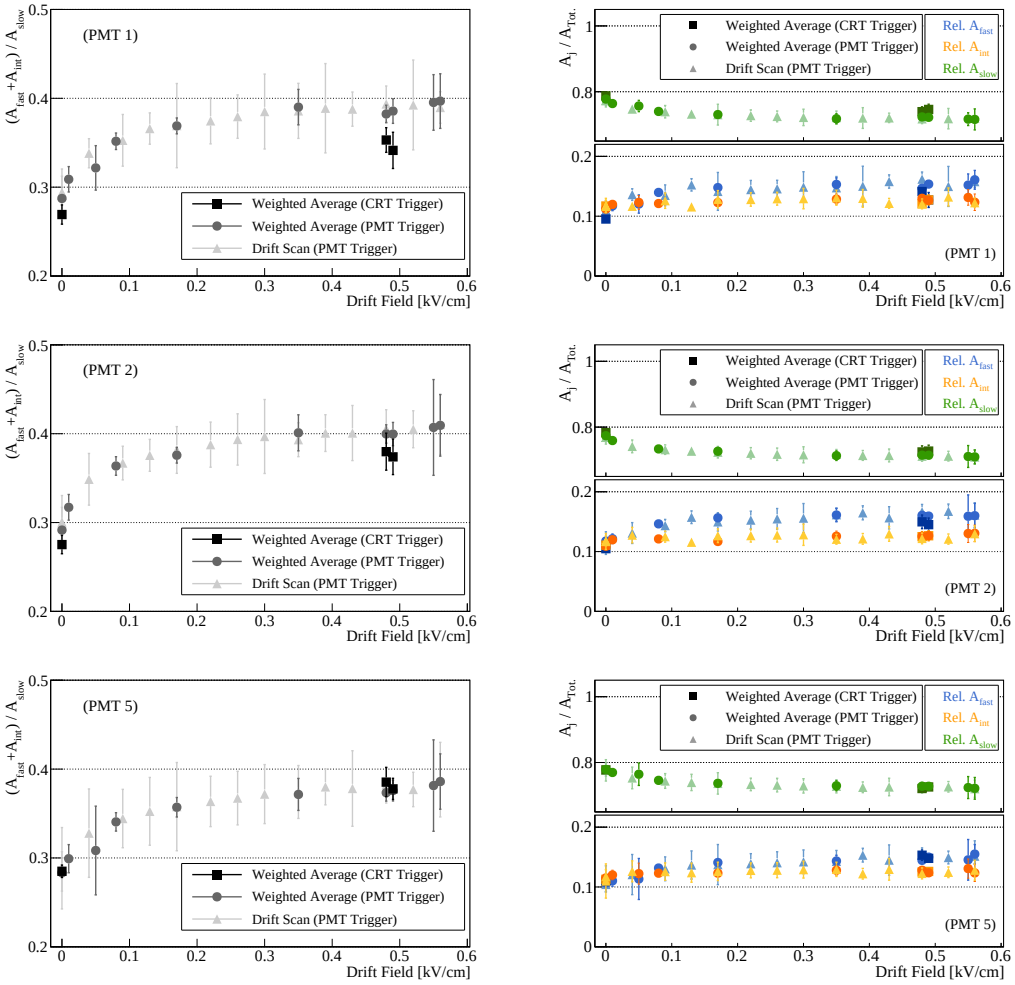

Figure 4.19.: Left: Dependence of the $(A_{fast} + A_{int})/A_{slow}$ ratio on the drift field; the result is shown for the three NB PMTs and in the two trigger configurations. **Right:** Single relative amplitudes as a function of the drift field; in contrast with the *intermediate* component (in orange shades) that remains stable, the *fast* (in blue shades) and the *slow* (in green shades) varies such that the $(A_{fast} + A_{int})/A_{slow}$ ratio increases as a function of the drift field strength.

$\sim$34% higher than the value found without the drift field. In Tab. 4.11, the values of the ratio measured by each NB PMT, and the corresponding variations compared to the value measured at the null drift field are reported. Similarly to what reported in absence of drift field, in both results, a discrepancy in the comparison between the results obtained from the data triggered by the CRT system and the PMT self-trigger is observed.

These results suggest that the fraction of singlet over triplet states created through recombination are lower than through direct excitation. This outcome is also studied by considering the dependence with the drift field of the f_{90} factor, that is independent of the waveform fit. The goal is to verify that the increase in the ratio has a physical meaning and it is not a possible artifact of the correlations between the fit parameters. The result is reported in Fig. 4.20; in Tab. 4.11, the values of the f_{90} factor measured at the nominal drift field are reported for the three NB PMTs. Each point in the graph is the mean of the f_{90} distribution fitted by a Gaussian-function and obtained including all the data collected with the same drift field conditions; the error assigned to each point is the RMS of the distribution. The data triggered by the two systems are kept separated. The f_{90} factor increases as a function of the drift field as well. Even if both the f_{90} factor and the $(A_{fast} + A_{int})/A_{slow}$ ratio show the same trend, the increase of the two observables follows a different rise which is stronger

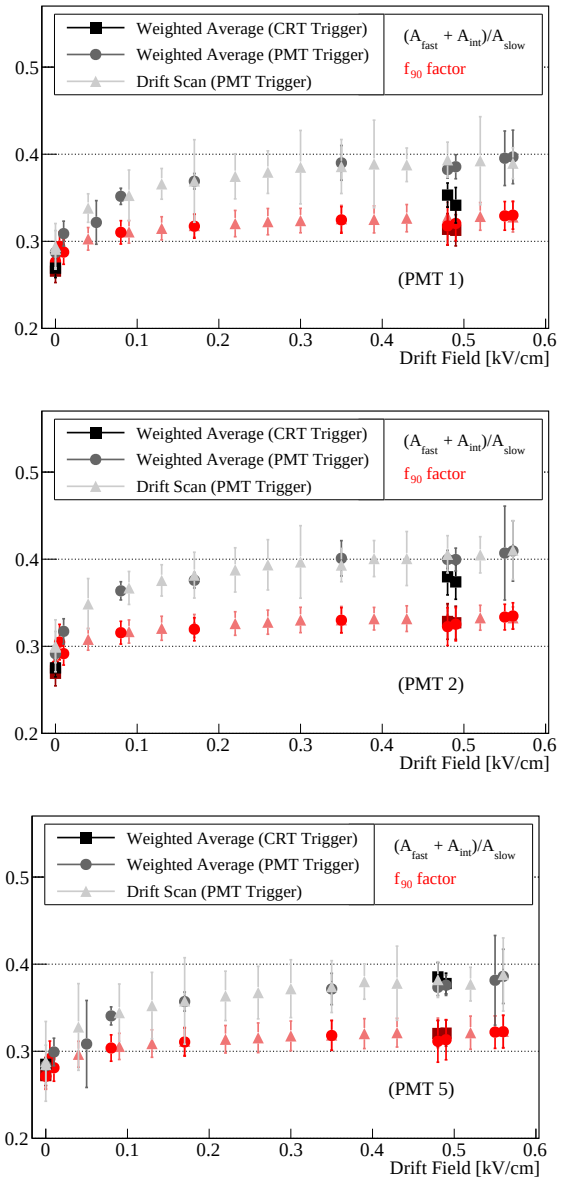

Figure 4.20.: Comparison of the f_{90} factor (red points) and the $(A_{fast} + A_{int})/A_{slow}$ ratio (in grey) dependences with the drift field strength measured in the NB PMTs.

for the $(A_{fast} + A_{int})/A_{slow}$ ratio.

This behavior is expected from the f_{90} definition itself since the total amount of light is considered in the denominator and not only the *slow* contribution. However, the increase observed in the f_{90} factor proves that the result obtained considering the $(A_{fast} + A_{int})/A_{slow}$ ratio is related with the LAr physics, implying different singlet and triplet fraction states are created through recombination. A trend similar to the increase observed in the f_{90} factor, that has never been explicitly studied in LAr, has been observed in LXe, as described in Ref. [214].

$(A_{fast}+A_{int})/A_{slow}$	PMT 1	PMT 2	PMT 5
CRT trigger	0.349±0.011	0.377±0.014	0.380±0.010
PMT trigger	0.383±0.008	0.400±0.008	0.374±0.007
average ± std	0.375±0.014	0.396±0.012	0.377±0.005
increase w.r.t. $(\mathcal{E} = 0)$	∼31%	∼37%	∼33%
f_{90}	**PMT 1**	**PMT 2**	**PMT 5**
CRT trigger	0.313±0.013	0.328±0.014	0.321±0.011
PMT trigger	0.319±0.015	0.324±0.014	0.312±0.017
average ± std	0.321±0.012	0.329±0.011	0.319±0.010
increase w.r.t. $(\mathcal{E} = 0)$	∼17%	∼18%	∼17%

Table 4.11.: $(A_{fast} + A_{int})/A_{slow}$ ratio and f_{90} factor measured in the three NB PMTs and both trigger configuration at the nominal drift field of 0.5 kV/cm; the results are obtained combining all the data collected in the (0.46; 0.54) kV/cm range.

Highlights

A complete study explicitly considering the effect of the drift field on the excimer formation in LAr has never been presented in the literature. Nonetheless, hints on the drift field impact on the dynamic of the recombination process have been mentioned in Ref. [125] concerning the effect on the slow decay time and the ratio A_{fast} /A_{slow}. The analyses presented here aimed to improve this understanding. Three important results have been pointed out:

- both the *fast* and the *slow* relative amplitudes are affected by the presence of

the drift field

- the increase of $(A_{fast} + A_{int})/A_{slow}$ ratio as a function of the drift field strength; this behavior is in contrast with what reported in Ref. [125]

- the *intermediate* relative amplitude remains unchanged also under the strongest applied drift field

As described in Sec. 2.2.2, the relative probability amplitude of populating the singlet or the triplet states have been observed to change as a function of the particle nature. Instead, for the same particle, the effect of the drift field should be related only to the recombination process as it is suppressed by the drift field. Despite that, the probability to go in the singlet or the triplet state should be independent of the mechanism process itself leading to the scintillation light formation (direct excimer formation or recombination). What is observed and reported by the previous analyses shows that the presence of the drift field affects as well as the probability of the Ar excimer to go in one of the excited states. If compared with the effect of the drift field on the total scintillation light, the two results confirm a consistent behavior: the total scintillation light decreases and this is reflected in the decreasing of the *slow* relative contribution to the total scintillation light. An additional confirmation of such behavior is given by the increase of the f_{90} factor at high drift field. A similar trend is observed in LXe and it is attributed to the effect of the drift field on the dynamics taking place in the two regimes, the recombination processes predominant in absence of drift field and the direct Ar excitation prevailing under the presence of a stronger drift field.

The last important observation regards the behavior of the *intermediate* relative amplitude. In contrast with the other two component contributions, the *intermediate* relative amplitude remains stable with the drift field. This is indirectly suggesting that the origin of this component is not related to the Ar de-excitation process.

4.3.4 An unexpected decrease of the τ_{slow} decay time

Under the hypothesis that the excimer formation through recombination processes is fast enough in comparison with the characteristic de-excitation time, τ_{slow}, the excimer needs to de-excite from the triplet to the ground state. The decay time is

not supposed to change if the drift field is applied, neither if the relative population of the singlet and the triplet states does. Nevertheless, the dependence of the τ_{slow} with the drift field is not constant and, in particular, its value becomes smaller for stronger values of the drift field, as reported in Fig. 4.21; on the left side of the figure, an example of the measurements obtained from an NB PMTs is shown and, as a comparison, the measurement obtained from a PB PMT is reported on the right side of the same figure, confirming the same trend. The five PMTs show the same trend, independently from the base or the trigger configurations. Aver-

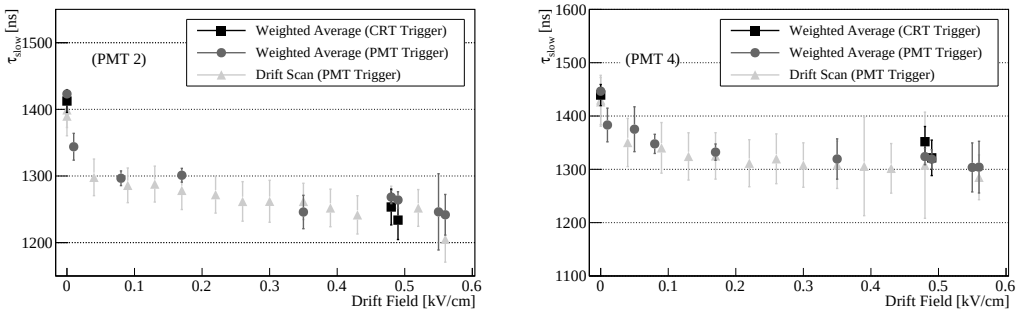

Figure 4.21.: Triplet lifetime τ_{slow} as a function of the drift field measured by an NB PMT on the **left**. Even though the absolute measurement of *slow* decay time obtained by PB PMTs could be biased, the decreasing trend is confirmed; an example is reported on the **right**. The results from all the other PMTs confirm the same behavior.

aging the results from the three NB PMTs, at the nominal value of the drift field (0.5 kV/cm), a $\tau_{\text{slow}} = (1276 \pm 44)$ ns is found. The value is ∼10% lower than the slow decay time measurement performed in the total absence of the electric fields. The τ_{slow} measured for each NB PMT at the nominal drift field and the variation with respect to the value found at zero field are given in Tab. 4.12. In contrast with

	PMT 1	**PMT 2**	**PMT 5**	mean ±std
τ_{slow} **at** $\mathcal{E}_{0.5\ kV/cm}$	1267±21	1263±21	1299±33	1276±44
decrease w.r.t. $(\mathcal{E} = 0)$	∼11%	∼11%	∼10%	∼10%

Table 4.12.: Measurement of the *slow* decay time at the nominal drift field strength of 0.5 kV/cm. The values reported are obtained from the NB PMTs combining the results found in the drift field range of (0.46; 0.54) kV/cm. The decrease reported for each PMT is calculated from the corresponding value observed at the null field.

what reported on the relative populations of the singlet and triplet states, this result is in agreement with the hint reported in Ref. [125]. The main reason identified so far able to decrease the τ_{slow} is the presence of impurities. However, if a drop of the LAr purity could be considered as an explanation for the results reported in Ref. [125], given the small τ_{slow} reported, this effect is excluded in the interpretation of this analysis. Two evidence support this conclusion:

- the result is confirmed by the drift scan data, collected in a very short time (∼2 hours)
- no variations in the LAr purity have been observed in the monitoring of the τ_{slow} over the complete data collection period

The data collected in the dedicated drift scan are reported in grey in the figure. At the nominal drift field value, a strong agreement on the τ_{slow} measurement with the other runs is observed in the five PMTs. As the dedicated drift scan has been performed in controlled purity conditions in less than two hours, the effect of the impurities is excluded from the interpretation of these results.

Highlights

Basing the scintillation time profile description on the mechanisms known so far and with the hypothesis that the excimer formation is always very fast in comparison with the de-excitation time, no variation of the decay time with the electric field is foreseen. Despite this, a hint of the τ_{slow} decreasing under a very strong drift field has been pointed out in Ref. [125]. On the other hand, the effect of the drift field on the scintillation light has been studied in LXe and the dependence of the effective decay time with the field strength has been observed and reported in Ref. [214]. It is important to notice that the decay times in LXe[9] are much smaller than the ones in LAr, especially in the case of the slow decay time; because of that, it is not possible to make a direct analogy between the two observations. An interpretation of the result observed in this analysis considering the dynamic of the recombination processes in LAr has been explored in Sec. 4.4.

[9]The LXe de-excitation is much faster than LAr ones, the τ_{fast} has been measured ∼2 ns and τ_{slow} ∼22 ns [125].

Given the novelty of the result and the motivation to find an explanation for it, the approach used to conclude this analysis is the following:

- a dedicated study to exclude artifacts in the fit caused by the correlations among the parameters has been performed
- consider and test different hypotheses, to the extent of the available data taken with WA105 DP demonstrator

In particular, the hypothesis of a variation of the relative population of singlet and triplet states but a constant value of the decay times as a function of the drift field is tested by doing a global fit to the scan runs with a common value for the decay times, whereas the normalization constants can vary with the field. Both items will be presented in the following sections; however, before describing them, a summary of the behavior of the remaining parameters, in particular the τ_{int} dependence with the drift field, will be presented hereafter.

4.3.5 Stability of the τ_{int} decay time

In contrast with what has been reported about the τ_{slow}, the *intermediate* decay time does not show any dependence with the drift field. The results for the three NB PMTs are reported in Fig. 4.23. The trend of τ_{int} as a function of the drift field is stable in both trigger conditions, as well as in the data collected during the drift scan. The average value, shown by the red line in each plot of the figure, confirms the measurements that have been done in the absence of the drift field: $\tau_{\text{int}} = (50.7 \pm 4.1)$ ns; both measurements are in agreement within the errors. It is interesting to highlight that neither the relative contribution of the *intermediate* components to the total scintillation light nor the *intermediate* decay time depends on the drift field; this behavior is in contrast with what measured for the *fast* and the *slow* component parameters. Because of that, these two empirical observations indirectly reinforce the hypothesis of the origin of the intermediate component being independent from the excimer formation and de-excitation. As described in Sec. 2.2.2.3, one of the most accepted descriptions of the *intermediate* origin is interpreted as due to the delayed re-emission of the photons absorbed by the wavelength shifter material. If this hypothesis was true, two delayed contribution would be foreseen: τ_{int} and τ_{fourth} (Ref. [148] and [144]). Nevertheless, from the conclusion of the analyses

presented so far, only a solid measurement of the *intermediate* decay time was possible; whereas, a likewise detailed analysis of the *fourth* component was not achievable. The limitation on exploring its presence is determined by the acquisition window and the conditions of the data collected. The preliminary measurement of the *fourth* component performed in absence of the drift field led to its observation around $\sim$6 μs. To guarantee its correct understanding also at higher values of the drift field, data collected in the absence of amplification field must be used. Moreover, high statistics is necessary to avoid its misinterpretation with pedestal fluctuations; but, unfortunately, no runs are available collected in these conditions.

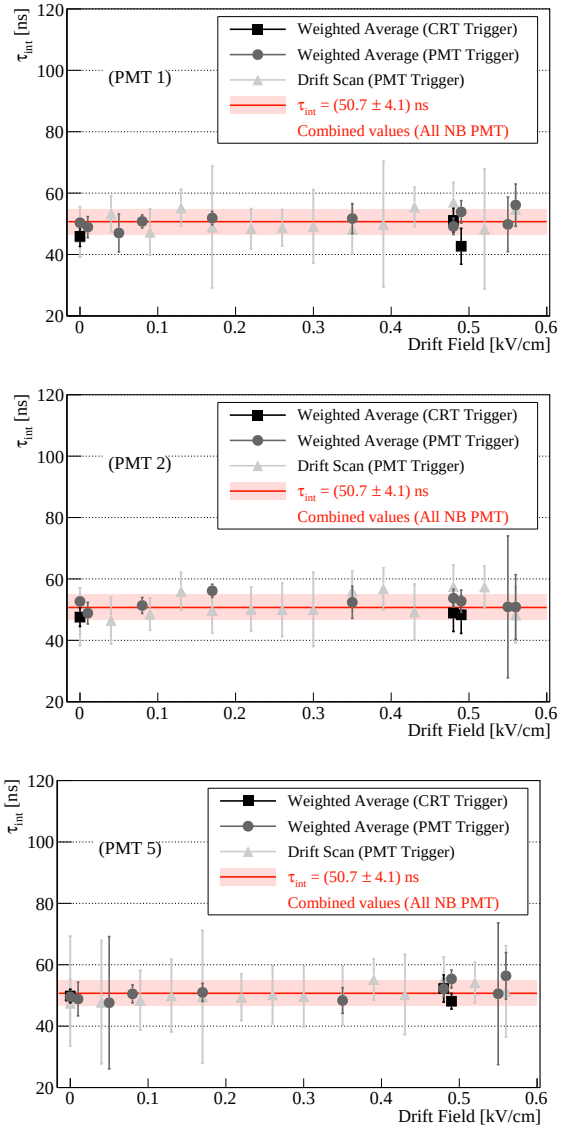

Figure 4.22.: Dependence of the *intermediate* decay time τ_{int} as a function of the drift field reported in the three NB PMTs; no variations are observed neither at the strongest drift field value reached.

The effect on the other parameters

In analogy with what has been reported in the absence of the drift field (Tab. 4.7), the fit parameters measured for the NB PMTs, at the nominal drift field are reported in Tab. 4.13. The values given in each column of the table for each PMT are the

weighted average of the results obtained from all the runs collected in the drift field range of (0.46, 0.54) kV/cm. The error assigned to each parameter is obtained by summing in quadrature the statistical error and the dispersion among all the runs. In the last column, the average of the three NB PMTs is showed. In addition to what commented on the decay times and the relative amplitudes, it is relevant to notice that both the t_0 and the σ do not depend on the drift field strength. Similarly, the absolute values of the *fast* and *intermediate* normalization constants remain constant within the errors also at the nominal drift field; whereas, the absolute value of the *slow* normalization constant decreases. The contribution of the *fast*, the *intermediate*, and the *slow* relative amplitudes to the total scintillation light produced at 0.5 kV/cm are 15%, 13%, and 72%, respectively.

fit parameter	**PMT1**	**PMT2**	**PMT5**	**average ± error**
t_0 [ns]	-2.30±0.25	-2.21±0.26	-2.42±0.26	-2.31±0.44
σ [ns]	6.38±0.36	6.37±0.36	6.56±0.44	6.44±0.67
τ_{fast} [ns]	6 [fixed]	6 [fixed]	6 [fixed]	—
τ_{int} [ns]	50±3	52±2	50±2	50.7±4.1
τ_{slow} [ns]	1267±21	1263±21	1299±33	1276±44
A_{fast} [a.u.]	3.95±0.18	3.96±0.14	4.00±0.17	3.97±0.28
A_{int} [a.u]	3.40±0.29	3.12±0.15	3.41±0.31	3.31±0.45
A_{slow} [a.u]	19.40±1.77	17.74±2.14	19.74±1.25	18.96±3.05

Table 4.13.: Measurement of all the fit parameters obtained by analysing all the data collected at the nominal value of the drift field 0.5 kV/cm. The error of each parameter is obtained including the statistical error and the dispersion among all the runs. In the last column, the average of the three NB PMTs is considered; in the error, the standard deviation among the three PMTs results is considered.

4.3.6 Multi-fit approach and interpretation of the results

Before looking for a physical explanation of this phenomenon, in this section a different analysis aiming to exclude a hidden effect introduced by the correlation between the parameters of the fit is presented. The alternative approach consists in performing a simultaneous multiple fit (*global-fit*) to all the average waveforms

corresponding to each value of the applied drift field. The scintillation time profile is still modeled by Eq. (4.1b) but separating the parameters that are expected to depend on the drift field from the ones that do not. The hypothesis behind the *global-fit* approach is that the drift field could affect only the de-excitation probabilities from the singlet or the triplet energy states but not the corresponding decay times. Consequently, in the simultaneous fit, the σ of the Gaussian and the decay times are supposed to be common parameters that cannot vary under different drift field strengths; whereas, all the others are considered local parameters. The main goal of the analysis is to disclose a possible artifact induced by the strong correlations between each normalization constant and the corresponding decay time. Hence, if this is the case and the *global-fit* converges finding a common value for $\tau_{\rm slow}$, the dependence of $A_{\rm slow}$ with the drift field strength should be modified in turn. Finally, since the purpose of the analysis is only to study the effect of the correlations, all the parameters, except the pedestal, are left free in the procedure; the fit procedure uses a χ^2 minimization obtained with the MINUIT package [213]. For that, only the runs collected in the drift scan are included.

In Fig. 4.23, for PMT-1, the fifteen average waveforms (for drift field values in the 0-0.56 kV/cm range) are shown by the black points. The two fit approaches, the global fit in light blue and the single fit in red, are reported for comparison. Given the RMS error assigned in each waveform bin, both methods converge; however, the relative position of the two fit curves is inverted if compared at null or at the highest drift field, determining the change in the slop calculated by the single-fit. This outcome is better described by the top-plots in Fig. 4.24, giving the comparison of the decay times obtained as common parameters in the *global-fit* procedure (light blue) and in the average value of the single calculations, performed *run-by-run* (red lines). In the case of the $\tau_{\rm fast}$ and $\tau_{\rm int}$, the two results are consistent; despite the values of the $\tau_{\rm slow}$ obtained in the single-fit vary with the field, its average is in agreement with the value retrieved by the *global-fit*. Moreover, despite the global fit is able to find a common value for $\tau_{\rm slow}$, the values found with the two approaches, for the normalization constants and the relative amplitudes remain exactly the same, as shown in the middle and bottom-plots of Fig. 4.24, excluding the possibility that the $\tau_{\rm slow}$ variation with the fit is artificial. Finally, it is interesting to notice the values the two fit procedures retrieve for $\tau_{\rm fast}$ and $\tau_{\rm int}$, after releasing the $\tau_{\rm fast}$ parameter. As expected from the toy-MC studies, both decay times are shifted at higher values.

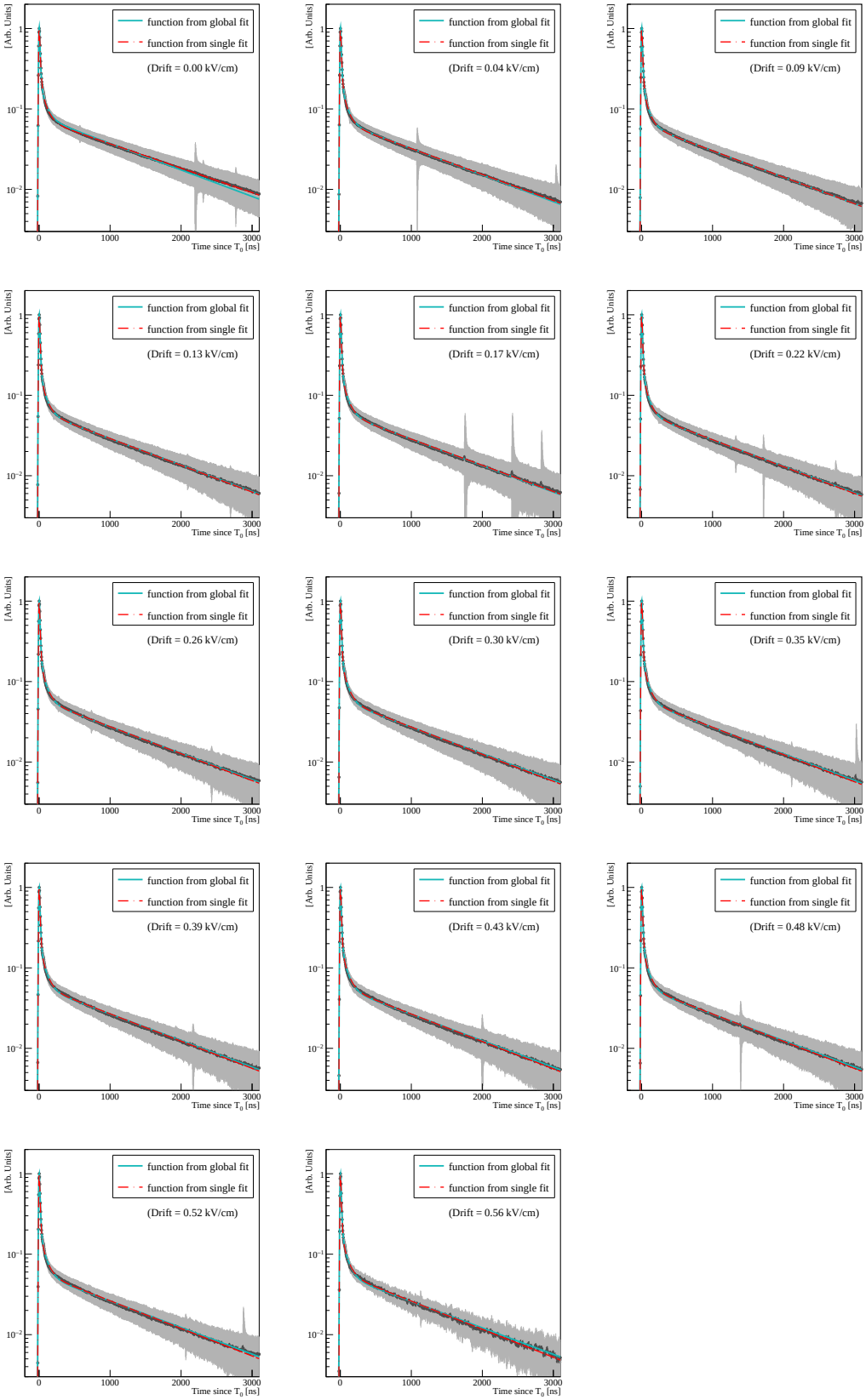

Figure 4.23.: Comparison of the two fit approaches, the *global-fit* (light blue lines) and the single fit (red lines) reported in the fifteen average waveforms collected under the presence of the increasing the drift field in the 0-0.56 kV/cm range.

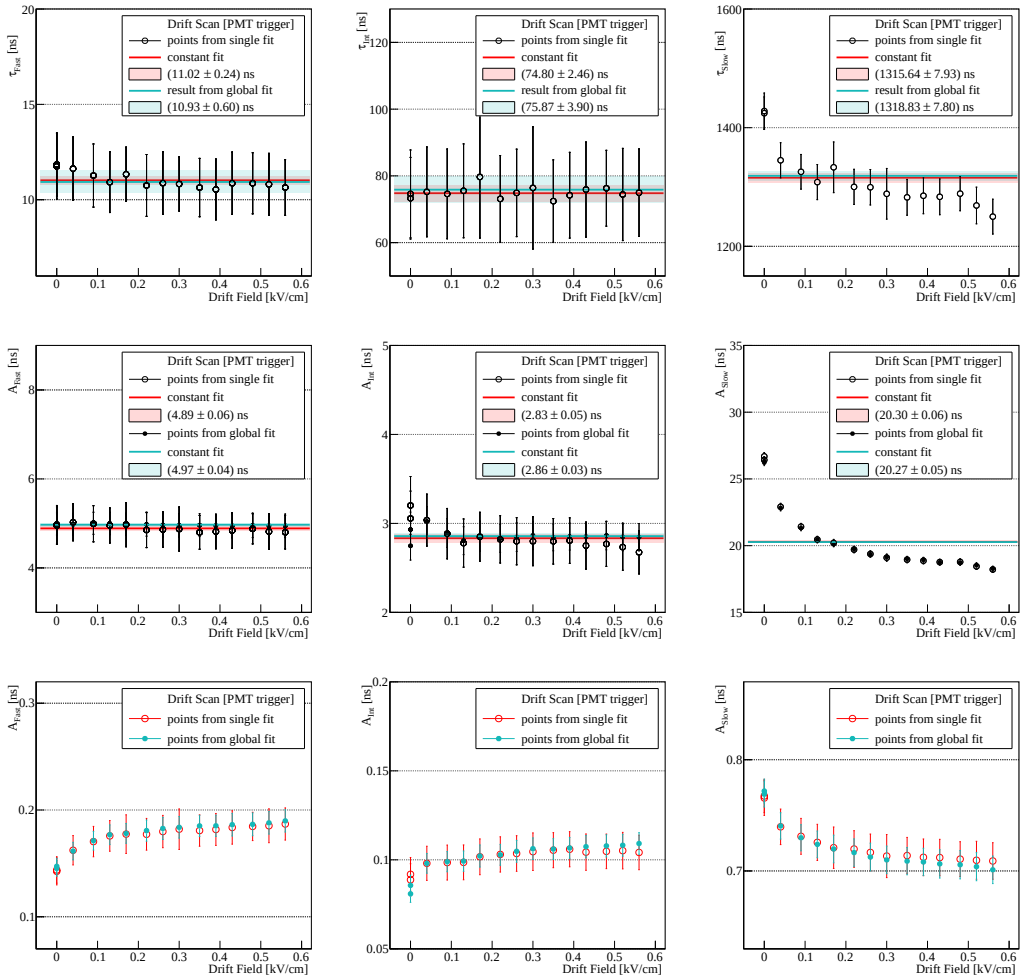

Figure 4.24.: Comparison of the results obtained for the scintillation time parameters retrieved by the two fit approaches. The results obtained by the *global-fit* approach are reported by the light blue lines and points; the results obtained by the single fits are reported by the red lines and points. The decay times are reported in the **top**-plots and the normalization constants in the **middle**-plots. In the **bottom**-plots the relative amplitudes obtained with the two approaches are compared.

Performing a linear fit of the values obtained by the single fits, the *fast* decay time is found at (10.9 ± 0.6) ns and the *intermediate* decay time is found at (75.9 ± 3.9) ns; the results obtained by the *global-fit* are in agreement with the others: $\tau_{\text{fast,global}}$=(11.0 ± 0.3) ns and $\tau_{\text{int,global}}$=(74.6 ± 2.6) ns. All the values of the decay times and normalization constants are summarised in Tab. 4.14; for the single fit results, the mean values are given. The same study has been performed also fixing

τ_{fast} at 6 ns and the conclusions are consistent with the ones described above, the main difference is observed in the value found for τ_{int} that, in both approaches, is lowered at ∼55 ns (average on the single-fits) and ∼61 ns (*global-fit*), still in agreement within the errors.

parameter	single fit	global fit
τ_{fast}	11.0 ± 0.3 [ns]	10.9 ± 0.6 [ns]
τ_{int}	74.6 ± 2.6 [ns]	75.9 ± 3.9 [ns]
τ_{slow}	1315.99 ± 8.22	1318.83 ± 7.80 [ns]
A_{fast}	4.88 ± 0.06 [arb. units]	4.97 ± 0.04 [arb. units]
A_{int}	2.83 ± 0.05 [arb. units]	2.86 ± 0.03 [arb. units]
A_{slow}	20.38 ± 0.06 [arb. units]	20.27 ± 0.05 [arb. units]

Table 4.14.: Evaluation of the average value of each scintillation time parameter retrieved by *global-fit* approach or by performing individual fits.

Highlights

The scintillation time profile described by Eq. (4.1b) is based on a modelization with strongly correlated parameters. The complexity in finding a physical explanation of the τ_{slow} decrease as a function of the drift field motivated the development of an alternative analysis aiming to exclude artifacts introduced by the modelization itself; in particular, due to the strong correlation between the *slow* normalization constant and decay time. The simultaneous fit of the drift field scan runs is based on the hypothesis that considering τ_{slow} as a global parameter independent from the drift field would remove, in turn, the dependence of A_{slow}, considered as a local parameter, with it. The fact that this interdependence is not removed by the *global-fit* approach confirms the physics origin of the phenomenon.

4.4 Discussion of the results and possible interpretations

The presence of the drift field has the role of suppressing the recombination processes and their contribution to the total scintillation light production. For this reason, the study of its effect on the scintillation time profile opens the possibility to

investigate how the dynamic of the recombination processes is affected. Two unusual behaviors have been observed compared with what was reported in the literature, related to the impact of the drift field on the probability of populating the singlet or the triplet state and the de-excitation time from these energy levels. Based on the results reported on both the total scintillation light yield (the $S_{1,drift}/S_{1,0}$ ratio) and the $(A_{fast} + A_{int})/A_{slow}$ ratio, it appears that the probability of exciting the Ar_2^* to the singlet or the triplet states is not equally affected; in particular, the probability of populating the latter energy level is preferred by the recombination processes more than by the direct excimer formation. Given the complexity of the excimer formation and the connection of the electron dynamics with the presence of even small amount of impurities and/or the Ar-ions present in the active volume, it is complicated to identify a conclusive explanation for the results observed. However, the second finding reporting the decrease of the *slow* decay time in all the runs analyzed where no variation of the LAr purity has been observed reinforces the hypothesis that the outcomes reported are due to the drift field influence on the recombination dynamic, possibly through the formation mechanisms.

The main difference between the direct excimer formation and its formation by the recombination process is in the characteristic times of the mechanisms leading to Ar_2^+ -e^-. Following the description given in [125], based on the Onsager's model, the recombination dynamic is expressed in terms of the evolution of the electron density, n_-, in the Onsager's cylinder, and of the electron escaping probability, η, from the Coulomb attraction within the cylinder: $n_-(t) = (1-\eta)n_0$, being n_0, the initial number of ion-e^- pairs. Consequently, the more general way to express the dependence of the scintillation light with the time (scintillation time profile) is the following:

$$L(t) = \frac{e^{-t/\tau}}{\tau} \int_0^t f(x) e^{x/\tau} dx \tag{4.6}$$

where the function f(x) has a different expression depending on the rapidity on which the ion-e^- pairs recombine and two extreme cases are considered. Only under the hypothesis that the time needed for the ion-e^- to recombine is negligible, compared to the excimer formation mechanism, the de-excitation from the excited state can be approximated by the usual expression: $L(t) \sim \exp(-t/\tau)/\tau$. On the opposite, the other possibility is an *infinite* (very slow) recombination time, T_R, compared to the excimer formation. In this second case, still under the hypothesis of $\eta = 0$, the

scintillation time profile is sensitive to T_R and their relation is the following:

$$L(t) \propto \frac{1}{(1+\frac{t}{T_R})^2}; \tag{4.7}$$

consequently, the shape of the scintillation time profile is also function of T_R. In Ref. [125], the variation of the scintillation time profile with both direct and recombination contributions to the scintillation light production (in absence of drift field) and considering only the direct excimer formation to it (in presence of a strong drift field) is reported for LAr and LXe in Fig. 4.25. Although neither the modelization

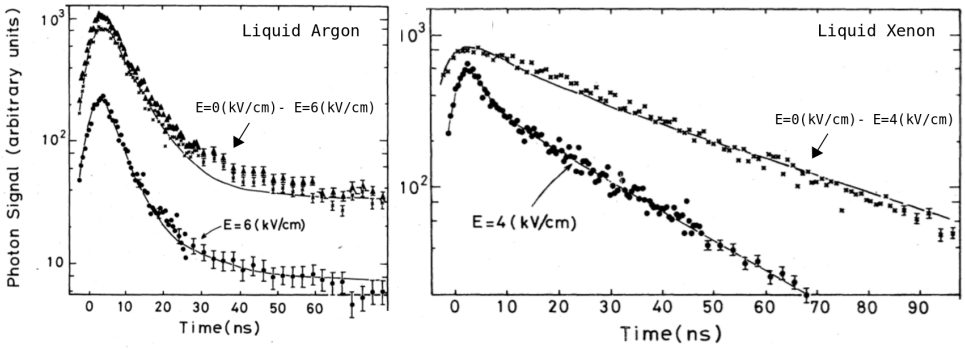

Figure 4.25.: Scintillation time profile measured, without (**triangles**) and with (**full-dots**) an applied electric field; the difference curve between the two represents the recombination contribution (×); the results referred to LAr are shown on the **left** and the ones referred to LXe on the **right**. The plots are taken from Ref. [125].

used for fitting the scintillation time profile nor the treatment of the *intermediate* component is explained, in LXe an evident variation of the scintillation light profile is observed. The behavior in the LAr is not so evident, instead. The interpretation is assigned to the measurement of the T_R reported for LAr, $T_R = (0.8 \pm 0.2)$ ns, considered too fast to have a significant influence on the scintillation time profile. It is important to remind that the value reported for T_R is the only measurement found in the literature, and the τ_{slow} reported in this study, in both drift field conditions, is in a range considered affected by the presence of photo-sensitive contaminants.

In the analyses presented in the previous sections, instead, a relation with this kind of interpretation is motivated by the comparison of the scintillation time profile in Fig. 4.18, the decrease of the τ_{slow} in Fig. 4.21, and by the variation of the relative amplitudes reported in Fig. 4.19. Finally, it is important to highlight the

opposite behavior mentioned for the ratios A_{fast} $/A_{slow}$, in Ref. [125], and the trend reported for the $(A_{fast} + A_{int})/A_{slow}$ ratio, in the analysis presented. In this analysis, the *intermediate* component is explicitly considered and found to be independent of the drift field, and the trend reported for the $(A_{fast} + A_{int})/A_{slow}$ ratio can be explained only if the A_{fast} $/A_{slow}$ ratio in the recombination process is lower than the A_{fast} $/A_{slow}$ ratio caused by the only contribution due to the direct excimer excitation. Both the dependence of the $S_{1,drift}/S_{1,0}$ ratio on the integrated light (Tab. 4.10) and the dependence of the f_{90} factor on the drift field (Fig. 4.3.3) reinforce this hypothesis. However, the data analyzed in the WA105 DP demonstrator reaches the maximum drift field of ∼0.5 kV/cm, where 40% of scintillation light comes from recombination process (see Fig. 4.15); hence, dedicated measurements to verify this interpretation of the results, but reaching higher drift field able to completely suppress the recombination contribution to the total scintillation light, are very encouraged. This finding, in fact, can be even more interesting in LAr-TPCs experiments (e.g. DM experiments) using the pulse shape discrimination for particle identification, since this approach is motivated by the A_{fast} $/A_{slow}$ ratio behavior.

"Fais apparaître ce qui sans toi ne serait peut-être jamais vu."

R. Bresson

CHAPTER 5

THE SCINTILLATION LIGHT PROPAGATION IN THE LIQUID PHASE

In big detectors, a key role is covered by the impact of the Rayleigh scattering length that attenuates the light. However, the Rayleigh scattering length measurement is complicated by the competition of several factors contributing to the scintillation light attenuation, as the presence of optically active impurities or absorbent elements. In this chapter, a first estimation of the VUV light attenuation length observed in the WA105 DP demonstrator will be given (Sec. 5.1). Hence, with the purpose of disentangling the effect of the Rayleigh scattering from the other contributions attenuating the light (VUV light absorption and reflection in the TPC components), a detailed Monte Carlo (MC) simulation has been developed.

In Sec. 5.2, the general description of the simulation will be given separating the three fundamental steps on which the simulation is based: the approach used to propagate the light inside the demonstrator (Sec. 5.2.3), the event generation (Sec. 5.2.2), and the simulation of the physics processes leading to the scintillation light signal detected by the PMTs (Sec. 5.2.4). The validation of the MC will be illustrated (Sec. 5.3) both from the geometrical point of view (Sec. 5.3.1) and considering the collected light by each PMT (Sec. 5.3.2). Finally, in Sec. 5.4, the study dedicated to evaluate the impact of both the Rayleigh scattering length and the reflectivity of the detector elements (Sec. 5.4.1) will be discussed.

A brief discussion on the extrapolation to bigger detectors will be given in Sec. 5.5.

5.1 Study of the attenuation length in the WA105 DP demonstrator

As described in Sec. 2.2.3, the attenuation length is the result of competing factors as the presence of optically active impurities, absorption of the light in the detector material, and Rayleigh scattering. The goal of the analysis presented in this section is the evaluation of the attenuation length for the VUV scintillation light produced by the muons crossing the LAr volume of the WA105 DP demonstrator; whereas, in Sec. 5.4, the discussion will be focused on the Rayleigh scattering length by comparing the WA105 DP demonstrator data with the MC simulations. For the analyses presented in this chapter, all the data detected with the CRT external trigger in shifted geometry and in absence of drift field are included. The CRT trigger selection described in Sec. 3.8 is applied; in addition to these cuts, only the muons crossing the field cage (FC) volume are accepted, rejecting all the tracks whose closest point is in the LAr AV between the FC cathode and PMT surface. The reason for that is related to the absorption of the photons by the cathode and ground-grid surfaces. As will be clarified in Sec. 5.2.3.1, even if transparent, both surfaces drastically dampen the probability of a VUV photons to be detected.

In order to estimate the attenuation length, the dependence of the primary scintillation light on the minimum approach distance from the muon track to the PMT surface is considered; the amount of attenuated light during the propagation is manifested as an exponential decay as a function of the distance from the charged particle track to the PMT. In Fig. 5.1, the 2-D plot of the S1 light as a function of the minimum approach distance is presented for three of the five PMTs. In these plots, the detected S1 light is obtained integrating the recorded PMT waveform over the whole 4 μs time window. It is relevant to notice that the collected light (y-axis) is shifted at lower values for the PMTs with the TPB coated on the PMMA plate, as explained in the Sec. 3.9.2; but, at a given track-PMT distance, the amount of detected light is the same if the WLS configuration is similar. However, the position of the most populated region, in each plot, changes depending on the PMT number; the reason for that is in the CRT panel position and the diagonal topology of the selected tracks in such geometry.

Defining x as the minimum approach distance, the estimation of the attenuation

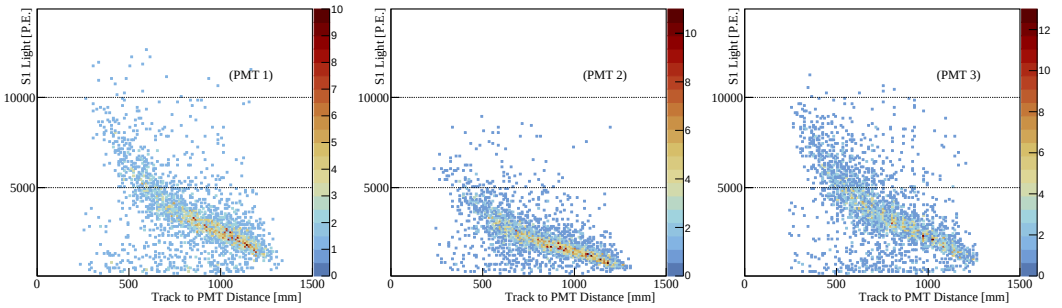

Figure 5.1.: 2-D distributions of the S1 light, integrated over 4 μs, as a function of the minimum approach distance. The typical *muon-like* event selection for track triggered by the CRT panels is applied; only muons inside the FC volume are accepted.

length can be performed fitting the scintillation light detected by each PMT as a function of x. The S1 mean charge is calculated from a Gaussian-fit of the S1 charge projection distribution, every track-PMT distance bin of 20 mm; the mean and the sigma retrieved by the fit represent respectively the S1 mean and the corresponding error. An example of the Gaussian fit is shown in Fig. 5.2. The simplest way to model the correlation between the S1 integrated light and the minimum approach distance can be described by the following equation:

$$\mathrm{L}(x) = \mathrm{A}\exp(-x/\lambda_{\mathrm{Att}}) \qquad (5.1)$$

where λ_{Att} is the attenuation length. In Fig. 5.3, examples of the mean S1 light, blue points, as a function of the minimum approach distance are shown for PMT-1 and PMT-2; the fit is done separately for every PMT. The red

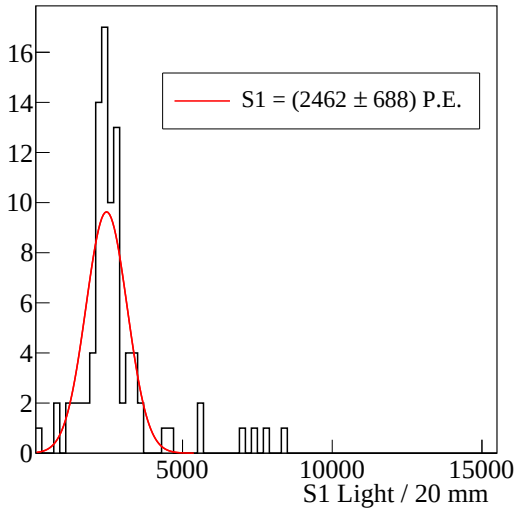

Figure 5.2.: Example of S1 light distribution obtained in one 20 mm bin. In red, the Gaussian fit to retrieve the S1 mean light at each bin is shown; the Gaussian σ is assigned as the error.

lines in Fig. 5.3 correspond to the fitted function obtained using Eq. (5.1), for the extracted value of λ_{Att} shown in the legends. The results for the five PMTs are

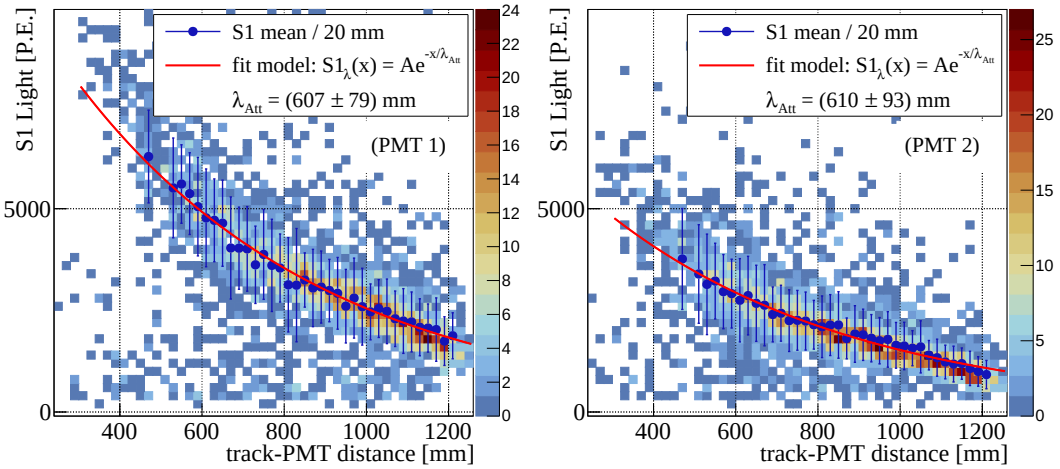

Figure 5.3.: Mean of the S1 light (blue points) as a function of the minimum approach distance modelled by Eq. (5.1) (red line).

represented by the blue points on the left of Fig. 5.4; averaging the results from the five PMTs, the attenuation length is estimated to be (551 ± 27) mm. Given the

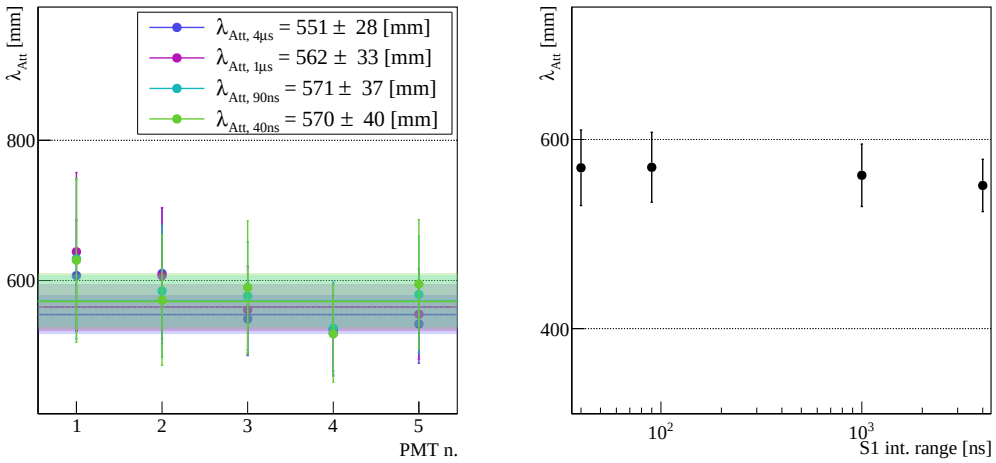

Figure 5.4.: Left: Measurement of the attenuation length measured by the five PMTs in the four integration time ranges: 40 ns in green, 90 ns in cyan, 1 μs in magenta, and 4 μs in blue. **Right:** The average on the five PMTs is reported as a function of the integrated charge range.

dependence on the track topology of the scintillation light pointed out in the previous chapter, the dependence of the attenuation length with the integration range has been considered. Since the impact has been found to be more evident in the slow contribution to the total scintillation light; the measurement of the attenuation length has been performed considering different ranges for the S1-charge integration. For the five PMTs, the results are reported on the left of Fig. 5.4. The results obtained from the fit of the distribution with the S1 light integration range in 40 ns are shown in green, the ones from 90 ns in cyan, from 1 μs in magenta, and the results obtained considering the S1 light integration in the whole 4 μs acquisition windows are drawn in dark-blue. Independently from the integration range, the five PMTs give consistent results. The average value for λ_{Att} at each integration range is obtained by performing a linear fit of the five points; the results are summarized in Tab. 5.1. The attenuation length as a function of the integrated S1 light is shown in the right-plot reported in Fig. 5.4. The trend shows a slight increase of the mean value of the attenuation length for shorter integration ranges, however, always covered by the error bars. In particular, the average value of the VUV attenuation

PMT n.	**1 (NB) direct**	**2 (NB) plate**	**3 (PB) direct**	**4 (PB) plate**	**5 (NB) direct**
$\lambda_{\mathrm{Att,S1\ 4\mu s}}$ [mm]	607±79	610±93	545±52	525±54	538±56
$\lambda_{\mathrm{Att,S1\ 1\mu s}}$ [mm]	641±113	607±97	558±62	530±66	552±64
$\lambda_{\mathrm{Att,S1\ 90ns}}$ [mm]	631±114	585±94	578±77	532±66	580±83
$\lambda_{\mathrm{Att,S1\ 40ns}}$ [mm]	629±117	572±93	590±95	524±69	595±92

Table 5.1.: Attenuation length measured by the five PMTs in the four integration time ranges.

length when the integrated light is in 40 ns, λ_{Att} is found (570 ± 46) mm. The error reported is the sum in quadrature of the error from the fit, the dispersion among the PMTs, and the systematic uncertainty taking into account the precision of the minimum approach distance allowed by the width of the CRT strips, which is of the order of 3%.

Comparing the effect of the O_2 concentration to the light transmittance described in Ref. [152], given the measurement of the electronegative impurity concentrations in the WA105 DP demonstrator at the end of the filling (0.1 ppm and 7 ppm, for O_2 and H_2O respectively) and the measurement of the τ_{slow} (1.426 μs), a large attenuation of the light caused by the impurities concentration is not expected. Despite that, in the WA105 DP demonstrator, the TPB is present only on the PMTs; because of that, the short reported attenuation length suggests the possibility that absorptions introduced by the material of the internal field cage elements can be responsible for the value found in this analysis. In particular, the measured attenuation length in each PMT is much smaller than the most recent measurements of the Rayleigh scattering length ($\sim$99.9 cm) [166] and does not show an evident correlation with the PMT position inside the detector. For these reasons, the strong light absorption is interpreted as taking place in the cathode and/or in the ground-grid. The impact of their contributions to the attenuation length, as well as of the other detector components, will be investigated from the data-MC comparison that will be discussed in the following sections.

5.2 Light MC simulation for the WA105 DP demonstrator

With the objective of further studying the effects influencing the scintillation light propagation and collection, a detailed Monte Carlo (MC) simulation has been developed to be compared with the results obtained from the data analysis. The event generation is driven by data, mimicking the *CRT-shifted* geometry. Due to the large number of photons produced by each interacting particle, an innovative approach is used to propagate the light inside the detector. The method has been developed to make the MC simulation faster, and performing the simulation of the light propagation inside the whole detector volume only once and storing the key parameters in dedicated 3-D *light-maps*, accessible for each generated event.

The main steps leading to the MC simulation will be presented in this section: the simulation of the detector geometry, the event generation, the simulation of the light propagation inside the detector, and the simulation of the physics mechanism allowing to simulate the scintillation light signal detected by each PMT.

5.2.1 Detector geometry

In order to properly take into account the light propagation inside the detector, a detailed simulation of the detector geometry has been implemented in GEANT 4 [215]; it includes the CRP, the field cage, the cathode plane, the ground grid as well as the five PMTs with their photocathode design and characteristic WLS configurations. The reflectivity of both the VUV and visible light on the FC structure may not be negligible; however, it strongly depends on their manufacturing. In the MC simulation developed for the WA105 DP demonstrator, the default values set for the reflectivity of stainless steel and copper surfaces are 0% and 50% for VUV and visible light, respectively; in Sec. 5.4.1, the impact of these values on the light propagation will be discussed. The PMT geometry is well reproduced including the two configurations used for the TPB coating, with the PMMA plates above PMT-2 and PMT-4; for the VUV photons, a 100% TPB efficiency is assumed. The converted visible photons are consequently emitted isotropically with the wavelength peaked at 435 nm. The PMT acceptance takes into account the position of the incident angle with respect to the normal vector to the PMT surface, expressed by the ϕ-angle [217] in Fig. 5.5, and the θ-angle of the photon related to the photocathode [218], expressed by the θ-angle in the same figure. Consequently, the function describing the PMT response is the following: $f(\theta) \times g(\phi)$; its dependence with the photon incident angle is represented in Fig. 5.5.

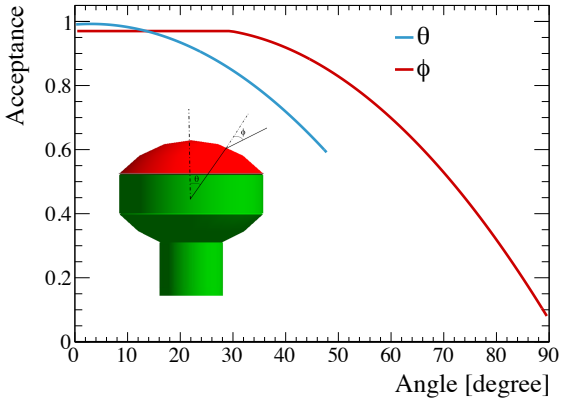

Figure 5.5.: Characteristic dependence of the PMT acceptance with the incident angles of the VUV photons [216].

5.2.2 Event generation

The *muon-like* event generation in the MC reproduces the *CRT-shifted* geometry studied in the data. In the MC, only the LAr AV, as defined in Sec. 3.3.1, is

simulated; hence, neither the CRT panels nor the optical inactive regions in the detector are simulated. The *muon-like* events are considered as muons at the MIP

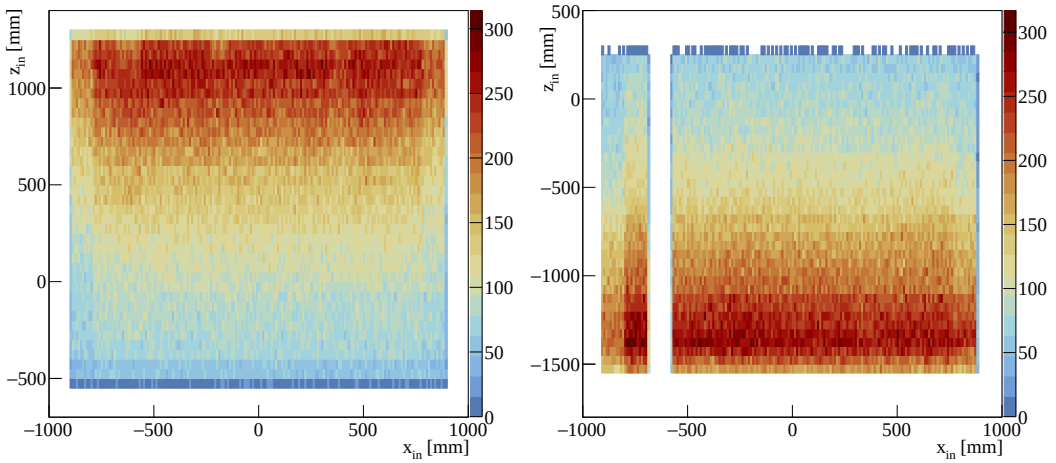

Figure 5.6.: *CRT-maps* corresponding to the upper panel (*wall*-side, on the **left**) and the lower panel (*door*-side, on the **right**) obtained from ∼61 hours of data taking in *CRT-shifted* geometry.

energy; hence, 4 GeV/c muons are generated in GEANT 4, following the *CRT-shifted* geometry. The generation of the cosmic muons is directly done in the LAr AV with a data-driven topology. In particular, the typical (θ, ϕ) space phase shown on the right of Fig. 3.13 is reproduced in the MC by generating events with the same coordinates as the ones observed in the data. From the data recorded in a long *CRT-shifted* run (∼61 days) collected to monitor the CRT system operation, the two *CRT-maps* corresponding to the upper panel (*wall*-side) and the lower panel (*door*-side)[1] are obtained, as shown in Fig. 5.6 on the left and the right, respectively. In the data, the distribution along ϕ (represented by x_{in} and x_{out} in the figure) is fairly uniform; whereas, along θ (z_{in} and z_{out}) the distribution is asymmetric. In the MC, the *muon-like* events are simulated entering the detector from the upper to the lower panel; consequently, a map of z_{wall}-z_{door} is constructed, as reported in Fig. 5.7; the random throw on this map assigns the two CRT z-coordinates. The x-coordinates, instead, are generated from uniform distributions.

For each interacting muon entering the LAr AV, a large number of photons is

[1]The white strip shown in the right-plot represents a dead strip present in the panel.

produced, $\sim 10^5$ photons/cm, and propagates in the LAr bulk. If the whole tracking of each photon would be simulated, a huge amount of CPU consumption and time would be needed to evaluate how many of them would be detected by the PMTs. Hence, in alternative to that, the simulation of all the possible trajectories is done only once. After the tracking is simulated, the key parameters related to the light propagation from the production to the detection point are stored in dedicated *light-maps*. Finally, this information is accessed for each produced photon, at the level of the physics simulation, in order to retrieve the probability whether it will be detected or not by the PMTs. A summary of the *light-maps* production will be given in the next section; a detailed description of this approach is available in Ref. [219].

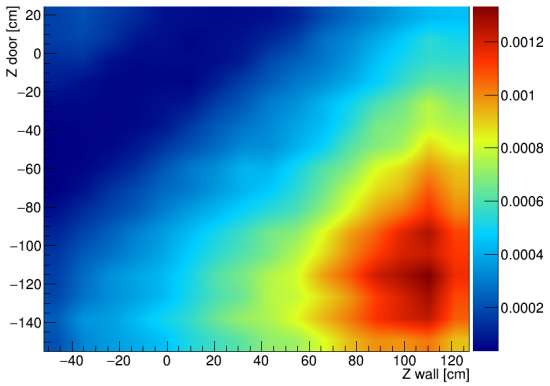

Figure 5.7.: Interpolation of the characteristic asymmetry present in the z-coordinate of events triggered by the CRT external system; in the plot, the z-coordinates are from the data [216].

5.2.3 Light maps: a faster way to propagate the light

The *light-maps* production is a faster way to store the principal parameters describing the photon propagation in big LAr volumes. Their generation is based on five steps:

- the LAr volume is divided into 3-D *voxels*
- a high number of photons (10^8 VUV) is isotropically generated in each *voxel*
- each photon is tracked across the detector
- the arrival time distribution and the detection probability of each VUV photon is obtained for each PMT
- each time distribution is fitted and the parameters are stored in a file called *light-map*

Consequently, the light propagation is expressed in terms of the probability to detect the VUV photons generated in each *voxel* by each PMT, including the possibilities that the photons can suffer a Rayleigh scattering and/or being absorbed (or reflected) touching the detector's surfaces.

For the *voxelization* of the WA105 DP demonstrator, the LAr volume considered corresponds to the LAr AV defined in Tab. 3.1 divided, in total, into 1920 *voxels*. Due to the absorption of the cathode surface, this volume is divided into two sub-volumes with a different number of *voxels* and sizes, as shown in Fig. 5.8. In particular, 1536 *voxels* are needed above the cathode and 384 below; the size of each *voxel* is $131.5 \times 144.4 \times 125$ mm^3 above the cathode and $131.5 \times 144.4 \times 92$ mm^3 below it. The probability of each photon to be detected is called *visibility*, w_0, and it is expressed by the following equation [219]:

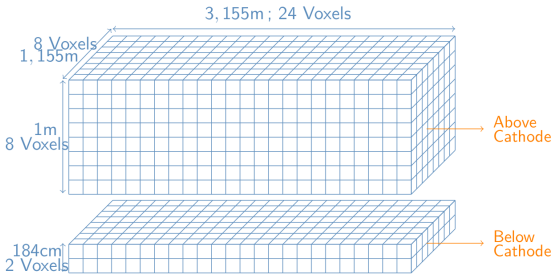

Figure 5.8.: MC voxelization of the WA105 DP demonstrator LAr AV; due to the VUV light absorption in the cathode surface, the LAr volume is split in two sub-volumes above and below it [216].

$$w_0 = \frac{N_{\gamma,PMT}}{N_\gamma} \tag{5.2}$$

being N_γ the number of photons initially generated in each *voxel* and $N_{\gamma,PMT}$ the ones reaching the PMT. Each photon reaches the PMT with a different arrival time, strictly dependent on the distance between the production and the detection point, implicitly influenced by the Rayleigh scattering length; as a consequence, the proper parametrization to describe the earliest arrival time distribution is not straightforward. Dedicated studies have been performed considering the light propagation in bigger detectors (e.g. ProtoDUNE-DP) and a Landau function gave satisfactory results to reproduce most PMT-*voxel* pair arrival time distributions [219]. However, in smaller detectors as the WA105 DP demonstrator, this parametrization is not optimized for short PMT-*voxel* distances, as the arrival time distribution gets quickly suppressed. Hence, an exponentially-modified Landau function has been used; the complete function used to fit the arrival time distribution is the following:

$$f(t) = A \cdot \text{Landau}(t, MPV, \sigma) \cdot e^{\frac{-(t-t_0)^2}{\tau}}. \tag{5.3}$$

In this expression, A is the normalization constant, t_0 is the earliest photon arrival time, MPV and σ are the Landau-function parameters, and τ represents the exponential slope of the function. Examples of the time distributions for two PMT-*voxel* pairs distant 587.1 mm and 1641.8 mm, respectively, are reported in Fig. 5.9.

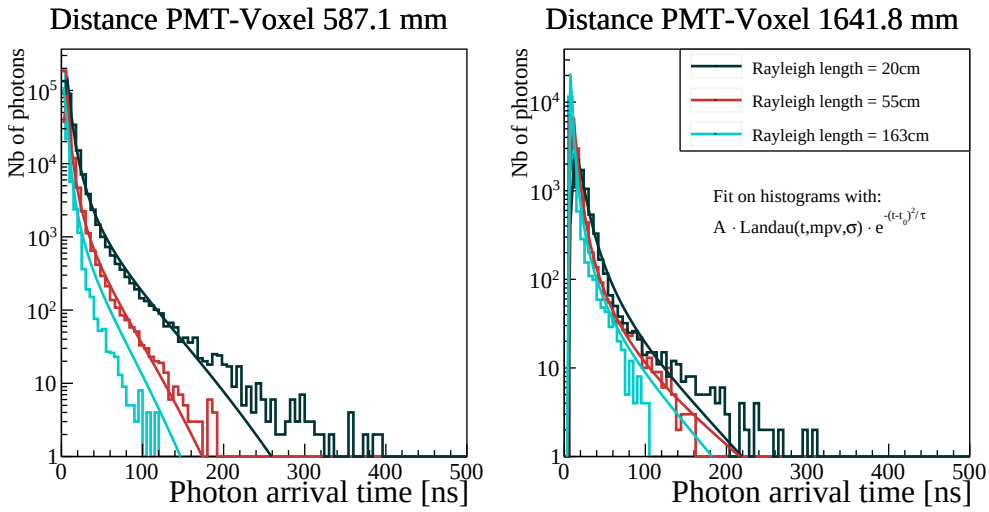

Figure 5.9.: Exponentially-modified Landau function used to fit the PMT-Voxel pair arrival time distributions; for comparison, the arrival time distribution is shown for three different values of the Rayleigh scattering length. Two examples of a PMT-*voxel* pair distant 587.1 mm (**left**) and 1641.8 mm (**right**) are shown [216].

Once the whole tracking of the VUV photons is done and the key information is extracted, five parameters are stored in the *light-maps*: the *visibility*, w_0, the MPV and the σ of the fitted Landau function, the earliest photon arrival time, t_0, and the exponential slope, τ. Assuming a smooth variation of all parameters in nearby *voxels*, a 3-D interpolation of all the stored parameters is done to avoid discontinuities between nearby *voxels* when using the *light-maps* at the level of the physics simulation.

Given the precise simulation of the TPC components, the detection probability of each VUV photon is evaluated tracking it inside the LAr volume and stored in the *light-maps*. Each *light-map* is generated assuming input values for the reflectivity of the TPC elements and for the Rayleigh scattering lengths; the former, with the default values given in Sec. 5.2.1, and the latter as will be commented in the next section.

5.2.3.1 Optical parameters influencing the propagation

The two optical parameters introduced to consider the attenuation of the light are due to the absorption and the Rayleigh scattering lengths; the measurement of the latter is controverted, hence different values have been simulated to estimate it from the comparison of the MC simulation with the light data collected in the WA105 DP demonstrator.

Given the measurements reported on the absorption length [221] as a function of the concentration of the optical active impurities (N_2 and O_2), its value is set to infinite in the MC simulation. On the other hand, three different *light-maps* have been generated with a Rayilegh scattering length, λ_{Ray}, of the VUV photons at 20 cm, 55 cm [161], and 163 cm [164]. The first unrealistic value has been used with the only intention to test the MC simulation itself. In Fig. 5.11, a description of how the light propagation would look like inside the WA105 DP demonstrator when the Rayleigh scattering length is of 20 cm or 163 cm is visible on the left and the right, respectively. In the same figure, also the simulation of the detector components are visible. In all the cases, the Rayleigh scattering length for the visible photons is set equal to 350 cm [156]. Considering the *light-map* simulation with λ_{Ray} = 55 cm, the absorption of the cathode surface on the photon visibility is represented in Fig. 5.10 for PMT-3; in particular, by showing the visibility of the same PMT seen from the y-z plane.

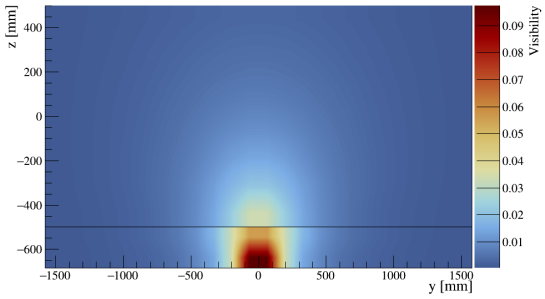

Figure 5.10.: Photon visibility in the y-z plane (at x = 0) for PMT-3. The loss of visibility due to photon absorption by the cathode is visible at z = -500 mm [216].

5.2.4 Physics simulation

As a final step of the simulation, the physics processes leading to the scintillation light production are introduced. First, the generated cosmic muon interacts with the LAr volume and the amount of energy lost per track length is computed by GEANT 4. Secondly, the number of ionization electrons and photons produced as

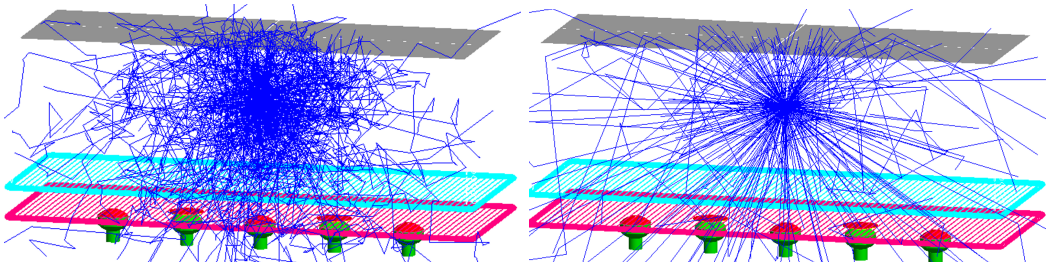

Figure 5.11.: Description of the light propagation inside the WA105 DP demonstrator when the simulated Rayleigh scattering length is of 20 cm (**left**) or 163 cm (**right**) [216].

well as the fraction of photons produced by excitation or recombination are estimated following the NEST predictions [220]. According to Ref. [137], the initial number of photons produced is 5.13×10^4 photons/MeV; in absence of drift field, 1/3 of them are considered to be produced by direct excimer excitation and 2/3 by recombination. Hence, for every photon produced, the number of them reaching each PMT is obtained from the *visibility* stored in the *light-maps*. The arrival time of each collected photon is obtained by adding the track timing, the photon emission delay due to the isospin de-excitation state, and the propagation delay; the latter is obtained by random throw on the reconstructed time distribution from the interpolated parameters stored in the *light-maps*. Therefore, the scintillation time profiles of each detected photon is simulated by including only the contributions from singlet and triplet states; the *intermediate* component is not simulated. For simplicity, neither the differences in the polarity of the PMT bases nor the PMT response saturation observed in the data are taken into account in the simulation. The PMT Q.E. is included at this stage of the simulation, as multiplicative factors to the photon detection probability, assigning 20% as a default value. The presence of impurities can be simulated at this level by introducing an exponential factor, $\exp(-\lambda_{path}/\lambda_{abs})$, to the visibility; in this expression, λ_{path} is the path length of the photons which can be derived from the computed photon travel time. However, in the results that will be presented, this contribution is not included.

5.3 Validation of the MC simulation

An analog selection of *muon-like* events carried out on the data sample is reproduced in the MC simulation based on the selection reported in Sec. 3.8. However,

in contrast with it, the cuts related to the PMT response are not applied in the simulation because of the assumed ideal PMT response. In the MC simulation, the analysis of a sample of 5000 muons of 4 GeV/c following the *CRT-shifted* geometry described in Sec. 5.2.2 is provided. In the data, all the runs triggered by the CRT system in the same geometry and in absence of drift field are included.

5.3.1 Geometrical track reconstruction

As a first step, the event generation simulated in the MC has been validated from the geometrical point of view. The topology of the selected events in the MC is compared with the ones obtained from the data and the same distributions described in Sec. 3.8.1 are overlapped in Fig. 5.12. In all of them, the MC simulation, using $\lambda_{\text{Ray}} = 55$ cm, is reported in cyan; the data are reported in the other three colors: in red, if the complete CRT selection is applied with the requirement of considering only the tracks with the closest point from the PMT surface inside the FC, in grey if the tracks are inside the AV, and in blue if the events laying in the *comet*-region are included. All the distributions are shown as a PDF. This differentiation in the data is needed to have a proper comparison with the MC where none of the waveform saturations are simulated. In the top-plots, the minimum approach track-to-PMT distance for each PMT is reported. From the data-MC comparison, a relative good agreement is visible in all the PMTs, except for PMT-5. The discrepancy is due to the rejection of events saturating the PMT response in the data, not simulated in the MC. As described in Fig. 3.27, these kinds of tracks cross the LAr AV close to the PMTs; consequently, their rejection tends to shift the mean of the minimum approach distance distribution to higher distances. In the bottom plots, the angular distributions ($\tan\theta$, in the left-plot, and $\tan\phi$, in the middle-plot), and the track length computed in the AV (in the right-plot) are shown. The absence of the peak in the positive region of the $\tan\theta$-distribution is due to the generation of the events only *wall-to-door*. The symmetry present in $\tan\phi$-distribution in the MC that is not visible in the data is also due to the event generation that does not take into account the asymmetry in the x-coordinate due to the Jura mountains mentioned in Sec. 5.2.2. Despite these differences in the angular distributions, the typical track length for muons crossing the LAr AV is in a very good agreement, confirming the correctness of the even generation.

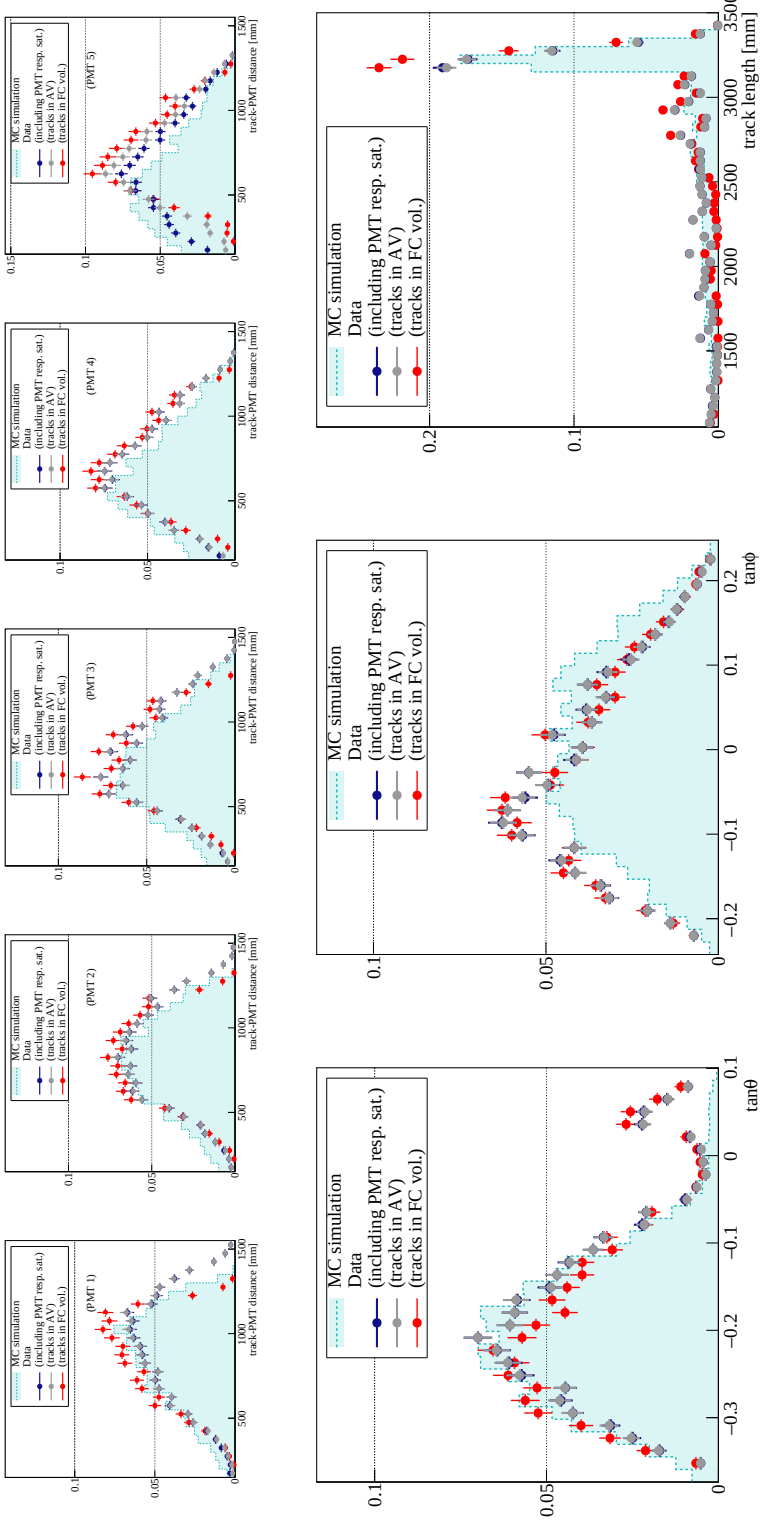

Figure 5.12.: Geometrical Monte Carlo validation of the CRT reconstructed variables, based on the comparison of a simulation using a Rayleigh scattering length of 55 cm with the data collected in absence of drift field.

5.3.2 Collected S1 light

As a second step, the collected S1 light distributions, integrated in the whole 4 μs range, are compared on the right of Fig. 5.13. The red distributions are obtained from the data (corresponding to the distribution of the scintillation light produced by *muon-like* events, whose track crosses the FC volume, and excluding the events saturating both the PMT response and the ADC dynamic range) and in cyan the *muon-like* events inside the FC, obtained from the MC simulation with λ_{Ray}=55 cm; each distribution is shown as a PDF. Following the same approach described in Sec. 3.9.1, the S1 light distribution is fitted with a Landau-function; in the two most left-plots, the MPV and the σ parameters are compared in the top and bottom plots, respectively. As already introduced in the data analysis, given the CRT geometry, the detected light in PMT-1 is smaller than in PMT-5 and this trend is confirmed in the MC. The central PMT-3 is the one collecting the maximum light in the data as in the MC simulation; however, the agreement in the MPV between data and MC observed in this PMT gets worse for the PMTs closer to the FC walls and the same WLS design. This result confirms the hypothesis of a partial reflection of the VUV light inside the FC, instead of their total absorption as simulated in the MC. In addition to that, the data-MC comparison confirms the light suppression induced by the PMMA plate discussed in Sec. 3.9.1. Both in the MC simulation and in the data, the two PMTs with the TPB coating on the PMMA plate show a suppression of the total amount of detected light. Being the PMMA plate simulated in the same way, the suppression in both NB and PB PMTs should be symmetric; however, a discrepancy is observed comparing PMT-2 and PMT-4, confirming that a different bias is introduced in the waveform integration by the presence of the signal reflections due to the different reflection shape in the PB-PMTs. This interpretation is reinforced by the behavior arising from the data-MC comparison when considering the two PMTs having a positive HV design (PMT-3 and in PMT-4).

Overall, quite good agreement arises from the data-MC comparison, validating the scintillation light production simulation implemented the demonstrator. The same analysis has been performed also integrating the light up to 1 μs after the S1-peak and consistent results have been obtained.

The data-MC comparison related to the σ of the Landau distribution shows the general trend of narrower distributions in the data than in the MC; especially for

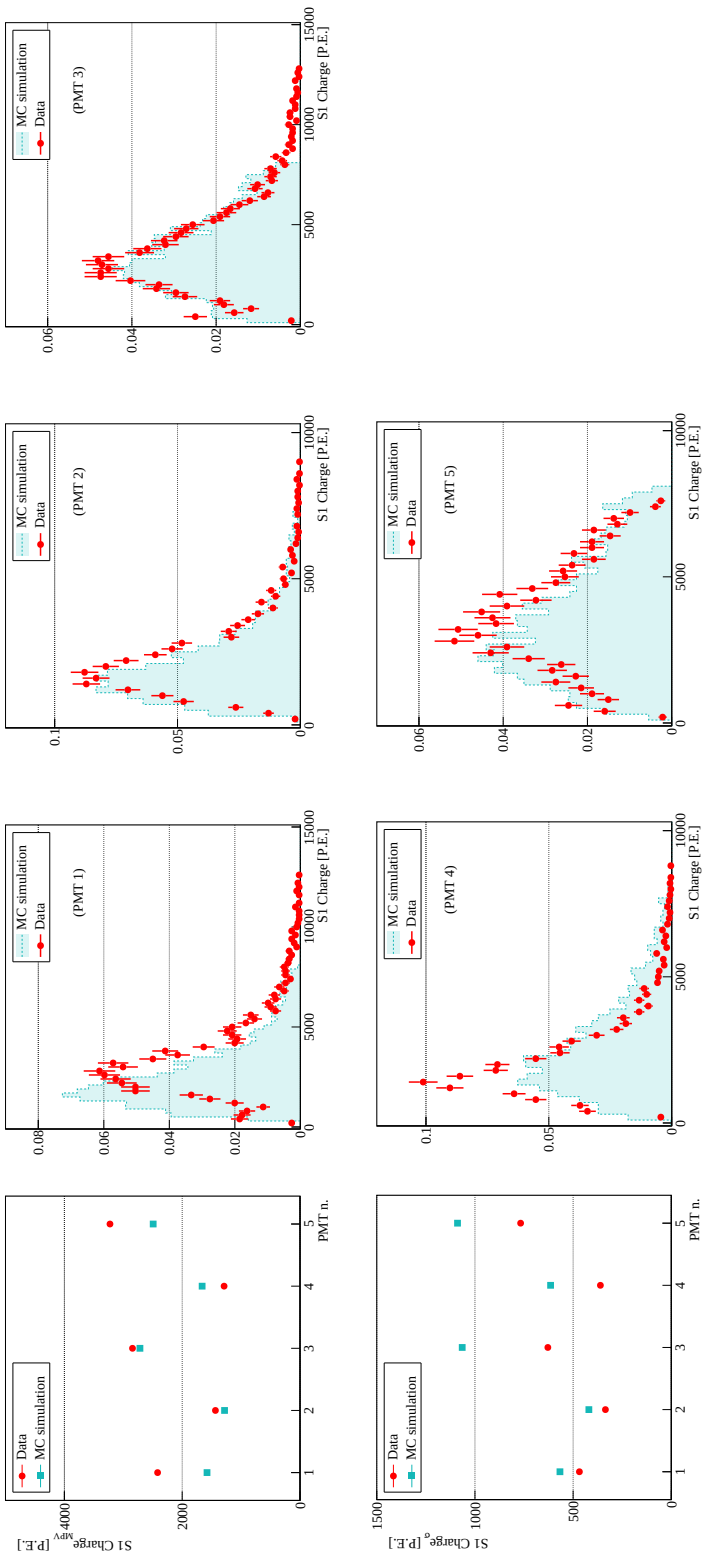

Figure 5.13.: Data-MC comparison of the collected S1-charge spectrum of the data collected in absence of drift field with the simulation of the Rayleigh scattering length = 55cm.

the PMTs whose corresponding track minimum approach distance becomes shorter. This trend could be due to the rejection of events saturating the PMT response, applied only in the data. Nevertheless, based only on this study, it is not possible to quantify the influence of the contributions in the discrepancies due to the simulated value related to the VUV light reflectivity and for the Rayleigh scattering length ($\lambda_{\text{Ray}} = 55$ cm). A dedicated discussion of their impact is given in the next session.

5.4 Study of the Rayleigh scattering length parameter

The goal of the analysis presented in this section is to evaluate the Rayleigh scattering length parameter in order to optimize the data-MC comparison discussed so far[2]. As a first approximation, the default values for the VUV reflectivity (0%) given in Sec. 5.2.1 are used. Similarly to the discussion introduced in Sec. 5.1, the correlation of the collected S1 light as a function of the minimum approach distance is considered. The approach proposed in this study compares the aforementioned distribution obtained in the data (as for the previous study, only tracks crossing the FC volumes are included and the events saturating the PMT response and the ADC dynamic range are rejected) with the one obtained in the MC simulation using three simulated Rayleigh scattering length: $\lambda_{\text{Ray}} = 20$ cm, 55 cm, and 163 cm. The comparison is reported in Fig. 5.14 for the five PMTs. In all of them, the data are shown in red, whereas the MC simulations are shown in orange ($\lambda_{\text{Ray}} = 20$ cm, in blue ($\lambda_{\text{Ray}} = 55$ cm), and in green ($\lambda_{\text{Ray}} = 163$ cm). In the top plots, the correlation between the S1 scintillation light, integrated over 4 μs, and the minimum approach distance is shown; as for the study reported in Sec. 5.1, the profile of the S1 charge in each 20 mm bin is considered. In the bottom plots, the ratio of the data over each of the three MC simulations is reported. From the comparison between the data and MC simulations, a transition point around d_i ~600 mm is observed in all the PMTs, corresponding to a change in the slope of the distribution. In addition to that, two further outcomes arise from the comparison between data and the MC simulations:

- the agreement at shorter distances ($d_i < 600$ mm) is better than for longer

[2]Preliminary studies on the evaluation of the Rayleigh scattering length in the WA105 DP demonstrator have been already discussed in Ref. [219], [211], and [210]; in this section, a considerable improvement in the MC simulations and in the event selection, both in data and MC, are applied.

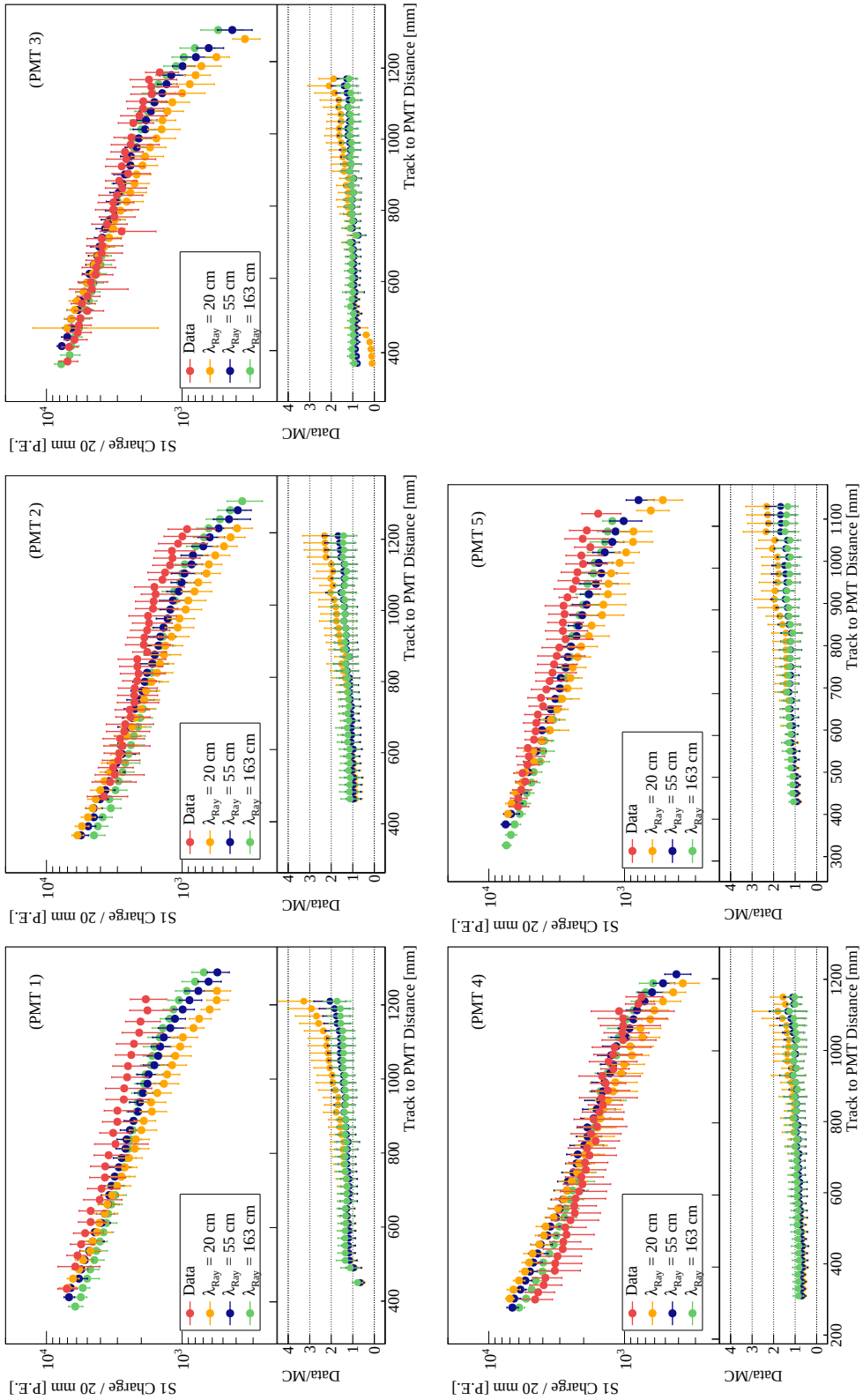

Figure 5.14.: Top: Correlation of the S1 scintillation light, integrated over 4 μs, with the minimum approach distance; the data are shown in red, whereas the MC simulations are shown for λ_{Ray} = 20 cm (orange), λ_{Ray} = 55 cm (blue), and λ_{Ray} = 163 cm (green). Each point is computed from a Gaussian fit of the distribution as described in Sec. 5.1; the error bars represent the 1σ spread obtained in each fit. **Bottom:** Ratio of the data over each of the three MC simulations; the colors are consistent with the curves in the top-plots.

distances than the transition point, for the three λ_{Ray} simulations

- by considering the data/MC ratio, at higher distances than 600 mm, the agreement with $\lambda_{\text{Ray}} = 20$ cm is clearly discarded; whereas, it is not possible to find a preference between the MC simulation of $\lambda_{\text{Ray}} = 55$ cm or 163 cm.

The equally good agreement of the data with both λ_{Ray} simulations of 55 cm and 163 cm is interpreted as an effect induced by the dimensions of the detector that do not allow to have a precise measurement of the Rayleigh scattering length if higher than 55 cm. For this reason, a comparison with the recent measurement of the Rayleigh scattering length at 99.9 cm [166] has not been included in this study.

By looking at the behavior of the distributions after the transition point in the data/MC ratio, it comes that more light is detected in the data than in the MC simulations; this finding suggests that the effect is induced by the VUV light reflection in the FC walls. The disentangling of these competing factors (the unknown value of λ_{Ray} and the VUV reflectivity in the detector elements) is not trivial, but a first study has been performed and discussed in the next sub-section.

5.4.1 Impact of the detector material reflectivity

In order to have a preliminary evaluation of the impact of the reflectivity of the TPC components on the collected light, two further simulations have been produced by changing the input values used for the VUV absorption from 100% to 50%; a first simulation includes such decreasing only in the FC elements, whereas, a second one introduces it also in the cathode and the ground-grid surfaces. For all the simulations, the *light-maps* are produced with $\lambda_{\text{Ray}} = 55$ cm. The results are reported in the top plots of Fig. 5.15, for PMT-2 and PMT-5, showing the S1 charge as a function of the track to PMT distance. In red the usual distribution obtained from the data and in blue the same distribution obtained with $\lambda_{\text{Ray}} = 55$ cm and VUV reflectivities at zero for all the demonstrator components are reported as a reference; in addition to them, in orange, the simulation with the increased reflectivity only in the FC elements and, in green, the ones with the increased reflectivity in all the elements are shown. From the comparison between the orange and the blue curves, the change in the correlation slope appears, reinforcing the hypothesis that the increased light observed in the data after the transition point

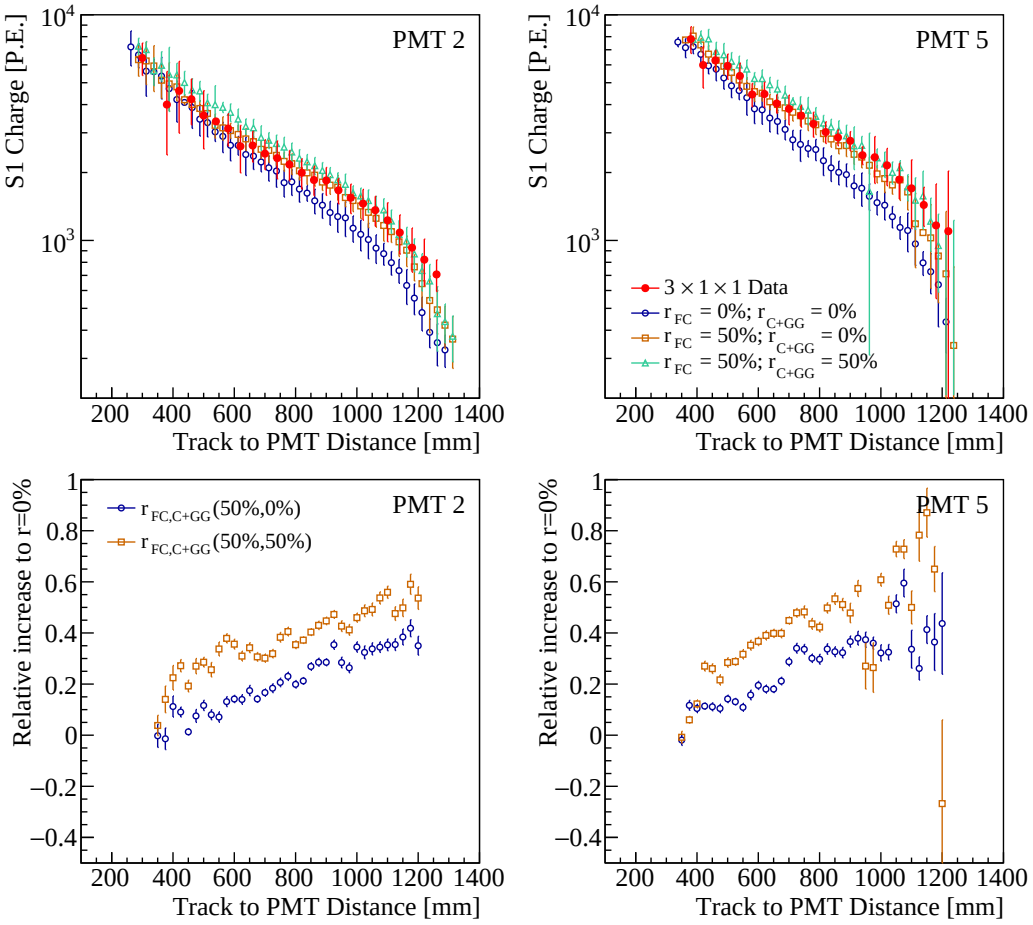

Figure 5.15.: Top: Correlation of the S1 scintillation light, integrated over 4 μs, with the minimum approach distance when 50% VUV photon reflectivity is set for different elements of the detector.
Bottom: Corresponding relative increase of the amount of the collected S1-charge reported for PMT-2 and PMT-5.

(d_i >600 mm) is due to the light reflection in the FC walls. However, when the reflectivity is added in the cathode and the ground-grid, a global increase of the amount of light is observed, independently from the distance of the tracks from the PMT surface.

In the bottom plots of the same figure, the ratio of the integrated S1-charge at the varied VUV reflectivities with the case of full absorption is reported. In both cases, the ratio increases as a function of the track-to-PMT distance. From the comparison between the orange and the blue curves at long track-to-PMT distances,

$\sim$40% of the light increase is due to the FC walls. However, the impact of the VUV reflectivity is function of the distance of the track from the PMT, meaning that this contribution could be handled in a better way in a bigger detector. For instance, applying a stronger fiducial cut in the event selection to consider only tracks crossing the central volume of the detector, better sensitivity to both the VUV reflectivity and the Rayleigh scattering length parameters could allow a better separation of the two contributions and a consequent measurement of the Rayleigh scattering length.

Although the analysis discussed here is only qualitative, it confirms the importance of tuning the reflectivity as well as the Rayleigh scattering length to obtain a precise simulation. Due to the unavailability of a direct measurement of the VUV light absorption in the WA105 DP demonstrator, it is not possible to quantify the impact of these parameters on this detector. Finally, it is important to remind that the contributions induced by other effects, as the concentration of impurities, could play a not negligible role but they have not been taken into account in these studies.

5.5 Comments and prospects

The understanding of the scintillation light propagation in LAr still suffers from an incomplete description because of the inconsistencies reported in the literature about the measurement of the Rayleigh scattering length, found in a relatively wide range of values, $\lambda_{\mathrm{Ray}} \in (52;\ 163)$ cm. Its impact, especially in big detectors, is critical since it quenches the scintillation light yield. For all these reasons, having an estimation of λ_{Ray} in the WA105 DP demonstrator is crucial to extrapolate its impact in bigger detectors as ProtoDUNE-DP and the DUNE FD module. In addition to that, further attenuation of the scintillation light can be induced by the presence of impurities or, in the detectors with a geometry similar to the WA105 DP demonstrator, by its reflection on the detector components.

In order to disentangle these contributions in the WA105 DP demonstrator, the light propagation has been studied in different steps:

1. developing a MC simulation dedicated to confirming the overall detector efficiency observed in the data

2. evaluating the impact of the Rayleigh scattering length from the comparison of different MC simulations with the data

3. investigating the impact of the demonstrator components reflectivity

With these purposes, dedicated simulations have been developed in order to extract as much information as possible from their comparison with the data. The Rayleigh scattering length, as well as the reflectivity of the light on the demonstrator components, have been introduced as parameters; for all the values used, different simulations have been produced. As a default simulation, $\lambda_{\mathrm{Ray}} = 55$ cm and 0% (50%) VUV (visible) light reflectivity of stainless steel and copper surfaces have been considered. From the data comparison with this simulation, an overall good agreement is observed in the scintillation light spectra for the five PMTs, confirming the effects induced by the WLS configurations (Fig. 5.13). Successively, the correlation of the collected scintillation light with the minimum approach distance between the cosmic muon track and the PMT surface has been considered. For this study, two different MC simulations, considering two values of the Rayleigh scattering length ($\lambda_{\mathrm{Ray}} = 55$ cm and 163 cm), have been compared with the data in order to measure the Rayleigh scattering length in the demonstrator. However, given its limited dimensions, the data were equally in agreement with both simulations (Fig. 5.14). For this reason, it was not possible to obtain a direct estimation of the Rayleigh scattering length but equally important features regarding the other optical parameters have been pointed out, related to the geometry and dimensions of the demonstrator, as well as the position of the photon detection system, making the scintillation light yield particularly sensitive to the VUV absorption and reflection in the detector components. This interpretation of the results has been reinforced by the comparison of the data with two alternative simulations including an increased reflectivity for the detector components (Fig. 5.15). As a consequence, two important effects must be considered in order to pursue this kind of studies in big detectors with a similar geometry:

- the absorption of the VUV light in the cathode and the ground grid (shadowing the PMT efficiency)
- the VUV reflectivity induced by the FC elements

The first point has been remarked, on one side, by the measurement of the attenuation length in the data (Fig. 5.3 and Tab. 5.4) and, on the other, by the study of the visibility in the MC simulation (Fig. 5.10). The second point, instead, has

been highlighted by the change in the slope of the mentioned correlation for tracks crossing the demonstrator more than ∼600 mm far away from the PMT surface (Fig. 5.14). This behavior, initially observed in the data, has been confirmed by the MC simulation considering a different value for the reflectivity in the FC components (Fig. 5.15).

The conclusions achieved from the data-MC comparison carried out in the demonstrator was mainly qualitative; however, improvement in the simulation would be possible considering information present in the literature on the VUV absorption on these materials or performing a direct measurement of the VUV reflectivity on the detector components. Regarding the WA105 DP demonstrator, the analysis cannot be improved because of the small sensitivity to the impact of the Rayleigh scattering length. Nevertheless, the same analysis technique, implemented in bigger detectors, is expected to be much more sensitive on the Rayleigh scattering length and, consequently, on its estimation.

"Non basta guardare,
occorre guardare con occhi che vedono,
che credono in quello che vedono."
G. Galilei

CHAPTER 6

THE ELECTRO-LUMINESCENCE LIGHT PRODUCED IN THE GAS PHASE

In the last chapter of this thesis, the study of the electroluminescence signal, produced by the ionization electrons extracted and amplified in the GAr phase, is discussed. Being the amplification of the electrons in the LEMs a relatively innovative mechanism, the features of the produced electroluminescence light signal is not well known yet. The electroluminescence produced in the LEMs has been characterized for the first time in the WA105 DP demonstrator.

First, in Sec. 6.1, the description of the dedicated algorithm developed to identify the S2 signal is explained. Thanks to it, the measurement, at relatively low electric fields, of the drift velocity of the ionization electrons is possible and it is described in Sec. 6.2. Finally, the dependence of the S2 signal with the amplification field strength is discussed in Sec. 6.3.

In Sec. 6.4, a brief discussion on the outcomes obtained in the WA105 DP demonstrator and their extrapolation to other experiments are reported.

6.1 Characterization of the electro-luminescence light

As explained in Sec. 2.4, the electroluminescence light is produced by the extraction and amplification of the drifted ionization electrons toward the GAr phase. Their extraction in GAr is sufficient to produce the S2 signal; hence, the amplification of the electrons between the LEMs adds a further multiplication of the

extracted ionization electrons and the consequent enhancement in the electroluminescence light signal. The S2-signal is the convolution of the electroluminescence signals of each ionization electron extracted in the GAr pocket with the electroluminescence produced by the electrons amplified by the LEMs. However, given the strong electric field applied for the amplification ($\mathcal{O}$ tens of kV/cm) and the very short distance between the extraction grid and the bottom LEM, as well as between the two LEMs layers (∼mm), the extraction and the amplification contributions to the S2 signals are impossible to be distinguished in time. Finally, mainly because of the opacity of the LEMs to the electroluminescence light, the contribution of the induction field to the S2-signal is considered to be negligible. Qualitatively, the effect of the extraction and amplification fields is reported in Fig. 6.1 by comparing the cumulative average waveform of the five PMTs in four long runs collected in different conditions of the drift, extraction, and amplification fields. In dark grey,

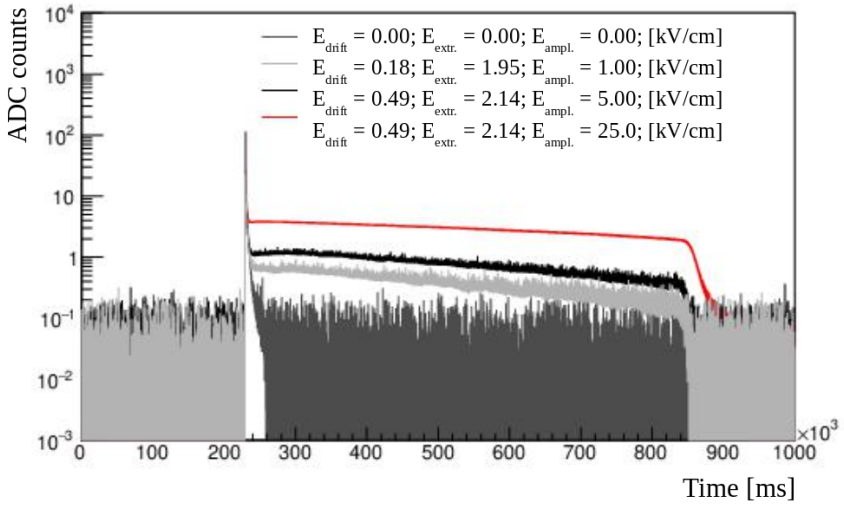

Figure 6.1.: Cumulative average waveforms of the five PMTs collected in different extraction and the amplification field condition. The average waveform collected in absence of all the electric fields is shown in dark grey. From the comparison between the light grey and black average waveforms, the effect of even a small extraction field ($\mathcal{E}_{\rm extr}$= 1.95 kV/cm) is visible. The other two waveforms have been collected at the nominal drift field value ($\mathcal{E}_{\rm drift}$=0.49 kV/cm) with the extraction field, $\mathcal{E}_{\rm extr}$, at ∼2.1 kV/cm in liquid and $\mathcal{E}_{\rm extr}$ at ∼3 kV/cm in gas; the net enhancement due to the amplification field arises from the comparison between the red ($\mathcal{E}_{\rm ampl}$= 25.0 kV/cm) and the black ($\mathcal{E}_{\rm ampl}$= 5.0 kV/cm) average waveforms.

the average waveform collected in absence of all the electric fields is shown and only the primary scintillation light signal is present. From the comparison between the light grey and black average waveforms, the effect of even a small extraction field ($\mathcal{E}_{\text{extr}}$= 1.95 kV/cm) is visible. The net enhancement due to the amplification field arises from the comparison between the red ($\mathcal{E}_{\text{ampl}}$= 25.0 kV/cm) and the black ($\mathcal{E}_{\text{ampl}}$= 5.0 kV/cm) average waveforms collected at the nominal drift field value of 0.49 kV/cm and $\mathcal{E}_{\text{extr}}$= 2.1 kV/cm (3.2 kV/cm) in liquid (gas), corresponding to G_{eff} ∼3.5[1].

The S2-signal is full of information: the S2-signal intensity (integrated charge and amplitude) provides the knowledge about the drifted charge while the signal time and duration, respectively, give information about the drift distance and the track inclination relative to the CRP. With the purpose of identifying these features, an S2 reconstruction algorithm has been developed and will be described in the next section.

6.1.1 S2-algorithm description

The goal of the algorithm is the reconstruction of the electroluminescence signal directly accessing the recorded waveform by the PMT readout, as shown in Fig. 6.3. The S2 identification can be very difficult because of its small amplitude and possible overlap with the S1 signal. The definition of the S2-algorithm is based on two fundamental steps:

- searching for the local minimum after the t_0 time, which allows retrieving the S2-time and S2-amplitude
- searching for the starting and ending time of the S2-signal, in order to obtain the S2-duration and S2-charge integration

Since the S2-shape is strongly dependent on the topology of the track whose ionization electrons are extracted in GAr, the S2-algorithm has been initially defined from the S2 characteristic shape consequent of the crossing muons triggered by the CRT panels. In this case, the CRT reconstruction and selection (see Sec. 3.8) ensure

[1] As a reference, the nominal and the operation values of the fields expected and reached in the WA105 DP demonstrator are reported in Tab. 3.4.

the identification of one muon per triggered event; hence, only the S2 signal corresponding to the triggered S1 is expected. The PMT trigger events, instead, suffer from more *pile-up*, that cannot be mitigated if the anode track reconstruction is not available. Despite the PMT quality cuts mentioned in Sec. 3.7.2 already suppress the possibility to include *muon-bundles* events, this event topology is more sensitive to the presence of *off-time* tracks; they are manifested as more S1 signals in addition to the one giving the trigger (referred as *spurious S1* signals in the text), and, consequently, they can generate a less defined S2 signal. This situation is defined as *pile-up*, and a sketch representing it is given in Fig. 6.2. Only if the *spurious S1*

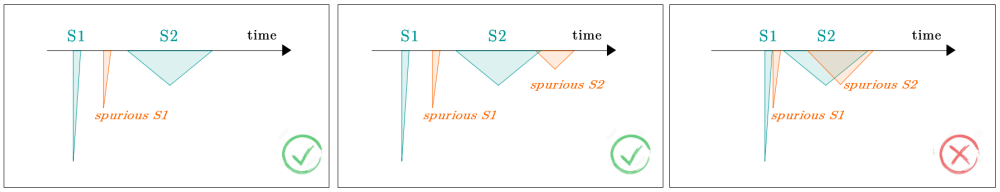

Figure 6.2.: Schematic description of possible *pile-up* situations handled (or not) by the S2 reconstruction algorithm. The *pile-up* is typically caused by *spurious off-time* tracks collected in addition to the one that gave the trigger. The first two sketches correspond to situations well handled by the algorithm; while the third is not possible to be discarded.

signals and/or the corresponding *spurious S2* signals lie within the leading S2-signal, the algorithm is not able to disentangle between the *spurious S1* and the S2 signals. Nevertheless, this possibility affects mostly the S2-charge integration and dedicated studies demonstrated that its contribution to the S2-charge is negligible.

Nevertheless, once the S2- algorithm performance has been validated, through MC simulations, as reported in Appendix A, and the algorithm optimized, its generalization also to *muon-like* PMT triggered events has been successfully applied. As will be described in the next sections, the algorithm is able to handle quite well pile-up events by excluding their contribution to the S2-signal reconstruction; the way how this is done will be clarified in the text.

Searching for the S2-maximum amplitude

As a first step, the local minimum corresponding to the S2-signal is identified; the search is done in the waveform range opened just after the S1 signal, as shown on

the top of Fig. 6.3. In order to define the starting time of this region, the knowledge of the S1 time ending is needed. In Sec. 3.6.1, the algorithm giving the t_0 time has been explained; hence, by scanning forward the waveform after the t_0 time position, the S1 ending time, $t_{S_1,end}$, is defined as the first time sample with the amplitude ≤ 0. In events crossing the detector close to the anode, the S2 and the S1 signals

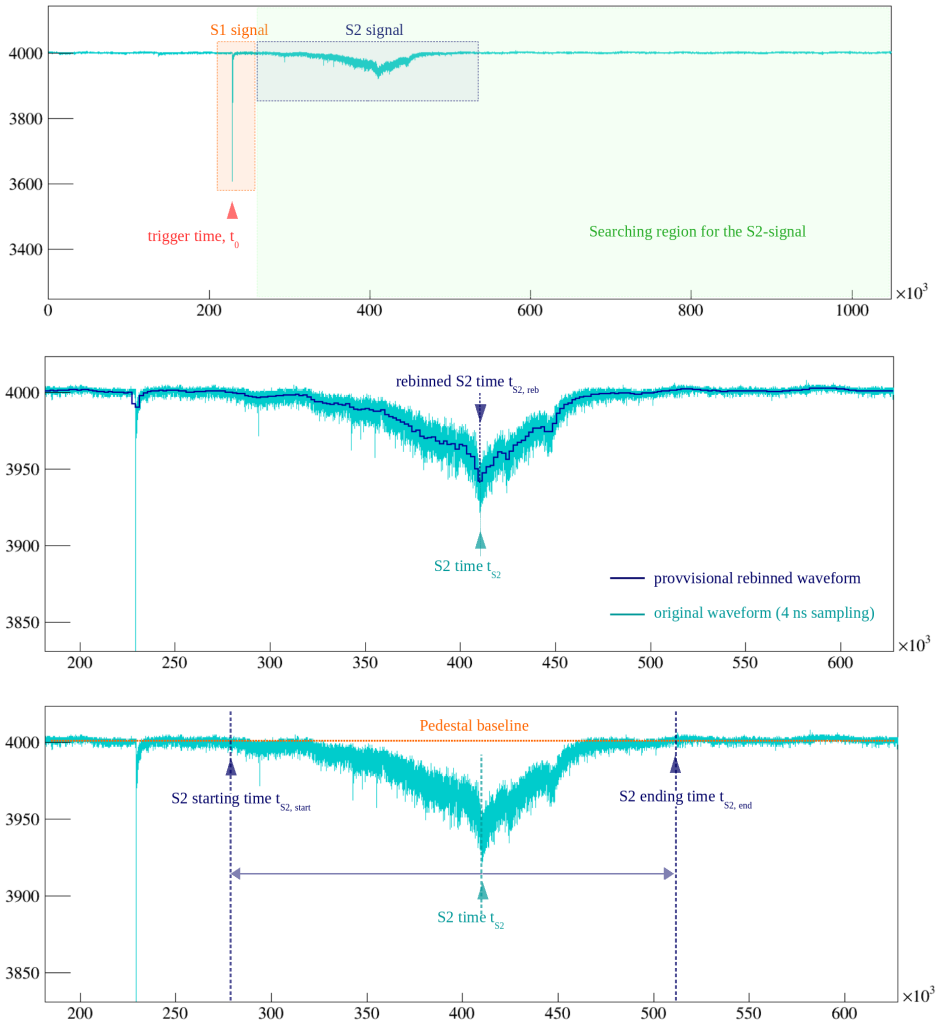

Figure 6.3.: Description o the S2-algorithm steps from the example of a single-event waveform detected by a NB PMT; in the x-axis the time in ns is reported. **Top:** Definition of the region of interest for the searching of the S2-minimum. **Middle:** Identification of the S2-minimum in a rebinned and un-rebinned waveform. **Bottom:** Definition of the characteristic quantities defining the electroluminescence signal retrieved by the S2-algorithm.

overlap; hence, given its definition, the $t_{S_1,end}$ would not be found by the algorithm. These kinds of events are flagged such to be analyzed a-posteriori, if needed.

The S2 amplitudes for the 4 ns sampling are small (of the order of few P.E.); consequently, in order to avoid the misassignment of the S2 amplitude, a provisional rebinning of the waveform (512 ns sampling) is applied; as first step, the local minimum is found in the rebinned waveform. Once the maximum amplitude and the corresponding peak time ($t_{S_2,reb}$) are found, a new search for the local minimum is done over the 4 ns sampling waveform in the time range of [$t_{S_2,reb}$ - 256; $t_{S_2,reb}$ + 256] ns. In this way, the S2-peak time, t_{S_2}, is retrieved with the 4 ns precision. The amplitude of this peak will be referred hereafter as S2-amplitude and $\Delta T_{S_2-S_1} = t_{S_2}$- t_0 as the drift time.

Calculation of the S2-duration and integrated charge

Once the S2 peak time has been obtained, the waveform is scanned backward and forward from the t_{S_2}time; the $S_{2,start}$ and $S_{2,end}$ are defined as the time sample at which the S2-amplitude is ≤ 0, as shown in the bottom-plot of Fig. 6.3. The S2-duration is given by the difference between the ending and the starting times. In this way, any possible S1-spurious peak before or after the S2-signal is excluded from the electroluminescence light signal.

For the NB-PMTs, the S2-charge is calculated by integrating the S2-waveform between the starting and the ending of the S2-signal as follows:

$$S2_{Charge} = \frac{\Delta T \cdot \text{ADC conv.}}{\text{Resistence}} \frac{q_{e^-}}{\text{Gain}} \Big[\text{Tot. S2 Charge} - \text{Ped}_{mean} \times R\Big], \tag{6.1a}$$

$$\text{Tot. S2 Charge} = \sum_{T_{S2,start}}^{T_{S2,end}} \text{Light(t) dt}, \tag{6.1b}$$

in analogy with Eq. (3.2b), the meaning of the symbols is the same. Because of the distortion of the waveform induced by the design of the decoupling capacitor in the PB PMTs, the S2-charge is still given by the previous equations but only after an offline correction of the waveform, as explained in the next section. A reliably estimation of the S2-charge and amplitude in the PB PMTs are possible only after this correction.

Corrections implemented for the PB waveforms

Due to the capacitor used in the PB divider circuits, a baseline oscillation (also referred as *overshooting*[2]) is observed in the S2-signal. This signal distortion is generated by the charging current of the capacitor produced by high-frequency S2 pulses when the charge collected in the PMT anode overpasses the discharging rate of the capacitor (the 1/RC constant). The *overshooting* has been corrected offline by processing the waveforms event by event and correcting the charging and the discharging of the capacitor bin-by-bin. An example of the corrected waveform is reported in green in Fig. 6.4.

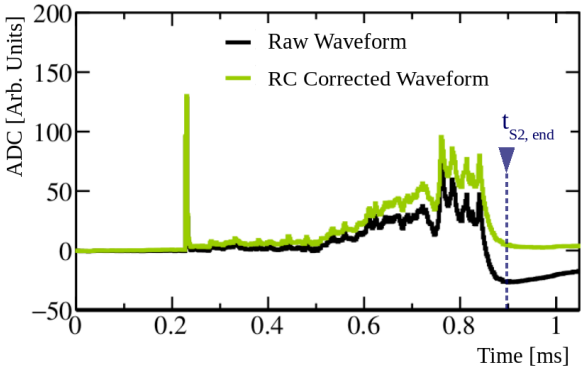

Figure 6.4.: Average waveform collected in a PB PMT, in the long acquisition window showing both the S1 and S2 signals; the overshooting affecting the S2-signal is visible in the raw waveform (in black), the offline corrected waveform is compared in green. In order to have a better visual comparison, the two signals are shown after the pedestal subtraction and with inverted sign.

Since only the S2-charge and amplitudes are modified by the *overshooting*, neither t_{S_2}nor the S2-duration are affected by the correction. In fact, as shown by the blue line in Fig. 6.4, the S2 ending time remains the same both in the raw and corrected waveforms. However, if applied on the raw waveforms, the condition for searching the S2 ending time must be adapted.

[2]The nomenclature *overshooting* is typical of waveforms showed with a negative sign in the peaks, as reported in Fig. 6.3; hence, for waveforms showed as in Fig. 6.4 the proper way to name the baseline oscillation is *undershooting*; the terms "*under*(*over*)" are referred to its position under(over) the pedestal.

Summary of the S2-algorithm variables

In Fig. 6.5, an example of the reconstruction of a cosmic muon crossing the LAr AV, both from the CRT panels and the charge reconstruction in the anode is shown. The event has been triggered by the CRT external trigger; on the left of the figure,

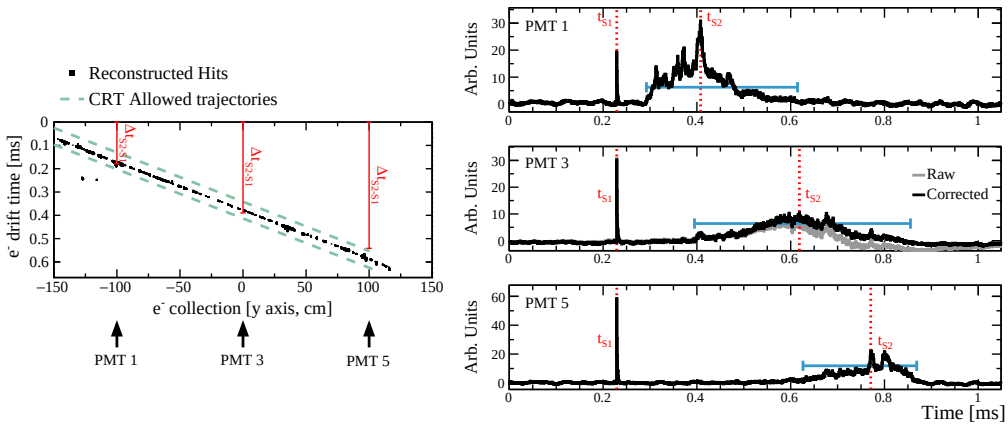

Figure 6.5.: Left: Example of a CRT trigger event crossing the LAr AV of the WA105 DP demonstrator demonstrator. The track reconstruction in the anode plane is shown on the left (black line) within the CRT reconstructed track (cyan lines).
Right: The waveforms detected by PMT-1, PMT-3, and PMT-5 are shown on the right, after the pedestal subtraction and inverting the sign of the S1 and S2 peaks; the correction of the raw PB waveform is visible in the middle-right plot.

the CRT reconstruction is reported in black, and it is compared with the track reconstruction in the anode plane, shown by the cyan dotted lines. On the right of the same figure, three over the five waveforms detected by the PMTs are reported with the most important features that can be retrieved by the S2-algorithm. In particular, the drift time, $\Delta T_{S_2-S_1}$, which is determined by the drift velocity of the ionization electrons, in red, and the S2-duration, which is determined by the track position with respect to the anode plane, in cyan, are shown. In the middle plot on the right, the comparison between the PB raw and corrected waveforms is reported for comparison.

6.2 Measurement of the drift velocity

The drift time obtained from the S2 analysis can be used to measure the drift velocity by considering its correlation with the drift length covered by the ionization electrons up to the anode plane, as defined in Sec. 3.3.1. In the WA105 DP demonstrator, two analyses have been performed: the first considering the track geometrical reconstruction given by the CRT panels, and the second based on the anode plane reconstruction of *muon-like* events.

For the the first analysis, three runs triggered by the CRT external trigger at $\mathcal{E}_{\text{drift}}$= 0.485 kV/cm, $\mathcal{E}_{\text{ampl}}$= 25.0 kV/cm and $\mathcal{E}_{\text{extr}}$= 2.14 kV/cm have been analyzed together; all of them have been collected at the LAr temperature of 87 K. The result is reported in Fig. 6.6, in the 2-D plot where the drift length is shown in correlation with the corresponding $\Delta T_{S_2-S_1}$. Each 8 μs, a Gaussian fit of the drift length

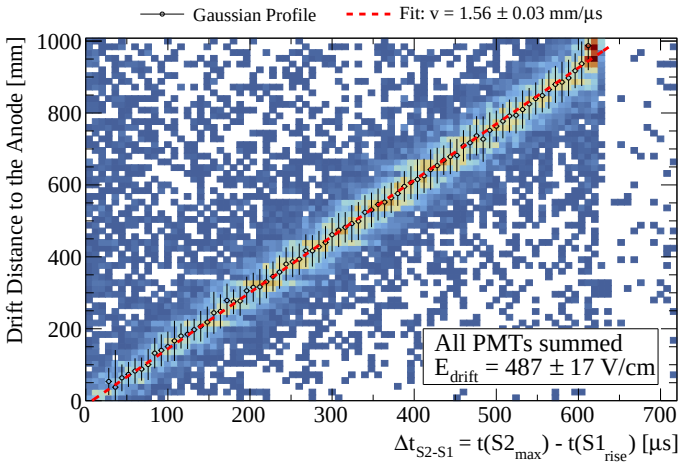

Figure 6.6.: Measurement of the drift velocity, based on the CRT track reconstruction, performed in presence of a 0.485 kV/cm drift field.

distribution is performed in order to obtain the black points superimposed on the 2-D histogram; the error assigned to each point is the σ of the Gaussian distribution. From the slope of a linear fit of these points, the drift velocity is measured and it is found to be v_{drift}=(1.56 $\pm$ 0.03) mm/μ[3]. Due to the precision in the CRT event

[3]Preliminary analyses dedicated to measuring the drift velocity with the same approach have been already reported in [211] and [210]. The significant enhancement reported in this section is given by the event selection that includes only muons crossing the LAr FV as defined in Fig. 3.14.

reconstruction given by the width of the CRT strips, an additional 2% systematic uncertainty is considered. With the same method, a further measurement of the v_{drift} at the drift field of 0.435 kV/cm, and at the same temperature, has been obtained by including the analysis of a CRT run collected during the detector commissioning phase with the CRT panels operation in the *parallel*-geometry. In this case, the drift velocity is found at (1.51 ± 0.07) mm/μs; the bigger error is due to the low statistics of the run.

A complementary analysis has been performed by considering runs collected with the PMT self-trigger. For performing this analysis and to select *muon-like* events, the charge-anode reconstruction and PMT light information are matched offline by requiring a time coincidence with ms precision. The track selection is based on the charge reconstruction in the anode [222] obtained by using several algorithms that:

- remove noise with a periodic behavior (noise filtering),
- search for physical hits, on both anode plane views, based on a standard threshold discrimination (hit finding),
- merge neighboring hits to obtain bi-dimensional clusters (2-D clustering),
- match the cluster in the two views in the 3-D space (3-D merger).

In order to measure the drift velocity, only long tracks entering the demonstrator from anode-to-cathode have been selected. The events with more *off-time* tracks have been discarded to avoid biases in the S2 signal reconstruction and the residual electromagnetic showers are removed based on requirements related to the event deposited energy around the reconstructed track line [222]. For this track-topology, the drift length of the ionization electrons drifted toward the GAr phase is known and it corresponds to the anode-cath-

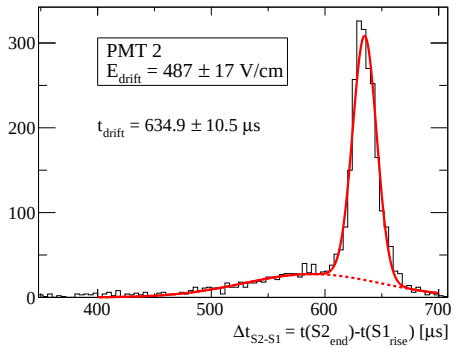

Figure 6.7.: Measurement of the drift velocity, including data triggered by the PMT self-trigger, considering a *muon-like* event selection based on the track reconstruction in the anode-plane.

ode distance, d_{AC}, (corresponding to the 1 m drift); moreover, the ending time of the S2-signal corresponds to the later time the drifted electrons from the cathode reached the anode.

The characteristic $S_{2,end}$ time distribution is reported in Fig. 6.7; in particular, the $S_{2,end}$ is obtained by considering the mean of the peaked Gaussian distribution emerging from the continuum. In the figure, the distribution corresponds to the one observed in PMT-1, but the five PMTs give consistent results and are combined together for the measurement of the v_{drift}. As a result, the drift velocity is obtained through the simple relation: $v_{drift} = d_{AC}/S_{2,end}$. At the temperature of 87 K and under the $\mathcal{E}_{drift}$=0.485 kV/cm, the drift velocity found with this analisys is v_{drift}= (1.58 ± 0.02) mm/μs. Both this and the previous analysis at the same drift field give consistent results. It is important to notice that in the CRP plane, a variation in the field strengths is present, however its effect on the electrons is considered to be negligible.

6.2.1 Comparison with other measurements in the literature

As explained in Sec. 2.2.4.1, the measurements of the drift velocity under relatively low fields ($\lesssim$0.5 kV/cm) pointed out several discrepancies. For this reason, getting new measurements in this drift field region is very important. In Fig. 6.8, the results obtained in the WA105 DP demonstrator, at the LAr temperature of 87 K, are compared with the measurements and the parametrizations of the drift velocity available in the literature in the [0.3, 0.5] kV/cm regime. At the same temperature and drift field strength, no other measurements are reported; consequently, a direct comparison is possible only with the parametrization provided by both Walkoviak [169] and Li [174]. In both cases, the drift velocity measurements obtained in the WA105 DP demonstrator are below the predictions but consistent within 2-σ. A better agreement is observed at the lower drift field (0.435 kV/cm), partially justified by the bigger error reported in the measurement. By comparing the other measurements reported in the same drift field range by Icarus [170] and Rossi *et al.* [173], independently from the temperature, a disagreement with the drift velocity parametrizations have been already observed[4]; the results obtained in the WA105 DP demonstrator tends to confirm this trend.

[4]See Sec. 2.2.4.1 for more details on the discussion.

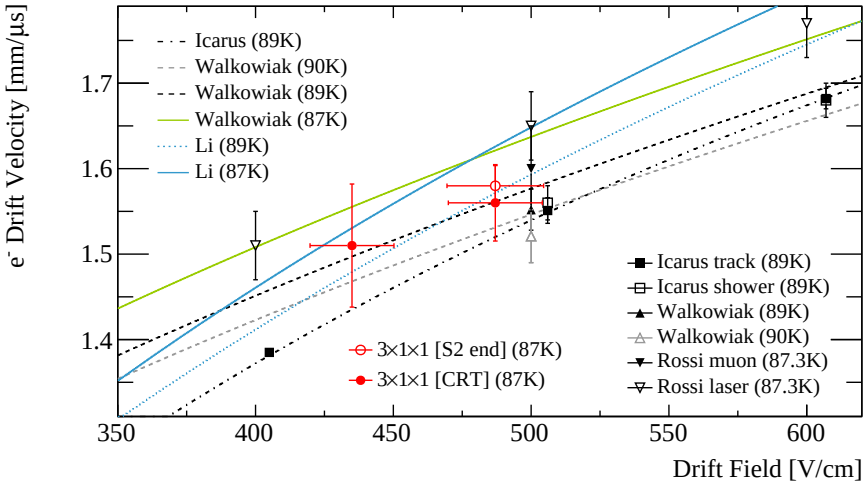

Figure 6.8.: Comparison of the drift velocity results obtained in the WA105 DP demonstrator with the ones reported in the literature. The solid lines represent the drift velocity parametrization reported in the literature by both Walkoviak (green) [169] and Li (cyan) [174].

For completeness, it is needed to remind that a variation of the drift velocity could be induced by Space Charge Effects (SCE), as explained in Sec. 2.2.4.3. In the WA105 DP demonstrator, the presence of SCE cannot be excluded because of the observation of bending tracks found in their reconstruction in the anode-plane but its contribution to these analyses has not been considered. In the WA105 DP demonstrator, disentangling the SCE contribution to the drift velocity calculation from a possible feature of the drift velocity at these fields is not straightforward. Most of the other experiments reporting the same trend, instead, were operated underground such that the SCE contribution is considered to be negligible. Hence, additional analyses acted to enhance the number of measurements of the drift velocity in LAr, either in bigger detectors or in small dedicated setups, are strongly recommended and the results obtained in the WA105 DP demonstrator contributed to this.

6.3 Impact of the amplification field on the electro-luminescence light

The last analysis presented in this section has been performed to evaluate the dependence of the electroluminescence light signal with the amplification field. For this purpose, runs taken in both CRT and PMT trigger configurations under the drift field of 0.485 kV/cm, the extraction field in the liquid of 2.1 kV/cm and in the gas at 3.2 kV/cm are included; the amplification field is scanned between (25, 27.5) kV/cm in steps of 0.5 kV/cm. In these runs, the induction field varies between 1 and 1.25 kV/cm, despite that, no effects on the S2-signal are expected such that all the runs are included in the analysis. In both trigger configurations, the selection of *muon-like* events is applied for the data triggered by the CRT system and based on the track-reconstruction in the anode plane, for the data collected by using the PMT self-trigger.

The effect of the amplification field is expected to influence both the amplitude and the charge of the S2-signal. The corresponding distributions are considered for each of the five PMTs and are fitted by a Landau and Gaussian functions, respectively. An example, for PMT-2, is reported on the left of Fig. 6.9; in the top-plot,

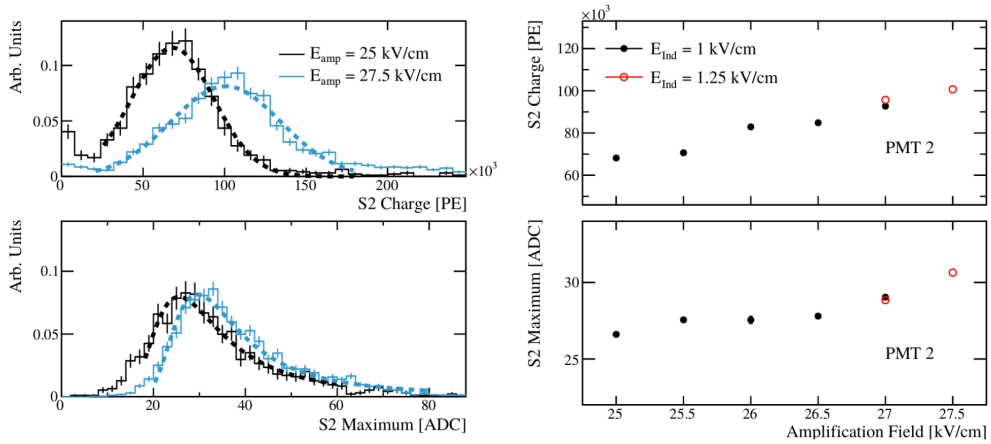

Figure 6.9.: Reconstructed S2-charge (**top**) and S2-amplitude (**bottom**) shown as a function of the amplification field, at two induction fields, for PMT-2. On the right, the corresponding spectra under two different amplification field strengths are compared.

the S2-charge and, in the bottom-plot, the S2-amplitude distributions are shown. On the right of the same figure, their behavior as a function of the amplification field

is displayed for the same PMT. In both cases, as expected, an increasing trend is observed, corresponding to a factor of ∼1.5, for the S2-charge and a factor of ∼1.2, for the S2-amplitude. The distinct increase induced by the amplification in the amplitude and the integrated charge of the S2-signal can be qualitatively explained by comparing the results obtained in the WA105 DP demonstrator with MC simulations, mentioned in Sec. 2.4.2 and reported in Ref. [201], dedicated to describing the electron amplification between the LEMs planes and the consequent electroluminescence photons formation. In the same amplification field range, the expected increase corresponds to a factor of 1.5 to 2. As would be expected intuitively, the S2-charge is expected to be proportional to the amplification field strength. According to Ref. [201], the electroluminescence photons are not produced isotropically but boosted in the backward and forward regions due to the LEMs holes; in particular, in the forward region between the bottom-LEM and the extraction grid they reach the LAr-GAr interface within a narrow angle, as schematically shown in Fig. 6.10. The solid angle is function of the amplification field strength and becomes narrower for stronger amplification field since the photon production point is moved closer to the anode. Because of that, the increase determined in the S2 gain is higher than the increase of the electroluminescence light reaching the LAr interface, corresponding to a mitigate increment of the S2-amplitude. An additional factor needs to be considered in order to explain the different enhancement of the S2-charge and amplitude which is the relative position of the PMTs to the LEMs. In fact, the PMTs are positioned underneath the inactive junctions among the LEMs units; because of that, by considering the S2-amplitude as the net result of the photons directly arriving to the PMT surface, a further reduction on their

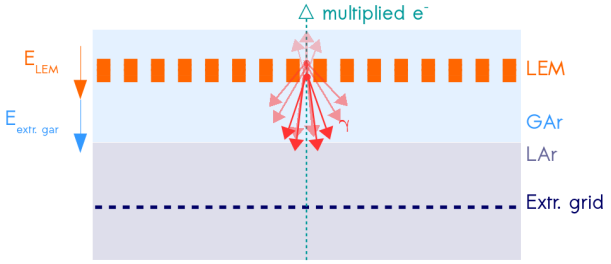

Figure 6.10.: Schematic description of the electroluminescence photons production under different amplification field strengths. Because of the opacity of the LEMs, the contribution to the S2 signal of the photons produced above them is negligible.

fraction can be observed. On the other hand, by considering the S2-charge as the overall electroluminescence light produced and propagated toward the PMTs, the effect of the inactive region can be considered as a secondary contribution to it.

6.4 Comments and prospects

The detection of the electroluminescence light allows accessing important information related to the calorimetric reconstruction of the event.

Two interesting analyses have been performed in the WA105 DP demonstrator : on one side, the measurement of the drift velocity of the ionization electrons at low fields; on the other, the characterization of the electroluminescence signal produced through the charge amplification in the innovative CRP design.

The drift velocity has been measured, under the drift field strength of $\sim$0.5 kV/cm and at the temperature of 87 K, by two different methods, providing compatible results ($\sim$1.57 mm/μs) and in agreement with predictions within 2-sigmas. Within the other measurement performed at 0.435 kV/cm, summarised in shown in Fig. 6.8, additional inputs for a better parametrization of the drift velocity in LAr at low fields is given.

The measurements of the S2-charge and S2-amplitude as a function of the amplification field (Fig. 6.9) contribute to the understanding of the S2 production in the LEMs. The different increase obtained in the electroluminescence light charge and amplitude has been qualitatively explained due to the dependence of the production of photons inside the LEMs with the amplification field, taking place boosted instead of isotropically. This understanding allows for the improvement of the electroluminescence light simulation for future detectors.

"C' é sempre qualcosa in piú, un po' piú in lá, non finisce mai.

J. Kerouac

CHAPTER 7

TOWARDS LARGER STRUCTURES: CONCLUSIONS AND PROSPECTS

The operation of the WA105 DP demonstrator at the ton scale represented a breakthrough in the scalability of the DP technology toward bigger detectors.

The advantage of the LAr-TPC operation for the detection of the particles created in the neutrino interaction is the precise track reconstruction at mm precision. Additionally, the main improvement introduced by DP technology is in the single and homogeneous LAr volume where the drift field is applied vertically and the ionization electrons are amplified in the GAr phase, offering the possibility to cover a much longer drift length, and reducing the number of nonactive materials in the LAr. In addition to the track projection in the anode, the detection of the primary scintillation light provides the time of the event, allowing its full 3 D reconstruction. Because of that, the good performance of the photon detector system is essential for the optimal operation of these detectors.

The photon detection system operated in the WA105 DP demonstrator included five 8-inches Hamamatsu R5912-02Mod PMTs. In order to optimize its design for the DUNE DP far detector module, different configurations, in terms of wavelength shifter and PMT bias voltage polarization, have been installed and tested. The work carried out in this thesis includes the main results achieved in the analysis of the primary and electroluminescence light produced in the WA105 DP demonstrator and collected by this photon detection system.

The discussion has been articulated in four main steps:

1. study of the performance of the photon detection system
2. characterization of the scintillation light production mechanisms induced by the cosmic muons and its dependence with the drift field
3. study of the VUV light propagation in LAr
4. analysis of the amplification field impact on the electroluminescence light

the achievement of these goals allowed identifying important findings for the optimization of the photon detection system design for larger LAr detectors and for the understanding of the expected scintillation light signals in these kinds of detectors in LBL experiments.

Performance of the photon detection system

The photon detection system demonstrated very good performance during the whole WA105 DP demonstrator operation period in terms of PMT noise and stability. Thanks to that, the characterization of both the primary and secondary electroluminescence light signals, produced 1 m away from the PMTs, was possible. In the five PMTs, the VUV scintillation light is converted in visible light by the TPB, either directly coated on the PMT photocathode or above a PMMA plate. This second configuration, although has clear advantages in terms of handling and installation, shown a reduction of the detection efficiency larger than 40%. Because of that, the direct TPB coating on the PMT photocatode has been preferred for DUNE DP baseline photon detection system design. The PMTs have been operated either with a negative or a positive polarization; the second option, necessitating only one coaxial cable per PMT, has been preferred for being used in big detectors in order to optimize the costs and the installation feasibility; however, the operation of the decoupling circuit to split the HV and the PMT signal requires a fine tuning of its capacitance in order to avoid distortion in the PMT signal.

Scintillation light production

The study of the primary scintillation light is based on the characterization of its time profile. During the WA105 DP demonstrator operation, several drift field

conditions have been tested. From the comparison of the scintillation light profile, with and without the drift field, a deeper study on the LAr micro-physics has been possible. In absence of drift field, the *slow* decay time, used also for monitoring the LAr purity stability, has been found to be $\tau_{\text{slow}} = (1426 \pm 24)$ ns. Furthermore, the presence of an *intermediate* component in the scintillation light profile is confirmed. Its characteristic decay time lays between the *fast* and the *slow* components and it is measured to be $\tau_{\text{int}} = (50.7 \pm 4.1)$ ns and its contribution to the total scintillation light corresponds to the 11%. Neither the *intermediate* decay time nor the *intermediate* relative amplitude show a dependence with the drift field, reinforcing the hypothesis of its origin as something else than the Ar excimers de-excitation.

In contrast to what has been reported in the literature so far, the relative fraction of the *fast* over *slow* contributions created by recombination is found to be lower than the ones created by the direct excimer excitation. This finding is based on the study of the ratio $(\text{A}_{\text{fast}} + \text{A}_{\text{int}})/\text{A}_{\text{slow}}$ dependence on the drift field; in particular, at the nominal drift field of 0.5 kV/cm the ratio increases 34% with respect to the measurements reported in absence of drift field. Additionally, a decrease of the *slow* decay time of about 10% at the nominal drift field is observed. Both trends are independent of the two trigger conditions and, consequently, on the specific event selection. Finally, by considering the total scintillation light produced by the cosmic muons traversing the LAr bulk, the measurement of the recombination suppression induced by the nominal drift field strength is performed, confirming that at least 40% of total scintillation light at null field is produced by the recombination processes.

Although these studies are not strictly related to the scalability of DP technology at the giant scale, they are essential to improve the knowledge on the scintillation light production mechanism and get accurate simulations for the studies carried out to validate the current photon detection system designs for future experiments.

Scintillation light propagation

The presence of the external CRT trigger ensures the selection of *muon-like* events based on the track reconstruction in the two sides of the detector, independently from the field conditions. This system allows the characterization of the detector response to the scintillation light produced by the cosmic muons also in absence of drift field.

The analysis of these data demonstrated to be particularly useful in the study of the light propagation in the liquid phase. The propagation of VUV photons depends on the Rayleigh scattering length, whose estimation lays in the range [52, 163] cm. The approach used in the WA105 DP demonstrator for its measurement is based on the comparison of the data with two detailed MC simulations considering $\lambda_{\mathrm{Ray}} = 55$ cm and $\lambda_{\mathrm{Ray}} = 163$ cm. However, given its dimensions, the WA105 DP demonstrator showed limited sensitivity to this parameter. Nevertheless, the results obtained from the data-MC comparison points out a small effect of the VUV reflectivity simulation on the light attenuation that is difficult to be disentangled from the impact of the Rayleigh scattering length. This finding remarked the necessity of having good treatment of both contributions in order to pursue the Rayleigh scattering length measurement in big detectors.

Despite the uncertainty on the parameters affecting the light propagation, it is important to highlight the overall agreement found in the data-MC comparison in terms of the total scintillation light. This result validates the approach developed for the MC simulation.

Electroluminescence light

The analysis of the electroluminescence light signal allowed the interesting measurement of the LAr drift velocity at relatively low fields where some discrepancies between measurements and parametrizations are reported in the literature. At the drift field of ∼0.5 kV/cm and at the temperature of 87 K, two analyses have been carried out. The first analysis is based on the correlation of the ionization electron drift time obtained from the electroluminescence signal with the drift length reconstructed by the CRT planes; the second one is obtained from the measurement of the ending time of the electroluminescence signal of muons reconstructed in the anode plane and crossing the detector from anode to cathode. The results obtained from the two analyses gave $\mathrm{v_{drift}} = (1.56 \pm 0.03)$ mm/μs and $\mathrm{v_{drift}} = (1.58 \pm 0.02)$ mm/μs; both of them are in agreement with the predictions within 2 σ. Finally, the dependence of the electroluminescence signal with the amplification field is evaluated by considering the S2-charge and amplitude. Both observables increase for stronger amplification fields but with a different gradient. A qualitative explanation for this finding is found in the dependence of the solid angle of the photon emission from the

LEMs with the amplification field strength, which seems to have a different impact on the two quantities.

The operation of DP LAr-TPC allowing the amplification of the signal in the LEMs is a relatively innovative design and the study of the amplification field effect on the electroluminescence signal has been detailed in the WA105 DP demonstrator for the first time.

The main results presented in this thesis strongly enhanced the understanding of the scintillation light signals produced in the liquid and the gas argon phases of a DP LAr-TPC with both the charge and light readouts operated at the ton scale. In particular, a comprehensive analysis of the scintillation light produced in a LAr and based on the cosmic muons tracks reconstruction has been reported for the first time. The outcomes gained from the study of the LAr micro-physics, especially the dependence of the scintillation light production with the electric drift field, are very significant for the LAr-TPC community. Because of their transversal impact, an influence is expected in both neutrino and dark matter LAr experiments.

The main analyses have been included in the paper reporting the study of the light production, propagation, and detection in the WA105 DP demonstrator, submitted to the peer-reviewed Journal of Instrumentation that is currently under review; it is available in Ref. [223].

Lastly, the principal conclusions reported in this dissertation, thanks to input supported to the Monte Carlo simulations, represent a milestone toward the scalability of the photon detection system to large detectors, as reported in Ref. [41] for the DP DUNE far detector module. Similarly, the ProtoDUNE-DP photon detection system design benefited from the performance studies reported in this thesis and from the complete characterization of the PMTs carried out in the CIEMAT neutrino group, as reported in Ref. [91].

APPENDIX A

S2-ALGORITHM VALIDATION AND PERFORMANCE

The S2 reconstruction algorithm challenges are mostly determined by the small amplitude of the secondary scintillation light signal, and by its possibility to be overlapped to single spurious S1 and corresponding electroluminescence signals. In order to validate the S2 algorithm, its performance has been tested by using it to reconstruct the electroluminescence signal over the waveform obtained from dedicated MC samples where muons at MIP cross the LAr volume in different topologies mimicking both the *CRT-shifted* and PMT trigger geometries (Sec. A.1). The algorithm performance at the MC level and the validation of the drift velocity measurement will be discussed (Sec. A.2).

Successively, the main observables identified in the MC analyses are studied in the data (Sec. A.3) by comparing the algorithm reconstruction of the S2 signal produced by *muon-like* events triggered by the CRT external system and by the PMT self-trigger.

A.1 MC simulation description

The S2 signal is produced by the drifted ionization electrons amplified in the LEMs holes before reaching the anode; for this reason, the production of the ionization electrons, their drift toward the GAr phase, as well as their amplification, need to be included in the light MC simulation.

The simulations used for the analyses that will be discussed in this appendix

follow the description given in Ref. [219]; the number of ionization electrons reaching the GAr phase is computed by considering the LAr recombination factor, r, as a function of the drift field, measured for the ionization electrons in LAr as reported in Ref. [133]: $N_e = (1 - r)\, N_i$, being the N_i the initial number of ion-e^- pairs. Hence, the number of extracted electrons, N_{ex}, in GAr is:

$$N_{ex} = N_e \times e^{\frac{t_{drift}}{\tau_e}} \tag{A.1}$$

dependent on the drift velocity of the ionization electrons, taken from Ref. [169] through the drift time, t_{drift}, and the drift length, d_i as defined in Sec. 3.3.1, and the electron lifetime in LAr, τ_e[1]. Based on this parametrization, at 0.5 kV/cm and the temperature of 87 K, the drift velocity is 1.622 mm/μs.

Finally, the number of electroluminescence photons, $N_{\gamma,S2}$, is expressed in terms of the multiplicative factor G_{el}, the electroluminescence gain, defined as the number of photons produced per each extracted electron:

$$N_{\gamma,S2} = G_{el} \times N_{ex}. \tag{A.2}$$

The measurement of the electroluminescence gain is not well known; in the simulations developed for the WA105 DP demonstrator a $G_{el} = 160$ photons/electron is used. This number is adapted from the evaluation of the electroluminescence gain given in Ref. [197], through a qualitative comparison of the simulations developed for the WA105 DP demonstrator with the data collected in the demonstrator at the nominal drift field (0.5 kV/cm); in particular, the G_{el} has been qualitatively adjusted until a comparable S2-charge is collected both in the MC simulation and in the data. The choice of G_{el} ∼160 photons/electron is also supported by a more recent LEM simulation pointing out the lower G_{el} ∼150 photons/electron, being the photons produced in the PMT direction [224].

Finally, in analogy with the description given in Sec. 5.2, the electroluminescence light propagation is simulated using a separated *light-map*, where the information related to each GAr *voxel*-PMT pair is stored. In particular, a single layer of *voxels*[2] is considered and $5{\times}10^8$ photons are isotropically generated in each *voxel* [219].

Given the discussions related to the scintillation light production mechanisms reported in Sec. 4.3.1 and the outcomes related to the dependence of the S2-charge

[1] In these MC simulations, no impurities have been simulated; hence, the electron lifetime is supposed to be infinite.

[2] The size of each *voxel* is 250 × 250 × 5 mm^3, as reported in Ref. [219].

and amplification described in Sec. 6.3, the MC simulations do not reproduce exactly the electroluminescence signal observed in the data; consequently, a precise data-MC comparison is not possible. In particular, the absence of the boosted production, within a narrower solid angle than 4π, of the electroluminescence photons in the GAr *light-maps* could not well reproduce all the features reported in the data. Nevertheless, the key elements describing the S2 signal are well reproduced in the MC simulations, such that they can be used to validate the S2 reconstruction algorithm performance that will be discussed in the next section.

A.2 Algorithm validation using dedicated MC samples mimicking CRT and PMT like events

The goal of the analyses that will be discussed in this section is to verify the capabilities of the S2 reconstruction algorithm to retrieve the true S2-signal information. Hence, the S2 algorithm is used to reconstruct the S2 electroluminescence light signal corresponding to the ionization electrons produced by muons at MIP drifted toward the GAr pocket under a drift field of 0.5 kV/cm, with $G_{el} = 160$ photons/electron. The muons are generated entering the LAr volume following three characteristic track topologies:

- the first mimicking the *CRT-shifted* geometry already described in Sec. 5.2.2
- the second made of more horizontal tracks entering the LAr volume perpendicularly to the FC side (referred in the text as *side*-geometry)
- the third one including more vertical tracks (referred in the text as *diagonal*-geometry)

In Fig. A.1, the three geometries are compared in terms of the tanθ distribution.

In the second geometry, the distribution is symmetric and centered around 0, reaching the maximum open angle of $\sim |22|^0$; the tanθ-distribution corresponding to the third topology is peaked around -17^0 but reaches the maximum open angle of $\sim$52^0. In all MC samples, the same reconstructing S2-algorithm used in the data and described in Sec. 6.1.1, is applied to the electroluminescence signal; the comparison of the algorithm performance in the three MC simulated geometry will be discussed in the following section.

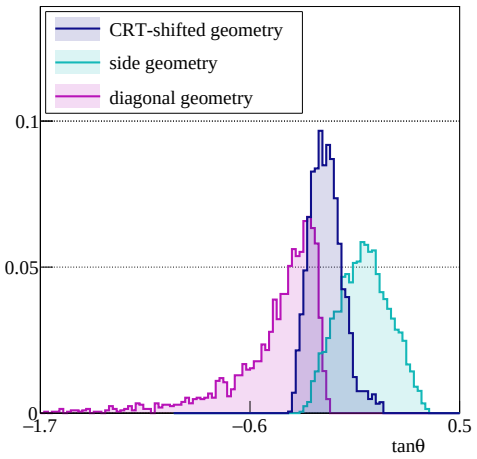

Figure A.1.: Tanθ distributions corresponding to the events generated in the three MC simulated geometries.

A.2.1 S2 algorithm performance evaluated with MC samples

As a first step, the ability of the S2 algorithm of identifying the complete electroluminescence signal by searching for the S2 time, and starting and ending times is studied; for comparison, the algorithm is used for reconstructing the secondary scintillation light of muons that are generated following the three above mentioned geometries. The results, consistent in all the PMTs, are shown in Fig. A.2; as an example, only the distributions of two over the five PMTs are reported. In the top plots, the average waveforms over which the algorithm is applied and the S2 drift time obtained from the algorithm are shown; the S2 starting and the ending time distributions are reported in the middle and bottom plots. By comparing with the average waveforms of each geometry, the peak around zero in the S2 starting time distribution corresponds to the default value assigned by the algorithm when the electroluminescence signal is overlapped with the ending S1 time, for tracks crossing the LAr bulk close to the anode plane. On the other hand, the peak around $\sim$620 μs present in the S2 ending time distribution of events mimicking the *CRT-shifted* geometry corresponds to very latest electrons reaching the anode-plane at the drift

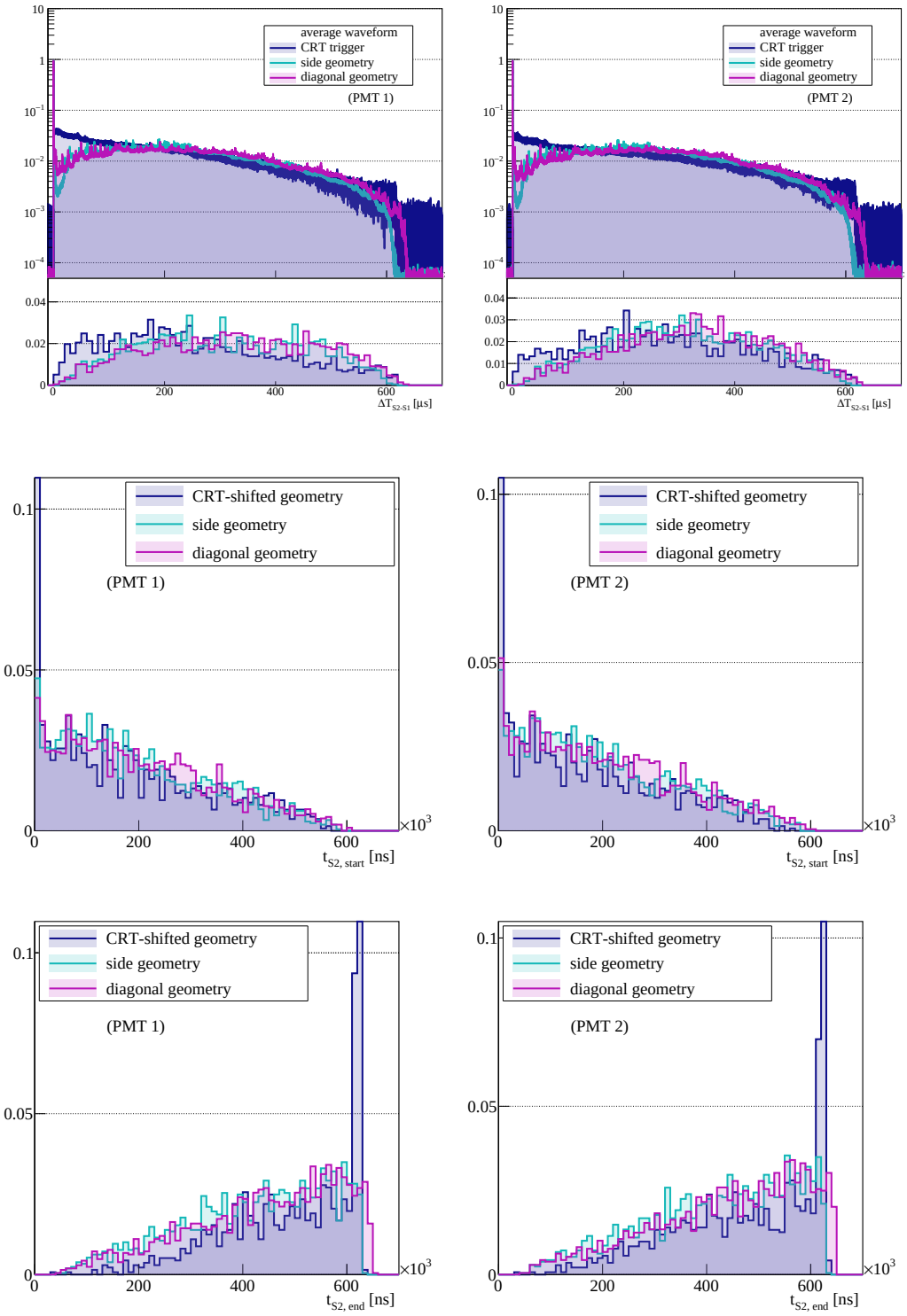

Figure A.2.: Average waveforms and S2 signal reconstruction corresponding to muons entering the LAr bulk in the three MC simulated geometries: *CRT-shifted* like (**dark blue**), *side*-geometry (**magenta**), and *diagonal*-geometry (**cyan**). **Top:** Average waveforms and reconstructed S2 drift time distributions. **Middle:** Reconstructed S2 starting time. **Bottom:** Reconstructed S2 ending time.

velocity used in the simulation.

Secondly, the capability of retrieving the true S2 time is studied. By centering the S1 time in zero, the true S2 time corresponds to the drift time that can be retrieved by knowing the true value of the drift velocity through the simple relation:

$$t_{S2,true} = \frac{d_i}{v_{drift}} \; ; \tag{A.3}$$

being d_i the drift length of the ionization electrons defined as in Sec. 3.3.1, and the drift velocity of 1.622 mm/*mus*. In the top of Fig. A.3, the $(t_{S2,true} - t_{S2})/t_{S2,true}$ distribution is reported for two over the five PMTs, showing the discrepancy of the reconstructed S2 time from the true one. As shown for events generated mimicking the *CRT-shifted* geometry, each distribution is a Gaussian centered around zero; the result is consistent in all the PMTs and all simulated geometries. The fit results are reported in Tab. A.1; the corresponding distributions are shown in the bottom-plots of Fig. A.3. Independently from the event generation geometry, a small bias

Geometries	**PMT-1 direct**	**PMT-2 plate**	**PMT-3 direct**	**PMT-4 plate**	**PMT-5 direct**
CRT-shifted	(5.7±0.7)%	(3.0±0.6)%	(1.4±0.5)%	(1.7±0.5)%	(0.7±0.4)%
side	(3.4±0.3)%	(1.5±0.4)%	(0.6±0.3)%	(1.0±0.3)%	(2.7±0.3)%
diagonal	(8.4±0.3)%	(6.4±0.4)%	(5.4±0.4)%	(6.2±0.3)%	(8.3±0.3)%

Table A.1.: Discrepancy of the reconstructed S2 time from the true S2 time reported for the five PMTs; for each PMT, the error corresponds to the error of the Gaussian fit. The S2-algorithm performance are compared by reconstructing the S2 waveform of events generated in the three simulated geometries.

through positive discrepancies is present in all the PMTs; however, its value is different depending on the PMT position inside the demonstrator or the typical event topology simulated in the MC samples. Despite that, as will be discussed in Sec. A.2.2, the impact of the bias on the measurement of the drift velocity, for instance, is negligible.

Finally, the relation of the S2 signal with the track topology is discussed; in particular, the dependence with the track inclination with respect to the anode-plane is considered by looking at the S2 duration as a function of $\Delta z = z_{in} - z_{out}$. Through this correlation, the dependence of the S2 duration with the track topology is shown,

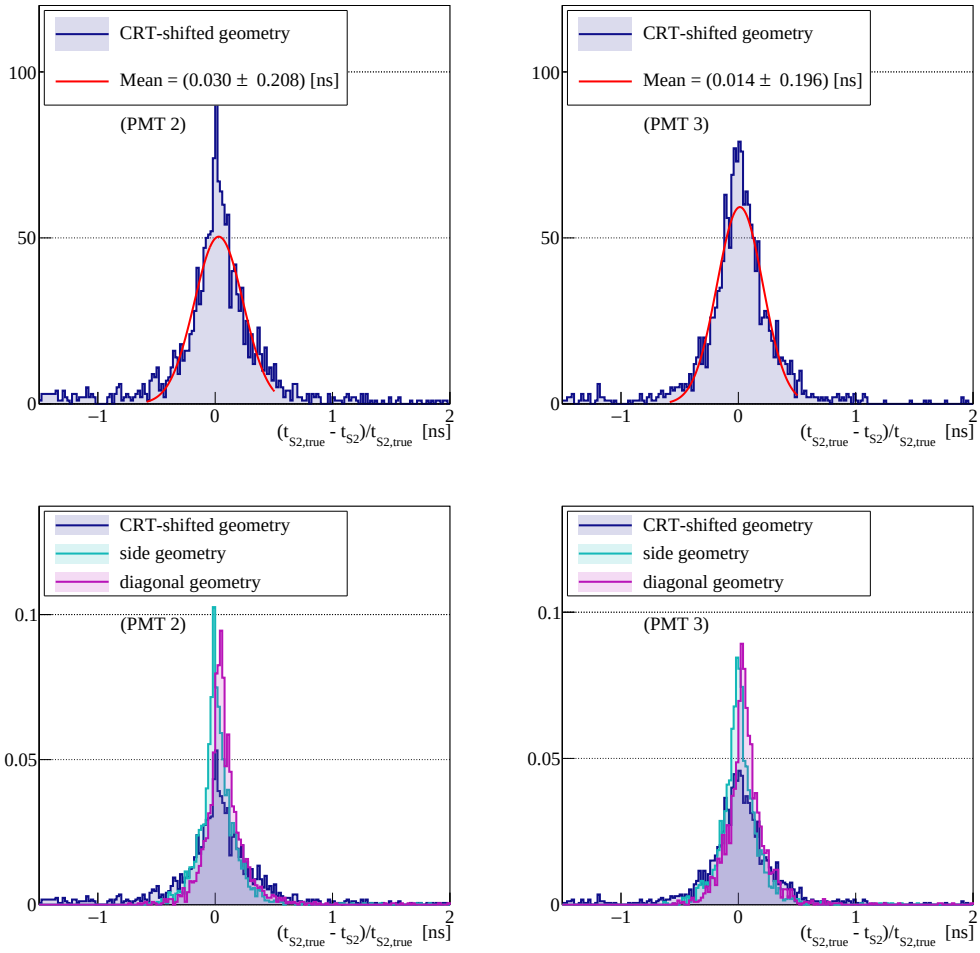

Figure A.3.: Discrepancy of the reconstructed S2 time from the true one is shown by considering the $(t_{S2,true} - t_{S2})/t_{S2,true}$ distribution. **Top:** Example of Gaussian fit reported for the reconstruction of events generated mimicking the *CRT-shifted* geometry; in the legend, the mean and the σ of the Gaussian distribution are reported. **Bottom:** The S2-algorithm capability is compared by considering its performance in the waveform reconstruction of events generated in the three geometries: *CRT-shifted* like (**dark blue**), *side*-geometry (**magenta**), and *diagonal*-geometry (**cyan**).

pointing out that the more vertical the track is, the longer the S2 duration is. The results are reported for PMT-3 in Fig. A.4, the reconstructed waveforms of the muons entering the LAr bulk following the three geometries are considered; the same behavior is observed in the five PMTs. The result reported in Fig. A.3 and the algorithm ability of reconstructing the S2 signal of muons generated following dif-

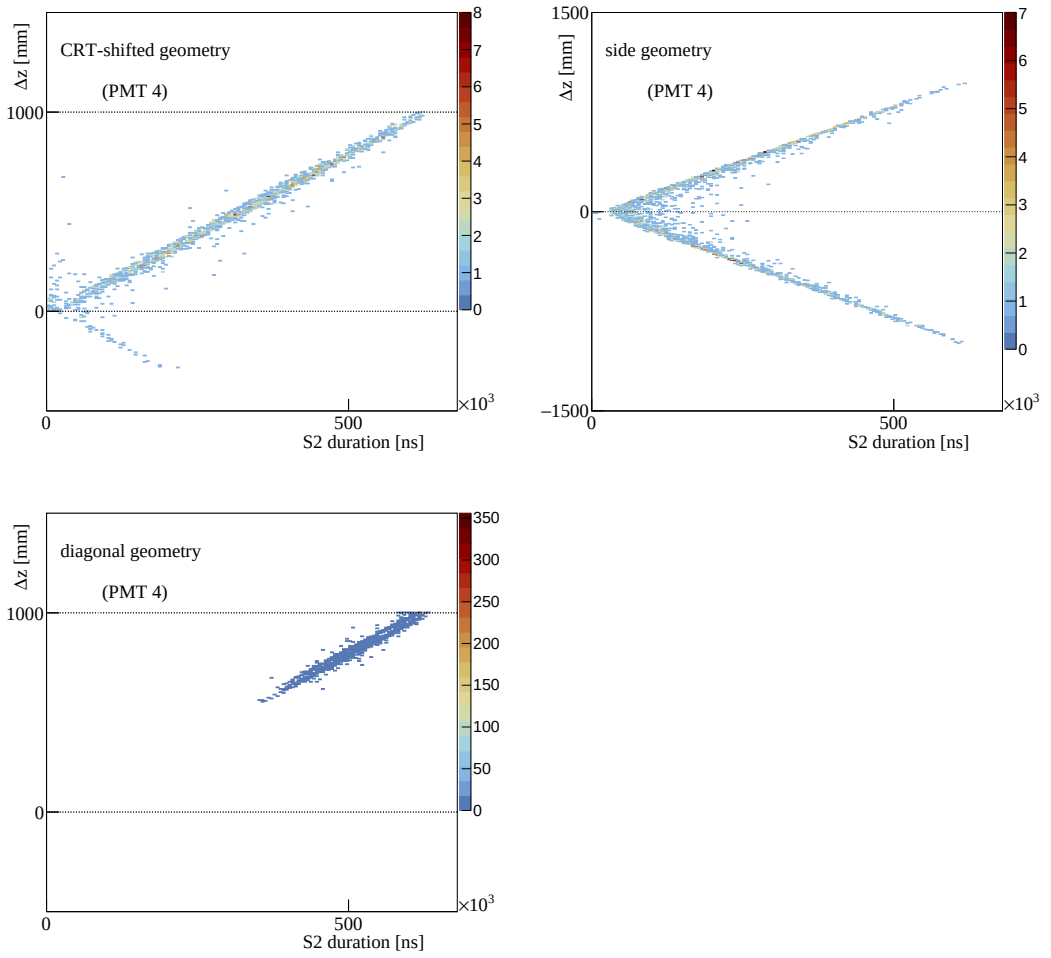

Figure A.4.: Correlation of the S2 duration with the track inclination with respect to the anode plane expressed in terms of $\Delta z = z_{in} - z_{out}$ for muons entering the LAr bulk following the three MC topologies *CRT-shifted* like (**dark blue**), *side*-geometry (**magenta**), and *diagonal*-geometry (**cyan**).

ferent geometries, reported in Fig. A.2 and Fig. A.4, show good performance in the reconstruction of the S2-signal, independently from the track topology. Furthermore, other studies using muon MC samples in the *side*-geometry have been performed considering different G_{el} values (from 50 to 300 photons/electron), simulating different S2 amplification conditions; also MC samples with a small G_{el} confirmed fairly good performance of the S2 reconstruction algorithm.

A.2.2 Validation of the drift velocity measurement method

The results reported in Fig. A.3 have already shown the S2 algorithm capability to retrieve the proper reconstruction of the S2 time in comparison with the true S2 time obtained by knowing the drift velocity. In this way, the correlation between the drift time and the drift length is indirectly demonstrated. However, an additional validation of the drift velocity measurement method described in Sec. 6.2 is presented here, at the MC level.

In Fig. A.5, the MC sample mimicking the *CRT-shifted* geometry is analyzed. The drift length is defined with respect the z-coordinate of the anode-plane and it is computed from the entry and exit coordinates of the track in the LAr bulk, whereas the drift time is retrieved by the S2 reconstruction algorithm. By performing a linear fit of the two variables the drift velocity is found to be (1.614 ± 0.031) mm/μs, in agreement within the statistical error with the drift velocity of 1.622 mm/μs introduced in the simulation.

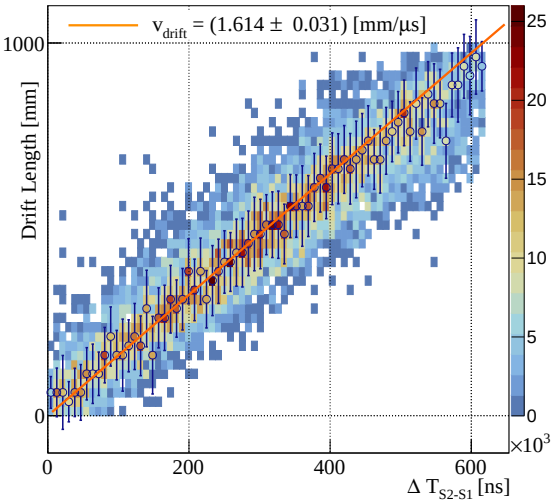

Figure A.5.: Validation of the drift velocity measurement through the correlation of the drift time with the drift length computed from the entry and exit track coordinates; simulated muons follows the *CRT-shifted* geometry.

In order to study qualitatively the impact of space charge effect (SCE), an additional MC sample, in the *side*-geometry, has been produced including the possibility that 50% of positive ion back flow (IBF) from the GAr to the LAr phase. The presence of positive ions back flowed to the LAr bulk determines a drift field line distortion similar to the ones induced by the SCE present in LAr. In Fig. A.6, the correlation between the drift length, d_i, and the drift time, ΔT_{S2-S1}, is shown for the same *side*-geometry with and without the IBF simulation. The overall effect is the decreasing of the drift velocity due to the distortion of the drift field line, as

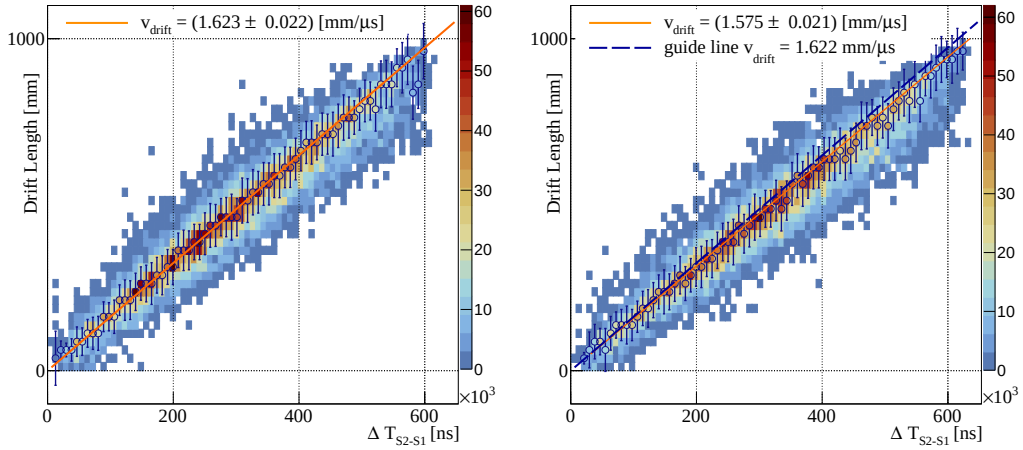

Figure A.6.: Drift velocity measurement in the ideal case of homogenous drift field in the LAr bulk (**left**) and including the simulation of the distorted drift field lines (**right**); in both cases, muons are simulated following the *side*-geometry.

arises from the comparison of the guide line at the simulated drift velocity and the measured one.

A.3 Comparison of the S2 algorithm performance in the data, collected in the two trigger configurations

The last analysis described in this appendix is dedicated to the comparison of the S2-algorithm performance in the WA105 DP demonstrator data collected in the two trigger configurations. In particular, two long runs collected with $\mathcal{E}_{\text{drift}}$= 0.485 kV/cm, $\mathcal{E}_{\text{extr}}$= 2.14 kV/cm, and similar number of initial events (∼25000) are analysed; however, the amplification field is slightly different: $\mathcal{E}_{\text{ampl,CRT}}$=25.3 kV/cm and $\mathcal{E}_{\text{ampl,PMT}}$=26.0 kV/cm. For this analysis, the CRT *muon-like* event selection is applied to the events collected with the CRT external trigger, and only events inside the LAr FV[3] are accepted. In the case of the PMT self-trigger, only events saturating the ADC dynamic range or the PMT response are rejected. In both cases, the raw PB waveforms are considered.

In Fig. A.7, the average waveforms and the drift time distributions are compared in the two trigger configurations for the five PMTs; in the case of the CRT external

[3]See Sec. 3.3.1 for the corresponding definition.

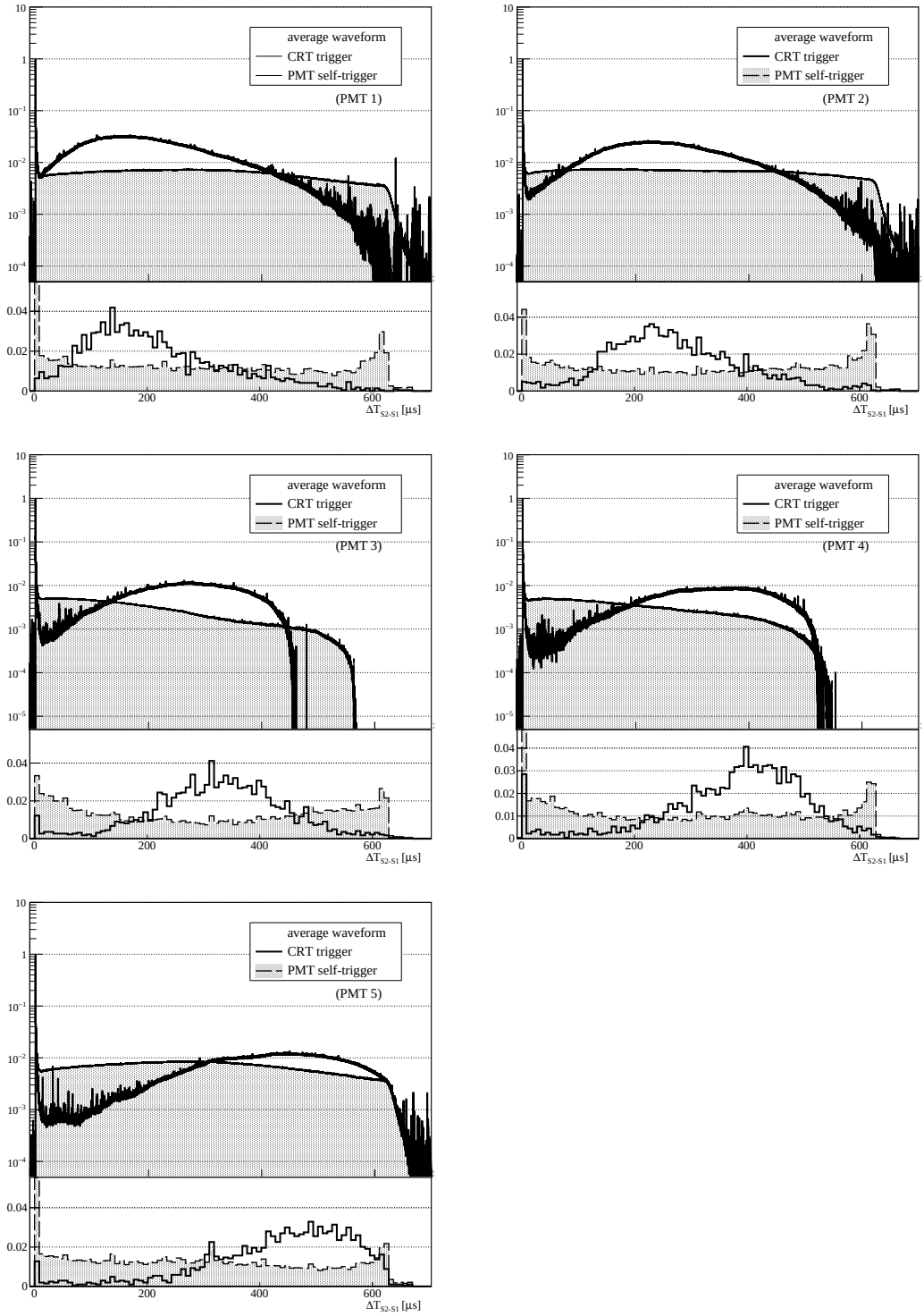

Figure A.7.: Top: Average waveforms corresponding to muons triggered by the CRT external system in the *CRT-shifted* geometry (**black**) and events triggered by the PMT self-trigger (**gray**). **Botton:** S2 reconstructed drift time distribution, Δ_{S2-S1}, of events corresponding to the two data samples.

trigger, due to the shifted geometry, both the mean S2-peak and the drift time reflect the track-topology. In contrast with the average waveforms simulated in the MC for events mimicking the *CRT-shifted* geometry, the characteristic drift time is correlated with the PMT position inside the detector; this feature could be interpreted as a consequence of the boosted photon production, not included in the simulation. On the other hand, in the case of the tracks selected by using the PMT self-trigger, no asymmetries are pointed out in the drift time distributions because there is not a preferred track direction; consequently, a flat drift time distribution is obtained. The maximum drift time around ∼625 μs corresponds to the ionization electrons produced close to the cathode.

In Fig. A.10, the reconstruction of the S2 drift time, as well as the S2 starting and ending times are reported in the top, middle, and bottom plots, respectively, for the five PMTs, in the two trigger configurations. As for the previous distributions,

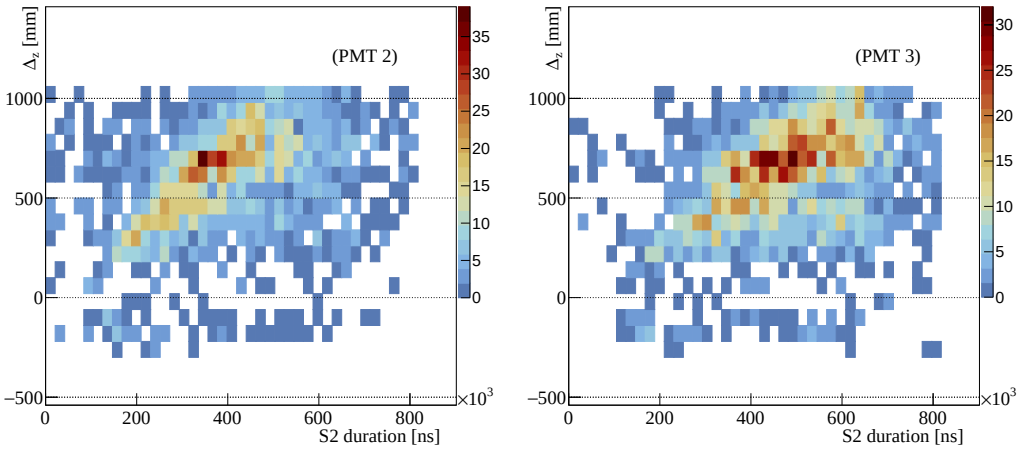

Figure A.8.: Correlation of the S2 duration with the track inclination with respect to the anode-plane expressed in terms of Δz; as an example, results from PMT-2 (**left**) and PMT-3 (**right**) are shown, the behavior is confirmed by all PMTs.

in the ones corresponding to the events collected in the *CRT-shifted* geometry, the S2-signal reconstruction reflect the typical diagonal track-topology. On the other hand, in the S2 time and ending time distributions, the peaks corresponding to the tracks entering the detector from anode-to-cathode are visible; this feature is much more evident in the PMT self-trigger distributions because of the presence of more vertical tracks in this data sample. Independently from the characteristic track-

topology typical of the two trigger configurations, the S2-algorithm is always able to reconstruct completely the electroluminescence light signal.

Finally, by considering only the run collected with the CRT external trigger, the S2 signal correlation with the track topology is investigated in more details. First of all, the S2 duration is considered as a function of the tanθ and tanϕ, as reported in left and right, respectively, of Fig. A.9, for PMT-2 and PMT-3. For both PMTs,

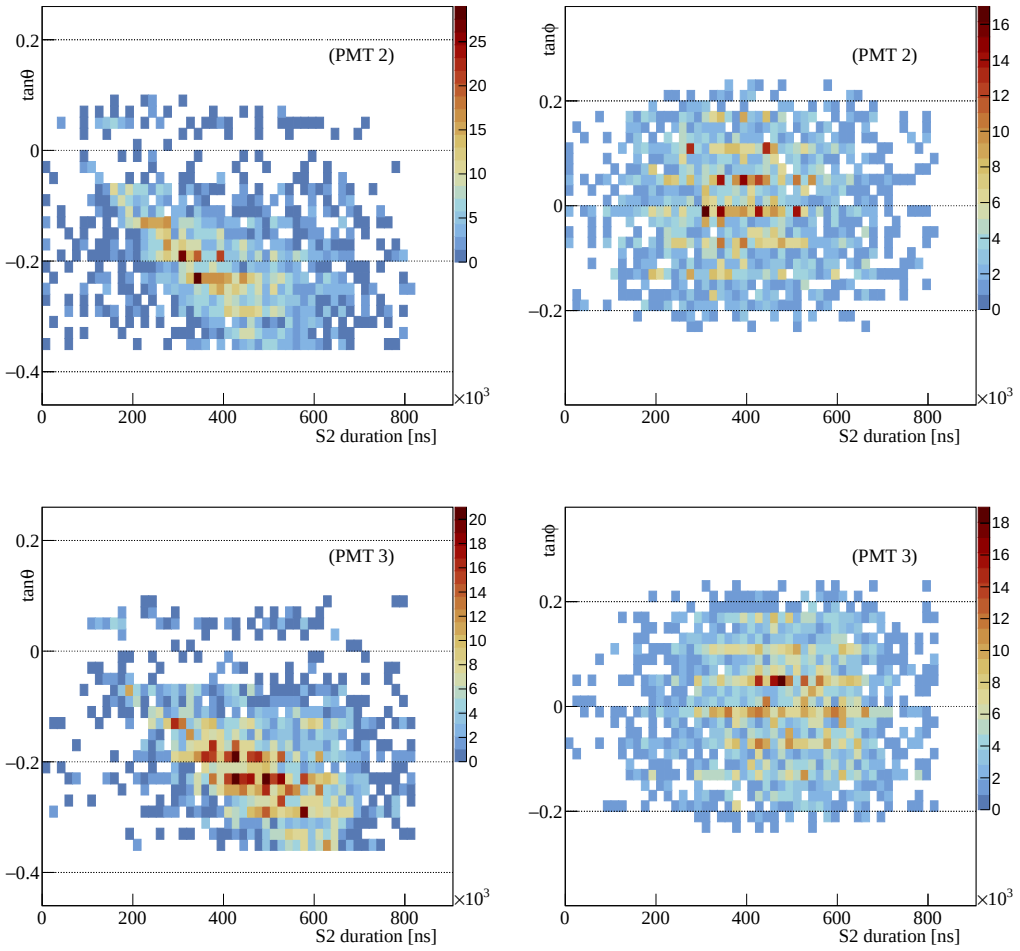

Figure A.9.: Correlation of the S2 duration with the track topology expressed in terms of the tanθ (**left**) and tanϕ (**right**) distributions; as an example, results from PMT-2 and PMT-3 are shown, the behavior is confirmed by all PMTs.

only a correlation with the tanθ angle is present, whereas the distribution of the S2 duration as a function of the tanϕ is very homogenous. The behavior is confirmed

by the five PMTs.

Consequently, and in order to compare with the result showed in the MC simulations, the correlation of the S2 duration with Δz is reported in Fig. A.8. The same trend as in the MC simulations of longer S2 durations for more vertical tracks is reported.

In conclusion, thanks to results obtained from applying the S2 algorithm reconstruction both in different MC simulations and in data, the S2 algorithm logic is demonstrated to be general enough for reconstructing also faint S2-signals, independently of the way how the tracks cross the detectors and the consequent shape of the S2 signal. The main limitation remains the superimposition of the S2 signal with spurious primary and secondary signals. Despite that, the tagging of events with more spurious S1 peaks in addition to the one expected at the trigger time allows analyzing them separately from the single muon event.

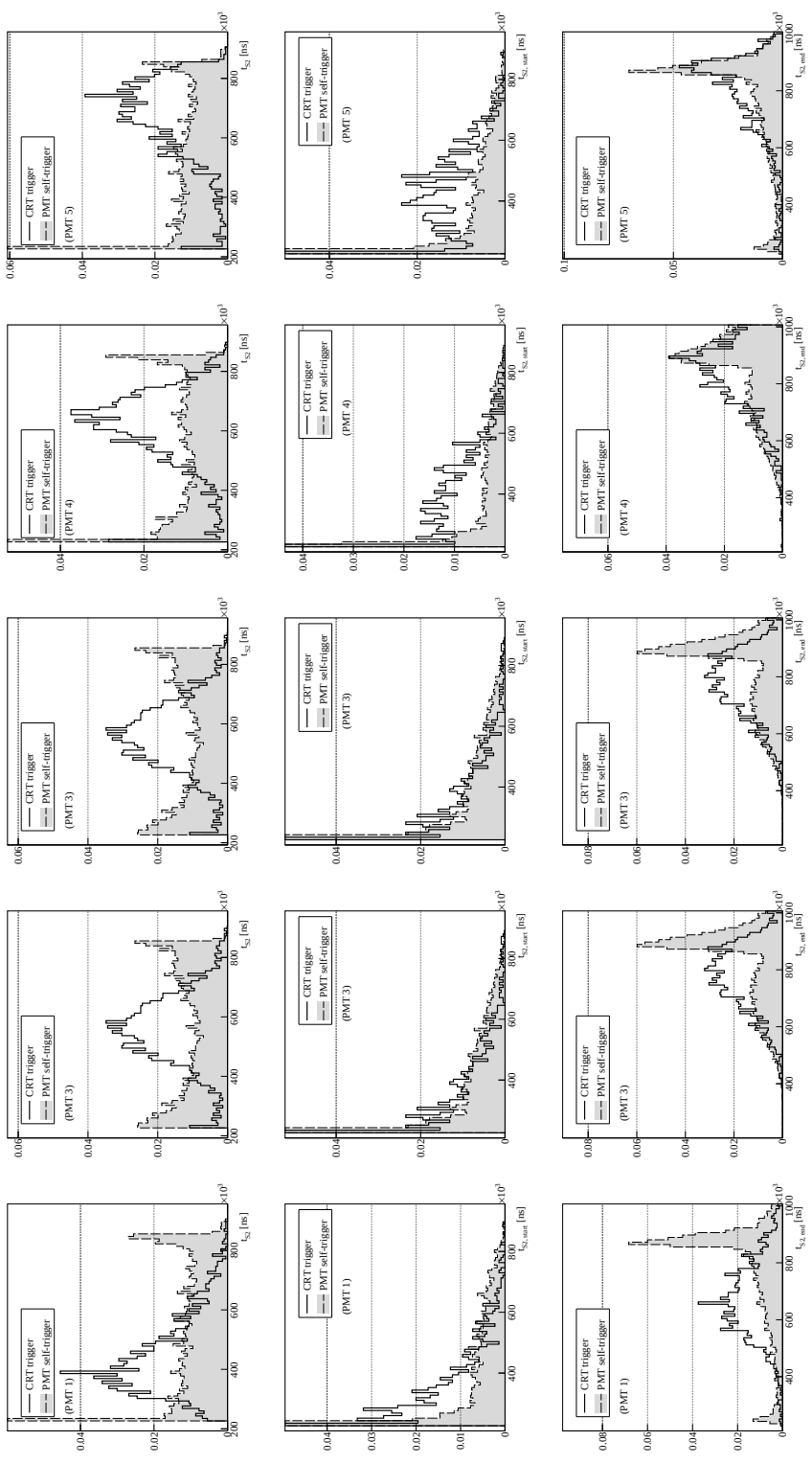

Figure A.10.: Comparison of the S2 algorithm performance in the data for reconstructing the average waveforms corresponding to events triggered by the CRT external trigger (**black**) or by the PMT self-trigger (**gray**). **Top:** S2 starting time distributions. **Middle:** S2 ending time distributions. **Bottom:** S2 time distributions.

BIBLIOGRAPHY

[1] W. Pauli, "*Letter to the Tbingen conference* (1930)

[2] E. Fermi, "*Tentativo di una Teoria Dei Raggi β* , Nuovo Cim. 11-1 (1934), pp. 1-19, DOI: 10.1007/BF02959820, http://link.springer.com/10.1007/BF02959820

[3] F. Reines and C. L. Cowan, "*Detection of the Free Neutrino*, Phys. Rev. 92-3 (1953), pp. 830-831, DOI:10.1103/PhysRev.92.830, https://link.aps.org/doi/10.1103/PhysRev.92.830

[4] C. L. Cowan et al. "*Detection of the Free Neutrino: a Confirmation*, Science 124.3212 (1956), pp. 103-104, DOI:10.1126/science.124.3212.103, http://www.sciencemag.org/cgi/doi/10.1126/science.124.3212.103

[5] G. Danby et al., "*Observation of High-Energy Neutrino Reactions and the Existence of Two Kinds of Neutrinos*, Phys. Rev. Lett. 9-1 (1962), pp. 36-44, DOI:10.1103/PhysRevLett.9.36, https://link.aps.org/doi/10.1103/PhysRevLett.9.36

[6] M. L. Perl et al., "*Evidence for Anomalous Lepton Production in e + e Annihilation*, Phys. Rev. Lett. 35 **22** (1975), pp. 1489-1492, DOI:10.1103/PhysRevLett.35.1489, https://link.aps.org/doi/10.1103/PhysRevLett.35.1489.

[7] K. Kodama et al., "*Observation of tau neutrino interactions*, Phys. Lett. B 504.3 (2001), pp. 218-224, DOI:10.1016/S0370-2693(01)00307-0, https://linkinghub.elsevier.com/retrieve/pii/S0370269301003070.

[8] LEP Collaboration, "*Precision electroweak measurements on the Z resonance*, Physics Reports 427.5 (2006), pp. 257-454, DOI:https://doi.org/10.1016/j.physrep.2005.12.006, http://www.sciencedirect.com/science/article/pii/S0370157305005119.

[9] Bruce T. Cleveland et al., "*Measurement of the Solar Electron Neutrino Flux with the Homestake Chlorine Detector*, Astrophys. J. 496.1 (1998), pp. 505-526, DOI:10.1086/305343, http://stacks.iop.org/0004-637X/496/i=1/a=505

[10] GALLEX Collaboration, "*Solar neutrinos observed by GALLEX at Gran Sasso*, Physics Letters B, Volume 285, Issue 4, 16 July 1992, Pages 376-389

[11] V. N. Gavrin et al., "*Solar neutrino results from SAGE*, Nuclear Physics B - Proceedings Supplements 91(1-3):36-43, (2001), DOI: 10.1016/S0920-5632(00)00920-8

[12] Y. Fukuda et al., "*Measurements of the Solar Neutrino Flux from Super-Kamiokandes First 300 Days*, Phys. Rev. Lett. 81.6 (1998), pp. 11581162, DOI:10.1103/PhysRevLett.81.1158, https://link.aps.org/doi/10.1103/PhysRevLett.81.1158

[13] Y. Fukuda et al., "*Evidence for Oscillation of Atmospheric Neutrinos*, Phys. Rev. Lett. 81 **8** (1998), pp. 1562-1567, DOI:10.1103/PhysRevLett.81.1562, https://link.aps.org/doi/10.1103/PhysRevLett.81.1562

[14] Q. R. Ahmad et al., "*Measurement of the Rate of* $\nu_e + d \rightarrow p + p + e$ *Interactions Produced by* ^8B *Solar Neutrinos at the Sudbury Neutrino Observatory*, Phys. Rev. Lett. 87 (7 2001), p. 071301. DOI:10.1103/PhysRevLett.87.071301, https://link.aps.org/doi/10.1103/PhysRevLett.87.071301

[15] N. Agafonova et al., "*Observation of tau neutrino appearance in the CNGS beam with the OPERA experiment* Progress of Theoretical and Experimental Physics 2014.10 (2014), DOI:10.1093/ptep/ptu132, eprint:http://oup.prod.

sis.lan/ptep/article-pdf/2014/10/101C01/4414189/ptu132.pdf, https://doi.org/10.1093/ptep/ptu132

[16] B. Pontecorvo, "*Mesonium and anti-mesonium*, Zh. Eksp. Teor. Fiz.33 (1957), p. 429, http://inspirehep.net/record/2884?ln=en

[17] Z. Maki, M. Nakagawa, and S. Sakata, "*Remarks on the Unified Model of Elementary Particles*, Prog. Theor. Phys. 28.5 (1962), pp. 870-880, DOI:10.1143/PTP.28.870, https://academic.oup.com/ptp/article-lookup/doi/10.1143/PTP.28.870

[18] M. A. Acero et al., "*New constraints on oscillation parameters from ν_e appearance and ν_μ disappearance in the NOvA experiment*, Phys. Rev. D 98 **3** (2018), DOI:10.1103/PhysRevD.98.032012, https://link.aps.org/doi/101103/PhysRevD.98.032012

[19] P. Adamson et al., "*Measurement of Neutrino and Antineutrino Oscillations Using Beam and Atmospheric Data in MINOS*, Phys. Rev. Lett. 110 **25** (2013), DOI:10.1103/PhysRevLett.110.251801, https://link.aps.org/doi/10.1103/PhysRevLett.110.251801

[20] K. Abe et al., "*Search for CP Violation in Neutrino and Antineutrino Oscillations by the T2K Experiment with 2.2 10 21 Protons on Target*, Phys. Rev. Lett. 121 **17** (2018), DOI:10.1103/PhysRevLett.121.171802, https://link.aps.org/doi/10.1103/PhysRevLett.121.171802

[21] M. G. Aartsen et al. "*Measurement of Atmospheric Neutrino Oscillations at 6-56 GeV with IceCube DeepCore*, Phys. Rev. Lett. 120 **7** (2018), DOI:10.1103/PhysRevLett.120.071801, https://link.aps.org/doi/10.1103/PhysRevLett.120.071801

[22] D. Adey et al., "*Measurement of the Electron Antineutrino Oscillation with 1958 Days of Operation at Daya Bay*, Phys. Rev. Lett. 121 **24** (2018), DOI:10.1103/PhysRevLett.121.241805, https://link.aps.org/doi/10.1103/PhysRevLett.121.241805

[23] Y. and Abe et al., "*Improved measurements of the neutrino mixing angle q 13 with the Double Chooz detector*, Journal of High Energy Physics

2014.10 (2014), DOI:10.1007/JHEP10(2014)086, https://doi.org/10.1007/JHEP10(2014)086

[24] G. Bak et al., "*Measurement of Reactor Antineutrino Oscillation Amplitude and Frequency at RENO*, Phys. Rev. Lett. 121 **20** (2018), DOI:10.1103/PhysRevLett.121.201801, https://link.aps.org/doi/10.1103/PhysRevLett.121.201801

[25] G. Fantini et al., "*The formalism of neutrino oscillations: an introduction*, arXiv: arXiv:1802.05781 [hep-ph]

[26] F. Capozzi, E. Lisi, and A. Marrone, "*Probing the neutrino mass ordering with KM3NeT-ORCA: Analysis and perspectives*, J. Phys. G45.2 (2018), DOI:10.1088/1361-6471/aa9503, arXiv:1708.03022 [hep-ph]

[27] Steven Wren, "*Neutrino Mass Ordering Studies with PINGU and IceCube/DeepCore*, Proceedings, Prospects in Neutrino Physics (NuPhys2015): London, UK, December 16-18, 2015 (2016), arXiv:1604.08807 [physics.ins-det]

[28] K. Abe et al., "*Hyper-Kamiokande Design Report* arXiv:1805.04163 (2018)

[29] Fengpeng An et al."*Neutrino Physics with JUNO*, J. Phys. G43.3 (2016), DOI:10.1088/0954-3899/43/3/030401, arXiv: 1507.05613 [physics.ins-det]

[30] I. Girardi, S. T. Petcov, and A. V. Titova, "*Predictions for the Majorana CP Violation Phases in theNeutrino Mixing Matrix and Neutrinoless Double Beta Decay*, SISSA 26/2016/FISIIPMU16-0064, arXiv:1605.04172v2

[31] S. T. Petcov, "*Leptonic CP violation and leptogenesis*, Int. J. Mod. Phys. A29 (2014), arXiv:1405.2263 [hep-ph]

[32] A. Baha Balantekin, "*Addressing the Majorana vs. Dirac Question with Neutrino Decays*, FERMILAB-PUB-18-418-T, NUHEP-TH/18-09, arXiv:1808.10518v2

[33] A. Osipowiczet al., "*KATRIN: A next generation tritium beta decay experiment with sub-eV sensitivity for the electron neutrino mass*, arXiv:0109033 (2001)

[34] M. Dentler et al., "*Updated Global Analysis of Neutrino Oscillations in the Presence of eV-Scale Sterile Neutrinos*, JHEP 08 (2018) 010, DOI: 10.1007/JHEP08(2018)010, e-Print:1803.10661 [hep-ph]

[35] http://www.nu-fit.org/?q=node/228

[36] M. Bass et al., "*Baseline optimization for the measurement of CP violation, mass hierarchy, and θ_{23} octant in a long-baseline neutrino oscillation experiment*, FERMILAB-PUB-14-379-PPD, BNL-106192-2014-JA, arXiv:1311.012v3 [hep-ex]

[37] K. Abe et al., "*Observation of Electron Neutrino Appearance in a Muon Neutrino Beam*, Phys. Rev. Lett. 112.6 (2014), DOI:10.1103/PhysRevLett.112.061802, https://link.aps.org/doi/10.1103/PhysRevLett.112.061802

[38] K. Abe et al., "*Combined Analysis of Neutrino and Antineutrino Oscillations at T2K*, Phys. Rev. Lett. 118.15 (2017), DOI:10.1103/PhysRevLett.118.151801, arXiv: 1701.00432 [hep-ex]

[39] Dune Collaboration, *The DUNE Far Detector Interim Design Report, Volume 1: Physics, Technology & Strategies*, arXiv: 1807.10327v1

[40] Dune Collaboration, *The DUNE Far Detector Interim Design Report, Volume 2: Single-Phase Module*, arXiv: 1807.10327v1

[41] Dune Collaboration, *The DUNE Far Detector Interim Design Report, Volume 3: Dual-Phase Module*, arXiv: 1807.10340v1

[42] D. R. Nygren, *The Time Projection Chamber: A New 4 π Detector for Charged Particles*, eConf C740805 (1974) 58 PEP-0144

[43] Y. Li et al., *Measurement of Longitudinal Electron Diffusion in Liquid Argon*, arXiv:1508.07059v2

[44] L. Rolandi et al., *Particle Detection with Drift Chambers*, Springer, doi:10.1007/978-3-540-76684-1

[45] C. Rubbia *The Liquid Argon Time Projection Chamber: A New Concept for Neutrino Detectors*, CERN-EP-INT-77-08 (1977).

[46] Table of the Isotopes, LBNL Isotopes Project (http://ie.lbl.gov/toi/)

[47] Ch. Tegler et al., *A new equation of state for argon covering the fluid region for temperatures from the melting line to 700 K at pressures up to 1000 MPa*, J. Phys. Chem. Ref. Data, **28** (1999) 779

[48] P. Benetti, et al., *Measurement of the specific activity of* ^{39}Ar *in natural argon*, NIM **A574** (2007) 83

[49] http://pdg.lbl.gov/2018/AtomicNuclearProperties/HTML/liquid_argon.html

[50] V.D. Ashitkov, et al., *New experimental limit on the* ^{42}Ar *content in the Earths atmosphere*, NIM **A416** (1998) 179.

[51] M. Diwan et al., "*Future Long-Baseline Neutrino Facilities and Detectors*, Adv. High Energy Phys., 2013 (2013) 460123, http://dx.doi.org/10.1155/2013/460123

[52] D. Cline et al., *"A WIMP detector with two-phase xenon"*, Astroparticle Physics, vol. 12, no. 4, pp. 373-377 (2000)

[53] P. A. N. Machado et al., *"The Short-BaselineNeutrino Program at Fermilab"*, arXiv:1903.04608 [hep-ex] (2019)

[54] M. Antonello et al., "*Precise 3D track reconstruction algorithm for the ICARUS T600 liquid argon time projection chamber detector*, Adv.High Energy Phys. 2013 (2013) 260820, arXiv:1210.5089 [physics.ins-det]

[55] ICARUS Collaboration, *"Operation and performance of the ICARUS-T600 cryogenic plant at Gran Sasso underground Laboratory"*, JINST 10 P12004

[56] J. Spitz, *"The ArgoNeuT Experiment"*, 35th International Conference of High Energy Physics, ICHEP 2010

[57] I. Nutini, *"The LArIAT Experiment"*, FERMILAB-PUB-16-511-ND

[58] D. L. Adams et al., *"Photon detector system timing performance in the DUNE35-ton prototype liquid argon time projection chamber"*, arXiv:1803.06379v3 [physics.ins-det] (2018)

[59] SBND Collaboration, *"SBND: Status of the Fermilab Short-Baseline Near Detector"*, IOP Conf. Series: Journal of Physics: Conf. Series 888 (2017) 012148, doi:10.1088/1742-6596/888/1/012148

[60] MicroBooNE collaboration, *"Design and Construction of the MicroBooNE Detector"*, arXiv:1612.05824, JINST 12, P02017 (2017)

[61] B. Abi et al., DUNE Collaboration, *"Deep Underground Neutrino Experiment (DUNE) Technical Design Report - Vol I: Introduction to DUNE"*, JINST 15 T08008 (2020) - arXiv:2002.02967

[62] DUNE Collaboration, *"Deep Underground Neutrino Experiment (DUNE) Technical Design Report - Vol II: DUNE Physics"*, (2020) - arXiv:2002.03005

[63] B. Abi et al., DUNE Collaboration, *"Deep Underground Neutrino Experiment (DUNE) Technical Design Report - Vol IV: DUNE Far Detector Single-phase Technology"*, JINST 15 T08010 (2020) - arXiv:2002.03010

[64] A. Ereditato and A. Rubbia, *The liquid Argon TPC: a powerful detector for future neutrino experiments and proton decay searches*, arXiv: https://arxiv.org/abs/hep-ph/0509022v1

[65] B. A. Dolgoshein et al., *"New method of registration of ionizing-particle tracks in the condensed matter"*, JETP Lett. , **11**, 351 (1970)

[66] B.A. Dolgoshein et al., *"Electronic particle detection method for two-phase systems: liquid-gas"*, Sov. J. Part. Nucl. 4 (1973) 70

[67] WArP Collaboration, *"First results from a dark matter search with liquid Argon at 87 K in the Gran Sasso underground laboratory"*, Astroparticle Physics, vol. 28, n.6, pp. 495507, 2008

[68] F. Sauli, *"GEM: A new concept for electron amplification in gas detectors"*, Nucl. Instrum. Meth. **A 386** (1997) 531-534

[69] A. Rubbia, *"Underground neutrino detectors for particle andastroparticle Science: The Giant Liquid ArgonCharge Imaging ExpeRiment (GLACIER)"*, Journal of Physics: Conference Series 171 (1) (2009) 012020 URL:http://stacks.iop.org/1742-6596/171/i=1/a=012020.

[70] I. De Bonis et al., *"Technical Design Report for large-scale neutrino detectors prototyping and phased performance assessment in view of a long-baseline oscillation experiment"*, Tech. Rep. CERN-SPSC-2014-013. SPSC-TDR-004 (Apr 2014) URL https://cds.cern.ch/record/1692375

[71] A. Buzulutskov, *"Physics of multi-GEM structures"*, Nucl. Instrum. Meth. **A 494** (2002) 148-155

[72] C. Shalem et al., *Advances in thick GEM-like gaseous electron multipliers - Part I: Atmospheric pressure operation*, Nucl. Instrum. Meth. **A558** (2006) 475-489.

[73] C. K. Shalem et al., *Advances in thick GEM-like gaseous electron multipliers - Part II: Low-pressure operation*, Nucl. Instrum. Meth. **A558** (2006) 468-474.

[74] R. Chechik et al., *Thick GEM-like hole multipliers: properties and possible applications*, Nucl. Instrum. Meth. **A535** (2004) 303-308.

[75] A. Buzulutskov, *"Advances in Cryogenic Avalanche Detectors (review)"*, JINST7, C02025 (2012, arXiv:1112.6153 [physics.ins-det]

[76] A. Badertscher et al., "*Construction and operation of a Double Phase LAr Large Electron Multiplier Time Projection Chamber*", arXiv:0811.3384v1 [physics.ins-det] (2008)

[77] A. Stahl, et al., "*Expression of Interest for a very long baseline neutrino oscillation experiment (LBNO)*, SPSC-EOI-007

[78] B. Aimard et al., *"A 4 tonne demonstrator for large-scale dual-phase liquid argon time projection chambers"*, JINST 13 P11003 (2018) - arXiv:1806.03317 [physics.ins-det]

[79] A. Rubbia, *Experiments for CP-violation: A giant liquid argon scintillation, Cerenkov andcharge imaging experiment?*, arXiv:hep-ph/0402110.

[80] , A. Badertscher et al., *"First operation and performance of a 200 lt doublephase LAr LEM-TPC with a 40*
times76 cm^2 readout", arXiv:1301.4817v1 [phyisics.ins-det] (2013)

[81] J. A. Formaggio and G. P. Seller, *From eV to EeV: Neutrino Cross-Sections Across Energy Scales*, Reviews of Modern Physics, **84**, 1307

[82] B. Abi et al. (DUNE Collaboration), *"The DUNE Far Detector Interim Design Report, Volume 3: Dual-Phase Module"*, (2018) - arXiv:1807.10340

[83] S. Sldner-Rembold and E. Blucher, *"DUNE Status and the Module of Opportunity"* presentation at the Module of Opportunity Workshop, (Nov 2019) - Brookhaven

[84] S. Wu, *"Study of alternative double phase LAr TPC charge readout systems"*, Ph.D. thesis, ETH

[85] DUNE Collaboration, *"The DUNE Far Detector Interim Design Report - Volume 1: Physics, Technology & Strategies"*, arXiv: 1807.10334v1 [physics.ins-det] (2018)

[86] DUNE Collaboration, *"The DUNE Far Detector Interim Design Report - Volume 2: Single-Phase Module"*, arXiv: 1807.10327v1 [physics.ins-det] (2018)

[87] DUNE Collaboration, *"The DUNE Far Detector Interim Design Report - Volume 3: Dual-Phase Module"*, arXiv: 1807.10340v1 [physics.ins-det] (2018)

[88] A. Bross, *"The DUNE Near Detector Complex"*, Presentation from PONDD 2018 session DUNE Near Detector Hall

[89] C. J. Mossey, *"Update on the LBNF status"*, Presentation at the DUNE Collaboration meeting, September, 23th (2019)

[90] A. Himmel, *"Noble Element Light Detection for Neutrinos"*, Talk at the LIDINE 2019: Light Detection in Noble Elements conference, August 28th (2019)

[91] D. Belver et al., *"Cryogenic R5912-20Mod photomultiplier tube characterization for the ProtoDUNE dual phase detector"*, JINST **13** T10006

[92] DUNE Collaboration, "*The Single-Phase ProtoDUNE Technical Design Report*", arXiv:1706.07081v1

[93] B. Abi et al., DUNE Collaboration, "*First results on ProtoDUNE-SP liquid argon time projection chamber performance from a beam test at the CERN Neutrino Platform*", FERMILAB-PUB-20-059-AD-ESH-LBNF-ND-SCD, CERN-EP-2020-125, arXiv:2007.06722 [physics.ins-det]

[94] A.A. Machado1and et al., *"The X-ARAPUCA: An improvement of the ARAPUCA device"*, arXiv:1804.01407v1

[95] A. A. Machado and E. Segreto, *"ARAPUCA a new device for liquid argon scintillation light detection"*, Proceeding of the Light Detection in Noble Elements conference (LIDINE2015) August 2830, (2015)

[96] B. Howard et al., *"A novel use of light guides and wavelength shifting plates for the detection of scintillation photons in large liquid argon detectors"*, NIM Volume 907, 1 November 2018, Pages 9-21 - https://doi.org/10.1016/j.nima.2018.06.050

[97] L. Bugel et al., *"Demonstration of a lightguide detector for liquid argon TPCs"*, NIM Volume 640, Issue 1, 1 June 2011, Pages 69-75 - https://doi.org/10.1016/j.nima.2011.03.003

[98] C. Cantini et al., *"Long-term operation of a double phase LAr LEM-Time Projection Chamber with a simplified anodeand extraction-grid design"*, arXiv:1312.6487v1 [phyisics.ins-det] (2013)

[99] A. Badertscher et al., *"First operation of a double phase LAr Large Electron Multiplier Time Projection Chamber with a two-dimensional projective readout anode*, arXiv:1012.0483 [physics.ins-det] (2010)

[100] A. Badertscher et al., *"Operation of a double-phase pure argon Large Electron Multiplier Time Projection Chamber: Comparison of single and double phase operation"*, Nucl. Instr. and Meth. in Phys. Res. A 617 (2010) 188-192

[101] A. Badertscher et al., "*First operation and drift field performance of a large area double phase LAr Electron Multiplier Time Projection Chamber with an immersed Greinacher high-voltage multiplier* (2012) JINST 7 P08026

[102] A. Badertscher et al., *First operation and performance of a 200 lt double phase LAr LEM-TPC with a 40×76 cm^2 readout* (2013) JINST 4 P04012

[103] A. Rubbia, "*ArDM: A Ton-scale liquid Argon experiment for direct detection of dark matter in the universe*, J. Phys. Conf. Ser. 39 (2006) 129 [hep-ph/0510320]

[104] C. Cantini, et al., *Performance study of the effective gain of the double phase liquid Argon LEM Time Projection Chamber*, JINST 10 (03) (2015) P03017. arXiv:1412.4402, doi:10.1088/1748-0221/10/03/P03017

[105] E. M. Gushchin et al., *Emission of "hot" electrons from liquid and solid argon and xenon*, Sov. Phys. JETP 55(5) (1982) 860862

[106] D. Lussi, *"Study of the response of the novel LAr LEM-TPC detector exposed to cosmic rays"*, Ph.D. thesis, ETH Zurich (2013)

[107] W. R. Leo, *"Techniques for Nuclear and Particle Physics Experiments. A How-to Approach*, Springer-Verlag, Berlin Heidelberg (1994)

[108] H. Bichsel, D.E. Groom, S.R. Klein, *Particle Data Group - Passage of particles through matter.*, 2018

[109] B.L. Berman and S.C. Fultz, Rev. Mod. Phys. 47, 713 (1975)

[110] R.M. Sternheimer, *The Density Effect for the Ionization Loss in Various Materials*, Phys. Rev. **88**, 851 (1952)

[111] W. Lohmann, R. Kopp, and R. Voss, *Energy loss of muons in the energy range 1-10000 GeV*, CERN-EP/75-03, (1985)

[112] S.P. Moller et al., *Direct measurements of the stopping power for antiprotons of light and heavy targets*, Phys. Rev. A **56**, 2930 (1997)

[113] *"Stopping Powers and Ranges for Protons and Alpha Particles*, ICRU Report No. 49 (1993); tables and graphs of these data are available at http://physics.nist.gov/PhysRefData/

[114] H. Bichsel, *A method to improve tracking and particle identification inTPCs and silicon detectors*, Nucl. Instrum. Methods **A562**, 154 (2006)

[115] S.M. Seltzer and M.J. Berger, *Evaluation of the collision stopping power of elements and compounds for electrons and positrons*, Int. J. of Applied Rad. **33**, 1189 (1982)

[116] S.M. Seltzer and M.J. Berger, *Improved procedure for calculating the collision stopping power of elements and compounds for electrons and positrons*, Int. J. of Applied Rad. **35**, 665 (1984)

[117] T. Doke, *"Ionization and excitation by high energy radiation* in *"Electronic Excitations in Liquefied Rare Gases* - W. F. Schmidt and E. Illenberg eds. pp. 71-93, American Scientific Publishers (2005)

[118] V. Chepel and H. Ara/ujo, *Liquid noble gas detectors for low energy particle physics*, arXiv:1207.2292v3 [physics.ins-det] (2013)

[119] G. Baldini, *"Ultraviolet absorption of solid argon, krypton, and xenon*, Phis. Rev. **128** (1962) 1562-1567

[120] S. D. Druger and R. S. Knox, J. Chem. Phys. 50, 3143 (1969)

[121] K. S. Song, Can. J. Phys. 49, 26 (1971)

[122] A. Hitachi and T. Doke, *"Luminescence quenching in liquid argon under charged-particle impact: Relative scintillation yield at different linear energy transfers* Phys. Rev. B Vol **46**, n. 18 (1992)

[123] T. Doke et al., *"Estimation of absolute photon yiels in liquid argon and xenon for relativistic (1 MeV) electrons*, Nucl. Instr. and Meth. in Phys. Res. **A** 291 (1990) pp. 617-620

[124] M. Miyajima et al., *"Average energy expended per ion pair in liquid argon*, Phys. Rev. A, **9**, n.3 (1974)

[125] S. Kubota et al., *"Dynamical behavior of free electrons in the recombination process in liquid argon, krypton, and xenon*, Phys. Rev. B **20** (1979) 3486-3496

[126] L. Onsager, *"Initial recombination of ions*, Phys. Rev. **54** (1938) 554

[127] E. Shibamura et al., *"Drift velocities of electrons, saturation characteristics of ionization and W-values for conversion electrons in liquid argon, liquid argon-gas mixtures, liquid xenon* Nucl. Instr. and Meth. 131 (1975) 249-258

[128] R. T. Scalettar et al., *"Critical test of geminate recombination in liquid argon*, Phys. Rev. A Vol. 25, n.4 (1982)

[129] E. Aprile, et al., "*Energy Resolution Studies of Liquid Argon Ionization Detectors*, Nucl. Instr. and Meth. A 261 (1987) 519

[130] J. Thomas and D. A. Imel, *"Recombination of electron-ion pairs in liquid argon and liquid xenon* Phys. Rev. A (1987) Vol. 36, n.2

[131] T. Heindl et al., *"The scintillation of liquid argon*, EPL 91 62002 (2010)

[132] P. Cennini et al., *"Detection of scintillation light in coincidence with ionizing tracks in a liquid argon time projection chamber*, Nucl. Instr. and Meth. in Phys. Res. A 432 (1999) 240-248

[133] S. Amoruso et al., *"Study of electron recombination in liquid argon with the ICARUS TPC*, Nucl. Instr. and Meth. in Phys. Res. A 523 (2004) 275-286

[134] G. Jaffe, *"Zur Theorie der Ionisation in Kolonnen*, Ann. d. Phys., vol 42, pp-330-344 (1913)

[135] T. Doke et al., *Absolute Scintillation Yields in Liquid Argon and Xenon for Various Particles*, Jpn. J. Appl. Phys. **41**, 1538 (2002)

[136] P. Agnes et al., *"Measurement of the liquid argon energy response to nuclear and electronic recoils*, Phys. Rev. D 97, 112005 (2018), arXiv:1801.06653v2 [physics.ins-det]

[137] T. Doke et al., *"LET dependence of scintillation yields in liquid argon*, Nucl. Instr. and Meth. in Phys. Res. **A** 269 (1988) pp. 291-296

[138] T. Doke, *Ionization and excitation by high energy radiation, in Electronic Excitations in Liquefied Rare Gases*, W.F.Schmidt and E.Illenberg, (American Scientific Publishers), 71-93, (2005)

[139] J. B. Birks, *The theory and practice of scintillation counting*, Pergamon Press (1964)

[140] S. Kubota et al., *"Recombination luminescence in liquid argon and in liquid xenon*, Phys. Rev. B **17** (1978), n. 6, pp. 2762-2765

[141] S. Kubota et al., *"Evidence for a triplet state of the self-trapped exciton states in liquid argon, krypton and xenon*, J. Phys. C: Solid State Phys. Vol. 11 (1978) pp. 2645-2651

[142] M. J. Carvalho et al., *Luminescence decay in condensed Argon under high energy excitation*, J. Lumin. **487** (1979) 18-19

[143] R. Acciarri et al., *Effects of nitrogen contamination in liquid argon*, JINST **5** (2010) P06003

[144] D. Whittington et al., *Scintillation Light from Cosmic-Ray Muons in Liquid Argon*, arXiv:1408.1763v5

[145] A. Hitachi et al., *Effect of ionization density on the time dependence of luminescence from liquid argon and xenon*, Phys. Rev. B **27** (1983) 5279-5285

[146] M. Babicz et al., *"A particle detector that exploits Liquid Argon scintillation light*, Nucl. Instrum. Meth. A 958 (2020) 162421

[147] W. Lippincott et al., *Scintillation time dependence and pulse shape discrimination in liquid argon*, Phys.Rev.C 78 (2008) 035801

[148] E. Segreto, *Evidence of delayed light emission of TetraPhenyl Butadiene excited by liquid Argon scintillation light*, arXiv:1411.4524v2 [physics.ins-det] (2015)

[149] H. Cao et al., *"Measurement of scintillation and ionization yield and scintillation pulse shape from nuclear recoils in liquid argon*, Phys. Rev. D 91, 092007 (2015)

[150] B. Krilov et al., *"Channels of energy transfer to atomic Nitrogen in excited Argon-Nitrogen mixtures*, J. Phys. B 35 (2002) 4257

[151] B.K. Lubsandorzhievet al., *"Photoelectron backscattering in vacuum phototubes*, Nucl. Instrum. Meth. A 567 (2006) 12 [physics/0601157]

[152] R. Acciarri et al., *Oxygen contamination in liquid argon: combined effects on ionization electron charge and scintillation light*, JINST **5** (2010) P05003

[153] Lord Rayleigh, *" On the transmission of light through an atmosphere containing small particles in suspension, and on the origin of the blue of the sky* Philos. Mag., 47 (1899)

[154] A. Einstein and L. Hopf, *"Statistische Untersuchung der Bewegung eines Resonators in einem Strahlungsfeld*, Annalen der Physik, 338(16):1105-1115 (1910)

[155] L. D. Landau and E.M. Lifshitz, *"Electrodynamics of Continuous Media*, vol. 8, Pergamon Press (1960)

[156] G.M Seidel et al., *"Rayleigh scattering in rare-gas liquids*, NIM A 489 (2002) 189, arXiv:hep-ex/0111054v2

[157] H. A. Lorentz, *"Ueber die Beziehung Zwischen der Fortpflanzungs-geschwindigkeit des Lichtes und der Krperdichte*, Wiedem. Ann., 9:641-665 (1880)

[158] L Lorenz. *"Ueber das leitungsvermgen der metalle fr wrme und electricitt*, Annalen der Physik, 249(7):422-447 (1881)

[159] A. C. Sinnock, B. L. Smith, *"Refractive indices of the condensed inert gases*, Phys. Rev. 181, (1969) 1297-1307

[160] A. Bideau-Mehu, *"Measurement of refractive indices of neon, argon, krypton and xenon in the 253.7-140.4 nm wavelength range. Dispersion relations and estimated oscillator strengths of the resonance lines*, Journal of Quantitative Spectroscopy and Radiative Transfer 25, (1981) 395-402

[161] E. Grace et al., *"Index of refraction, Rayleigh scattering length, and Sellmeier coefficients in solid and liquid argon and xenon*, arXiv:1502.04213v4 [physics.ins-det] (2017)

[162] N. Ishida et al., *"Attenuation length measurements of scintillation light in liquid rare gases and their mixtures using an improved reflection suppresser*, Nuclear Instruments and Methods in Physics Research Section A: Accelerators, Spectrometers, Detectors and Associated Equipment 384 (23) (1997) 380-386

[163] J. Calvo et al., *"Measurement of the attenuation length of argon scintillation light in the ardm LAr-TPC*, arXiv:1611.02481

[164] A. Neumeier et al., *"Attenuation of vacuum ultraviolet light in liquid argon* Eur. Phys. J. C (2012) 72:2190

[165] A. Neumeier et al., *"Attenuation measurements of vacuum ultraviolet light in liquid argon revisited* NIM A (2015) arXiv:1511.07726v1 [physics.ins-det]

[166] M. Babicz et al., *"Light Propagation in Liquid Argon*, arXive:2002.09346v1 [physics.ins-det] (2020)

[167] D. W. Swan, *"Electron Attachment Processes in Liquid Argon containing Oxygen or Nitrogen Impurity*, Proc. Phys. Soc., **82** (1963)

[168] E. Shibamura et al., *"Ratio of diffusion coefficient to mobility for electrons in liquid argon*, Phys. Rev. A, Vol. 20, n. 6 (1979)

[169] W. Walkowiak, *"Drift velocity of free electrons in liquid argon*, Nucl. Instrum. and Meth. in Phys. Res. A 449 (2000) 288-294

[170] S. Amoruso et al., *"Analysis of the liquid argon purity in the ICARUS T600 TPC*, Nucl. Instr. and Meth. in Phys. Res. A 516 (2004) 68-79

[171] P. Cennini et al., *"Performance of a three-ton liquid argon time projection chamber*, Nucl. Instr. and Meth. in Phys. Res. A 345 (1994) 230-243

[172] F Arneodo et al., *"Performance of the 10 m^3 ICARUS liquid argon prototype*, Nucl. Instrum. Meth. A 498 (2003) 292-311, DOI: 10.1016/S0168-9002(02)01989-7

[173] B. Rossi on behalf of LHEP liquid Argon group, *"Monitoring the parameters of a large size liquid Argon Time Projection Chamber using UV laser beams*, Journal of Physics: Conference Series 308 (2011) 012025 doi:10.1088/1742-6596/308/1/012025

[174] Y. Li et al., *"Measurement of Longitudinal Electron Diffusion in Liquid Argon*, arXiv:1508.07059 [physics.ins-det]

[175] S. E. Derenzo et al., *"Test of a Liquid Argon Chamber with 20-Micrometer RMS Resolution*, Nucl. Instrum. Meth. 122 (1974) 319

[176] T. H. Dey and T. J. Lewis *"Ion mobility and liquid motion in liquefied argon* J. Phys. D: Appl. Phys. 1 (1968) 1019

[177] M. Torti on behalf of the ICARUS Collaboration, *"Search for space charge effects in the ICARUS T600 LAr-TPC*, EPJ Web of Conferences 126 , 05013 (2016) DOI: 10.1051/ epjconf/2016 12605013

[178] R. Santorelli et al., *"Impact of the positive ion current on large size neutrino detectors and delayed photon emission*, 2018 JINST 13 C04015 [arXiv:1712.07971]

[179] M. Antonello et al., *"Study of space charge in the ICARUS T600 detector*, arXiv:2001.08934

[180] T.K. Gaisser et al. (Particle Data Group), http://pdg.lbl.gov/2015/reviews/rpp2015-rev-cosmic-rays.pdf

[181] The MicroBooNE Collaboration, *"Study of Space Charge Effects in MicroBooNE*, MICROBOONE-NOTE-1018-PUB

[182] L. Romero et al., *"Dynamics of the ions in Liquid Argon Detectors and electron signal quenching*, Astropart. Phys. 92 (2017) 11-20 [arXiv:1609.08984]

[183] X. Luo and F. Cavanna, *"Ion transport model for large LArTPC* J. Inst. 15 C 03034 (2020)

[184] G. Bakale et al., *"Effect of an Electric Field on Electron Attachment to SF_6, N_20, and O_2 in Liquid Argon and Xenon*, J. of Phys. Chem., Vol. 80, No. 23, 7976

[185] K. Mavrokoridis et al., *"Argon purification studies and a novel liquid argon-circulation system*, JINST 6 (2011) P08003

[186] A.F. Borghesani et al., *"Electron transmission through the Ar liquid-vapor interface*, Phys. Let. A Volume 149, number 9 (1990)

[187] A. Y. Bolozdynya, *"Two-phase emission detectors and their applications*, Nucl. Instrum. and Meth. in Phys. Res. A 422 (1999) 314-320

[188] E. M. Gushchin et al., *"Emission of hot electrons from liquid and solid argon and xenon*, Sov. Phys. JETP 55(5), May 1982

[189] W. Shockley, *"Currents to Conductors Induced by a Moving Point Charge*, J. Appl. Phys., vol. 9, pp. 635-636, (1938)

[190] S. Ramo, *"Current Induced by Electron Motion*, Proc. IRE, vol. 27, pp. 584-585, (1939)

[191] A. J. P. L. Policarpo, *"Light Production and Gaseous Detectors*, Physica Scripta, Vol. 23, pp. 539-549 (1981)

[192] A. Zani, *"The WArP Experiment: A Double-Phase Argon Detector for Dark Matter Searches*, Hindawi Publishing Corporation, Advances in High Energy Physics, Vol. 2014, 205107, http://dx.doi.org/10.1155/2014/205107

[193] J. Calvo et al., *"The ArDM Liquid Argon Time Projection Chamber at the Canfranc Underground Laboratory: a ton-scale detector for Dark Matter Searches* [arXiv:1612.06375] (2016)

[194] DarkSide Collaboration, *"Electroluminescence pulse shape and electron diffusion in liquid argon measured in a dual-phase TPC*, Nucl. Instr. and Meth. A, 904 (2018) pp 23-34 [arXiv: 1802.01427]

[195] T. Dandl *"Optical Properties of Liquid Noble Gas Detector Media*, https://www.mll-muenchen.de/forschung/astroteilchenphysik/liquid_noble_gases.pdf

[196] T. Takahashi et al., *"Emission spectra from Ar-Xe, Ar-Kr, Ar-N_2 , Ar-CH_4 , Ar-CO_2 and Xe-N_2 gas scintillation proportional counters*, Nucl. Instrum. Meth. 205 (1983) 591-596

[197] C. M. B. Monteiro et al., *"Secondary scintillation yield in pure argon"*, Phys. Let. B 668 (2008) 167-170

[198] M. A. Feio et al., *"Thresholds for secondary light emission by noble gases*, Jpn. J. Appl. Phys. 21 1184 (1982)

[199] P. Benetti et al., *"First results from a Dark Matter search with liquid Argon at 87 K in the Gran Sasso Underground Laboratory*, Astropart. Phys. Vol. 28, Issue 6 (2008) pp. 495-507

[200] F. P. Santos et al., *"Three-dimensional Monte Carlo calculation of the VUV electroluminescence and other electron transport parameters in xenon* J. Phys. D: Appl. Phys. 27 42 (1994)

[201] T. Lux, *"Charge and Light Production in the Charge Readout System of a Dual Phase LAr TPC*, J. of Instr., Vol. 14 (2019)

[202] L. T. Specht et al., *"Electron ionization and excitation coefficients for argon, krypton, and xenon in the low E/N region*, Journal of Applied Physics 51, 166 (1980); doi: 10.1063/1.327395

[203] P. Fonte et al., *"Feedback and breakdown in parallel-plate chambers*, Nucl. Instrum. Meth. in Phys. Res. A 305 (1991) 91-110

[204] C. A. B. Oliveira et al., *"Simulation of VUV electroluminescence in micropattern gaseous detectors: the case of GEM and MHSP*, arXiv:1206.1646 [physics.ins-det] (2012)

[205] P. Bhattacharya et al., *"Investigation of Ion Backflow in Bulk Micromegas Detectors*, arXiv:1605.02896 [physics.ins-det] (2016)

[206] V. Boccone, et al., *"Development of wavelength shifter coated reflectors for the ArDM argon dark matter detector*, Journal of Instrumentation 4 (06) (2009) P06001 http://stacks.iop.org/1748-0221/4/i=06/a=P06001

[207] Midas (Maximum Integration Data Acquisition System) http://midas.psi.ch

[208] M. Auger et al., *"A Novel Cosmic Ray Tagger System for Liquid Argon TPC Neutrino Detectors*, Instruments 1 (2017) 2 [arXiv:1612.04614].

[209] A. Williams et al., *"An efficient and robust Ray-Box intersection algorithm*, DOI: 10.1145/1198555.1198748, https://dl.acm.org/doi/10.1145/1198555.1198748

[210] C. Lastoria, "*Analysis of the light production and propagation in the 4-tonne dual- phase demonstrator* 2020 JINST 15 C06029, DOI:10.1088/1748-0221/15/06/C06029, arXiv:1911.06880v2 [physics.ins-det]

[211] C. Lastoria, on behalf of DUNE Collaboration, "*Scintillation light production, propagation and detection in the 4-ton dual-phase LAr-TPC demonstrator (data analysis and simulations)* PoS LeptonPhoton2019 (2019) 156, DOI:10.22323/1.367.0156, arXiv:1911.06874v1 [physics.ins-det]

[212] https://root.cern.ch/doc/master/classTMinuit.html

[213] F. James, "*MINUIT Function Minimization and Error Analysis: Reference Manual Version 94.1*, CERN-D-506, https://inspirehep.net/literature/1258343

[214] E. Hogenbirk et al., "*Field dependence of electronic recoil signals in a dual-phase liquid xenon time projection chamber*, arXiv:1807.07121 [physics.ins-det] (2018)

[215] S. Agostinelli et al., "*GEANT4: A Simulation toolkit*, Nucl. Instrum. Meth. A 506 (2003) 250-303

[216] Light Analysis Working Group, "*Scintillation light collation, production, and propagation in the WA105-DP demonstrator*", https://indico.fnal.gov/event/20144/contributions/55817/attachments/34849/42584/DUNECollMeet_DPPDSession_CLastoria28012020.pdf

[217] J. May et al., "*Operational properties of photomultiplier tubes in the miniboone experiment*, in 2002 IEEE Nuclear Science Symposium Conference Record, vol. 1, pp. 446-449 vol.1, 2002

[218] Hamamatsu Photonics, "*Photomultiplier tubes: Basic and applications (v3a)*

[219] A. Chappuis, "*Study and simulation of the scintillation light produced and propagating in a dual phase liquid argon time projection chamber, in the context of the DUNE experiment*, Theses, Universit Grenoble Alpes (2018)

[220] M. Szydagis et al., "*NEST: A Comprehensive Model for Scintillation Yield in Liquid Xenon*, JINST 6 (2011) P10002

[221] C. Benson et al., "*Measurements of the intrinsic quantum efficiency and absorption length of tetraphenyl butadiene thin films in the vacuum ultraviolet regime*. Eur. Phys. J. C78.4 (2018)

[222] A. Scarpelli, "*Performance studies of the dual-phase Liquid Argon TPC for the DUNE experiment and analysis of the 4-tonne prototype detector data*, PhD thesis, Universit de Paris, 30/09/2019

[223] B. Aimard et al., "*Study of scintillation light collection, production and propagation in a 4 tonne dual-phase LArTPC*, arXiv:2010.08370 [physics.ins-det] (2020), prepared for submission on JINST

[224] G Balik, "*Yearly progress report on WA105/ProtoDUNE dual phase* (2016). Rapp. tech. CERNSPSC-2016-017, SPSC-SR-184